PhD THESIS

prepared at
INRIA Sophia Antipolis

and presented at the
University of Nice-Sophia Antipolis
Graduate School of Fundamental and Applied Sciences

A dissertation submitted in partial fulfillment
of the requirements for the degree of

DOCTOR OF MATHEMATICS
Specialized in Neuroscience

Mesoscopic models of cortical structures

François GRIMBERT

Advisor	Pr. Olivier Faugeras	INRIA Sophia Antipolis, France
Reviewers	Pr. Steven Coombes	University of Nottingham, UK
	Pr. Jacques Henry	INRIA futurs Bordeaux, France
Examiners	Dr. Frédéric Chavane	INCM Marseille, France
	Pr. Pascal Chossat	UNSA Nice, France
	Pr. Yves Frégnac	UNIC Gif-sur-Yvette, France

UNIVERSITÉ NICE-SOPHIA ANTIPOLIS - UFR Sciences

École Doctorale SFA
(Sciences Fondamentales et Appliquées)

THÈSE

pour obtenir le titre de
DOCTEUR EN MATHEMATIQUES
de l'UNIVERSITÉ de Nice-Sophia Antipolis
Discipline: Neurosciences

présentée et soutenue par

François GRIMBERT

Modèles mésoscopiques de structures corticales

Thèse dirigée par Pr. Olivier FAUGERAS

Soutenue le 7 mars 2008

Composition du jury:

Rapporteurs	Pr. Steven Coombes	University of Nottingham, UK
	Pr. Jacques Henry	INRIA futurs Bordeaux, France
Examinateurs	Dr. Frédéric Chavane	INCM Marseille, France
	Pr. Pascal Chossat	UNSA Nice, France
	Pr. Yves Frégnac	UNIC Gif-sur-Yvette, France

Abstract

This thesis deals with *mesoscopic* models of cortical columns and cortical areas. Here, *mesoscopic* means that we use coarse-grained cortical units, called *neural masses*, as elementary building blocks in our models. *Neural masses* are homogeneous neuronal populations confined in a *cortical column*. So we model a cortical column as a small network of interacting neural masses, and a cortical area as a two-dimensional, continuous network of such cortical columns, forming then a *neural field*. Mesoscopic models have two main advantages. First, they are very economic in terms of the number of parameters and variables needed for their description. This allows easier computations as well as more tractable mathematical models compared to networks using neurons as elementary building blocks. Second, most of the biophysical data needed to model cortical structures at the mesoscopic scale is available. In particular, a considerable amount of mesoscopic intracolumnar and intercolumnar connectivity data has been collected in the last decade. Such data is still missing at the level of single neurons.

The first part of this thesis is dedicated to cortical columns. We discuss the most well-known biological principles that allow to define cortical columns, review the intracolumnar circuitry and propose a mesoscopic approach to cortical column models. Then we present a mathematical study of a mesoscopic column model –known as *Jansen's model*– based on bifurcation techniques. In the second part, we study two nonlinear neural field models with very different mathematical techniques. The first model consists in an infinite two-dimensional field using a Heaviside distribution to convert the average membrane potential of neural masses into their average firing rate. This model needs a precise instantiation of the connectivities and a precise definition of the patterns we expect it to produce to make its analysis tractable. Then we can make a linear stability analysis of its solutions. In this framework, we focus on the analysis of *two-dimensional bumps* (i.e. localized areas of high activity). The second neural field model is defined on a compact domain and uses a sigmoid instead of a Heaviside distribution. We discuss its well-posedness, stability and ability to show *synchrony* via functional analysis techniques. The last part of this thesis deals with the modeling of *voltage sensitive dye optical imaging* (VSDOI) signals. We show that neural fields can naturally integrate biophysical data and hence constitute suitable models of cortical areas. Then we propose a biophysical formula, based on neural fields, for the direct problem of VSDOI. Finally, we make numerical simulations of this direct problem and reproduce optical signals that have been observed in the visual cortex of mammals and the barrel cortex of the rat.

Résumé

Cette thèse traîte de modèles mésoscopiques de colonnes et d'aires corticales. Dans ce contexte, "mésoscopique" signifie que nous utilisons dans nos modèles des briques de base relativement grossières, appelées "masses neuronales". Les masses neuronales sont des populations de neurones homogènes confinées à une colonne corticale. Nous modélisons donc une colonne corticale comme un petit réseau de masses neuronales en interaction, et une aire, comme un réseau continu de telles colonnes, formant un champ neuronal. Les modèles mésoscopiques ont deux principaux avantages. Premièrement, ils sont peu coûteux en nombre de paramètres et de variables nécessaires à leur description. Ceci rend les calculs numériques moins lourds et les équations plus faciles à traîter mathématiquement que pour des réseaux qui utilisent les neurones comme constituant élémentaire. Deuxièmement, l'essentiel des données biophysiques nécessaires à la modélisation de structures corticales à l'échelle mésoscopique est disponible. En particulier, une quantité considérable de données mésoscopiques sur les connectivités intra- et inter-columnaires a été mise au jour au cours de la dernière décennie. De telles données font encore défaut au niveau du neurone. La première partie de cette thèse est consacrée aux colonnes corticales. Nous y discutons des principes biologiques les mieux connus qui permettent de définir des colonnes, nous passons en revue les connaissances actuelles sur la microcircuiterie intracolumnaire et nous proposons une approche mésoscopique pour la modélisation de colonnes. Ensuite, nous présentons une étude mathématique d'un modèle mésoscopique de colonne –appelé modèle de Jansen– basée sur les bifurcations. Dans la seconde partie, nous étudions deux modèles non-linéaires de champs neuronaux sous deux angles mathématiques très différents. Le premier modèle consiste en un champ infini à deux dimensions où la conversion du potentiel de membrane des masses neuronales en taux de décharge moyen est faite avec une distribution de Heaviside. Ce modèle nécessite une instanciation précise des connectivités et de la forme des solutions que l'on cherche pour aboutir à un problème mathématique abordable. On peut ensuite faire une analyse de la stabilité linéaire de ces solutions. Dans le cadre de ce modèle, nous nous intéressons à l'analyse de bosses d'activité en deux dimensions (c'est-à-dire des zones localisées de haute activité). Le second modèle de champ neuronal est défini sur un domaine compact et la distribution de Heaviside y est remplacée par une sigmoïde. Nous discutons l'existence, l'unicité et la stabilité des solutions de ces équations de champ neuronal, et la capacité d'un tel modèle à exhiber de la synchronie, en utilisant des techniques d'analyse fonctionnelle. La dernière partie de cette thèse est consacrée à la modélisation des signaux d'imagerie optique extrinsèque utilisant des colorants sensibles au potentiel. Nous montrons d'abord que les champs neuronaux peuvent naturellement intégrer des données biophysiques et de ce fait, constituer des modèles d'aires corticales satisfaisants. Nous proposons ensuite une formule biophysique, basée sur les champs

neuronaux, pour le problème direct de l'imagerie optique extrinsèque. Finalement, nous présentons des simulations numériques de ce problème direct qui reproduisent des signaux optiques observés dans le cortex visuel des mammifères ainsi que dans le cortex barrelé du rat.

Acknowledgments

This thesis was performed in the Odyssée lab at INRIA Sophia-Antipolis, under the supervision of Olivier Faugeras. It was funded by Elekta AB and the Région Provence-Alpes-Côte-d'Azur.

I would like to thank my director, Olivier Faugeras, for having supervised my thesis. His deep scientific views and amazing energy to do mathematics are definitely an example for me.

Next, I would also like to express my deep thanks to Stephen Coombes and Jacques Henry for having accepted to review my manuscript despite the important amount of work this required. I am also very grateful to Frédéric Chavane, Pascal Chossat and Yves Frégnac for having kindly accepted to examine this thesis.

Many people have in various ways contributed to different parts of the work presented in this manuscript and I want to acknowledge them here: Camilo La Rota and Frédéric Chavane for having been very nice guides through the "real" brain, Thierry Viéville and Bruno Cessac for having kindly supported me, Christophe Lenglet and Théodore Papadopoulo for their help with computers (actually, many others helped me, but as Fermat would say: *marginis exiguitas non caperet*), Marie-Cécile Lafont for her kind technical assistance (especially on making T-shirt thesis gifts) and Rachid Deriche for his inspired advices on barbecues and German beer (...or his advices inspired by barbecues and German beer, I don't remember quite well...). A special thank also goes to Alain Destexhe, who has been an invaluable support for salt.

Finally, I cannot thank my friends and family here since they mainly distracted me from my thesis, using the most sophisticated techniques, among which *coinche*, small talk, never-ending discussions, trips, parties, food, support, friendship and love. So, I do not thank them, but I do love them.

Contents

Introduction **22**

I Cortical columns **23**

1 Cortical microcircuits and cortical columns **25**
- 1.1 Biological cortical columns . . . 26
  - 1.1.1 Basic organizing principles in the cortex . . . 26
  - 1.1.2 The anatomical column . . . 26
  - 1.1.3 Cortical columns as physiological units . . . 29
  - 1.1.4 From physiological to functional units . . . 30
  - 1.1.5 What drives the cortical column activity? . . . 33
- 1.2 Local connectivity in the cortex . . . 34
  - 1.2.1 Neuronal compartments and selectivity of synapses . . . 35
  - 1.2.2 Excitatory network . . . 36
  - 1.2.3 Inhibitory action . . . 41
- 1.3 The mesoscopic approach to cortical columns . . . 45
  - 1.3.1 Neural masses . . . 45
  - 1.3.2 An example of mesoscopic cortical column model . . . 47

2 Cortical column models **49**
- 2.1 Description of the model . . . 50
- 2.2 Bifurcations and oscillations . . . 55
  - 2.2.1 Fixed points . . . 55
  - 2.2.2 Bifurcations and oscillatory behaviour in Jansen's model . . . 57
  - 2.2.3 Synthesis . . . 61
  - 2.2.4 What about other parameters? . . . 62
- 2.3 Conclusion . . . 65

II Mathematical neural field models **67**

3 Infinite neural field models **69**
- 3.1 Neural field equations . . . 70
  - 3.1.1 Interactions between a few neural masses . . . 70
  - 3.1.2 Neural fields models . . . 72
- 3.2 Study of bump solutions . . . 72
  - 3.2.1 Stationary solutions . . . 73
  - 3.2.2 Stability of the solutions . . . 76
- 3.3 Construction of bump solutions . . . 78

3.3.1 Existence . . . 79
3.3.2 Stability . . . 79
3.4 Conclusion . . . 82

4 Bounded neural field models **83**
4.1 The models . . . 85
4.1.1 The local models . . . 85
4.1.2 Neural fields models . . . 87
4.2 Existence and uniqueness of a solution . . . 88
4.2.1 General solution . . . 89
4.2.2 Homogeneous solution . . . 90
4.2.3 Some remarks about the case $\Omega = \mathbb{R}^q$ . . . 92
4.3 Absolute stability of the general solution . . . 92
4.3.1 The general case . . . 93
4.3.2 The convolution case . . . 97
4.4 Absolute stability of the homogeneous solution . . . 99
4.4.1 The general case . . . 99
4.4.2 The convolution case . . . 102
4.4.3 Complete synchronization . . . 103
4.5 Extending the theory . . . 103
4.5.1 Existence, uniqueness and stability of a solution . . . 103
4.5.2 Locally homogeneous solutions . . . 104
4.5.3 Higher order PSPs . . . 107
4.6 Numerical examples . . . 109
4.6.1 The convolution case . . . 110
4.6.2 Homogeneous solutions . . . 112
4.6.3 Locally homogeneous solutions . . . 115
4.6.4 Absolute stability of pseudo locally homogeneous solutions . . . 118
4.7 Conclusion . . . 119

III Biophysical neural fields for VSD optical imaging modeling **123**

5 A neural field model for VSD optical imaging signals **125**
5.1 Neural field model of a cortical area . . . 126
5.2 Principle of VSD optical imaging . . . 130
5.3 Model of the OI signal . . . 132

6 Simulations of optical signals in the visual and barrel cortices **139**
6.1 Horizontal connectivity . . . 140
6.1.1 Mammals visual cortex . . . 140
6.1.2 Barrel cortex of the rat . . . 142
6.2 Simulations . . . 144
6.2.1 Visual cortex . . . 144
6.2.2 Barrel cortex . . . 152
6.3 Discussion . . . 155

Conclusion **162**

Appendix **163**

A Firing patterns of cortical neurons **165**

B Notations and background material **171**
B.1 Introduction 171
B.2 Matrix norms and spaces of functions 171
B.3 Summary of important notations 173

C Complements to the functional analysis of neural field models **175**
C.1 Global existence of solutions 175
C.2 Computation of operator norms 176
C.3 Complements to the study of higher order PSPs 176

Glossary **179**

Bibliography **181**

List of Figures

1.1 Cortical layers. 27
1.2 Cortical areas. 27
1.3 Vertical redistribution of sensory inputs. 28
1.4 Anatomical minicolumns. 28
1.5 Mountcastle's pioneering experiment. 29
1.6 Physiological columns. 29
1.7 Barrel organization of rat's sensory cortex. 30
1.8 Orientation preference columns. 31
1.9 Continuity and discontinuities in functional maps. 32
1.10 Non-columnar structure. 32
1.11 Spontaneous vs triggered activity. 33
1.12 Spread of activity among barrels. 34
1.13 Neuronal compartments and dendritic spines. 36
1.14 Dendritic and axonal trees of excitatory neurons. 37
1.15 Summation of EPSPs. 38
1.16 Excitatory projections. 39
1.17 Inhibitory neurons. 42
1.18 Diversity of the interneurons. 43
1.19 Simplified inhibitory network. 46
1.20 Weighted wiring diagram. 48

2.1 Neural mass model of a cortical unit. 50
2.2 PSP profiles. 51
2.3 Sigmoidal transform. 52
2.4 Alpha activity in Jansen's model. 54
2.5 Real and simulated ictal activities. 56
2.6 Bifurcations analysis. 59
2.7 Hopf bifurcation. 60
2.8 SNIC bifurcation. 61
2.9 Stable attractors. 63
2.10 Activities produced by Jansen's model. 64
2.11 Bifurcation analysis based on other parameters. 65

3.1 Interacting layers. 70
3.2 θ_e and θ_i. 80
3.3 Domain of local conditions fulfillment. 80
3.4 Pseudo-bumps profiles. 80
3.5 Stability analysis. 81
3.6 Stable bumps. 81

3.7 Stability domain. 82

4.1 Inputs in the convolution case. 111
4.2 Lack of synchrony in the convolution case. 112
4.3 Stability in the convolution case: spatial frequencies. 112
4.4 Stability in the convolution case: temporal behavior. 113
4.5 Lack of stability in the convolution case: spatial frequencies. 113
4.6 Lack of stability in the convolution case: temporal behavior. 114
4.7 Connectivities in the homogeneous case. 114
4.8 Synchrony in the homogeneous case. 115
4.9 Lack of synchrony in the homogeneous case. 116
4.10 Connectivities in the locally homogeneous case. 117
4.11 Inputs in the locally homogeneous case. 117
4.12 Locally homogeneous solutions, part 1. 118
4.13 Locally homogeneous solutions, part 2. 118
4.14 Lack of synchrony in the locally homogeneous case, part 1. 119
4.15 Lack of synchrony in the locally homogeneous case, part 2. 119
4.16 Locally pseudo-homogeneous solution, part 1. 120
4.17 Locally pseudo-homogeneous solution, part 2. 120

5.1 Simplified brain and layered cortical area. 126
5.2 Postsynaptic potential. 127
5.3 White matter afferents to V1. 128
5.4 Vertical connectivity diagram. 129
5.5 Horizontal connectivity. 130
5.6 Principle of VSDOI. 131
5.7 Distribution of dye molecules. 133
5.8 Light absorption/diffusion. 134
5.9 Contribution of one layer. 134
5.10 Microscopic level. 135

6.1 Distribution of axonal boutons in the visual cortex. 141
6.2 Connectivity patches in the visual cortex. 141
6.3 Non-patchy non-selective projections of a single neuron. 142
6.4 Comparative distribution of PCs and BCs projections. 143
6.5 Elongated axonal projections in the direction of barrel rows. 144
6.6 Cortical correlate to the line-motion illusion. 145
6.7 Color-coded vertical connectivity matrix. 147
6.8 Non-patchy projections. 148
6.9 Patchy projections. 149
6.10 Stimuli and inputs. 150
6.11 Line-motion illusion simulation. 152
6.12 Barrels and septa. 153
6.13 Barrel cortex connectivity. 153
6.14 Single whisker stimulations. 154
6.15 Simulation of the barrel cortex. 155
6.16 Unimodal vs multimodal excitation. 157

A.1 Basic features of firing patterns. 165
A.2 Regular spiking and chattering. 166

A.3 Intrinsic bursting. 167
A.4 Basic interneurons firing patterns. 167
A.5 Classes and subclasses of interneurons firing patterns. 169

Introduction

The brain is a complex system in the strong sense: it features a great number of units interacting in a nonlinear fashion. This system cannot be globally apprehended yet but some structures and functions, emerging at different spatial and temporal scales, can be observed and sometimes modeled.

At the microscopic scale, we know that certain neurons are highly specialized and can be related to precise functions, like e.g. neurons involved in face recognition. However in this thesis, we choose not to model brain structures at the scale of individual neurons. Instead we use a looser, *mesoscopic* scale, considering homogeneous localized populations of hundreds to thousands of neurons, called neural masses, as elementary building blocks. Our intention in this thesis is to model *cortical columns* and *cortical areas* composed of such mesoscopic blocks. Cortical columns are vertical cortical units spanning the whole depth of the cortical sheet, with a diameter comprised between $50\mu m$ and $1mm$. Cortical areas are wider domains of the cortex (centimeter scale) that we can see as horizontal networks of cortical columns.

There are at least three reasons why we think that the mesoscopic scale is relevant to do this modeling.

- In most cases, individual neurons cannot be labeled with a precise function nor linked to a specific stimulus. Hence they more likely blindly contribute to the computational power of bigger, specialized neuronal networks. The idea that individual neurons are not specialized is illustrated by neuronal plasticity: as a function stops (for example because an organ has been removed), neurons involved in this function are simply re-used by another function, after a period where the neuron learns its new task.

- While MEG and scalp EEG recordings mostly give a bulk signal of a cortical area, multi-electrode recordings, in vitro experiments on pharmacologically treated brain slices and new imaging techniques like extrinsic optical imaging can provide a spatially detailed description of populations dynamics in a macroscopic part of the brain like an area. Realistic modelling of an area at the scale of the neuron is still difficult for obvious complexity reasons. Starting from mesoscopic building blocks like neural masses, described by the average activity of their neurons, is therefore a reasonable choice.

- Finally, the population scale is in good agreement with available local connectivity data. Indeed, intracolumnar connectivity data is obtained by averaging correlations between the activities of different types of neurons inside a column and thus constitutes a mesoscopic connectivity information. The same holds for intercolumnar connectivity inside an area, since it is generally established by tracking the projections made by a whole local population of neurons. Moreover at this coarse-grained scale local connectivity is supposed to be spatially invariant within an area. Hence, we should be able to build biophysically relevant economic models (in terms of the number of parameters) of cortical columns and areas.

This thesis consists of three parts.

The first part focuses on cortical columns. In the first chapter we try to answer several questions on biological columns. When can we speak of a columnar organization in the cortex? How can we define a column? What is its spatial extent? What drives its dynamics? We will see that the notion of cortical column is tricky, that it is not relevant in all areas of the brain and strongly depends on the considered

species. There are at least two ways to define cortical columns, on the basis of anatomical data or by relating them to functions. Cortical columns cannot generally be considered as isolated units interacting via horizontal projections but more likely form continua of highly interconnected, overlapping units. Then, we explore the complex microcircuitry of a column. The columnar organization is not made of random connections between neurons. Instead, these are highly selective and must be described at the level of neuronal compartments. Despite the fact that the network formed by excitatory neurons is quite well understood, the action of inhibitory cells is way more complex, because of the variety of their anatomical types, firing patterns, connectivity and synaptic mechanisms. Then, we take a mesoscopic look at this microscopic organization and present some principles for building mesoscopic column models.
In chapter 2 we propose a mathematical study of a mesoscopic column model known as *Jansen's model*. We use bifurcations theory and the software *XPP-Aut* (available on Bard Ermentrout's webpage: `http://www.pitt.edu/~phase/`) to build a bifurcation diagram of the model and characterize its response to different stimulation intensities. This way we mainly explain two phenomena: alpha activity is related to Hopf bifurcations and epileptic spikes to a saddle-node bifurcation on an invariant circle (SNIC).

In the second part of the thesis, we form continuous networks of cortical columns and study the resulting *neural fields* with various mathematical techniques.
In chapter 3 we consider an infinite two-dimensional field composed of two layers of neurons (excitatory and inhibitory) and try to characterize some of its stationary solutions, namely, circularly symmetric *bumps* (i.e. localized areas of high activity). These patterns are interesting from a neuroscientific point of view since they have been linked to working memory tasks in the prefrontal cortex. We study the existence of bumps, depending on their radii, and make a linear stability analysis on them. We finally construct stable two-dimensional bumps in a principled manner, by imposing local conditions of existence and conditions of stability.
In chapter 4, we propose more realistic and general neural field models featuring an arbitrary number of neuronal populations. They are defined on compact domains and use smooth sigmoids as pulse-to-wave transforms (while discontinuous Heaviside distributions were used in the preceding chapter). We use functional analysis techniques to establish conditions of existence, uniqueness and stability of the solutions of these equations. We also discuss the conditions needed to obtain homogeneous or locally homogeneous solutions, accounting for global or local synchrony among the columns of the field.

The last part of this thesis is dedicated to the modeling of voltage sensitive dye optical imaging signals (VSDOI).
In chapter 5, we show that neural field models can naturally integrate the most recent data on intra- and inter-columnar connectivity and more generally, that they are natural biophysical models for cortical areas. Then we introduce the principles of VSDOI and finally propose a formula for the direct problem of optical imaging, based on a neural field description of an area.
In the last chapter, we simulate different phenomena observed by VSDOI in the visual cortex of mammals and in the rat's barrel cortex. We describe the functional organization of these cortices, parametrize the corresponding neural fields, extract

the OI signal by the formula developed in chapter 5 and finally display the results. We have been able to reproduce the principal features of two OI experiments: the cortical correlates of the line-motion illusion and the different modes of propagation of cortical activity in the rat's barrel cortex, depending on the strength of the whisker's stimulation.

Part I

Cortical columns

CHAPTER 1

CORTICAL MICROCIRCUITS AND CORTICAL COLUMNS

OVERVIEW

This chapter is dedicated to a better understanding of the concept of *cortical column*. We start with the different definitions of a cortical column as an anatomical, physiological or functional cortical subunit and discuss the relevance of columns and the question of their spatial extent. Then we present the most striking features of cortical microcircuits to get an insight of the neuronal organization inside a column. Finally we present some principles supporting mesoscopic models of cortical columns, with neural masses as their building blocks. Our goal here is not to build a detailed model of the cortical column like what is done in Roger Traub's work [114] or in the Blue Brain Project [77], but to shed light on the main components and interactions inside the column. This chapter is part of the technical report [45] (2007).

Contents

1.1 Biological cortical columns 26
  1.1.1 Basic organizing principles in the cortex 26
  1.1.2 The anatomical column 26
  1.1.3 Cortical columns as physiological units 29
  1.1.4 From physiological to functional units 30
  1.1.5 What drives the cortical column activity? 33
1.2 Local connectivity in the cortex 34
  1.2.1 Neuronal compartments and selectivity of synapses 35
  1.2.2 Excitatory network 36
  1.2.3 Inhibitory action 41
1.3 The mesoscopic approach to cortical columns 45
  1.3.1 Neural masses 45
  1.3.2 An example of mesoscopic cortical column model 47

1.1 BIOLOGICAL CORTICAL COLUMNS

1.1.1 Basic organizing principles in the cortex

The cortex is the superficial part of the encephalon and represents the biggest part of grey matter in the brain. It has a horizontal organization in layers (*laminae*) of different types of cells (figure 1.1). The number of layers, their cell composition, their thickness and organization are not the same over the surface of the cortex. Those differences led neuroanatomists to divide the cortex into small regions called *areas* (figure 1.2) where those characteristics were homogeneous and that corresponded to different functions, e.g., vision or motion. Nevertheless most of the cortex is made up of six layers of neurons, from layer I at the surface of the cortex to layer VI that lies next to the white matter. For humans, its thickness varies from 3 to 6 mm.

About fourty types of neurons have been identified through the cortex but they can essentially be divided into only two classes: *projection neurons* and *local interneurons*. Projection neurons (also called *principal neurons*) are excitatory cells, most of them having a pyramidal cell body and being situated in layers III, V and VI of the cortex. Interneurons can be found in all layers but they just amount to 20 up to 25% of cortical neurons and are often inhibitory. Information processing in the cortex is multi-step and the axons of projection neurons carry information from one stage to the next, sometimes in distant groups of neurons. Interneurons can receive the same input as principal neurons but just convey it to local cells implied in the same stage of information processing. More detailed information about cortical structure and function can be found in [60, 61, 87].

The organization of the cortex is not only laminar. It has been observed that neurons one runs across when moving perpendicular to the cortex tend to be connected to each other and to respond to precise stimulations with similar activities throughout the layers. They form a *cortical column*.

1.1.2 The anatomical column

Many cortical neurons throw their axons and dendrites from the cortex surface to the white matter thereby forming the anatomical basis of the columnar organization in the cortex (figure 1.3-B and 1.4). Nervous fibers from the thalamus mostly end in layer IV where they are connected to stellate neurons. These neurons throw their axons towards the surface of the cortex, parallel to apical dendrites of neighboring pyramidal neurons, and establish connections with them (figure 1.3-C). The thalamo-cortical input is therefore conducted within a thin column of strongly connected cells so that the same information is shared throughout the depth of the cortex perpendicular to its surface [61].

Several studies have shown biological evidences for such small aggregates of about one hundred neurons, 20 up to 50 μm wide, called *minicolumns* or *microcolumns* (see figure 1.4). Their formation is due to the radial migration of neurons during brain development [18, 82].

However the minicolumn hypothesis does not solve the problem of defining cortical columns. They have not been extensively observed among species, nor among cortical areas. Moreover, horizontal connectivity should not be underestimated and neighboring minicolumns, far from being isolated, make numerous connections. These

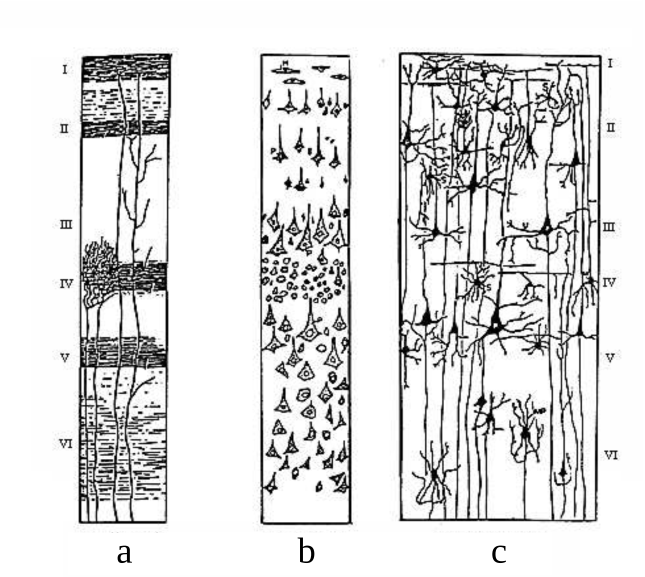

Figure 1.1: *Layer organization of the cortex (a) Weigert's coloration shows myelinated fibers (axons) and so the connections inside and between layers, (b) Nissl's coloration only reveals cell bodies (c) Golgi's coloration shows the whole cells (From [83]).*

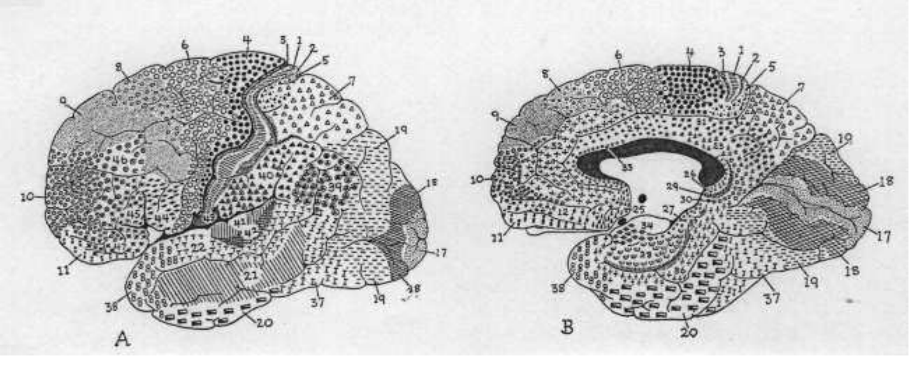

Figure 1.2: *In 1909, Brodmann [17] divided the cortex into 52 cytoarchitectonic areas according to the thickness of the cortical layers. For example, layer IV is very thin in the primary motor cortex (area 4) while it is very thick in the primary visual cortex (area 17).*

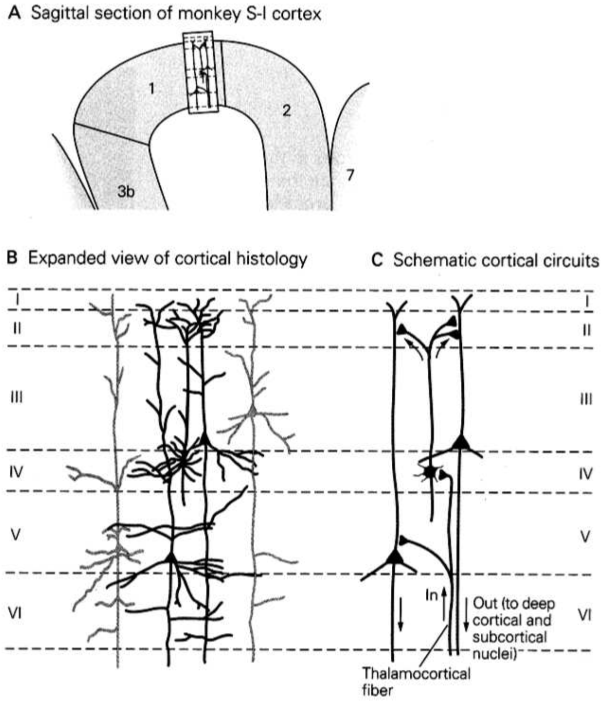
A Sagittal section of monkey S-I cortex
1
2
3b
7
B Expanded view of cortical histology
C Schematic cortical circuits
I
II
III
IV
V
VI
In
Out (to deep cortical and subcortical nuclei)
Thalamocortical fiber

Figure 1.3: *(A) Sagittal section of the primary somatosensory cortex of the monkey (S-I) (B) Morphology of relay cells from layers III to V. Stellate neurons (layer IV) receive information from the thalamus and transmit it to neighboring pyramidal cells in superficial layers of the cortex. Pyramidal cells throw their axons towards deep layers of the cortex and other cortical or sub-cortical regions. They also establish horizontal connections with neighboring columns sharing the same physiological properties (C) Diagram of intra-cortical excitatory circuitry (From [61]).*

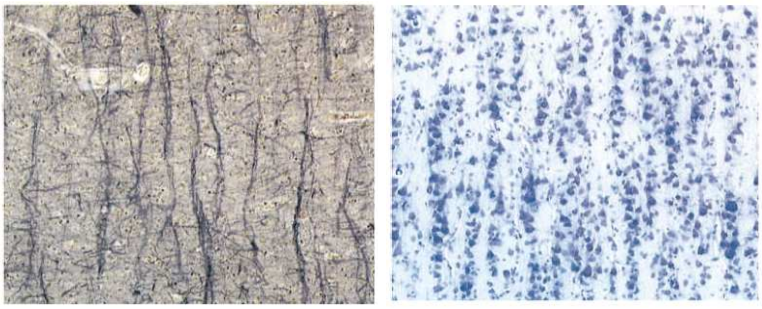

Figure 1.4: *Myelinated fibre bundles (left) and cell soma aggregates (right) in the same cortical region. These observation suggest minicolumnar organization in the cortex(From [18]).*

horizontal connections explain the observation of larger columnar units, as we will see in the following.

1.1.3 Cortical columns as physiological units

In 1957, Mountcastle discovered a columnar organization in the cortex [81] (see figure 1.5).

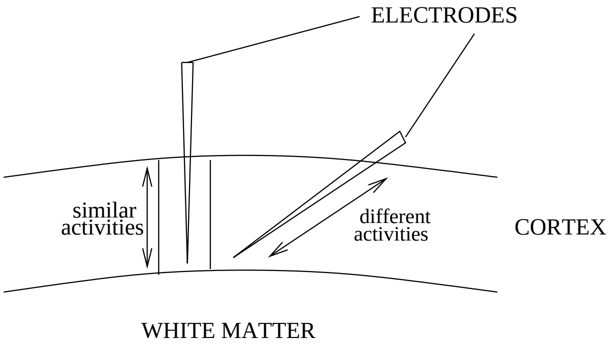
ELECTRODES
similar activities
different activities
CORTEX
WHITE MATTER

Figure 1.5: *Mouncastle's pioneering experiment. When he moved an electrode perpendicular to the cortex surface, he encountered neurons with similar electrical activities while moving the electrode obliquely gave him different types of recordings. So he showed the existence of 300-500 μm wide columns in the cortex.*

With electrode recordings, he showed that neurons inside columns of 300 to 500 μm of diameter displayed similar activities. Those physiological units are usually called *macrocolumns*. In figure 1.6, we see physiological columns obtained from the diffusion of a radioactive substance.

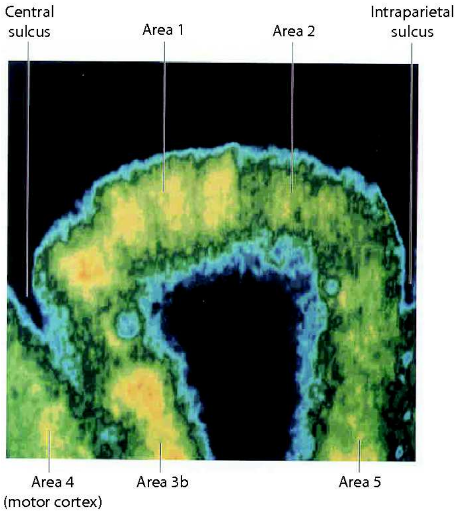
Central sulcus
Area 1
Area 2
Intraparietal sulcus
Area 4 (motor cortex)
Area 3b
Area 5

Figure 1.6: *Columns from the primary somatosensory cortex revealed by autoradiography after 45 minutes of stroking the hand of a monkey, which is then sacrificed, with a brush. On this sagittal section of the cortex a high activity (proportional to the concentration of a radioactive substance) can be viewed in areas 1 and 3b. Columns are well defined in area 1 but not in area 3b (From [61]).*

Some of them are spatially well defined while some others are more difficult to distinguish from one another. What is the functional role of such units?

1.1.4 From physiological to functional units

Many experiments on somatosensory and visual cortices made it possible to relate physiological columns to sensory functions [53, 54, 61, 74, 81] (see figure 1.6, 1.7 and 1.8). In some cases the processing site of a given function seems quite clearly defined like in rat's sensory cortex where every whisker is associated with a sharply bounded cortical site in layer IV (see figure 1.7). However such a *barrel* structure is less evident in other layers so that it is harder to distinguish columns and label them with a given whisker.

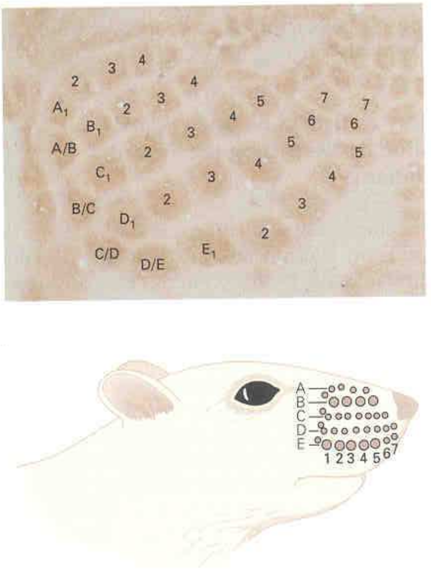

Figure 1.7: *Layer IV of rat's sensory cortex (stained for serotonin). Every whisker of the rat corresponds to a well defined area of the cortex mostly responsible for processing information from it. These processing units have the same distribution as whiskers on the muzzle. (From [61]).*

Although, this particular case sheds light on the important role afferent thalamic fibers play in shaping columns in sensory cortices [74]. These axonal fibers project in layer IV in the form of tufts spanning horizontally a range of a few hundreds of micrometers, therefore exciting and, up to horizontal connectivity, defining the width of physiological columns processing input for a given sensory function. Actually, the picture is more complex since different thalamic outputs may project on the same cortical column and one thalamic output may project on different cortical columns.

Anyway, functional columns usually overlap if the corresponding functions are close and information processing columnar sites move continuously across the surface of the cortex as function "continuously" varies, as it is observed in somatotopy, retinotopy, or orientation preference experiments (figure 1.8-B, left image, and figure 1.9, left image) [43, 53, 54, 84]. Nevertheless, functional columns may have partial well-defined boundaries at the discontinuities of the functional map. Examples of these discontinuities are given, in the visual cortex, by pinwheel points in the primary visual cortex (V1) or reversal direction lines in area 18 (V2), where functional columns are sharply separated (see figure 1.8 and 1.9, right image).

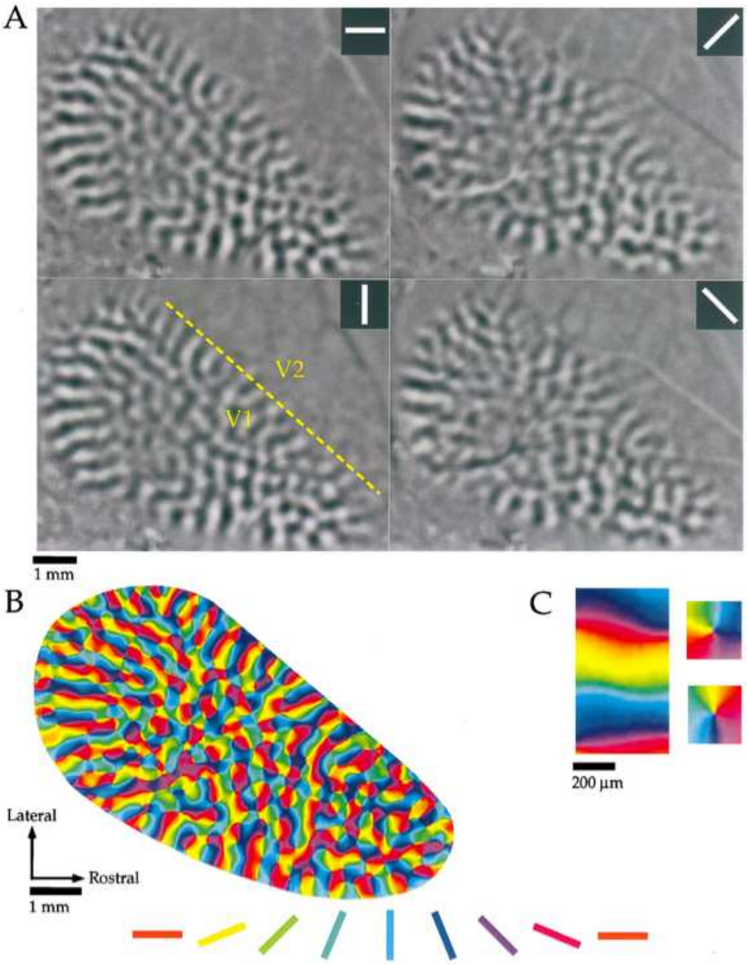

Figure 1.8: *Optical imaging of intrinsic signals in tree shrew visual cortex. A, Difference images obtained for four stimulus angles. Dark signal indicates areas that were active during presentation of the stimulus. B, Orientation preference map. Orientation preference of each location is color-coded according to the key shown below the map. C, Portions of the orientation preference map shown in B have been enlarged to demonstrate that the orientation preference maps contained both linear zones (left), and pinwheel arrangements (right) that are functional discontinuities (From [14]).*

To finish our discussion on functional columns, it is to be noted that these structures have not been observed in all regions of mammals cortex and show species dependency. For example, there is no orientation preference columnar structure in rat primary visual cortex, which means that locally, cells with all orientation preference are represented. One usually speaks of it as a “salt and pepper” structure. This has been illustrated in [84] (see figure 1.10).

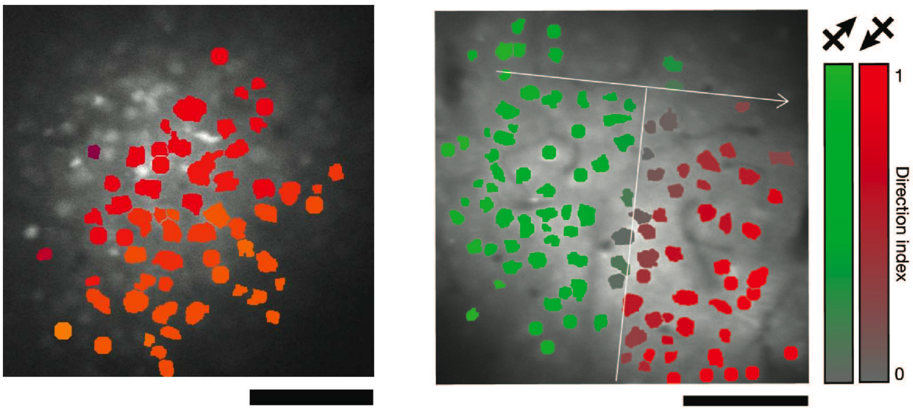

Figure 1.9: *Functional maps of selective responses in superficial layers of cat area 18 with single-cell resolution obtained by calcium imaging. Left: spatially smooth direction selectivity of neurons responding to a moving bar stimulus (preferred direction of movement:* 45° *for purple cells,* 90° *for red cells and* 135° *for orange cells). Right: discontinuity of direction selectivity giving partial boundaries to direction columns (From [84]).*

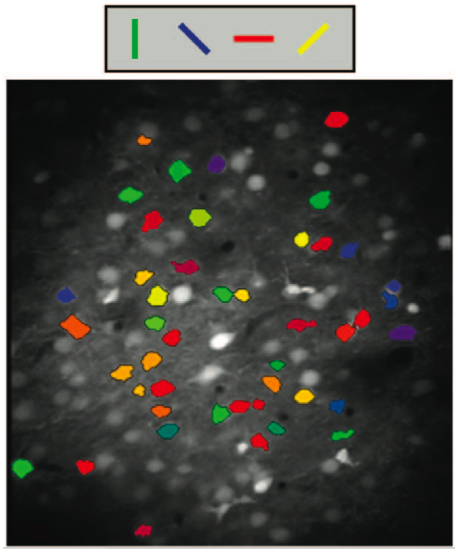

Figure 1.10: *Non-columnar orientation preference organization of rat primary visual cortex. Cells with different orientation preferences (see color code) are locally mixed together (From [84]).*

1.1.5 What drives the cortical column activity?

We now raise the question of the driving forces that shape the activity of a cortical column. What is the respective influence of intrinsic columnar organization, thalamic input and neighbouring columns?
In [76], the authors use calcium imaging to observe the activity of neurons in *in vitro* thalamo-cortical slices of a few millimeters wide. They investigated the relation between spontaneously generated cortical activity (i.e. in the absence of thalamic stimulation to the cortex) and the cortical activity induced by thalamic stimulation. Surprisingly, very similar spontaneous and triggered activities have been observed. The similarities concerned the set of activated cells as well as the temporal sequence of their activation (figure 1.11).

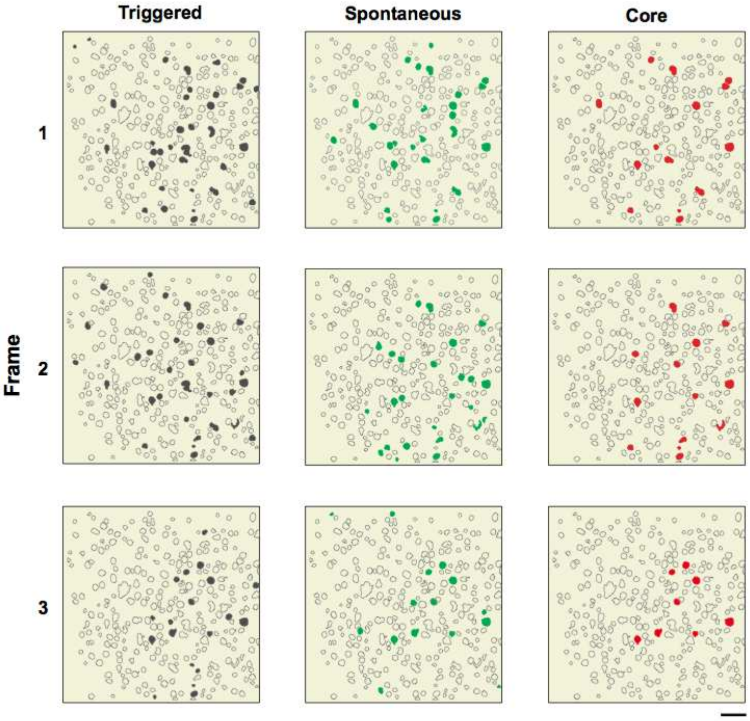

Figure 1.11: *Spatiotemporal dynamics of activation in spontaneous and triggered activity. Cells activated in the same order (frames 1, 2 and 3), over several activations. The three frames on the left show an example of spatiotemporal activation of the network when triggered by thalamic input (activated cells in gray). The three central frames correspond to spontaneous activation (green). Core frames indicate cells active in the same order across all movies from this slice (red), regardless of the triggered or spontaneous nature of the activation. Scale bar, 50μm. (From [76]).*

These results suggest that the thalamic input would just serve to awaken circuit dynamics that are intrinsic to the cortex. So, intracortical connectivity would play a primary role in determining the cortical response to thalamic input.

However, the intensity of the thalamic input to a column has a strong impact on the cortical response. We illustrate this with an optical imaging experiment in the rat barrel cortex (figure 1.12) [89]. A single whisker of a rat is deflected with

different angles and speed. Because of the structure of the rat barrel cortex, this stimulus provokes a very localized input to the cortical barrel corresponding to the excited whisker, in layer IV. The experiment shows that for weak stimulation, only one column will be activated: the one corresponding to the whisker. As the stimulus intensity increases, the activation is not anymore restricted to one column but spreads horizontally to neighbouring columns. When the stimulation is strong enough, the whole barrel cortex is activated.
In addition to the influence of thalamic input on cortical response, this experiment shows that an excited column can activate its neighbours without the help of a thalamic stimulation of these. Hence a column can be a major driving force for the activity of its neighbours.

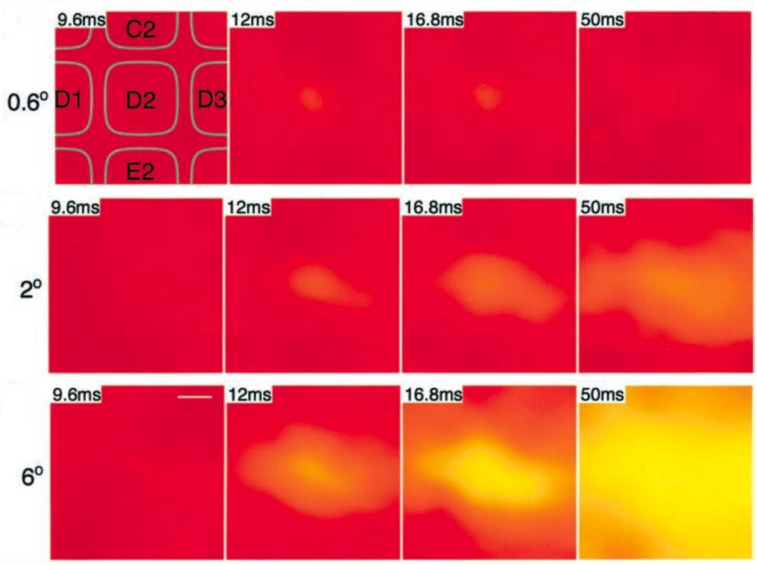

Figure 1.12: *Response sequences in the rat barrel cortex observed by optical imaging. A single whisker of the animal is stimulated with an increasing angle and speed (top to bottom). In the upper left image, a map of the barrels in layer IV is superimposed. A weak stimulation of the whisker provoke an activation in the column of barrel D2 (upper sequence). Stronger stimulation results in graded horizontal spread of activity (middle and bottom sequences) (From [89]).*

A recent study has shed light on the multi-scale nature of columnar organization in the cortex by showing that functional columns are composed of finer scale, partially segregated, minicolumnar subnetworks [122]. So there are many ways of speaking of a cortical column. Together they form a complex and sometimes blurred or misused concept.

Now we try to understand the organization of columns by exploring cortical microcircuitry.

1.2 LOCAL CONNECTIVITY IN THE CORTEX

Local connectivity studies have been conducted on many species, in different areas of their cortices, with various theoretical approaches and experimental tools.

Although, most of them concern sensory cortices (especially the primary visual cortex, V1) of mammals (monkey, cat, rat, human...), which have shown lots of similarities in their composition (types of neurons, relative proportions of cell types) and structure. Here we will try to synthetize the main results of those studies. We want to get a good description of local connectivity inside a cortical area, like V1. So, we concentrate on connections between neurons in the same area, passing through gray matter (intracortical connections). Afferent and efferent connections coming from and going to other areas or thalamus, via white matter, do not belong to microcircuitry. Such connections will be separated from intracortical connections when we will have to mention them.

Cortical microcircuits show stereotypy, i.e. structural and functional repeating patterns, through lots of their features like cell types, cell arrangements or patterns of synaptic connectivity [100]. As long as considering a given area, age and species, it is reasonable to think of the cortical tissue as repeating a common local template with subtle variations. Yet microcircuits cannot be known with cell-by-cell precision across an area, stereotypy makes it possible to speak of an average connectivity pattern revealed by statistical connectivity studies.

1.2.1 Neuronal compartments and selectivity of synapses

Neurons are composed of several compartments: a cell body (*soma*), dendritic trees, and axonal branches (see figure 1.13 and 1.14). Usually the whole cell crosses several layers of the cortex, but neurons are commonly said to belong to a specific layer: the one their soma belongs to. However, this tells nothing on the location of the neuron's dendritic trees or axon terminals. For example, deep layers pyramidal cells have apical dendrites in the superficial layers of the cortex (see figure 1.14). So two neurons may contact in a layer none of their cell bodies belong to.

Excitatory cells (pyramidal cells (PCs) and spiny stellate cells (SSCs)) axons target dendrites of post-synaptic cells. Inhibitory cells axons have various target compartments on post-synaptic cells. Chandelier cells almost exclusively target the axon hillocks of pyramidal neurons. Large, small and nest basket cells provide most of the somatic and perisomatic inhibitory synapses for excitatory and inhibitory neurons. Dendrites are preferentially targeted by double bouquet, bitufted, bipolar, neurogliaform and Martinotti cells, with some types favoring either spines or their supporting branches (shafts).

Several teams have recorded a huge amount of data on neuron, axon, dendrite and synapse density in the cortex of rodents and cat, by different techniques including 2D microscopy and 3D reconstruction of neurons [8, 9, 15, 28, 29, 87, 88]. These studies have led to connectivity estimations based on the idea that neurons establish *non-specific* synaptic contacts. This means that neurons project their axonal boutons across the cortex and locally make synapses with all represented types of neurons, proportionally to the fraction of dendritic surface these locally provide (Peters' rule, used by [15] and [13]).

Several recent studies show that connections are not just spatially uniformly random, depending on the local density of boutons and spines but are highly *selective* [7, 66, 103, 110, 111, 113, 118]. Dendrites and axons properties of pyramidal and inhibitory cells strongly suggest this *specificity* in intracortical connections. Pyramidal axons follow linear trajectories and typically form en passant boutons. These straight paths suggest that pyramidal axons do not search out specific postsynaptic partners.

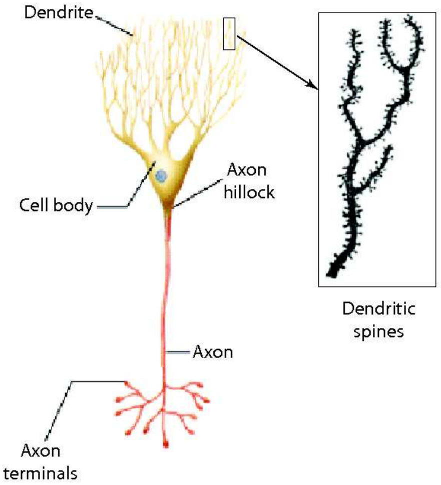

Figure 1.13: *Neuronal compartments and dendritic spines.*

On the other hand the dendrites of excitatory cells have large numbers of dendritic spines projecting up to 4 mm from the parent dendrite that are capable of movement and emerge at different angles from the dendritic shaft, suggesting that postsynaptic cells do seek out suitable excitatory inputs. Inhibitory neurones appear take the opposite approach with straight and largely spine free dendrites and axons that follow extremely complicated routes to make highly selective contacts with specific regions of their postsynaptic partners [7, 104, 106].

Connectivity studies taking specificity into account are mostly based on joint activity recordings, by calcium imaging or paired electrodes. Connections are established by physiological signals correlation and usually take the form of a connection probability between two types of neurons.

A quantitative description of interactions between each pair of neuronal types present in a local circuit has not yet been completed. However, some sub-networks are well known, like the excitatory pathway or certain intralaminar networks. The inhibitory network is way more complex, by the number of its neuronal types, their action and their role in the circuit.

1.2.2 Excitatory network

Excitatory cells account for approximately 70-80 % of neurons in the cortex and are divided into two main groups: pyramidal and spiny stellates. Both groups use glutamate as their primary neurotransmitter. Action potentials traveling down the axon of an excitatory neuron provoke the release of glutamate at the level of axonal terminal boutons. These neurotransmitter molecules bind to specific receptors on the postsynaptic neuron's membrane and modify its permeability to different ionic species. Ionic fluxes through the membrane of the postsynaptic cell result in the generation of transient changes in the membrane's polarization called *excitatory postsynaptic potentials* (EPSP). EPSPs are said to be *depolarizing* because they tend to increase the membrane potential and hence to bring the natural resting membrane potential of neurons, which is about -70mV, toward zero. They are called *excitatory* because as they summate on the postsynaptic membrane, they can trigger the generation of an

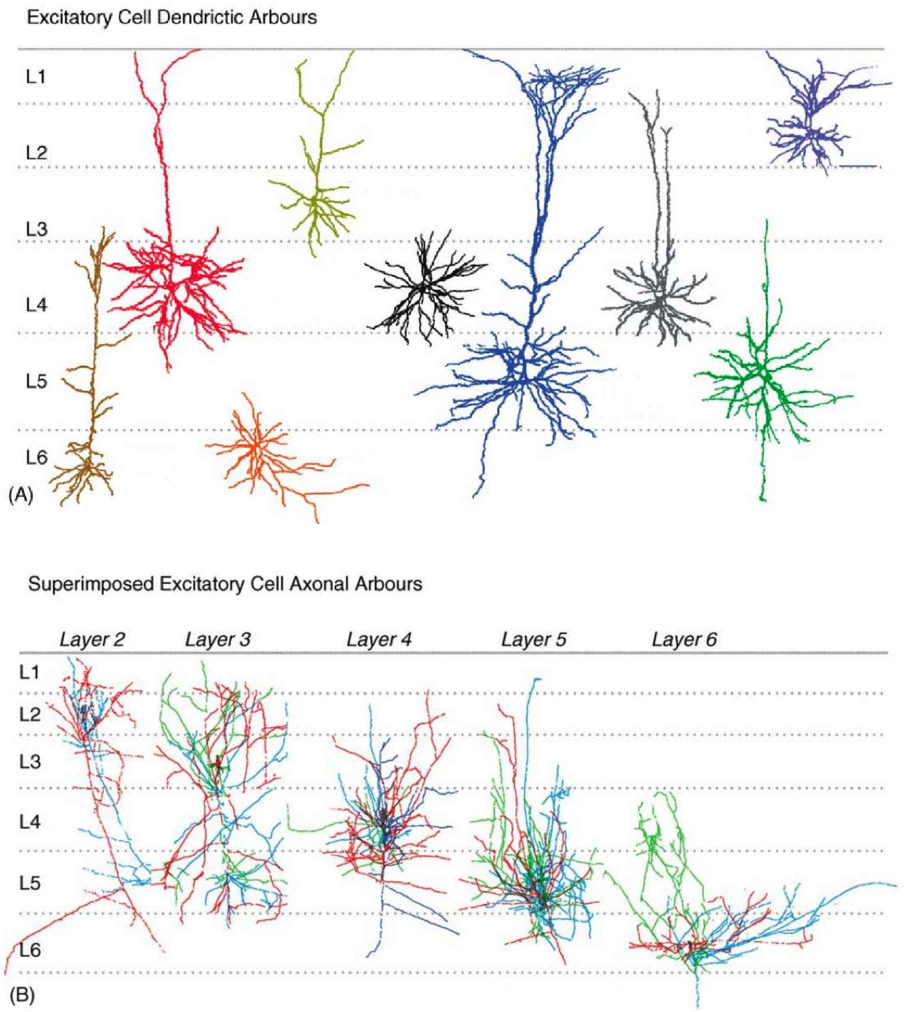
Excitatory Cell Dendritic Arbours
L1
L2
L3
L4
L5
L6
(A)
Superimposed Excitatory Cell Axonal Arbours
Layer 2
Layer 3
Layer 4
Layer 5
Layer 6
L1
L2
L3
L4
L5
L6
(B)

Figure 1.14: *Dendritic arbors (upper panel) and axonal trees (lower panel) of excitatory neurons. In the lower panel, the different axonal trees belonging to the same neuron are distinguished by different colors (From [7]).*

action potential in the postsynaptic cell (see figure 1.15).

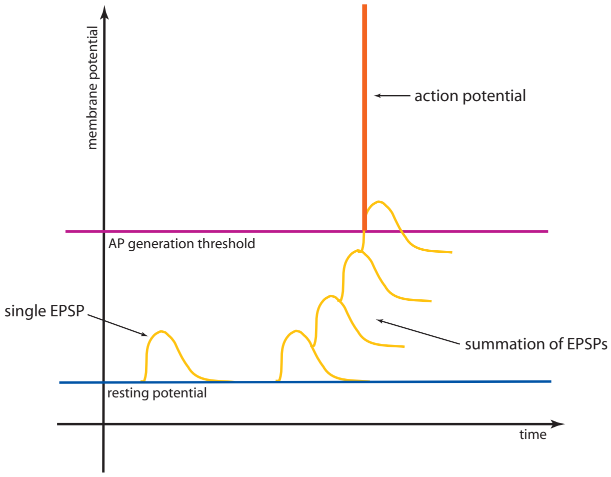

Figure 1.15: *Summation of EPSPs leading to the generation of an action potential.*

PCs somata are situated in layers II to VI and SSCs somata are situated within layer IV of primary sensory areas. The two classes have spiny dendrites. For that reason, excitatory cells in the cortex are often referred to as *spiny cells*. SSCs lack the long vertically oriented apical dendrite of PCs, so they do not get input from superficial layers. Moreover SSCs only establish local intracortical connections, while PCs project myelinated axons to the thalamus (cortico-thalamic projections) and other cortical areas (cortico-cortical projections). PCs show a lot of variability. While their anatomy is relatively stereotypical, their dendritic, axonal trees and spike discharge patterns vary among and inside layers [7].

The excitatory network is usually divided into two pathways. The feedforward pathway goes from layer IV (receiving cortical input from the thalamus) to layer II/III and then project to deep layers V and VI. It corresponds to the most basic and well-known trajectory of the thalamic input through cortical layers. The feedback pathway mainly consists in projections from deep layers (V-VI) to more superficial layers (III-IV), and from superficial layers (especially layer III) to layer IV. All layers display dense intralaminar excitatory projections targeting all types of neurons (see figure 1.16).

Layer IV

Layer IV is the main target of afferent thalamic fibers. These target both excitatory and inhibitory neurones in the highly interconnected networks in layer IV, but of all the synapses made with layer IV basket cells, thalamic inputs constitute only 13% and with SSCs only 6%. Yet, thalamocortical terminals are generally highly efficacious so that they reliably activate layer IV and sensory information from the thalamus strongly influences computations in the cortex. Moreover the majority of excitatory synaptic contacts to layer IV excitatory cells are supplied by other cells receiving direct input from the thalamus. Layer IV PCs and SSCs have extensive intralaminar axonal arbours and focussed projections to layer III. Less dense projections may also target the deeper layers V and VI. So, layer IV spiny cells appear to have two major roles: amplify the input received in layer IV and feed excitation to

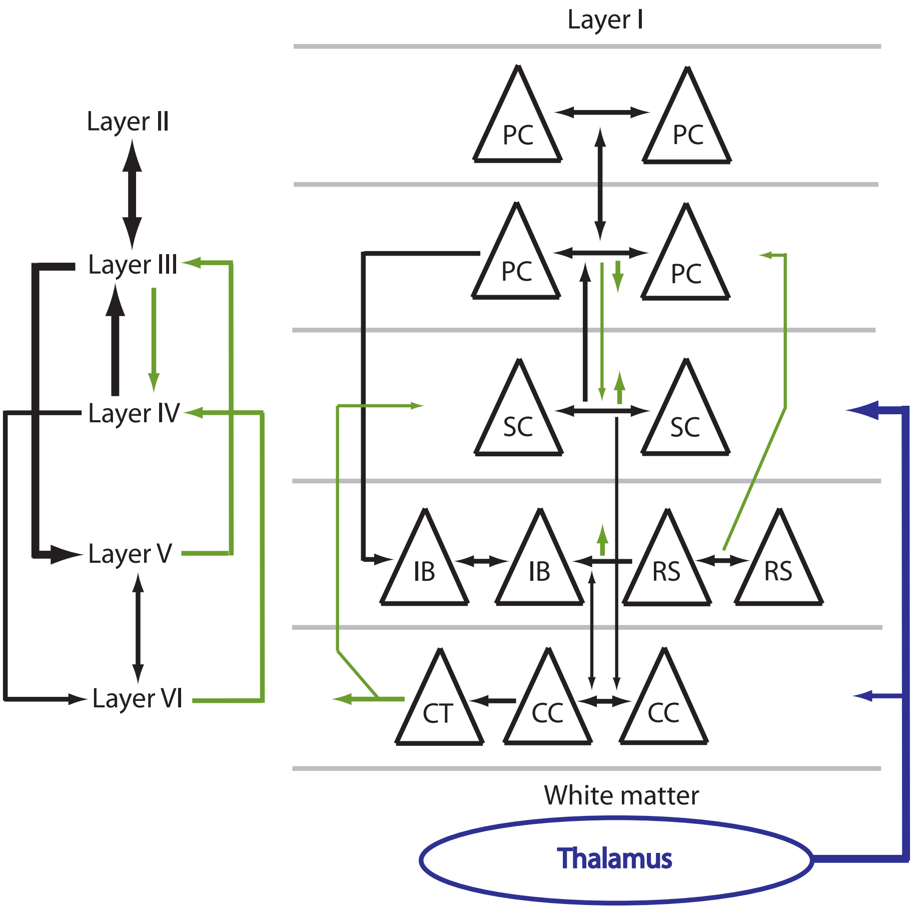

Figure 1.16: *Main intracortical projections made by excitatory neurons. The diagram on the left is a simplified version of the detailed diagram on the right, showing only the most salient features of the excitatory pathway. Interlaminar projections, including the feedforward and feedback pathways are represented on the left. Black arrows indicate projections to excitatory neurons (PC: pyramidal cells, SC: spiny cells including both PCs and SSCs, IB: intrinsically bursting PCs, RS: regular spiking PCs, CT: cortico-thalamic PCs, CC: cortico-cortical PCs, see text for details) and green arrows projections to inhibitory neurons (not represented on this figure). Projections from the thalamus are indicated in purple. All layers display dense intralaminar excitatory projections targeting all types of neurons. The thickness of the different arrows gives an insight of the relative importance of the different connections. Thinner arrows indicate weaker or less well identified interlaminar connections, often involving layer VI.*

layer III (see figure 1.16).

Layer II/III

Layer II pyramidal axons ramify most extensively in layers II and III where they make frequent connections with other local pyramidal cells. They also make long range projections through white matter. Layer III pyramidal axons ramify most extensively in layer II/III and V and make frequent synaptic connections with spiny cells there. Connections from layer III to V are highly selective. Layer III PCs mainly target large, tufted and intrinsically bursting (IB) PCs in layer V and make very few connections to the smaller regular spiking (RS) cells[1]. The rate of connectivity to IB cells is also dependent on the distance over which the two cells are separated laterally, the highest probability of connection being when the presynaptic cell is within $\sim 50\mu m$ of the ascending post-synaptic apical dendrite. Layer III PCs also make back projections to layer IV with preferential innervation of inhibitory cells (see figure 1.16).

Layer V

The IB and RS pyramidal cells in layer V have similar patterns of axonal arborization. The axons of both classes ramify most extensively in layer V, indicating that they prefer to innervate cells in their own layer since the pyramidal cells in more superficial layers do not have dendritic access to these dense arbours in layer V. Paired intracellular recordings reveal that while both classes are indeed synaptically connected, the RS cells are almost exclusively presynaptic to IB cells, which are in turn presynaptic to other IB cells. In addition to these dense intralaminar projections, layer V PCs project back to all other layers of the cortex, hence representing a major source of excitation to superficial laminae. Layer V PCs make very few and weak projections to layer III excitatory cells, but they do innervate inhibitory cells in this layer (see figure 1.16).

Layer VI

Layer VI is the secondary main target of thalamic afferent fibers and also provides cortico-thalamic (CT) and cortico-cortical (CC) projections via white matter. PCs of layer VI that provide either CT or CC outputs can be identified by their distinctive morphologies. CT cells are typically oriented vertically, have short apical dendrites terminating in layer IV or in upper layer V and vertically oriented axonal arbours terminating in the vicinity of their dendrites. CC cells generate dendritic arbours that rarely extend beyond layer V and a characteristically long and horizontally oriented axon confined to the deep cortical layers. Phasically firing cells would have CC-like morphology and tonically firing cells would have CT-like morphology[2]. The phasically firing CC-like cells principally innervate other layer VI PCs while tonically firing CT-like cells prefer to target interneurons, mostly in layer VI. They may also target layer IV inhibitory cells, but these projections have not been studied in detail to date. This specialization is not found in PCs subclasses of other layers. One possibility for the function of such selectivity in the connections of layer VI cells is that the CC cells may be responsible for conveying only the most novel information to other cortical regions via their phasic spike discharge. On the other hand, the CT cells which can maintain firing for longer, and prefer to activate interneurons, may therefore be responsible for the generation of powerful inhibition of the cortical columns in response to prolonged excitation both by thalamic afferents or by strong local circuit connections [7].

---

[1] For more explanations on the terms *intrinsically bursting* and *regular spiking*, the reader is referred to appendix A.

[2] See appendix A.

Layer VI PCs receive weak inputs from all other layers. They make few interlaminar projections, mostly weak ones from CC cells to layer V PCs. The relatively low involvement of layer VI in interlaminar connections and its evident specialization in targeting distant sites through white matter projections explain why it is often termed as an "output layer" and sometimes neglected in the intracortical network (see figure 1.16).

Back projections from PCs of layers III and V-VI

These back projections mainly target inhibitory cells in the previous layer of the feed-forward pathway. It suggests that pyramidal cells in each layer might, when generating outputs to integrated inputs, simultaneously initiate inhibition of their input layers via local circuit neurons (interneurons). This mechanism would be useful to prevent undesirable positive feedback loops and ensure the integrity of the excitatory flow through the cortex by silencing the cells responsible for their inputs as soon as appropriate outputs to the next stage of processing has been achieved [7] (see figure 1.16).

1.2.3 Inhibitory action

20 to 30 % of cortical neurons are inhibitory cells. These cells use gamma aminobutyric acid (GABA) as their primary neurotransmitter. The release of GABA in the synaptic cleft provokes a transient *hyperpolarization* of the postsynaptic membrane called *inhibitory postsynaptic potential* (IPSP), summating to other postsynaptic potentials with a negative contribution, then pulling the potential away from the firing threshold. Hence, IPSPs can prevent the generation of action potentials in the postsynaptic cell. GABA-ergic neurons do not only influence their post-synaptic targets by hyperpolarizing the post-synaptic membrane. GABA neurotransmitters exist in several forms in the cortex, the most prominent of which being $\mathrm{GABA_A}$. $\mathrm{GABA_A}$ inhibition is mediated by $\mathrm{Cl^-}$ channels and the concentration gradient for $\mathrm{Cl^-}$ across the cell membrane determines the nature of the inhibitory effect caused by GABA-ergic synapses. As an inhibitory synapse has a reversal potential near the resting potential of the neuron, it must elicit particularly large conductance openings in the neuron's membrane in order to produce a significant inhibitory current. A specific non-linear inhibitory effect, called *shunting inhibition*, can appear if these conductance openings get large enough to induce an important reduction of the cell's membrane resistance. Then, following Ohm's law, the amplitude of subsequent excitatory postsynaptic potentials can be dramatically reduced. This phenomenon is called "shunting" because the conductance short-circuits currents that are generated at adjacent excitatory synapses. Shunting synapses occuring between an excitatory synapse and the action potential initiation site (typically, on the perisomatic region of the post-synaptic cell) are more effective since they shunt the global contribution of many synapses.

The relative density of inhibitory cells compared to excitatory cells or comparing the different types of inhibitory cells vary in different species, brain regions and layers.

Most of these cells have aspiny dendrites, so that they are often termed as “smooth cells”. Their axons usually arborize within a cortical column and can project laterally across cortical columns but do not typically project down into the white matter to contact the thalamus or distant brain regions, so they are also called “local circuit neurons” or “interneurons”[3].
The complexity of the inhibitory network and inhibitory action in the cortex has been demonstrated in several reviews [78, 112] and is the largest obstacle to unraveling the organization of cortical microcircuits. One of the main problems arises from the difficulty to define subclasses of inhibitory cells. Indeed, there are about ten well-known morphological types of interneurons (see figure 1.17) and a dozen of electrophysiological types (see appendix A). Each anatomical type has multiple firing patterns, which in turn correspond to multiple anatomical types of neurons. Hence there are more than fifty anatomo-electrophysiological types of interneurons in the cortex (see figure 1.18).

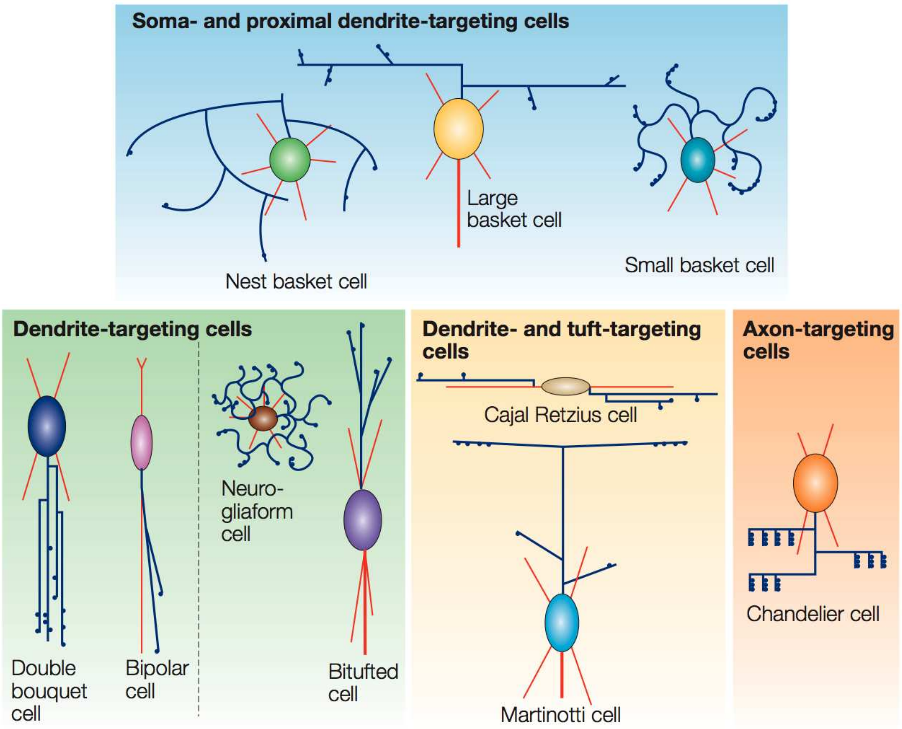
Soma- and proximal dendrite-targeting cells
Large basket cell
Small basket cell
Nest basket cell
Dendrite-targeting cells
Neuro-gliaform cell
Double bouquet cell
Bipolar cell
Bitufted cell
Dendrite- and tuft-targeting cells
Cajal Retzius cell
Martinotti cell
Axon-targeting cells
Chandelier cell

Figure 1.17: *Summary of the main anatomical properties of cortical inhibitory interneurons (dendrites in red and axons in blue) classified according to their preferred axonal targets (From [78]).*

Interneurons can be roughly classified according to the post-synaptic neuronal compartment their axons preferentially innervate and have typical axonal arbors (see figure 1.17).

---

[3] We will use the term interneurons to designate inhibitory interneurons, whereas there exist some classes of excitatory interneurons, like SSCs.

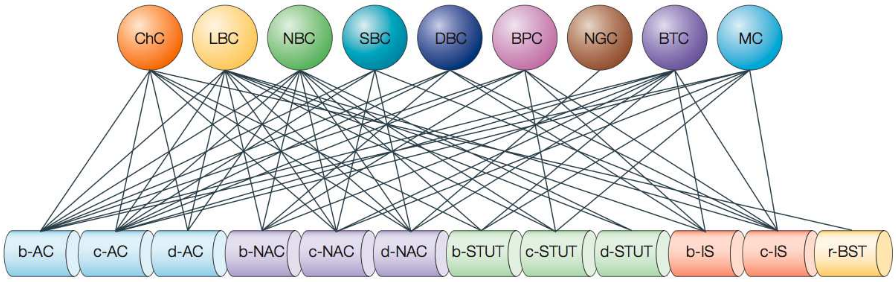

Figure 1.18: *Anatomical-electrophysiological diversity of cortical inhibitory neurons. Above circles: anatomical types (ChC: chandelier cell, LBC: large basket cell, NBC: nest basket cell, SBC: small basket cell, DBC: double bouquet cell, BPC: bipolar cell, NGC: neurogliaform cell, BTC: bitufted cell, MC: Martinotti cell). Bottom cylinders: types of firing responses to somatic current injections (AC: accomodating, NAC: non-accomodating, STUT: stuttering, IS: irregular spiking, BST: bursting) (From [78]).*

Main anatomical types of interneurons

- Basket cells (BC) represent 50% of inhibitory interneurons and are divided into three main subclasses on the basis of differences in dendritic and axonal morphologies. BCs are specialized in targetting the somata and proximal dendrites (i.e. those situated near the soma of a neuron) of their post-synaptic targets (PCs and interneurons). This position allows them to adjust the gain of integrated synaptic response and influence the action potential discharge, so that they play a role in phasing and synchronizing neuronal activity.
  - Large basket cells (LBC) provide lateral inhibition across columns in their layer of origin. They can also extend vertically, ramifying in several, often non adjacent layers. They have sparse axonal arbors with low terminal (also called “boutons”) density on them. LBCs are largely represented in layers II-VI.
  - Small basket cells (SBC) have a very local impact since their axonal arbors are usually confined in the same column and layer as their soma. They have curvy frequently branching axons. They are present in layers II-VI, especially in layer IV.
  - Nest basket cells (NBC) have local axonal clusters and lower boutons density than LBCs. They are present in layers II-VI, and especially in layers II-IV.
- Chandelier cells (ChC) are few compared to BCs. One finds them in layers II-VI, especially in layer II/III and V. Their local axonal clusters make numerous branchings and primarily target the axon initial segment (axon hillock) of pyramidal cells. ChCs hence influence the action potentials output of PCs by affecting their generation and timing, possibly silencing the firing of spikes.
- Martinotti cells (MC) are very numerous in all layers. They specialize in projecting their axons toward layer I where they inhibit pyramidal dendrites and can extend horizontally to neighbouring or distant columns. Some of them selectively target layer IV. MCs can also innervate proximal dendrites and somata.

- Double bouquet cells (DBC) have a fascicular axonal cylinder that can extend across all layers and make frequent branching. DBCs mainly innervate dendrites of post-synaptic PCs. They are present layers II-V.

- Bitufted cells (BTC) are similar to bipolar cells (see next item) and DBCs, but show a wider horizontal axonal span and less extensive vertical projections. They primarily target pyramidal dendrites.

- Bipolar cells (BPC) are relatively sparsely represented in the cortex and have a narrow vertical axonal tree (less than 50μm wide) that crosses all layers. They show low boutons density and mainly target PCs proximal dendrites. They are found in layers II-IV.

- Neurogliaform cells (NGC) have a dense, complex axonal arborization targetting dendrites of post-synaptic cells. There are few such cells in the cortex. They can be found in all layers but they have been mainly observed in layer I and IV of cortical sensory regions. They connect on PCs dendrites and make dense interconnections with other interneurons via gap junctions (electrical synapses).

- Layer I contains an heterogeneous population of small interneurons with various axonal arborizations and large neurons with horizontal processes confined to layer I, known as Cajal Retzius cells, that are mostly present during development.

Those neuronal types can be separated into two main classes, based on their morphologies, preferential post-synaptic targets and firing patterns[4]. The first class contains the *proximal targeting cells*, including basket and chandelier cells, that usually show fast spiking firing patterns, project on proximal compartments of PCs and whose dendrites radiate in all directions from the soma.

The second class is constituted from *low-threshold spiking (LTS) dendrite-preferring interneurons*, including Martinotti, double bouquet and bitufted cells, that preferentially target dendrites of post-synaptic PCs, usually show low-threshold spiking and bitufted dendritic trees (issuing from the apical and basal poles of the soma).

Although they preferentially target dendrites, bipolar and neurogliaform cells stand apart from these classes. Bipolar cells firing patterns are stuttering and contrary to LTS neurons, they may receive thalamic input. Neurogliaform cells do not display bitufted dendritic arborization and have very specific firing patterns [78, 112].

Interneurons in the microcircuit

Pyramidal cells receive most of their synapses from other PCs. Inhibitory synapses on PCs are less numerous and mostly arise from neighbouring interneurons. For example, only 16% of synapses on PCs in layer II/III are inhibitory and a majority of these arise from interneurons lying in the same cortical column and layer; only 15% of them come from interneurons belonging to an other column.

Nevertheless, the balance between excitation and inhibition in the brain is maintained over a large dynamic range and for many stimuli, suggesting a reliable activation of the inhibitory pathway [80]. This activation is crucial since the lack of inhibition has been linked to various pathologies, including epilepsy [22].

---

[4] See appendix A.

Recent findings have shown that layer V PCs evoke inhibitory responses in neighbouring PCs via the interplay of Martinotti cells [101]. Moreover, the probability for such a *disynaptic inhibition* has been observed to be more than double the probability of direct connections between layer V PCs, suggesting a high connection probability of Martinotti cells on layer V PCs.

Excitatory synapses onto interneurons mostly arise on dendrites and sometimes on somata. Intralaminar connections from spiny excitatory cells to interneurons are frequent and do not appear to show striking preference for any particular interneuronal class. We should also mention interlaminar back projections from PCs of layer III and V-VI (see above). Some classes of inhibitory interneurons even receive direct input from the thalamus, mainly proximal targeting cells and bipolar cells. LTS neurons seem to receive little or no input from the thalamus.

Relatively fewer studies have investigated connections between interneurons, but some of them indicate that connections between interneurons of all classes are dense and involve quite disparate classes and interneurons in different layers. Basket cells, especially LBCs, seem to have a prominent role in governing the activity of inhibitory networks in the cortex [109]. They make numerous connections with other neighbouring basket cells and also contact dendrite-preferring neurons [78, 112]. Dense networks of interneurons having similar properties, connected through gap junctions (i.e. electrical synapses), have also been observed in the cortex [50]. Cortical electrical synapses seem to be an exclusive property of interneurons since none have yet been found among PCs. They favor high synchronization between neighbouring inhibitory cells of the same class[5] [107, 108]. We summarize the essential features of the inhibitory network in figure 1.19.

1.3 THE MESOSCOPIC APPROACH TO CORTICAL COLUMNS

Several teams have modeled cortical columns from the most detailed information available on neurons and microcircuits [77, 114]. They have simulated networks with several thousands of neurons, taking into account the different neuronal compartments and ionic channels. This approach requires huge computational power and memory for simulations and information storage of many parameters, sometimes including 3D whole cell reconstructions. One of the main problems of such models resides in the difficulty of a mathematical investigation, due to their inherent complexity.

Here we propose a *mesoscopic* approach to cortical columns, i.e. a description at an intermediate level between the microscopic (cellular) scale and the macroscopic one (cortical areas). The complexity of the network is reduced to a few building blocks, allowing subsequent mathematical analysis (see next chapter).

1.3.1 Neural masses

The elementary building block we will use in mesocopic modeling is the *neural mass*. A neural mass is an assembly of several hundreds to several thousands of usually neighbouring, interconnected neurons that share similar properties (morphology, firing patterns...) and tend to activate together. Typically, a neural mass is a cluster of

---

[5] The probability of gap junction between two neighbouring interneurons of the same class is higher than 50%; this probability becomes inferior to 5% if the neurons belong to different classes.

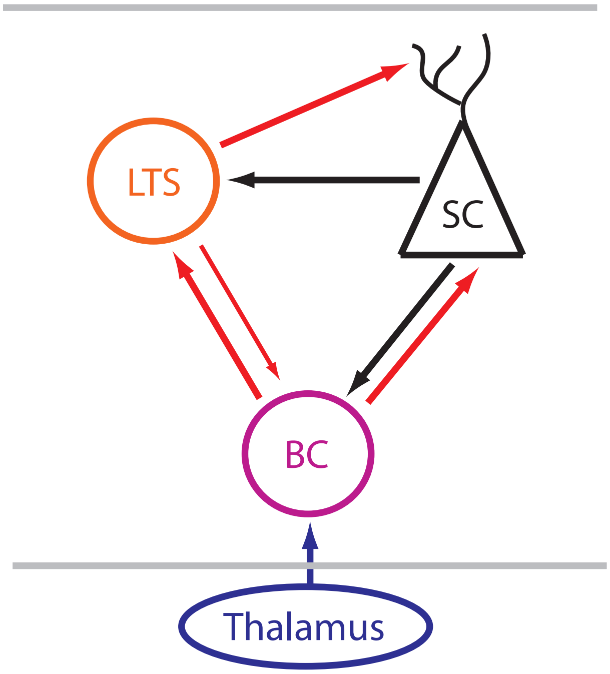

Figure 1.19: *Highly simplified cortical inhibitory network. Proximally targeting neurons are represented by their principal cellular type, basket cells (BC), and can receive thalamic input. LTS cells mostly target the dendrites of spiny cells (SC). Both groups form densely connected networks, possibly through gap junctions, and interact with each other though BCs seem to have a prominent driving role. Although interneurons can make and receive interlaminar projections, dense intralaminar connections with spiny cells are observed in most cortical layers and constitute one of the most salient features of the inhibitory network. Black arrows indicate excitatory projections and red arrows, inhibitory ones.*

neurons of similar anatomical type, confined in the same cortical column and layer. Its spatial extent is hence of the order of a few hundreds of micrometers. Neural masses are described in terms of the average membrane potential or average firing rate of their constitutive cells. So at the mesoscopic scale a cortical column is seen as a small layered network of homogeneous neural masses. This approach opens the door to a very compact description of cortical columns organization and activity in terms of the number of parameters and variables.
Besides, this mesoscopic description of cortical columns is consistent with most of the available data on local cortical connectivity derived from activity correlation between neurons. Indeed connections between neurons are usually investigated within columns of a few hundreds of micrometers wide and they are expressed as connection probabilities between cell types [112].

1.3.2 An example of mesoscopic cortical column model

Usually a column model does not need many different types of neural masses to be able to reproduce interesting phenomena. Most mathematical models from the literature use only two classes of neurons: excitatory and inhibitory (for a very general review, see for example [31]). In the next chapter we will present the analysis of a column model based on three neuronal populations (Jansen's model).

However in biophysical models of cortical columns, a wider variety of neural masses is needed to account for essential intra- and interlaminar connections in the cortex. Mesoscopic column models are basically build from a selection of prominent neural masses, connected if possible with biophysically based weights.
In [49], the authors propose a model of cortical connectivity grounded on the statistical description of cortical microcircuits achieved by A. Thomson and co-workers (figure 1.20).
As we said before, there is a match between the spatial scale of cortical columns and the one of connections reported in local connectivity studies. Hence, we can see the wiring diagram 1.20 as a biophysical cortical column model, considering the represented neuronal populations as neural masses and using average connectivity data as connection strengths between those. This model constitutes a good compromise between simplicity and biophysical relevance, and we will use it in the third part of this thesis.

The following chapter provides a mathematical analysis of a simpler cortical column model known as *Jansen's model*.

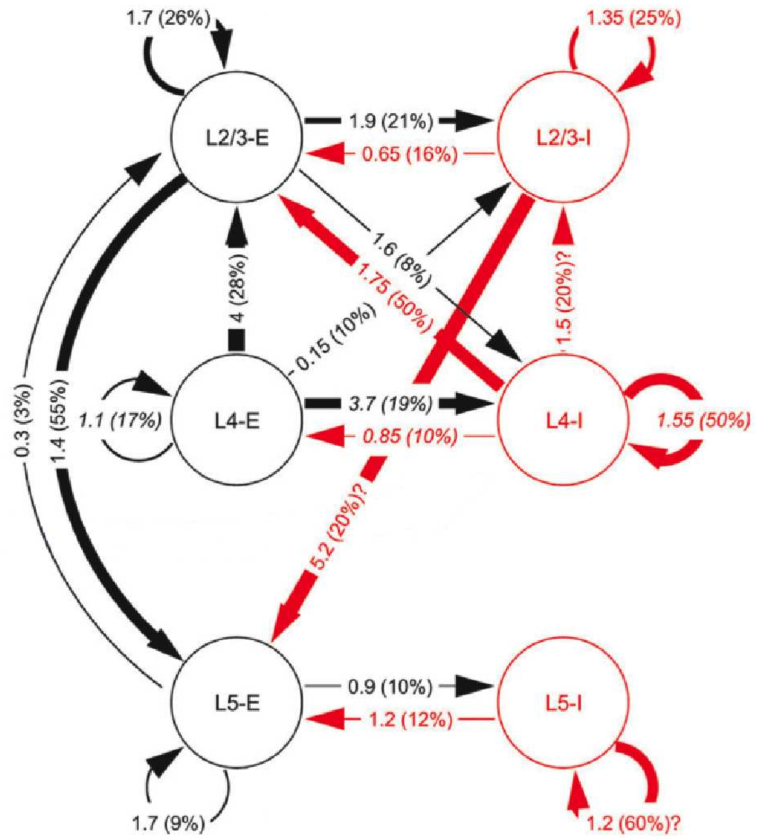
1.7 (26%)
1.35 (25%)
L2/3-E
1.9 (21%)
0.65 (16%)
L2/3-I
1.6 (8%)
1.75 (50%)
4 (28%)
0.15 (10%)
1.5 (20%)?
0.3 (3%)
1.4 (55%)
1.1 (17%)
L4-E
3.7 (19%)
0.85 (10%)
L4-I
1.55 (50%)
5.2 (20%)?
L5-E
0.9 (10%)
1.2 (12%)
L5-I
1.7 (9%)
1.2 (60%)?

Figure 1.20: *Simplified weighted diagram of cortical connections reported by A. Thomson and co-workers (excitatory projections in black and inhibitory ones, in red). The numbers indicated on arrows are the average amplitudes of postsynaptic potentials and in parenthesis, connection probabilities between two cell types. Question marks indicate values for which stronger experimental evidence is needed (From [49]).*

CHAPTER 2

CORTICAL COLUMN MODELS

OVERVIEW

We present a mathematical model of a neural mass developed by a number of people, including Lopes da Silva and Jansen. This model features three interacting populations of cortical neurons and is described by a six-dimensional nonlinear dynamical system. We address some aspects of its behavior through a bifurcation analysis with respect to the input parameter of the system. This leads to a compact description of the oscillatory behaviors observed in [58] (alpha activity) and [119] (spike-like epileptic activity). In the case of small or slow variation of the input, the model can even be described as a binary unit. Again using the bifurcation framework, we discuss the influence of other parameters of the system on the behavior of the neural mass model. This chapter almost exactly corresponds to the article [46], published in *Neural Computation* in 2006.

Contents

2.1 Description of the model 50
2.2 Bifurcations and oscillations 55
  2.2.1 Fixed points 55
  2.2.2 Bifurcations and oscillatory behaviour in Jansen's model . . . 57
  2.2.3 Synthesis 61
  2.2.4 What about other parameters? 62
2.3 Conclusion 65

Jansen's neural mass model is based on the work of Lopes Da Silva *et al.* and Van Rotterdam *et al.* [71, 72, 117]. They developed a biologically inspired mathematical framework to simulate spontaneous electrical activities of neurons assemblies recorded by electroencephalography (EEG), with a particular interest for alpha activity. In their model, populations of neurons interact by excitation and inhibition and can in effect produce alpha activity. Jansen and co-workers [58, 59] discovered that this model was also able to simulate evoked potentials, *i.e.* EEG activities observed after a sensory stimulation (by a flash of light, a sound, etc...). More recently, Wendling *et al.* used this model to synthesize activities very similar to those observed in epileptic patients [119], and David and Friston studied connectivity between cortical areas with a similar framework [25, 26].
The contribution of this chapter is a fairly detailed description of the behaviour of this particular cortical column model as a function of its input [46]. This description is grounded in the mathematics of dynamic systems and bifurcation theories. We briefly recall the model in section 2.1 and describe in section 2.2 the properties of the associated dynamical system.

2.1 DESCRIPTION OF THE MODEL

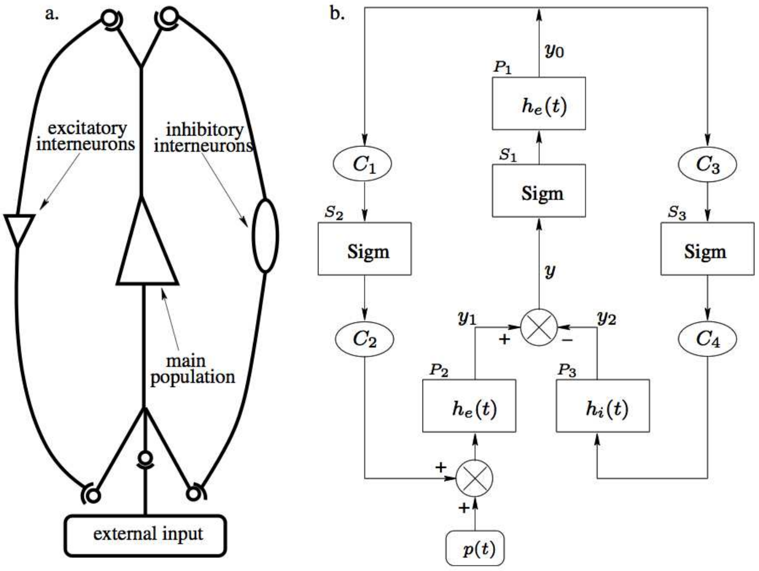

Figure 2.1: *a) Neural mass model of a cortical unit: it features a population of pyramidal cells interacting with two populations of inter-neurons, one excitatory (left branch) and the other inhibitory (right branch). b) Block representation of a unit. The* h *boxes simulate synapses between the neurons populations.* Sigm *boxes simulate cell bodies of neurons by transforming the membrane potential of a population into an output firing rate. The constants C_i model the strength of the synaptic connections between populations.*

The model features a population of pyramidal neurons (central part of figure 2.1.a.) that receive excitatory and inhibitory feedback from local interneurons and an excitatory input from neighbouring cortical units and sub-cortical structures like the thalamus. Actually the excitatory feedback must be considered as coming from both local pyramidal neurons and genuine excitatory interneurons like spiny stellate cells.

Equations of the model

Figure 2.1b. is a translation of figure 2.1.a in the language of system theory. It represents the mathematical operations performed inside such a cortical unit.
The excitatory input is represented by an arbitrary average firing rate $p(t)$ which can be random (accounting for a non specific background activity) or deterministic, accounting for some specific activity in other cortical units. The three families –pyramidal neurons, excitatory and inhibitory inter-neurons– and synaptic interactions between them are modeled by different systems.

The Post-synaptic systems $P_i, i = 1,2,3$ (labeled $h_e(t)$ or $h_i(t)$ in the figure) convert the average firing rate describing the input to a population into an average excitatory or inhibitory post-synaptic potential (EPSP or IPSP). From the signal processing standpoint, they are linear stationary systems that are described either by a convolution with an impulse response function or, equivalently, by a second-order linear differential equation. The impulse response function is of the form

$$h(t) = \begin{cases} \alpha\beta t e^{-\beta t} & t \geq 0 \\ 0 & t < 0 \end{cases} .$$

It has been proposed by van Rotterdam [117] in order to reproduce well the characteristics of real EPSPs and IPSPs (see figure 2.2).

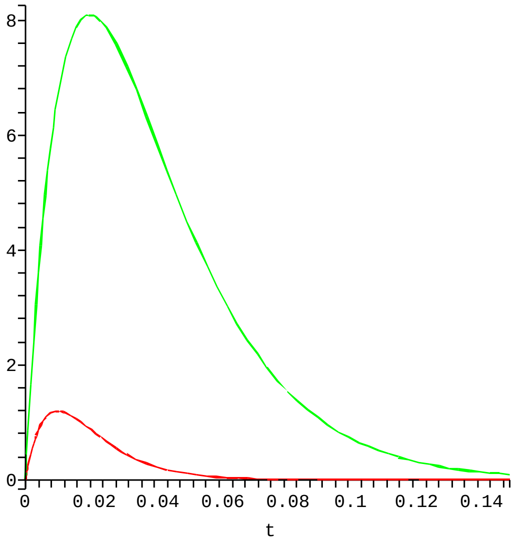

Figure 2.2: *Postsynaptic profiles obtained for different choices of α and β.*

In other words, if $x(t)$ is the input to the system, its output $y(t)$ is the convolution product $h * x(t)$.
The constants α and β are different in the excitatory and inhibitory cases. α, expressed in millivolts, determines the maximal amplitude of the post-synaptic potentials, β, expressed in s^{-1}, lumps together characteristic delays of the synaptic

transmission, i.e. the time constant of the membrane and the different delays in the dendritic tree [39, 59].
The corresponding differential equation is

$$\ddot{y}(t) = \alpha\beta x(t) - 2\beta\dot{y}(t) - \beta^2 y(t), \tag{2.1}$$

In the excitatory (respectively inhibitory) case we have $\alpha = A$, $\beta = a$ (respectively $\alpha = B$, $\beta = b$). This second-order differential equation can be conveniently rewritten as a system of two first-order equations

$$\begin{cases} \dot{y}(t) = z(t) \\ \dot{z}(t) = \alpha\beta x(t) - 2\alpha z(t) - \alpha^2 y(t) \end{cases}. \tag{2.2}$$

The *Sigmoid* systems introduce a nonlinear component in the model. They are the gain functions that transform the average membrane potential of a neural population into an average firing rate (see figure 2.3 and e.g. [41]):

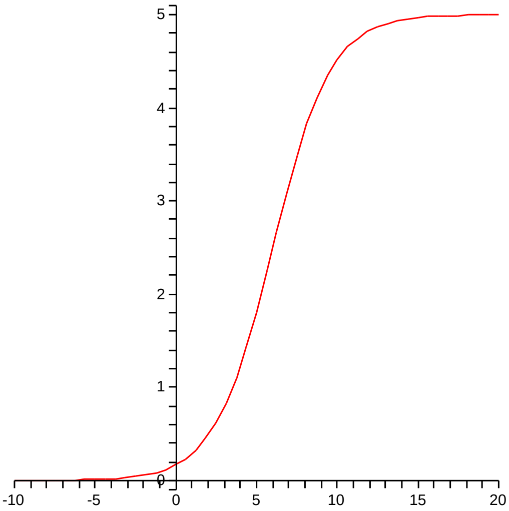

Figure 2.3: *Function Sigm used in this model. It converts the average membrane potential of a mass into its average firing rate.*

$$\text{Sigm}(v) = \frac{\nu_{max}}{2}(1 + \tanh\frac{r}{2}(v - v_0)) = \frac{\nu_{max}}{1 + e^{r(v_0 - v)}},$$

where ν_{max} is the maximum firing rate of the families of neurons, v_0 is the value of the potential for which a 50% firing rate is achieved and r is proportional to the slope of the sigmoid at v_0; v_0 can be viewed either as a firing threshold or as the excitability of the populations.
This sigmoid transformation approximates the functions proposed by the neurophysiologist Walter Freeman [39] to model the cell body action of a population.

The *connectivity constants* $C_1, \ldots, C_4$ account for the number of synapses established between two neurons populations. We will see that they can be reduced to a single parameter C.

There are three main variables in the model, the outputs of the three post-synaptic boxes noted y_0, y_1 and y_2 (see figure 2.1.b); we also consider their derivatives $\dot{y}_0$, $\dot{y}_1$, $\dot{y}_2$ noted y_3, y_4 and y_5, respectively. If we write two equations similar to (2.2) for each post-synaptic system we obtain a system of 6 first-order differential equations that describes Jansen's neural mass model:

$$\left\{\begin{array}{ll} \dot{y_0}(t) = y_3(t) & \dot{y_3}(t) = Aa\text{Sigm}[y_1(t) - y_2(t)] - 2ay_3(t) - a^2y_0(t) \\ \dot{y_1}(t) = y_4(t) & \dot{y_4}(t) = Aa\{p(t) + C_2\text{Sigm}[C_1y_0(t)]\} - 2ay_4(t) - a^2y_1(t) \\ \dot{y_2}(t) = y_5(t) & \dot{y_5}(t) = BbC_4\text{Sigm}[C_3y_0(t)] - 2by_5(t) - b^2y_2(t). \end{array}\right. \qquad (2.3)$$

We focus on the variable $y = y_1 - y_2$, the membrane potential of the main family of neurons (see figure 2.1.b). We think of this quantity as the output of the unit because in the cortex, the pyramidal cells are the main vectors of long range cortico-cortical connections. Besides, their electrical activity corresponds to the EEG signal: pyramidal neurons throw their apical dendrites to the superficial layers of the cortex where the post-synaptic potentials are summed, accounting for the essential part of the EEG activity [61].

Numerical values of the parameters

The parameters A, B, a and b have been adjusted by van Rotterdam [117] to reproduce some basic properties of real post-synaptic potentials and make the system produce alpha activity. These authors set $A = 3.25mV$, $B = 22mV$, $a = 100s^{-1}$ and $b = 50s^{-1}$. The excitability of cortical neurons can vary as a function of the action of several substances and v_0 could potentially take different values, though we will use $v_0 = 6mV$ as suggested by Jansen on the basis of experimental studies due to Freeman [40]. The works of the latter also suggest that $\nu_{max} = 5s^{-1}$ and $r = 0.56mV^{-1}$, the values used by Jansen and Rit.
The connectivity constants $C_i, i = 1, \ldots, 4$ are proportional to the average number of synapses between populations. On the basis of several neuroanatomical studies ([15] among others) where these quantities had been estimated by counting synapses, Jansen and Rit succeeded in reducing them to fractions of a single parameter C:

$$\left\{\begin{array}{ll} C_1 = C & C_2 = 0.8C \\ C_3 = 0.25C & C_4 = 0.25C \end{array}\right.$$

Jansen and Rit varied C to observe alpha-like activity and obtained it for $C = 135$ (see figure 2.4).
In summary, previous work shows that the following set of parameters allows the neural mass model described by equations (2.3) to produce a set of EEG-like signals:

$$\left\{\begin{array}{ll} A = 3.25 & B = 22 \\ a = 100 & b = 50 \\ v_0 = 6 & C = 135 \end{array}\right. \qquad (2.4)$$

We show in section 2.2.4 that the behaviour of the neural mass model is fairly sensitive to the choice of the values of these parameters. Indeed changes as small as 5% in these values produce some fairly different behaviours.

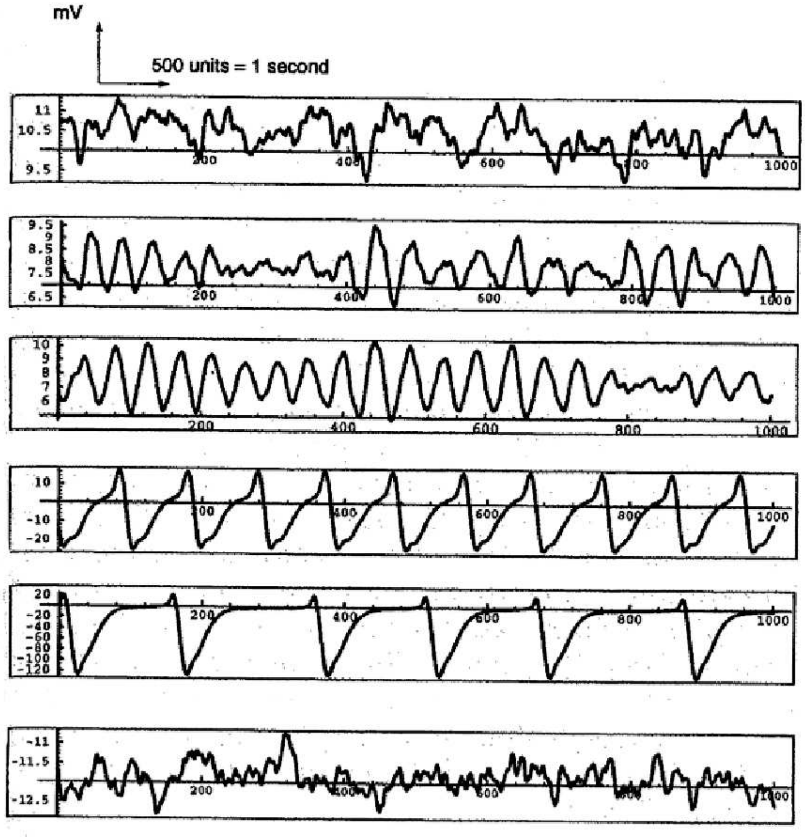

Figure 2.4: *Activities of the unit shown in figure 2.1 when simulated with a uniformly distributed white noise (between 120 and 320 Hz) as input. The different curves show different activities depending on the value of the parameter* C*. The third curve from the top looks like alpha activity and has been obtained for* $C = 135$ *(From [58]).*

The quantity p represents the lumped activity of the brain areas connected to the unit. Jansen and Rit chose $p(t)$ to be a uniformly distributed noise ranging from 120 to 320 pulses per second as they wanted to model non-specific input (they used the terms *background spontaneous activity*). This noise dynamics allowed them to produce alpha-like activity. Similarly, Wendling and his colleagues used a white Gaussian noise (mean 90 and standard deviation 30) for $p(t)$ and observed the emission of spikes that was reminiscent of an epileptic activity. We show in the next section that these two different behaviours can be nicely accounted for by a geometric study of the system (2.3) through its bifurcations.

2.2 BIFURCATIONS AND OSCILLATIONS

In this section we consider p as a parameter of the system and propose to study the behavior of a unit when p varies. We therefore study the dynamical system (2.3) all parameters, but p, being kept constant and equal to the values set by Jansen and Rit (see (2.4)). In section 2.2.4 we extend this analysis to other values of the parameters in (2.4).
Let $Y = (y_0, \dots, y_5)^T$, the system has the form

$$\dot{Y} = f(Y, p),$$

where f is the smooth map from $\mathbb{R}^6$ to $\mathbb{R}^6$ given by (2.3) and p is a parameter.

We are interested in computing the fixed points and periodic orbits of the system as functions of p because they will allow us to account for the appearance of such activities as those shown in figures 2.4 (alpha-like activity) and 2.5 (epileptic spike-like activity).

2.2.1 Fixed points

The one parameter family of fixed points

We look for the points Y where the vector field $f(.,p)$ vanishes (called *fixed points*, *critical points* or *equilibrium points*). Writing $\dot{Y} = 0$ we obtain the system of equations

$$\begin{cases} y_0 = \frac{A}{a}\text{Sigm}[y_1 - y_2] & y_3 = 0 \\ y_1 = \frac{A}{a}(p + C_2\text{Sigm}[C_1 y_0]) & y_4 = 0 \\ y_2 = \frac{B}{b}C_4\text{Sigm}[C_3 y_0] & y_5 = 0, \end{cases} \tag{2.5}$$

which leads to the (implicit) equation of the one-parameter family of equilibrium points in the $(p, y = y_1 - y_2)$ plane:

$$y = \frac{A}{a}p + \frac{A}{a}C_2\text{Sigm}\Big[\frac{A}{a}C_1\text{Sigm}(y)\Big] - \frac{B}{b}C_4\text{Sigm}\Big[\frac{A}{a}C_3\text{Sigm}(y)\Big] \tag{2.6}$$

As mentioned before, $y = y_1 - y_2$ can be thought of as representing the EEG activity of the unit and p is our parameter of interest. We show the curve defined by (2.6) in figure 2.6.a. The number of intersections between this curve and a vertical line of equation $p = constant$ is the number of equilibrium points for this particular value of p. We notice that for $p \approx 110 - 120$, the system goes from three equilibrium points to a single one. We also note that the curve has been drawn for some negative values of

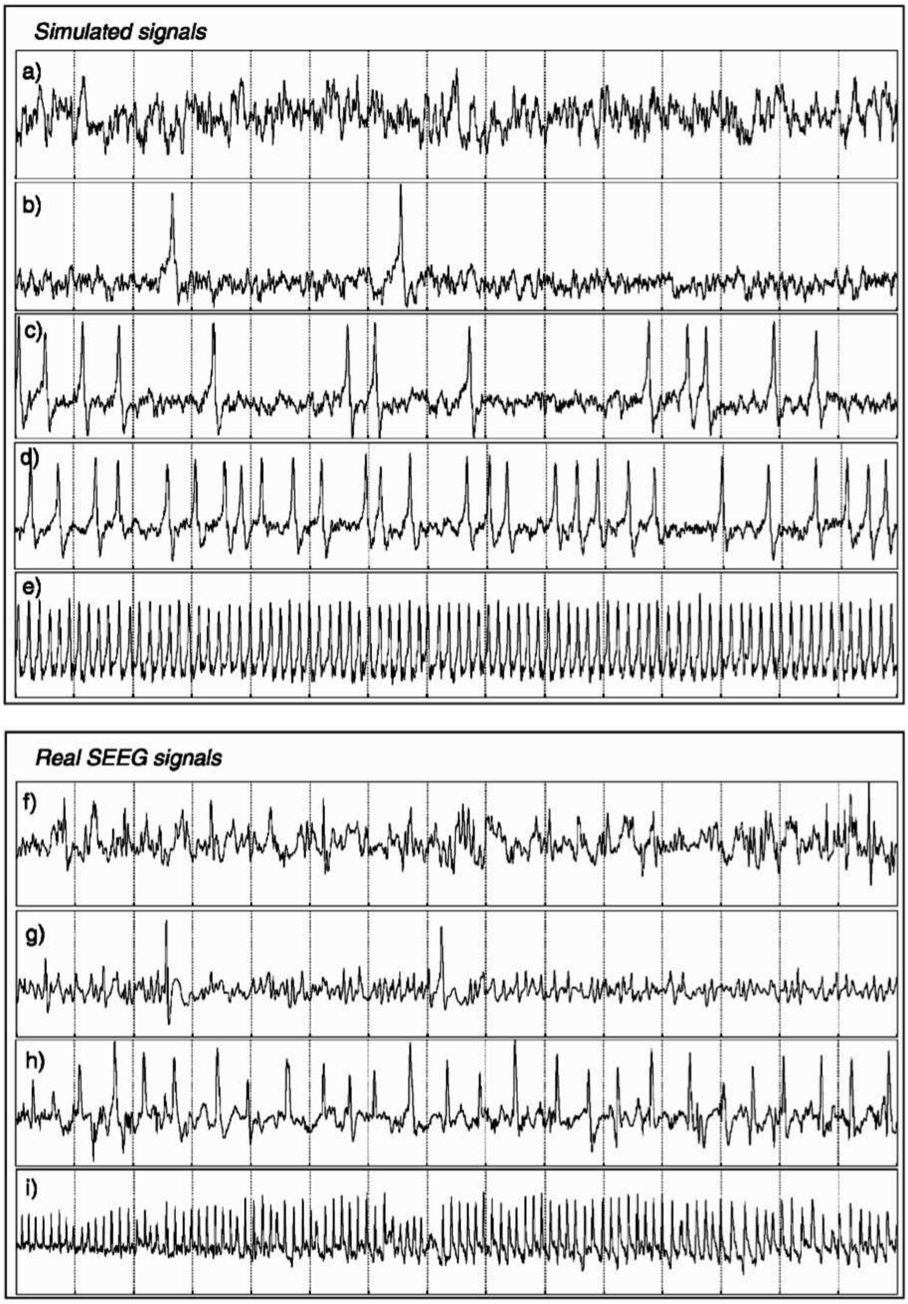

Figure 2.5: *(a)-(e) Activities of the unit shown in figure 2.1 when simulated with a white Gaussian noise as input (corresponding to an average firing rate between 30 and 150 Hz). The authors varied the excitation/inhibition ratio* A/B*. As this ratio is increased we observe sporadic spikes followed by increasingly periodic activities. (f)-(i) Real activities recorded from epileptic patients before (f,g) and during a seizure (h,i) (From [119]).*

p. These points do not have any biological meaning since p is a firing rate. It turns out though that they play a central role in the mathematical description of the model (see section 2.2.2).

The coordinates of the singular points cannot be written explicitely as functions of p but every singular point is completely determined by the quantity y. More precisely, the coordinates of every singular point $S(y)$ have the following form :

$$S(y) = \\ \left(\frac{A}{a}\text{Sigm}(y) \quad \frac{A}{a}(p + C_2\text{Sigm}[C_1\frac{A}{a}\text{Sigm}(y)]) \quad \frac{B}{b}C_4\text{Sigm}[C_3\frac{A}{a}\text{Sigm}(y)] \quad 0 \quad 0 \quad 0\right)^{\top} \tag{2.7}$$

p and y being related through equation (2.6).

Local study near the singular points

In order to study the behavior of the system near the fixed points we linearize it and calculate its Jacobian matrix, *i.e.* the partial derivative $\mathcal{J}$ of $f(.,p)$ at the fixed point $S(y)$. It is easy but tedious to show that at the fixed point $S(y)$ we have

$$\mathcal{J}(S(y)) = \begin{pmatrix} 0_3 & I_3 \\ KM(y) & -K \end{pmatrix},$$

where $K = 2\text{diag}(a, a, b)$, $M(y) = \begin{pmatrix} -a/2 & \gamma(y) & -\gamma(y) \\ \delta(y) & -a/2 & 0 \\ \theta(y) & 0 & -b/2 \end{pmatrix}$, I_3 is the three-dimensional identity matrix and 0_3 the three-dimensional null matrix.
The three functions γ, δ and θ are defined by

$$\begin{aligned} \gamma(y) &= \tfrac{A}{2}\text{Sigm}'(y) \\ \delta(y) &= \tfrac{AC_1C_2}{2}\text{Sigm}'(C_1 y_0(y)) \\ \theta(y) &= \tfrac{BC_3C_4}{2}\text{Sigm}'(C_3 y_0(y)), \end{aligned}$$

where $y_0(y)$ is the first coordinate of $S(y)$ and Sigm' is the derivative of the function Sigm.
We compute the eigenvalues of $\mathcal{J}$ along the curve of figure 2.6.a to analyze the stability of the family of equilibrium points. The results are summarized in figure 2.6.b. The solid portions of curve correspond to stable fixed points (all eigenvalues have a negative real part) and the dashed ones to unstable fixed points (some eigenvalues have a positive real part). Stars indicate points where at least one eigenvalue of the system crosses the imaginary axis, having therefore a zero real part. These points are precious landmarks for the study of bifurcations of the system.

2.2.2 Bifurcations and oscillatory behaviour in Jansen's model

A bifurcation is a drastic and sudden change in the behavior of a dynamic system that occurs when one or several of its parameters are varied. Often it corresponds to the appearance or disappearance of limit cycles. Describing oscillatory behaviours in

Jansen's model is therefore closely related to studying its bifurcations. In our case when p varies from $-\infty$ to $+\infty$ the system undergoes five bifurcations (remember that only the positive values of p are biologically relevant).

We now describe these bifurcations from a somewhat intuitive viewpoint but our results are grounded in the mathematical theory of bifurcations [10, 11, 55, 68, 86] and the extensive use of the software *XPP-Aut* due to Bard Ermentrout (available on `http://www.pitt.edu/~phase/`). We were also inspired by bifurcation studies of single neuron models (see [52, 56, 96]).

Hopf bifurcations and alpha activity in Jansen's model

When p is varied smoothly the eigenvalues of the fixed points move smoothly in the complex plane: when two complex conjugate eigenvalues cross the imaginary axis the system undergoes in general what is called a *Hopf bifurcation* (see figure 2.7).
Two of them happen in Jansen's model (if we ignore the negative values of p) for $p = 89.83$ and $p = 315.70$. A theorem due to Hopf [86] shows [1] that for $p = 89.83$ a one parameter family of stable periodic orbits appears at the fixed point that has two complex conjugate eigenvalues crossing the imaginary axis towards positive real parts. These periodic orbits persist till $p = 315.70$ where a second Hopf bifurcation occurs: the two eigenvalues whose real parts became positive for $p = 89.83$ see them become negative again, corresponding to the (re)creation of a simple attractive fixed point. This is shown in figure 2.6.c: for p between 89.83 and 315.70, there is a family of periodic orbits (we call them *Hopf cycles* from now on) parametrized by p for which the minimal and maximal y values have been plotted (thick oval curve). Numerically, using XPP-Aut, we find that these oscillations have a frequency around 10 Hz, which corresponds to alpha activity. So it appears that alpha-like activity in Jansen's model is determined by Hopf cycles. Interestingly enough, the system does not display any Hopf bifurcation if we approximate the sigmoid by a piecewise linear function, or if we try to reduce the dimensionality of the system using lower order postsynaptic responses or by singular perturbation theory [11]. In these cases the system is unable to produce alpha activity.

Let us interpret Jansen and Rit's results in the light of our mathematical analysis. They report observing alpha activity (third curve in figure 2.4) when they use a uniformly distributed noise in the range 120-320 Hz at the entry of the system. This is easy to account for if we look at figure 2.6.c: in this domain of p values, the Hopf cycles are essentially the only attractors of the dynamical system (2.3). So, at every time instant t, its trajectories will tend to coil around the Hopf cycle corresponding to $p = p(t)$. We will therefore see oscillations of constant frequency and varying amplitude leading to the *waxing and waning* activity reported by Jansen and Rit.

Global bifurcations and spike-like epileptic activity

Hopf bifurcations are called *local* because their appearance only depends on local properties of the dynamical system around the bifurcation point. In figure 2.5, we see that the system is able to display spike-like activities that resemble certain epileptic

---

[1] The proof of the existence of a Hopf bifurcation relies on the calculation of the *Lyapunov number* at the bifurcation points.

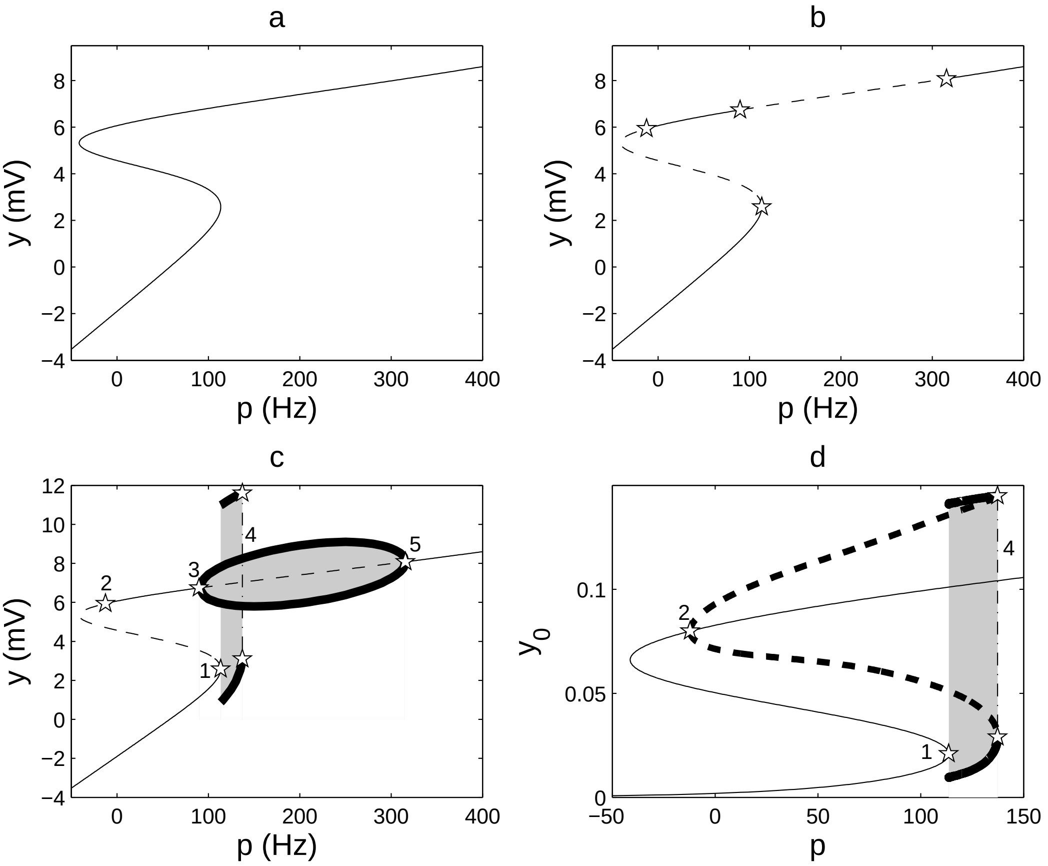

Figure 2.6: *a) Curve defined by equation (2.6). For each value of p, the curve yields the coordinate(s) y of the corresponding fixed point(s). b) Fixed points and their stability: stable fixed points lie on the solid portions of the curve and unstable points lie on the dashed ones. Stars correspond to transition points where the Jacobian matrix has some eigenvalues with zero real part. c) Curve of the fixed points with two branches of limit cycles (shaded regions bounded by thick black curves). The stars labeled 3 and 5 are* Hopf bifurcation *points. The oval between them is the branch of Hopf cycles: for each $89.83 \leq p \leq 315.70$, the thick black curves between points 3 and 5 give the highest and lowest y values attained by the Hopf cycle. The other branch of limit cycles lies in the domain between the star labelled 1, where there is a* saddle-node bifurcation with homoclinic orbit *and the dash-dotted line 4 representing a* fold bifurcation of limit cycles. *This kind of representation is called a* bifurcation diagram. *d) A Hopf bifurcation at the point labeled 2 ($p = -12.15$) gives rise to a branch of unstable limit cycles that merges with the branch of stable cycles lying between the point labeled 1 and the dashed line labeled 4. This phenomenon is called a* fold bifurcation of limit cycles.

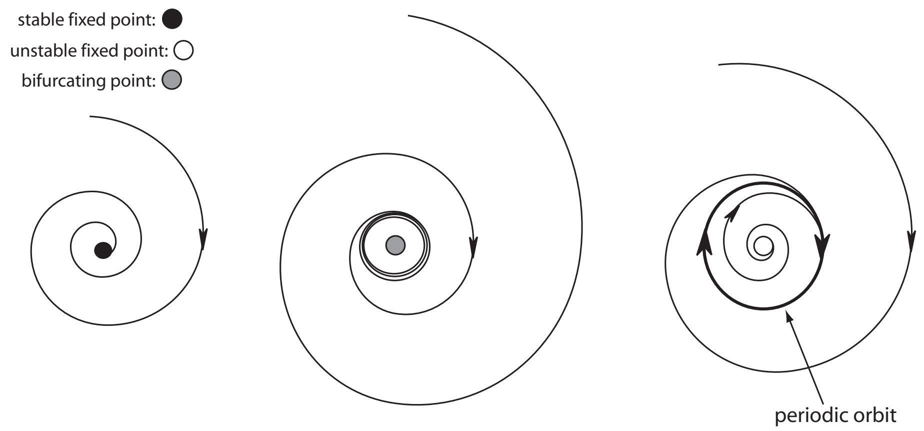

Figure 2.7: *Projection of a Hopf bifurcation in a subplane of the phase space. Left. Stable fixed point with an exponentially converging trajectory (all eigenvalues have a negative real part). Center. Bifurcating point with a trajectory converging infinitely slowly (a pair of complex conjugate eigenvalues lie on the imaginary axis, having therefore a negligible attractive power). Right. The bifurcating point has turned unstable (the two complex conjugate eigenvalues have a positive real part) and a periodic orbit has emerged from it.*

EEG recordings [119]. These activities arise from a branch of large stable periodic orbits delimited by a pair of *global* bifurcations (i.e. depending not only on local properties of the dynamical system) that correspond to the star labeled 1 and the dash-dotted line labeled 4 in figure 2.6.c. From now on, we will call these orbits *spike cycles*.
The branch of spike cycles begins for $p = 113.58$, thanks to a *saddle-node bifurcation with homoclinic orbit* [2] (see figure 2.8 and [68, 86]).
It ends for $p = 137.38$ because of a *fold bifurcation of limit cycles* that we identified with XPP-Aut. This bifurcation results from the fusion of a stable and an unstable family of periodic orbits. The stable family is the branch of spike cycles and the unstable family originates from a Hopf bifurcation occuring at $p = -12.15$.
Thanks to XPP-Aut, we have been able to plot the folding and the associated Hopf bifurcation with respect to the y_0 axis (see figure 2.6.d). So far we have shown the bifurcation diagrams in the (p, y) plane, but for technical reasons due to XPP-Aut, we show the bifurcation diagram in the (p, y_0) plane in this case. Its general properties are the same though. For example we recognize the S shape of the fixed points diagram and the relative position of landmarks 1, 2 and 4.
Contrary to the Hopf cycles whose periods remains around 10 Hz, the spike cycles can display every frequency in the range $0 - 5$ Hz (it increases with p) so that they are able to reproduce the various “spiking” activities observed in figure 2.5.

In this case also we can identify the central role played by p in shaping the output of the unit. Wendling *et al.* used a Gaussian noise with mean 90 and standard deviation 30 to produce the spikes in figure 2.5 resulting in an input to the unit essentially varying between 30 and 150 Hz, which is quite low compared to the range used by

---

[2] The proof of the existence of this saddle-node bifurcation with homoclinic orbit (SNIC) uses a theorem due to Shil’nikov [68].

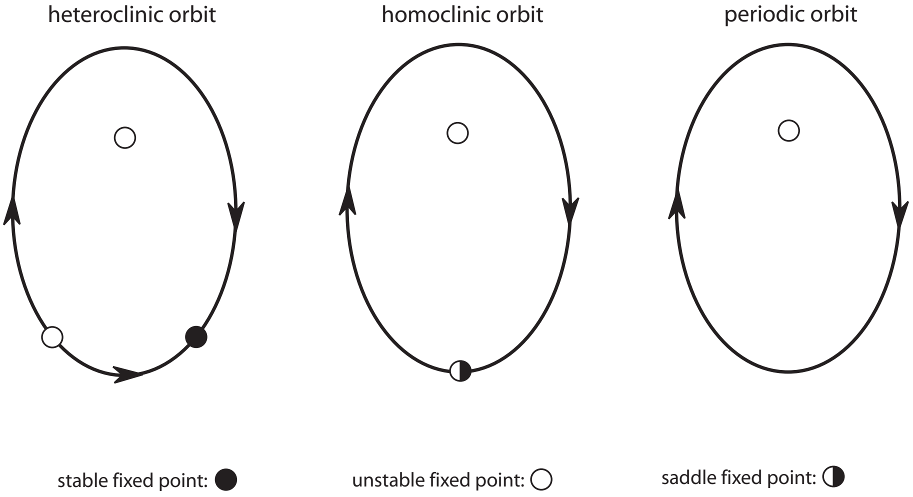

Figure 2.8: *Projection of a SNIC bifurcation in a subplane of the phase space. The figure features three invariant circles (i.e. closed curves composed of one or more trajectories). Left. An heteroclinic orbit (i.e. a curve composed of two trajectories emerging from the same unstable fixed point and converging to the same stable fixed point) surrounds an unstable fixed point. Center. The two fixed points belonging to the invariant circle merge into a semi-stable saddle fixed point. The resulting homoclinic orbit has an infinite period. Right. The invariant circle turns into a periodic orbit as the fixed points disappear.*

Jansen and Rit. Let us first distinguish two parts in the curve of fixed points in figure 2.6.c. We call *lower branch* the set of stable fixed points below the star labelled 1 and *upper branch* the one between the stars labelled 2 and 3. For p between 30 and 90 the system displays a classical bistable behaviour with two stable fixed points (one on each branch), the lowest fixed points appearing to be dominant: we found experimentally that the basin of attraction of the upper point is not very large, so that one has to start quite close to it in order to converge to it. As a result, a low input ($p \leq 90$) produces in general a low output: the trajectory is attracted by the lower branch. For p between 110 and 140, we are in the range of p values where spike-like activity can appear and where spiking competes with Hopf cycles, but trajectories near the lower branch are attracted by spike cycles (as we will see in 2.2.3) hence producing spike-shaped activities. These two facts – attraction to the lower branch and preference of the lower branch for spike cycles – allow us to understand how the model can produce epileptic-like activities.

2.2.3 Synthesis

We now have in hands all the ingredients to describe the activity of this neural mass model when stimulated by a slowly varying input. For that purpose we computed two trajectories (or *orbits*) of the system with p increasing linearly in time at a slow rate ($\mathrm{d}p/\mathrm{d}t = 1$). The system was initialized at the two stable fixed points at $p = 0$: the stable state on the lower branch and the one on the upper branch (see stars in figure 2.9).
As long as $p \leq 89.83$, the two trajectories are “flat”, following their respective branches

of fixed points (figure 2.10, $p = 80$). After the Hopf bifurcation occurring at $p = 89.83$ the orbit corresponding to the upper branch naturally coils on the Hopf cycles branch (figure 2.10, $p = 100$), resulting in alpha-like activity. The trajectory on the lower branch does the same with the spike cycles as soon as p reaches the value 113.58 (figure 2.10, $p = 125$). As $p \geq 137.38$, the only remaining attractor is the Hopf cycle branch so that the system can only exhibit alpha-like behaviour (figure 2.10, $p = 200$). For high values of p (≥ 315.70), there is only one stable fixed point and the trajectory is "flat" again.

These results lead us to distinguish two states, the lower and the upper, for the unit. The *lower state* is described by the combination of the lower branch of fixed points that correspond to rest, and the spike cycles (thick lines in figure 2.9). It corresponds to positive values of p less than 137.38. The *upper state* is described by the upper branch of fixed points, the Hopf cycle branch and the branch of fixed points following it (thin lines in figure 2.9). It corresponds to positive values of p. These states are relevant for slow dynamics of the input p. In effect, a trajectory starting near one of these states will stay in its neighborhood when p is varied slowly (increasing or decreasing). When the unit is in its lower state and p becomes larger than 137.38, it jumps to its upper state and cannot return to its lower state (if p varies slowly). Therefore, when in its upper state, a unit essentially produces alpha-like activity and its input must be decreased abruptly to bring it back to its lower state. Conversely, starting in the lower state a unit can be brought to the upper state by an abrupt increase of its input. It can also stay in its lower state regime, between rest and spiking, if the input and its variation remains moderate.

2.2.4 What about other parameters?

We think that the bifurcation analysis with respect to p is the most relevant since this parameter is expected to vary more and faster than the others, but it is interesting to build bifurcation diagrams with respect to p with different settings of the other parameters. We indeed observed that varying any parameter by more than 5% leads to quite drastic changes in the bifurcation diagram and to significantly less rich behaviours of the unit. These changes fall into two broad categories (see figure 2.11). For low values of A, B or C, or high values of a or b, the system is no longer able to produce oscillations (figure 2.11.a). For high values of A, B or C, or low values of a or b, we observed a new kind of bifurcation diagram (an example is given in figure 2.11.b). In this regime, the system has only one stable state for each value of p, except sometimes in a narrow range of p values (in the figure, $173.1 \leq p \leq 180.4$). The range where spiking can occur is broader and the one for alpha activity is severely truncated. Moreover, spiking does not coexist with alpha rhythm anymore so that (except for a very small range of p values) it is the only available behaviour on a broad interval of p values (in the figure, $112.6 \leq p \leq 173.1$). So spiking becomes really prominent.

The mathematical explanation for this new diagram is the fusion of the Hopf cycles branch with the branch of unstable periodic orbits that can be seen in figure 2.6.d. It results in a new organization of periodic orbit branches. We have two stable branches (for $112.6 \leq p \leq 180.4$ and $173.1 \leq p \leq 457.1$), linked by a branch of unstable orbits. Transitions between stable and unstable orbits are made via fold bifurcations of limit cycles like the one in figure 2.6.d.

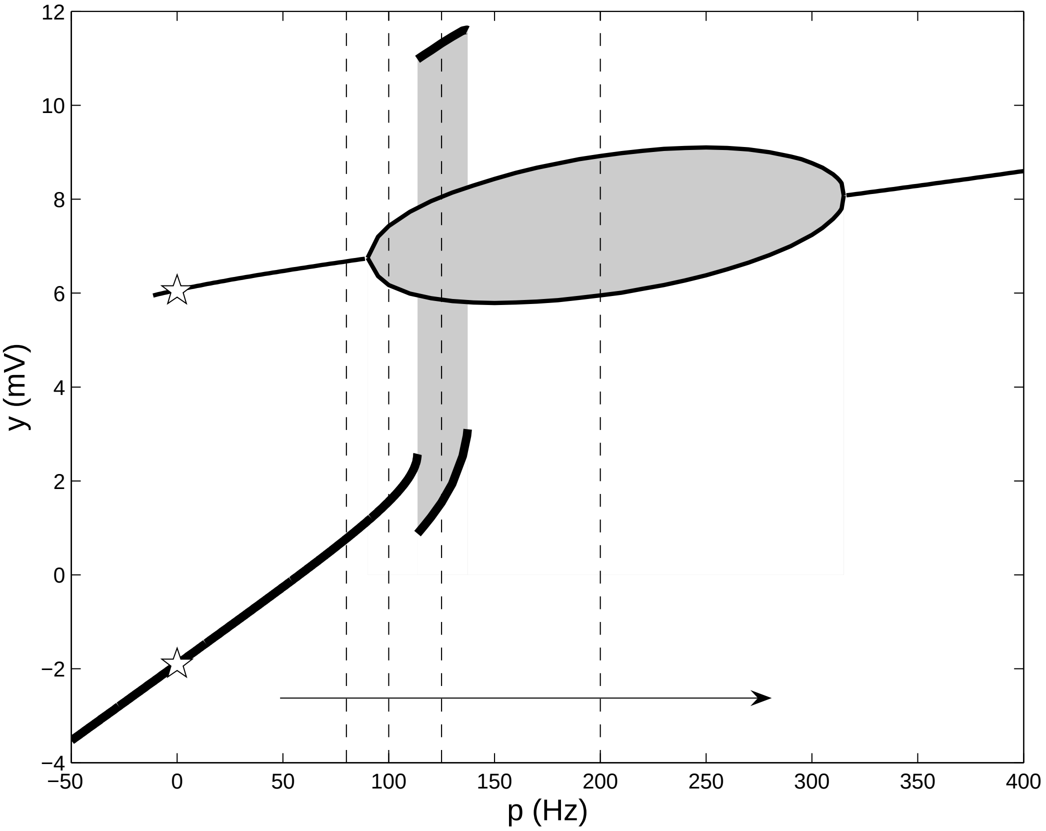

Figure 2.9: *Diagram of the stable attractors (stable fixed points and stable limit cycles) of the model described by equations (2.3). The stars show the starting points of the two trajectories we simulated with* p *slowly increasing. Their time courses have been frozen for* $p = 80$, 100, 125 *and* 200 *(as indicated by the vertical dashed lines on this figure) and can be seen in figure 2.10. Lower and upper states of the unit correspond to the thick and thin lines, respectively.*

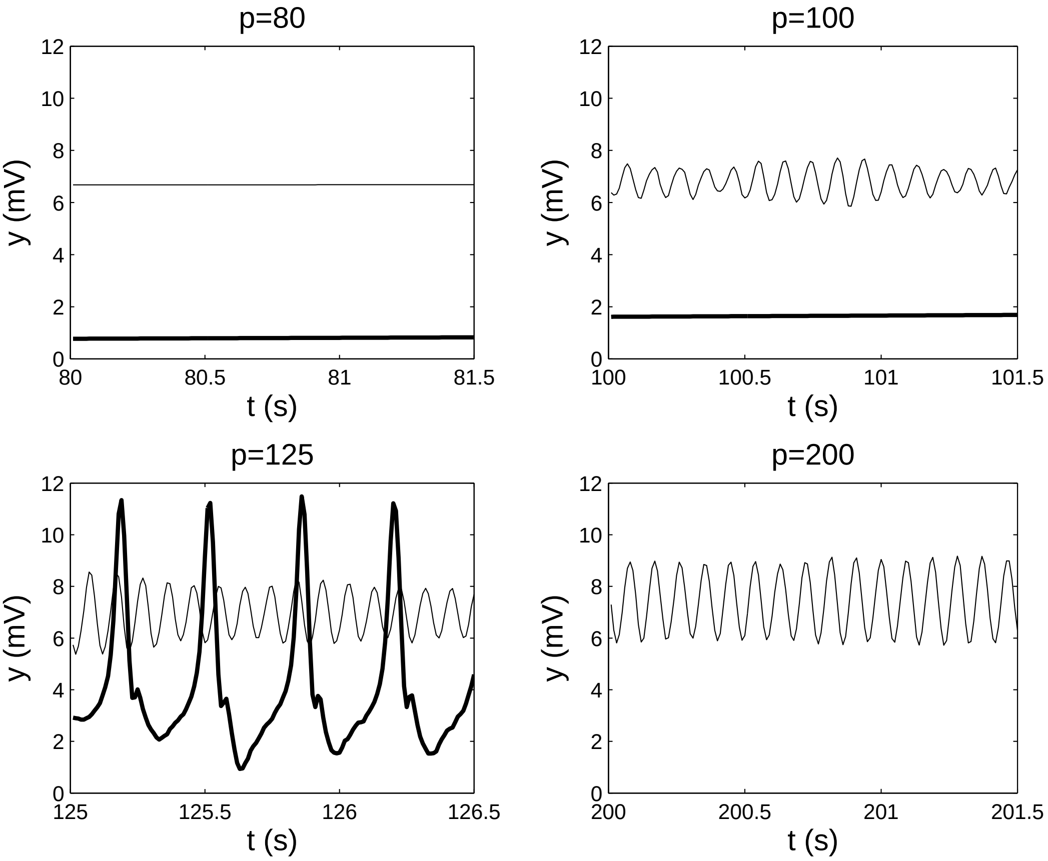

Figure 2.10: *Activities produced by Jansen's neural mass model for typical values of the input parameter* p *(see text). The thin (respectively thick) curves are the time courses of the output* y *of the unit in its upper (respectively lower) state. For* $p > 137.38$*, there is only one possible behaviour of the system. Note: in the case of oscillatory activities we added a very small amount of noise to* p *(a zero mean Gaussian noise with standard deviation* 0.05*).*

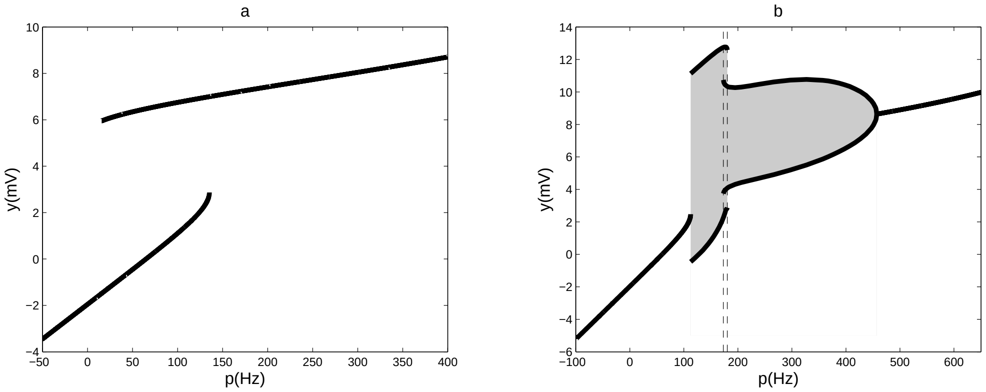

Figure 2.11: *The stable attractors of the system in two typical cases encountered for different settings of parameters A, B, C, a or b. a) corresponds to lower (respectively higher) values of A, B, C (respectively a and b) than those given by (2.4). Here, $A = 3$ instead of 3.25: there are no more limit cycles. b) corresponds to higher (respectively lower) values of A, B, C (respectively a and b). Here $C = 140$ instead of 135. The spiking behaviour is more prominent and is the only one available in a wide range of p values ($112.6 \leq p \leq 173.1$). Except in a narrow band ($173.1 \leq p \leq 180.4$), the system displays one single behaviour for each value of p.*

2.3 CONCLUSION

So, Jansen's model is a raw neuronal network model, essentially bistable, exhibiting oscillatory behaviours that matches certain oscillatory EEG signals from the cortex: 10Hz alpha activity and epileptic spikes up to 5Hz. Now we raise the question of the spatial scale of the cortical sources of such signals. Alpha activity is a common EEG signal arising from the synchronization of several thousands of neurons. EEG spatial resolution is relatively poor (centimeter scale). However, stereo-electroencephalography (SEEG) or magnetoencephalography (MEG) can provide a higher spatial resolution (millimeter scale) where alpha activity and epileptic spikes are also observed, which suggests that Jansen's model could also be adapted to this lower scale.

Jansen, Lopes Da Silva, David, Friston, Wendling and their co-workers have used neural masses to build large scale networks of cortical areas and thalamic nuclei connected via white matter fibers. In these models, units like Jansen's column actually stood for whole cortical areas or parts of epileptogenic networks. They have succeeded in modeling complex dynamic behaviours involved in epilepsy, evoked potentials or long range functional connectivity between different regions of the brain, that they have correlated with MEG/EEG/SEEG signals.

We would like to use the mesoscopic approach for finer scales of cortical modeling. In the next section, we study several models of *neural fields* seen as 2D continua of small cortical columns.

Part II

Mathematical neural field models

CHAPTER 3

INFINITE NEURAL FIELD MODELS

OVERVIEW

Neural field models first appeared in the 50's, but the theory really took off in the 70's with the works of Wilson and Cowan [120, 121] and Amari [3, 4]. Neural fields are continuous networks of interacting neural masses, describing the dynamics of the cortical tissue at the population level. In this chapter, we study homogeneous stationary solutions (i.e independent of the spatial variable) and bump stationary solutions (i.e. localized areas of high activity) in two kinds of infinite two-dimensional neural field models composed of two neuronal layers (excitatory and inhibitory neurons). We particularly focus on bump patterns, which have been observed in the prefrontal cortex and are involved in working memory tasks [42]. We first show how to derive neural field equations from the spatialization of mesoscopic cortical column models. Then, we introduce classical techniques borrowed from Coombes [24] and Folias and Bressloff [38] to express bump solutions in a closed form and make their stability analysis. Finally we instantiate these techniques to construct stable two-dimensional bump solutions. This chapter corresponds to the research report [34] (2007) and will be included in a future paper, currently in preparation.

Contents

3.1 Neural field equations 70
  3.1.1 Interactions between a few neural masses 70
  3.1.2 Neural fields models 72
3.2 Study of bump solutions 72
  3.2.1 Stationary solutions 73
  3.2.2 Stability of the solutions 76
3.3 Construction of bump solutions 78
  3.3.1 Existence 79
  3.3.2 Stability 79
3.4 Conclusion 82

We consider the formation of bumps in an infinite two-dimensional neural field composed of two interacting layers of neural masses: excitatory and inhibitory masses such as shown in figure 3.1. Each point of the field can be viewed as a cortical column composed of two neural masses (one in each layer). Columns are assembled spatially to form the neural field, which is meant to represent a macroscopic part of the neocortex, e.g. a cortical area.

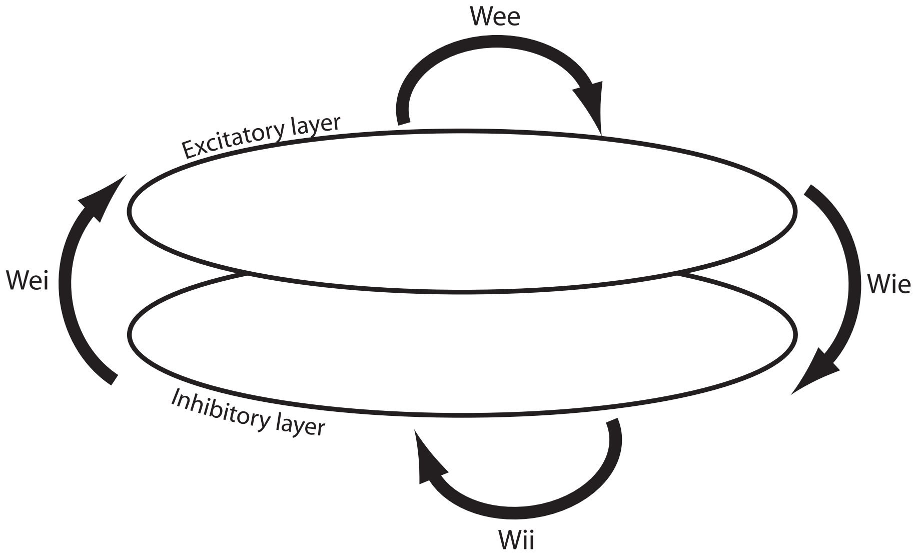

Figure 3.1: *Two interacting neuronal layers of excitatory and inhibitory cells.*

In this chapter, we consider an infinite neural field. Then each layer can be identified with $\mathbb{R}^2$. Neural masses are characterized by their layer, e or i, and their horizontal coordinates $\mathbf{r} = (r_1, r_2)$.

3.1 NEURAL FIELD EQUATIONS

3.1.1 Interactions between a few neural masses

The following derivation is built after Ermentrout's review [31]. We consider n interacting neural masses. Each mass k is described by its membrane potential $V_k(t)$ or by its instantaneous firing rate $\nu_k(t)$, the relation between the two quantities being of the form $\nu_k(t) = S_k(V_k(t))$ [27, 41], where S_k is sigmoidal and depends on the layer of neuron k. Here we consider the limiting case of a Heaviside function

$$S_x(V) = \overline{\nu}_x \, H(V - \theta_x), \quad x \in \{e, i\},$$

where H is the Heaviside distribution, $\overline{\nu}_x$ the maximal firing rate of neurons of type x and θ_x their excitabillity threshold.
The mass m is connected to the mass k. A single action potential from m is seen as a post-synaptic potential $PSP_{km}(t - s)$ by k, where s is the time of the spike hitting the terminal and t the time after the spike. We neglect the delays due to the distance travelled down the axon by the spikes. Assuming that the post-synaptic potentials

sum linearly, the membrane potential of the mass k is

$$V_k(t) = \sum_{m,p} PSP_{km}(t - t_p)$$

where the sum is taken over presynaptic masses and the arrival times of the spikes produced by them. The number of spikes arriving between t and $t + dt$ is $\nu_m(t)dt$. Therefore we have

$$V_k(t) = \sum_m \int_{t_0}^t PSP_{km}(t-s)\nu_m(s)\,ds = \sum_m \int_{t_0}^t PSP_{km}(t-s)S_m(V_m(s))\,ds,$$

or, equivalently

$$\nu_k(t) = S_k\left(\sum_m \int_{t_0}^t PSP_{km}(t-s)\nu_m(s)\,ds\right) \tag{3.1}$$

There are two main simplifying assumptions that appear in the literature [31] and yield two different models.

The voltage-based model

The assumption, made in [51], is that the post-synaptic potential has the same shape no matter which presynaptic neuron type caused it, the sign and amplitude may vary though. This leads to the relation

$$PSP_{km}(t) = W_{km}PSP_k(t).$$

If $W_{km} > 0$ mass m excites mass k whereas it inhibits it when $W_{km} < 0$. Finally, if we assume that $PSP_{km}(t) = W_{km}e^{-t/\tau_k}H(t)$ (where H is the Heaviside distribution), or equivalently that

$$\tau_k \frac{dPSP_{km}(t)}{dt} + PSP_{km}(t) = W_{km}\tau_k\delta(t), \tag{3.2}$$

we end up with the following system of ordinary differential equations

$$\frac{dV_k(t)}{dt} + \frac{V_k(t)}{\tau_k} = \sum_m W_{km}S_m(V_m(t)) + I_k^{\text{ext}}(t), \quad k = 1, ..., n, \tag{3.3}$$

that describes the dynamic behaviour of the network. We have added an external current $I_k^{\text{ext}}(t) \geq 0$ to model external input to mass k. We introduce the $n \times n$ matrix $\mathbf{W} = W_{km}$, and the function $\mathbf{S} : \mathbb{R}^n \to \mathbb{R}^n$ such that $\mathbf{S}(\mathbf{x})$ is the vector of coordinates $S_k(x_k)$. We rewrite (3.3) in vector form and obtain the following system of n ordinary differential equations

$$\dot{\mathbf{V}} = -\mathbf{L}\mathbf{V} + \mathbf{W}\mathbf{S}(\mathbf{V}) + \mathbf{I}^{\text{ext}}, \tag{3.4}$$

where $\mathbf{L}$ is the diagonal matrix $\mathbf{L} = \mathrm{diag}(1/\tau_k)$.

The activity-based model

The assumption is that the shape of a post-synaptic potential depends only on the nature of the presynaptic mass, that is

$$PSP_{km}(t) = W_{km}PSP_m(t).$$

As above we suppose that $PSP_{km}(t)$ satisfies the differential equation (3.2) and define the activity to be

$$A_m(t) = \int_{t_0}^{t} PSP_m(t-s)\nu_m(s)\,ds.$$

A similar derivation yields the following set of ordinary differential equations

$$\frac{dA_k(t)}{dt} + \frac{A_k(t)}{\tau_k} = S_k\left(\sum_m W_{km}A_m(t) + I_k^{\text{ext}}(t)\right), \quad k = 1, ..., n.$$

We rewrite this in vector form

$$\dot{\mathbf{A}} = -\mathbf{LA} + \mathbf{S}(\mathbf{WA} + \mathbf{I}^{\text{ext}}). \tag{3.5}$$

3.1.2 Neural fields models

Following the above rules for a discrete network of masses, we form a two layers continuum of masses.

We note $\mathbf{V}(\mathbf{r}, t)$ (respectively $\mathbf{A}(\mathbf{r}, t)$) the 2-dimensional state vector at the point $\mathbf{r}$ of the continuum and at time t. We introduce the 2×2 matrix function $\mathbf{W}(\mathbf{r}, \mathbf{r}')$ which describes how the mass at point $\mathbf{r}'$ influences that at point $\mathbf{r}$. More precisely, $W_{xy}(\mathbf{r}, \mathbf{r}')$ describes how the mass in layer y at point $\mathbf{r}'$ influences the mass in layer x at point $\mathbf{r}$. We call $\mathbf{W}$ the connectivity matrix function. Equation (3.4) can now be extended to

$$\dot{\mathbf{V}}(\mathbf{r}, t) = -\mathbf{LV}(\mathbf{r}, t) + \int_{\mathbb{R}^2} \mathbf{W}(\mathbf{r}, \mathbf{r}')\mathbf{S}(\mathbf{V}(\mathbf{r}', t))\,d\mathbf{r}' + \mathbf{I}^{\text{ext}}(\mathbf{r}, t), \tag{3.6}$$

and equation (3.5) to

$$\dot{\mathbf{A}}(\mathbf{r}, t) = -\mathbf{LA}(\mathbf{r}, t) + \mathbf{S}\left(\int_{\mathbb{R}^2} \mathbf{W}(\mathbf{r}, \mathbf{r}')\mathbf{A}(\mathbf{r}', t)\,d\mathbf{r}' + \mathbf{I}^{\text{ext}}(\mathbf{r}, t)\right).^1 \tag{3.7}$$

In detail, we have the following systems

$$\begin{cases} \dot{V}_e(\mathbf{r}, t) + \frac{V_e(\mathbf{r},t)}{\tau_e} = \int_{\mathbb{R}^2} W_{ee}(\mathbf{r}, \mathbf{r}')S_e(V_e(\mathbf{r}', t)) + W_{ei}(\mathbf{r}, \mathbf{r}')S_i(V_i(\mathbf{r}', t))\,d\mathbf{r}' + I_e^{\text{ext}}(\mathbf{r}, t) \\ \dot{V}_i(\mathbf{r}, t) + \frac{V_i(\mathbf{r},t)}{\tau_i} = \int_{\mathbb{R}^2} W_{ie}(\mathbf{r}, \mathbf{r}')S_e(V_e(\mathbf{r}', t)) + W_{ii}(\mathbf{r}, \mathbf{r}')S_i(V_i(\mathbf{r}', t))\,d\mathbf{r}' + I_i^{\text{ext}}(\mathbf{r}, t) \end{cases}, \tag{3.8}$$

and

$$\begin{cases} \dot{A}_e(\mathbf{r}, t) + \frac{A_e(\mathbf{r},t)}{\tau_e} = S_e\left(\int_{\mathbb{R}^2} W_{ee}(\mathbf{r}, \mathbf{r}')A_e(\mathbf{r}', t) + W_{ei}(\mathbf{r}, \mathbf{r}')A_i(\mathbf{r}', t)\,d\mathbf{r}' + I_e^{\text{ext}}(\mathbf{r}, t)\right) \\ \dot{A}_i(\mathbf{r}, t) + \frac{A_i(\mathbf{r},t)}{\tau_i} = S_i\left(\int_{\mathbb{R}^2} W_{ie}(\mathbf{r}, \mathbf{r}')A_e(\mathbf{r}', t) + W_{ii}(\mathbf{r}, \mathbf{r}')A_i(\mathbf{r}', t)\,d\mathbf{r}' + I_i^{\text{ext}}(\mathbf{r}, t)\right) \end{cases}. \tag{3.9}$$

In this study we will consider $\mathbf{W}$ translation invariant, $\mathbf{W}(\mathbf{r}, \mathbf{r}') = \mathbf{W}(\mathbf{r} - \mathbf{r}')$.

3.2 STUDY OF BUMP SOLUTIONS

This is an extension of the work of Bressloff, Coombes and Folias [24, 38]. Another interesting study on stationary patterns in two-dimensional neural fields can be found in [85].

---

[1] Although they are similar, equations (3.6) and (3.7) are not equivalent, as discussed in [31].

3.2.1 Stationary solutions

We look for stationary solutions of the systems (3.8) and (3.9):

$$\left\{\begin{array}{l} v_e(\mathbf{r}) = \tau_e \int_{\mathbb{R}^2} W_{ee}(\mathbf{r}-\mathbf{r}')S_e(v_e(\mathbf{r}')) + W_{ei}(\mathbf{r}-\mathbf{r}')S_i(v_i(\mathbf{r}'))\, d\mathbf{r}' + \tau_e\, I_e^{\text{ext}}(\mathbf{r}) \\ v_i(\mathbf{r}) = \tau_i \int_{\mathbb{R}^2} W_{ie}(\mathbf{r}-\mathbf{r}')S_e(v_e(\mathbf{r}')) + W_{ii}(\mathbf{r}-\mathbf{r}')S_i(v_i(\mathbf{r}'))\, d\mathbf{r}' + \tau_i\, I_i^{\text{ext}}(\mathbf{r}) \end{array}\right. \tag{3.10}$$

and

$$\left\{\begin{array}{l} a_e(\mathbf{r}) = \tau_e\, S_e\left(\int_{\mathbb{R}^2} W_{ee}(\mathbf{r}-\mathbf{r}')a_e(\mathbf{r}') + W_{ei}(\mathbf{r}-\mathbf{r}')a_i(\mathbf{r}')\, d\mathbf{r}' + I_e^{\text{ext}}(\mathbf{r})\right) \\ a_i(\mathbf{r}) = \tau_i\, S_i\left(\int_{\mathbb{R}^2} W_{ie}(\mathbf{r}-\mathbf{r}')a_e(\mathbf{r}') + W_{ii}(\mathbf{r}-\mathbf{r}')a_i(\mathbf{r}')\, d\mathbf{r}' + I_i^{\text{ext}}(\mathbf{r})\right) \end{array}\right. . \tag{3.11}$$

We introduce the terms $\widehat{W}_{xy} = \int_{\mathbb{R}^2} W_{xy}(\mathbf{r})\, d\mathbf{r}$.

Homogeneous solutions

Homogeneous stationary solutions (i.e., independent of the space variable) verify the systems

$$\left\{\begin{array}{l} v_e = \tau_e \left(\widehat{W}_{ee} S_e(v_e) + \widehat{W}_{ei} S_i(v_i) + I_e^{\text{ext}}\right) \\ v_i = \tau_i \left(\widehat{W}_{ie} S_e(v_e) + \widehat{W}_{ii} S_i(v_i) + I_i^{\text{ext}}\right) \end{array}\right. \tag{3.12}$$

and

$$\left\{\begin{array}{l} a_e = \tau_e\, S_e\left(\widehat{W}_{ee} a_e + \widehat{W}_{ei} a_i + I_e^{\text{ext}}(\mathbf{r})\right) \\ a_i = \tau_i\, S_i\left(\widehat{W}_{ie} a_e + \widehat{W}_{ii} a_i + I_i^{\text{ext}}(\mathbf{r})\right) \end{array}\right. . \tag{3.13}$$

These systems have at most four solutions. In the case of (3.12), (v_e, v_i) possibly have four values because there are two possible values for each $S_x(v_x)$ (namely, 0 and $\overline{\nu}_x$), depending on whether v_e and v_i are below or above the thresholds θ_e and θ_i. We obtain two expressions, for v_e and v_i, and they have to satisfy the threshold conditions, depending on $\widehat{\mathbf{W}}$, $\mathbf{I}^{\text{ext}}$ and τ_x, to be validated as actual solutions. In detail, the four possible solutions, with their threshold conditions are

$$\left\{\begin{array}{l} v_e = \tau_e\, I_e^{\text{ext}} \le \theta_e \\ v_i = \tau_i\, I_i^{\text{ext}} \le \theta_i \end{array}\right. \tag{3.14}$$

$$\left\{\begin{array}{l} v_e = \tau_e\, \widehat{W}_{ee}\, \overline{\nu}_e + \tau_e\, I_e^{\text{ext}} \ge \theta_e \\ v_i = \tau_i\, \widehat{W}_{ie}\, \overline{\nu}_e + \tau_i\, I_i^{\text{ext}} \le \theta_i \end{array}\right. \tag{3.15}$$

$$\left\{\begin{array}{l} v_e = \tau_e\, \widehat{W}_{ei}\, \overline{\nu}_i + \tau_e\, I_e^{\text{ext}} \le \theta_e \\ v_i = \tau_i\, \widehat{W}_{ii}\, \overline{\nu}_i + \tau_i\, I_i^{\text{ext}} \ge \theta_i \end{array}\right. \tag{3.16}$$

$$\left\{\begin{array}{l} v_e = \tau_e \left(\widehat{W}_{ee}\, \overline{\nu}_e + \widehat{W}_{ei}\, \overline{\nu}_i + I_e^{\text{ext}}\right) \ge \theta_e \\ v_i = \tau_i \left(\widehat{W}_{ie}\, \overline{\nu}_e + \widehat{W}_{ii}\, \overline{\nu}_i + I_i^{\text{ext}}\right) \ge \theta_i \end{array}\right. \tag{3.17}$$

One can easily see that some of these pairs of threshold conditions are mutually exclusive, namely (3.14) and (3.16), (3.15) and (3.16), and (3.15) and (3.17). Since in three pairs of solutions, at least two of them will be incompatible, there can be at most two homogeneous stationary solutions. The case of zero solutions is impossible because it would require two mutually exclusive conditions like $\tau_e\, I_e^{\text{ext}} > \theta_e$ and $\tau_e\, \widehat{W}_{ee}\, \overline{\nu}_e + \tau_e\, I_e^{\text{ext}} < \theta_e$. Hence, one and two solutions are the only possible scenarii and both can actually occur. For example, (3.14) and (3.15) are compatible, but if

$\tau_e\, I_e^{\text{ext}} > \theta_e$, only (3.15) remains true.

In the case of (3.13), we assign a value to each a_x (0 or $\tau_x \overline{\nu}_x$) and impose that the term inside each S_x verifies the corresponding threshold condition. We can derive a similar discussion as above and prove that this system can only have one or two solutions. Remark that in this second case, the input needs not to be homogeneous.

Circularly symmetric bumps solutions

Looking for bump solutions means that we pay special attention to the domain of the field where the components of $\mathbf{v}$ or $\mathbf{a}$ are "high". Indeed, bumps can be defined as localized high activity areas on the neural field. Here "high activity" means that the terms in the sigmoids are above the characteristic thresholds. We look at rotationally invariant (i.e. depending only on $r = \|\mathbf{r}\|$) stationary solutions centered at the origin of $\mathbb{R}^2$. It is not difficult to check on systems (3.10) and (3.11) that this only makes sense for $\mathbf{I}^{\text{ext}}$ and $\mathbf{W}$ rotationally invariant.
We look for bump solutions so that S_e and S_i are on a high state only in the disks D_{r_e} and D_{r_i}, of radii r_e and r_i respectively. If we define

$$b_{xy}(r,\rho) = \overline{\nu}_y \int_{D_\rho} W_{xy}(|\mathbf{r}-\mathbf{r}'|)\, d\mathbf{r}',^{2}$$

these bumps necessarily verify

$$\begin{cases} v_e(r) = \tau_e\ \big(b_{ee}(r,r_e) + b_{ei}(r,r_i) + I_e^{\text{ext}}(r)\big) \\ v_i(r) = \tau_i\ \big(b_{ie}(r,r_e) + b_{ii}(r,r_i) + I_i^{\text{ext}}(r)\big) \end{cases} \tag{3.18}$$

and

$$\begin{cases} a_e(r) = \tau_e\, S_e\ \big(\tau_e b_{ee}(r,r_e) + \tau_i b_{ei}(r,r_i) + I_e^{\text{ext}}(r)\big) \\ a_i(r) = \tau_i\, S_i\ \big(\tau_e b_{ie}(r,r_e) + \tau_i b_{ii}(r,r_i) + I_i^{\text{ext}}(r)\big) \end{cases} . \tag{3.19}$$

At this point, it looks like we have an explicit formula for the bumps in the voltage-based and the activity-based frameworks. It is not true, since for a general (r_e, r_i) the corresponding solution may not be consistent with the threshold conditions, which for the voltage case amount to

$$\begin{cases} \tau_e\ \big(b_{ee}(r,r_e) + b_{ei}(r,r_i) + I_e^{\text{ext}}(r)\big) > \theta_e, \text{ iff } r < r_e \\ \tau_i\ \big(b_{ie}(r,r_e) + b_{ii}(r,r_i) + I_i^{\text{ext}}(r)\big) > \theta_i, \text{ iff } r < r_i \end{cases} , \tag{3.20}$$

and for the activity case to

$$\begin{cases} \tau_e b_{ee}(r,r_e) + \tau_i b_{ei}(r,r_i) + I_e^{\text{ext}}(r) > \theta_e, \text{ iff } r < r_e \\ \tau_e b_{ie}(r,r_e) + \tau_i b_{ii}(r,r_i) + I_i^{\text{ext}}(r) > \theta_i, \text{ iff } r < r_i \end{cases} . \tag{3.21}$$

So, to solve the bumps existence problems, one has to find r_e and r_i such that the (necessary and) sufficient condition (3.20) or (3.21) is satisfied. We will refer to expressions (3.18) and (3.19) as *pseudo-bumps*.
As in [24] , we can rewrite $\mathbf{b}$ using Bessel functions. The Hankel transform of $W(r)$ is defined by

$$\widetilde{W}(k) = \int_0^\infty W(r) J_0(kr) r\, dr,$$

---

[2] Let us recall that $\overline{\nu}_y > 0$ and that the sign of W_{xy} depends on whether y is excitatory or inhibitory.

where J_ν is the Bessel function of the first kind of order ν, and we have the following property

$$\widetilde{W}(k) = \int_{\mathbb{R}^2} e^{i\mathbf{k}.\mathbf{r}} W(\mathbf{r})\, d\mathbf{r},$$

where we have considered the rotationally invariant 2D function $W(\mathbf{r}) = W(r)$. Then, we can write

$$W(r) = \int_0^\infty \widetilde{W}(k) J_0(rk) k\, dk.$$

According to [38], we obtain

$$\int_{D_\rho} W(|\mathbf{r}-\mathbf{r}'|)\, d\mathbf{r}' = 2\pi\rho \int_0^\infty \widetilde{W}(k) J_0(rk) J_1(\rho k)\, dk.$$

Then we can use the properties of Bessel functions. For example, we can get rid of integrals in the expression of the bumps with appropriate connectivity kernels. In [24] the author considers the following approximation

$$e^{-r} \approx \frac{4}{3}(K_0(r) - K_0(2r)),$$

where K_ν is the modified Bessel function of the second type of order ν, and exploit the fact that the Hankel transform of $K_0(pr)$ is equal to $H_p(k) = (k^2 + p^2)^{-1}$. So, if we choose to approximate exponential connectivities of the form

$$\begin{cases} W_{ee}(r) &= c_{ee} e^{-\delta_e r} \quad W_{ie}(r) = c_{ie} e^{-\delta_e r} \\ W_{ei}(r) &= c_{ei} e^{-\delta_i r} \quad W_{ii}(r) = c_{ii} e^{-\delta_i r} \end{cases},$$

we have

$$\begin{array}{rcl} \widetilde{W}_{ee}(k) &=& \frac{4}{3}c_{ee}\left(\dfrac{1}{k^2+\delta_e^2} - \dfrac{1}{k^2+4\delta_e^2}\right) \\ \widetilde{W}_{ei}(k) &=& \frac{4}{3}c_{ei}\left(\dfrac{1}{k^2+\delta_i^2} - \dfrac{1}{k^2+4\delta_i^2}\right) \\ \widetilde{W}_{ie}(k) &=& \frac{4}{3}c_{ie}\left(\dfrac{1}{k^2+\delta_e^2} - \dfrac{1}{k^2+4\delta_e^2}\right) \\ \widetilde{W}_{ii}(k) &=& \frac{4}{3}c_{ii}\left(\dfrac{1}{k^2+\delta_i^2} - \dfrac{1}{k^2+4\delta_i^2}\right) \end{array}, \tag{3.22}$$

and use the following property to obtain the explicit formula for the bumps

$$\int_0^{+\infty} H_x(k) J_0(rk) J_1(\rho k)\, dk = \begin{cases} \dfrac{1}{x} I_1(x\rho) K_0(xr) & r \geq \rho \\ \dfrac{1}{x^2\rho} - \dfrac{1}{x} I_0(xr) K_1(x\rho) & r < \rho \end{cases},$$

where I_ν is the modified Bessel function of the first type of order ν. Hence, we get

$$b_{xy}(r,\rho) = \frac{8}{3}\pi \frac{\overline{\nu}_y}{\delta_y} c_{xy}\,\rho \begin{cases} I_1(\delta_y\rho)K_0(\delta_y r) - \dfrac{1}{2} I_1(2\delta_y\rho)K_0(2\delta_y r) & r \geq \rho \\ \dfrac{3}{4\delta_y\rho} - I_0(\delta_y r)K_1(\delta_y\rho) + \dfrac{1}{2} I_0(2\delta_y r)K_1(2\delta_y\rho) & r < \rho \end{cases}. \tag{3.23}$$

This thus provide an expression for the pseudo-bumps (3.18) and (3.19) explicitly depending only on r.

In these developments we have seen how crucial is the choice of the connectivity kernels to make bumps calculations tractable.

3.2.2 Stability of the solutions

Homogeneous solutions

We make a linear stability analysis of the homogeneous solutions $\mathbf{v}$ of the system (3.8). We consider perturbations of the form

$$\mathbf{V}(\mathbf{r},t) = \mathbf{v} + \boldsymbol{\phi}(\mathbf{r})e^{\lambda t}$$

with $|\boldsymbol{\phi}| \ll |\mathbf{v}|$, inject them in the corresponding linearized equation, and simplify the exponential terms. We have therefore

$$(\lambda \mathrm{Id} + \mathbf{L})\boldsymbol{\phi}(\mathbf{r}) = \int_{\mathbb{R}^2} \mathbf{W}(|\mathbf{r}-\mathbf{r}'|)\, D\mathbf{S}(\mathbf{v})\boldsymbol{\phi}(\mathbf{r}')\, d\mathbf{r}',$$

and since $D\mathbf{S}(\mathbf{v}) = 0$, we obtain

$$(\lambda \mathrm{Id} + \mathbf{L})\boldsymbol{\phi}(\mathbf{r}) = 0,$$

which has two negative solutions $\lambda = -\frac{1}{\tau_e}$ and $\lambda = -\frac{1}{\tau_i}$.
Hence, the homogeneous solutions are stable. A similar derivation guarantees the stability of the homogeneous solutions in the activity case.

Bump solutions

Here we make a linear stability analysis of the bumps solutions $\mathbf{v}(r)$ and $\mathbf{a}(r)$ of systems (3.8) and (3.9). We consider perturbations of the form

$$\mathbf{V}(\mathbf{r},t) = \mathbf{v}(r) + \boldsymbol{\phi}(\mathbf{r})e^{\lambda t} \quad \text{and} \quad \mathbf{A}(\mathbf{r},t) = \mathbf{a}(r) + \boldsymbol{\psi}(\mathbf{r})e^{\lambda t},$$

with $|\boldsymbol{\phi}| \ll |\mathbf{v}|$ and $|\boldsymbol{\psi}| \ll |\mathbf{a}|$, inject them in their corresponding linearized equations, and simplify the exponential terms. We obtain

$$(\lambda \mathrm{Id} + \mathbf{L})\boldsymbol{\phi}(\mathbf{r}) = \int_{\mathbb{R}^2} \mathbf{W}(|\mathbf{r}-\mathbf{r}'|)\, D\mathbf{S}(\mathbf{v}(r'))\boldsymbol{\phi}(\mathbf{r}')\, d\mathbf{r}'$$

and

$$(\lambda \mathrm{Id} + \mathbf{L})\boldsymbol{\psi}(\mathbf{r}) = D\mathbf{S}\left(\int_{\mathbb{R}^2} \mathbf{W}(|\mathbf{r}-\mathbf{r}'|)\, \mathbf{a}(r')\, d\mathbf{r}' + \mathbf{I}^{\mathrm{ext}}(r)\right) \int_{\mathbb{R}^2} \mathbf{W}(|\mathbf{r}-\mathbf{r}'|)\, \boldsymbol{\psi}(\mathbf{r}')\, d\mathbf{r}'.$$

We will use the fact that

$$D\mathbf{S}(\mathbf{f}(r)) = \begin{bmatrix} \dfrac{\delta(r-r_e)}{|f_e'(r_e)|} & 0 \\ 0 & \dfrac{\delta(r-r_i)}{|f_i'(r_i)|} \end{bmatrix},$$

where functions f_xs only reach θ_x at r_x.
In the voltage case, we obtain

$$\begin{array}{rcl} \lambda_e \phi_e(\mathbf{r}) & = & \alpha_e \int_0^{2\pi} W_{ee}(|\mathbf{r}-\mathbf{r}_e'|)\, \phi_e(\mathbf{r}_e')\, d\theta' + \alpha_i \int_0^{2\pi} W_{ei}(|\mathbf{r}-\mathbf{r}_i'|)\, \phi_i(\mathbf{r}_i')\, d\theta' \\ \lambda_i \phi_i(\mathbf{r}) & = & \alpha_e \int_0^{2\pi} W_{ie}(|\mathbf{r}-\mathbf{r}_e'|)\, \phi_e(\mathbf{r}_e')\, d\theta' + \alpha_i \int_0^{2\pi} W_{ii}(|\mathbf{r}-\mathbf{r}_i'|)\, \phi_i(\mathbf{r}_i')\, d\theta' \end{array}, \tag{3.24}$$

where $\mathbf{r}_x' = [r_x, \theta']^T$, and

$$\lambda_x = \lambda + \frac{1}{\tau_x}, \quad \alpha_x = \frac{r_x}{|v_x'(r_x)|}.$$

In the activity case, we have

$$\begin{array}{rcl}\lambda_e\psi_e(\mathbf{r}) & = & \beta_e/r_e\,\delta(r-r_e)\int_{\mathbb{R}^2} W_{ee}(|\mathbf{r}-\mathbf{r}'|)\,\psi_e(\mathbf{r}') + W_{ei}(|\mathbf{r}-\mathbf{r}'|)\,\psi_i(\mathbf{r}')\,d\mathbf{r}' \\ \lambda_i\psi_i(\mathbf{r}) & = & \beta_i/r_i\,\delta(r-r_i)\int_{\mathbb{R}^2} W_{ie}(|\mathbf{r}-\mathbf{r}'|)\,\psi_e(\mathbf{r}') + W_{ii}(|\mathbf{r}-\mathbf{r}'|)\,\psi_i(\mathbf{r}')\,d\mathbf{r}'\end{array},$$

where

$$\beta_x = \frac{r_x}{|(\tau_e b'_{xe}(r_x,r_e)+\tau_i b'_{xi}(r_x,r_i)) + I_x^{\mathrm{ext}\prime}(r_x)|}.$$

We see that the mass of distributions ψ_e and ψ_i is concentrated on the circles $\{r=r_e\}$ and $\{r=r_i\}$ respectively because of the Dirac terms in the above formulas. So we can rewrite them as

$$\begin{array}{rcl}\lambda_e\psi_e(\mathbf{r}) & = & \beta_e/r_e\,\delta(r-r_e)\left(r_e\int_0^{2\pi} W_{ee}(|\mathbf{r}-\mathbf{r}'_e|)\,\psi_e(\mathbf{r}'_e)\,d\theta' + r_i\int_0^{2\pi} W_{ei}(|\mathbf{r}-\mathbf{r}'_i|)\,\psi_i(\mathbf{r}'_i)\,d\theta'\right) \\ \lambda_i\psi_i(\mathbf{r}) & = & \beta_i/r_i\,\delta(r-r_i)\left(r_e\int_0^{2\pi} W_{ie}(|\mathbf{r}-\mathbf{r}'_e|)\,\psi_e(\mathbf{r}'_e)\,d\theta' + r_i\int_0^{2\pi} W_{ii}(|\mathbf{r}-\mathbf{r}'_i|)\,\psi_i(\mathbf{r}'_i)\,d\theta'\right)\end{array}. \tag{3.25}$$

Separation of radial and angular variables

We specialize the perturbations by separating angular and radial variables

$$\boldsymbol{\zeta}^m(\mathbf{r}) = \boldsymbol{\zeta}^m(r)e^{im\theta}, \quad m\in\mathbb{Z},$$

with $\boldsymbol{\zeta}=\boldsymbol{\phi}$ or $\boldsymbol{\psi}$. By a change of variable $\varphi=\theta'-\theta$, we obtain

$$\int_0^{2\pi} W_{yx}(|\mathbf{r}-\mathbf{r}'_x|)\zeta_x^m(\mathbf{r}'_x)\,d\theta' = \zeta_x^m(r_x)e^{im\theta}\int_0^{2\pi} W_{yx}(|r-r_xe^{i\varphi}|)e^{im\varphi}\,d\varphi,$$

with $\boldsymbol{\zeta}=\boldsymbol{\phi}$ or $\boldsymbol{\psi}$, and set

$$h_{yx}^m(r) = \int_0^{2\pi} W_{yx}(|r-r_xe^{i\varphi}|)e^{im\varphi}\,d\varphi = \int_0^{2\pi} W_{yx}(\sqrt{r^2+r_x^2-2rr_x\cos\varphi})\cos(m\varphi)\,d\varphi.$$

Now, in the voltage case, equations (3.24) can be rewritten

$$\begin{array}{rcl}\lambda_e\phi_e^m(r) & = & \alpha_e\phi_e^m(r_e)\,h_{ee}^m(r)+\alpha_i\phi_i^m(r_i)\,h_{ei}^m(r) \\ \lambda_i\phi_i^m(r) & = & \alpha_e\phi_e^m(r_e)\,h_{ie}^m(r)+\alpha_i\phi_i^m(r_i)\,h_{ii}^m(r)\end{array}.$$

We evaluate these equations for respectively $r=r_e$ and $r=r_i$, and set

$$\mathbf{M}(m) = \left(\begin{array}{cc}\alpha_e h_{ee}^m(r_e) & \alpha_i h_{ei}^m(r_e) \\ \alpha_e h_{ie}^m(r_i) & \alpha_i h_{ii}^m(r_i)\end{array}\right).$$

Then we have

$$\left(\mathbf{M}(m)-\left(\begin{array}{cc}\lambda_e & 0 \\ 0 & \lambda_i\end{array}\right)\right)\left(\begin{array}{c}\phi_e^m(r_e) \\ \phi_i^m(r_i)\end{array}\right)=0,$$

or equivalently (as soon as $\phi_e^m(r_e)$ or $\phi_i^m(r_i)\neq 0$)

$$\det\left(\mathbf{M}(m)-\mathbf{L}-\lambda\mathrm{Id}\right)=0,$$

which is a second order polynomial in the variable λ.
System (3.24) is stable to a given perturbation (i.e. given m) if and only if both roots of the above second order polynomial have a negative real part. This condition is equivalent to

$$\det\left(\mathbf{M}(m)-\mathbf{L}\right)>0 \quad\text{and}\quad \mathrm{tr}\left(\mathbf{M}(m)-\mathbf{L}\right)<0. \tag{3.26}$$

For equations (3.25), the specialization of the perturbation gives

$$\begin{array}{rcl} \lambda_e \psi_e^m(r) & = & \beta_e/r_e\,\delta(r-r_e)\,(r_e\psi_e^m(r_e)\,h_{ee}^m(r)+r_i\psi_i^m(r_i)\,h_{ei}^m(r)) \\ \lambda_i \psi_i^m(r) & = & \beta_i/r_i\,\delta(r-r_i)\,(r_e\psi_e^m(r_e)\,h_{ie}^m(r)+r_i\psi_i^m(r_i)\,h_{ii}^m(r)) \end{array}.$$

We integrate these expressions on $\mathbb{R}^+$

$$\begin{array}{rcl} \lambda_e \psi_e^m(r_e) & = & \beta_e/r_e\,(r_e\psi_e^m(r_e)\,h_{ee}^m(r_e)+r_i\psi_i^m(r_i)\,h_{ei}^m(r_e)) \\ \lambda_i \psi_i^m(r_i) & = & \beta_i/r_i\,(r_e\psi_e^m(r_e)\,h_{ie}^m(r_i)+r_i\psi_i^m(r_i)\,h_{ii}^m(r_i)) \end{array},$$

and set

$$\mathbf{M}'(m) = \begin{pmatrix} \beta_e h_{ee}^m(r_e) & \frac{r_i}{r_e}\beta_i h_{ei}^m(r_e) \\ \frac{r_e}{r_i}\beta_e h_{ie}^m(r_i) & \beta_i h_{ii}^m(r_i) \end{pmatrix} \quad \text{and} \quad \mathbf{M}''(m) = \begin{pmatrix} \beta_e h_{ee}^m(r_e) & \beta_i h_{ei}^m(r_e) \\ \beta_e h_{ie}^m(r_i) & \beta_i h_{ii}^m(r_i) \end{pmatrix}.$$

Then the stability condition is

$$\det\big(\mathbf{M}'(m)-\mathbf{L}\big) > 0 \quad \text{and} \quad \operatorname{tr}\big(\mathbf{M}'(m)-\mathbf{L}\big) < 0, \tag{3.27}$$

which is equivalent to

$$\det\big(\mathbf{M}''(m)-\mathbf{L}\big) > 0 \quad \text{and} \quad \operatorname{tr}\big(\mathbf{M}''(m)-\mathbf{L}\big) < 0. \tag{3.28}$$

Hence we obtain the same condition as in the voltage case with β_xs instead of α_xs.

3.3 CONSTRUCTION OF BUMP SOLUTIONS

When the connections are weak, we see from (3.10) and (3.11) that

$$\mathbf{V} \to \mathbf{L}^{-1}\mathbf{I}^{\text{ext}} \quad \text{and} \quad \mathbf{A} \to \mathbf{L}^{-1}\mathbf{S}(\mathbf{I}^{\text{ext}}).$$

So the form of the stationary solution is similar to the input.
Moreover, the solution is stable because the equations become

$$\dot{\mathbf{V}} \approx -\mathbf{L}\mathbf{V} + \mathbf{I}^{\text{ext}} \quad \text{and} \quad \dot{\mathbf{A}} \approx -\mathbf{L}\mathbf{A} + \mathbf{S}(\mathbf{I}^{\text{ext}}),$$

and the corresponding eigenvalues are $\lambda = -\frac{1}{\tau_e}$ and $\lambda = -\frac{1}{\tau_i}$. Hence a stable bump solution is easily obtained by choosing a bump-shaped input.

From now on, we will look at another, more complex particular case: self-sustained states of localized high activity, corresponding to $\mathbf{I}^{\text{ext}} = 0$. Because of the similarities between the equations of the two cases for the existence and stability of bumps, we will focus on the voltage-case in the forthcoming derivations. We will consider continuous, integrable connectivity kernels with radially decreasing absolute value $|W_{xy}|'(r) < 0$. All illustrations and simulations will be performed with pseudo-bumps given by b_{xy}s of the form (3.23). The parameters we have used to produce them are shown in table 1.

Parameters	$\begin{pmatrix} c_{ee} & c_{ei} \\ c_{ie} & c_{ii} \end{pmatrix}$	(τ_e, τ_i)	(δ_e, δ_i)	$(\overline{\nu}_e, \overline{\nu}_i)$
Values	$\begin{pmatrix} 0.75\,\delta_e & -0.08\,\delta_i \\ 0.15\,\delta_e & -0.02\,\delta_i \end{pmatrix}$	$(0.01, 0.02)$	$(1, 2)$	$(1, 1)$

Table 3.1: *Parameters used in computations.*

3.3.1 Existence

Each pair $(r_e, r_i) \in {\mathbb{R}_+}^2$ defines a pseudo-bump by formula (3.18), but not all of these pseudo-bumps are actual bumps satisfying the threshold conditions. Our goal here is to identify subdomains of the (r_e, r_i) plane where real bumps can be found, and discuss the dependence of the solutions on the excitability thresholds θ_e and θ_i.

We first discuss the existence of putative bumps depending on the values of the excitability thresholds of the layers.

The difficulty for the fulfillment of the sufficient conditions of existence (3.20) resides in their global nature. So, we will first try to satisfy weaker, local criteria. A pair $(r_e, r_i) \in \mathbb{R}_+^2$ being given, the corresponding pseudo-bump must satisfy three necessary local conditions to be a real bump

$$\left\{ \begin{array}{ccc} v_x(0) & > & \theta_x \\ v_x(r_x) & = & \theta_x \\ v_x(+\infty) & < & \theta_x \end{array} \right. , \text{ for } x \in \{e, i\}.$$

Since $v_x(+\infty) = 0$[3], we can rewrite them more specifically as

$$\left\{ \begin{array}{l} \theta_e = \tau_e\ (b_{ee}(r_e, r_e) + b_{ei}(r_e, r_i)) \\ \theta_i = \tau_i\ (b_{ie}(r_i, r_e) + b_{ii}(r_i, r_i)) \end{array} \right. \tag{3.29}$$

and

$$\left\{ \begin{array}{l} 0 < b_{ee}(r_e, r_e) + b_{ei}(r_e, r_i) < b_{ee}(0, r_e) + b_{ei}(0, r_i) \\ 0 < b_{ie}(r_i, r_e) + b_{ii}(r_i, r_i) < b_{ie}(0, r_e) + b_{ii}(0, r_i) \end{array} \right. . \tag{3.30}$$

In particular, given a pair of radii (r_e, r_i) (and hence a pseudo-bump), a unique pair of thresholds could satisfy the above conditions. The two threshold surfaces corresponding to (3.29) have been plotted on figure 3.2.

Now that the thresholds are given, only a fraction of the pseudo-bumps satisfy the inequalities at 0 and $+\infty$. In figure 3.3, we have plotted the subdomain of the (r_e, r_i) plane where conditions (3.30) are fullfilled if we impose the adequate values for θ_e and θ_i.

However, even in this subdomain pseudo-bumps are not guaranteed to be real bumps. This is illustrated on figure 3.4.

3.3.2 Stability

Now that we have been able to construct a pair of real bumps, we study their stability. A pair of bumps is stable if and only if conditions (3.26) are fulfilled for all m.

---

[3] $v_x(r)$ is a sum of terms of the form $b_{xy}(r, \rho) = \overline{\nu}_y \int_{D_\rho} W_{xy}(|\mathbf{r} - \mathbf{r}'|)\, d\mathbf{r}'$, where ρ, the radius of the integration domain, is fixed. As $r \to +\infty$, the terms $W_{xy}(|\mathbf{r} - \mathbf{r}'|)$ pointwise converge to 0, because W_{xy} is radially decreasing and integrable. So, in virtue of Lebesgue's theorem, each term b_{xy} converges to zero.

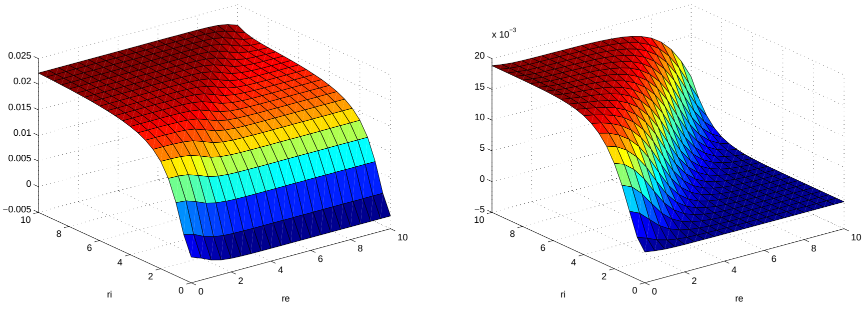

Figure 3.2: *Plot of* $\theta_e(r_e, r_i)$ *(left) and* $\theta_i(r_e, r_i)$ *(right).*

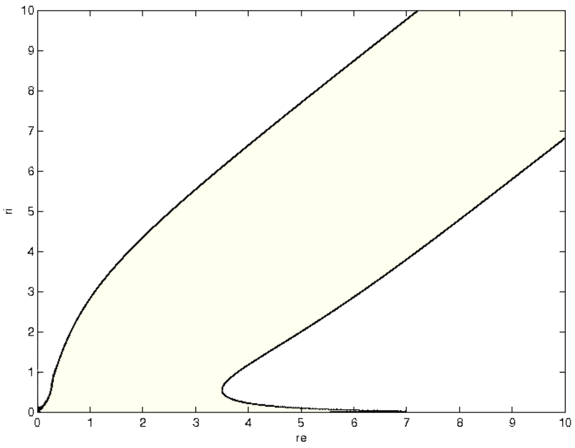

Figure 3.3: *Domain of the* (r_e, r_i) *plane where conditions (3.30) are all satisfied (light color).*

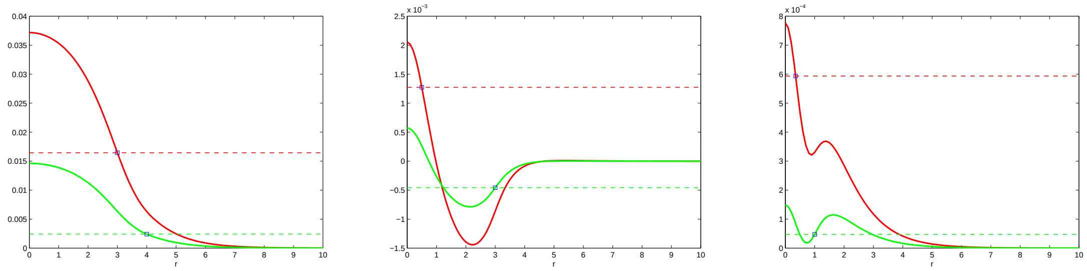

Figure 3.4: *Examples of pseudo-bumps profiles (solid lines, red for the excitatory layer and green for the inhibitory one) with their corresponding thresholds (dashed lines). The little blue squares indicate the points* (r_x, θ_x)*. Left. This pseudo-bumps pair is obtained for* $(r_e = 3, r_i = 4)$*, which belongs to the yellow domain in figure 3.3. It is actually a pair of real bumps, since it respects the global conditions (3.20). Middle. These pseudo-bumps are obtained for* $(r_e = 0.5, r_i = 3)$*. They do not even respect the local conditions (3.30), so they are not real bumps. Right. These pseudo-bumps corresponding to* $(r_e = 0.35, r_i = 1)$ *satisfy local conditions (3.30) but not global conditions (3.20), so they are not real bumps.*

The terms $h^m_{xy}(r_x)$ can be seen as Fourier coefficients. Hence they satisfy

$$\lim_{m \to +\infty} h^m_{xy}(r_x) = 0.$$

So $\mathbf{M}(m) \to 0$, and we have

$$\det(\mathbf{M}(m) - \mathbf{L}) \to \frac{1}{\tau_e \tau_i} > 0 \quad \text{and} \quad \text{trace}(\mathbf{M}(m) - \mathbf{L}) \to -\frac{1}{\tau_e} - \frac{1}{\tau_i} < 0.$$

So, one should particularly care about "small" values of m in the stability analysis. We show an example of stability analysis with the bump obtained for $(r_e = 3, r_i = 4)$ (see figure 3.4). This particular bump is not stable as can be seen on figure 3.5 since it will be destabilized by the isotropic component of a perturbation ($m = 0$).

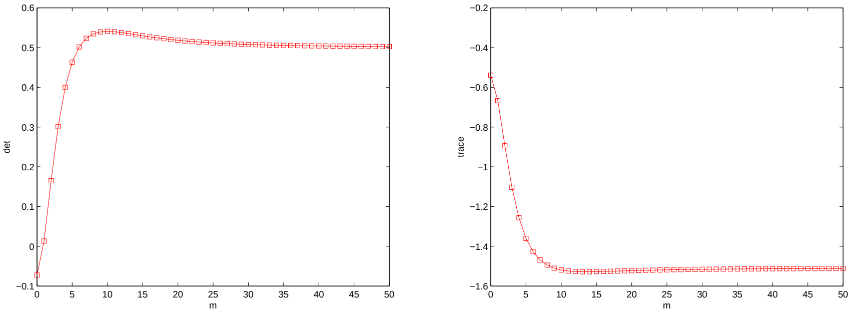

Figure 3.5: *Plots of the determinant (left) and trace (right) of the matrix giving stability conditions (3.26) for the bumps pair* $(r_e = 3, r_i = 4)$. *These bumps are not stable since the determinant is negative for* $m = 0$.

We can give an example of stable bumps. It is the case for $(r_e = 8, r_i = 8)$, as shown on figure 3.6.

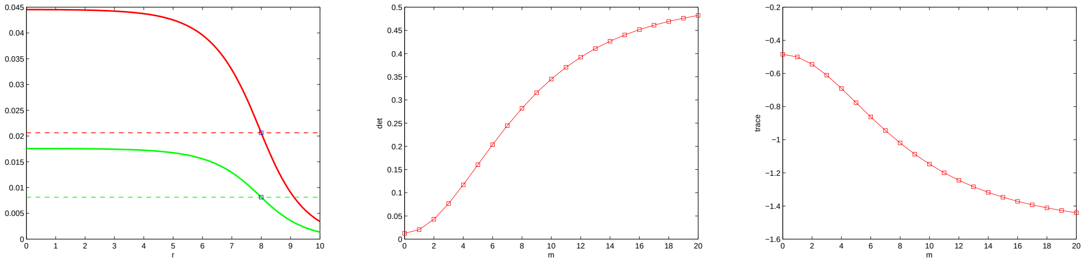

Figure 3.6: *Plots of the bumps profiles (left), and the determinant (center) and trace (right) of the matrix giving stability conditions for the stable bumps pair* $(r_e = 8, r_i = 8)$.

On figure 3.7, we show the domain of the (r_e, r_i) plane where pseudo-bumps are stable to all perturbations (i.e. all $m \in \mathbb{N}$)[4].

---

[4] In this particular parametrization of the neural field, it corresponds to the domain $\det(\mathbf{M}(0)-\mathbf{L}) > 0$ since all domains $\{\det(\mathbf{M}(m) - \mathbf{L}) \leq 0\}$ and $\{\text{trace}(\mathbf{M}(m) - \mathbf{L}) \geq 0\}$, $m \in \mathbb{N}$ are included in $\{\det(\mathbf{M}(0) - \mathbf{L}) \leq 0\}$

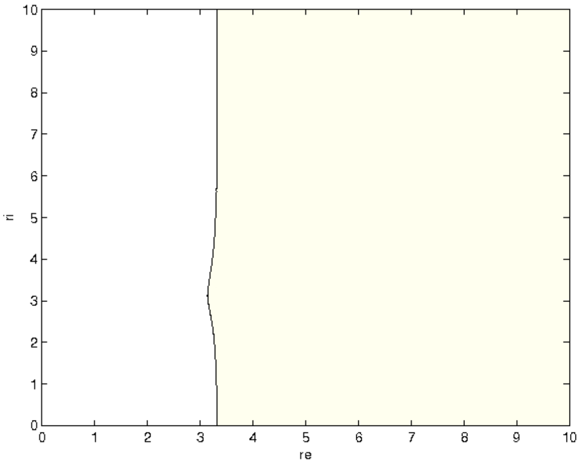

Figure 3.7: *Domain of the (r_e, r_i) plane where pseudo-bumps are stable to all perturbations (light color).*

3.4 CONCLUSION

In this chapter, we have studied some basic properties of bump solutions in a simplified neural field model. We have assumed that the field was infinite and that the wave-to-pulse transforms were Heaviside-shaped. This allowed us to use translation-invariant connectivity kernels and thanks to a right choice of these kernels, to express bump solutions in a closed form, perform a linear stability analysis on them and construct stable two-dimensional bumps.
However, those assumptions are of course unrealistic as one wants to model a part of the cortical tissue. In addition, the classical Cauchy problem of existence and uniqueness of solutions is ill-posed, because of discontinuities in the wave-to-pulse functions.
In the next chapter, we intend to overcome these problems by proposing a more realistic neural field model defined on a compact domain and featuring Lipschitz-continuous sigmoidal transforms.

CHAPTER 4

BOUNDED NEURAL FIELD MODELS

OVERVIEW

In this chapter, we investigate basic properties of bounded neural fields featuring an arbitrary number of neuronal populations. We first establish the well-posedness of neural field equations under certain conditions and discuss the stability of their solutions. Then, we look for homogeneous or locally homogeneous solutions, accounting for partial or global synchrony among the cortical columns composing the field. The theoretical results are finally illustrated through numerical examples. This chapter is based on the research report [36] (2007). The corresponding paper has been accepted for publication in *SIAM Journal of Applied Mathematics*.

Contents

4.1 The models 85
  4.1.1 The local models 85
  4.1.2 Neural fields models 87
4.2 Existence and uniqueness of a solution 88
  4.2.1 General solution 89
  4.2.2 Homogeneous solution 90
  4.2.3 Some remarks about the case $\Omega = \mathbb{R}^q$ 92
4.3 Absolute stability of the general solution 92
  4.3.1 The general case 93
  4.3.2 The convolution case 97
4.4 Absolute stability of the homogeneous solution 99
  4.4.1 The general case 99
  4.4.2 The convolution case 102
  4.4.3 Complete synchronization 103
4.5 Extending the theory 103
  4.5.1 Existence, uniqueness and stability of a solution 103
  4.5.2 Locally homogeneous solutions 104
  4.5.3 Higher order PSPs 107
4.6 Numerical examples 109
  4.6.1 The convolution case 110
  4.6.2 Homogeneous solutions 112
  4.6.3 Locally homogeneous solutions 115
  4.6.4 Absolute stability of pseudo locally homogeneous solutions . . 118

We model neural fields as continuous networks of cortical units, and investigate the ability of these units to completely synchronize, i.e. to produce the same output when receiving the same input independently of their initial state. We therefore emphasize the dynamics and the spatio-temporal behaviour of these networks. Contrary to the preceding chapter, we will here focus on compact neural fields, i.e., neural fields defined on a compact domain.

In section 4.1 we describe the local and spatial models of neural mass networks and derive the equations that govern their spatio-temporal variations, as in the previous chapter. In section 4.2 we analyze the problem of the existence and uniqueness of the smooth general and homogeneous solutions of these equations. In section 4.3 we study the absolute stability of these solutions, i.e. their robustness to arbitrary perturbations caused by changes of the initial conditions. In section 4.4 we extend this analysis to the absolute stability of the homogeneous, i.e. independent of space, solutions when they exist. A consequence of the absolute stability is the ability of the network to completely synchronize. In section 4.5 we revisit the functional framework of our analysis and extend our results to non-smooth functions with the effect that we can discuss the existence and absolute stability of locally homogeneous solutions. We also propose another extension of the model by generalizing the previous results to higher order synaptic responses. In section 4.6 we present a number of numerical experiments to illustrate the theory and conclude in section 4.7.

4.1 THE MODELS

4.1.1 The local models

We consider n interacting neural masses forming a column. We consider that each neural population i is described by its average membrane potential $V_i(t)$ or by its average instantaneous firing rate $\nu_i(t)$, the relation between the two quantities being of the form $\nu_i(t) = S_i(V_i(t))$ [27, 41], where S_i is sigmoidal. The functions S_i, $i = 1, \cdots, n$ satisfy the following properties introduced in the

Definition 4.1.1. *For all* $i = 1, \cdots, n$, *S_i and S'_i are positive and bounded (S'_i is the derivative of the function S_i). We note* $S_{im} = \sup_x S_i(x)$, $S_m = \max_i S_{im}$, $S'_{im} = \sup_x S'_i(x)$ *and* $DS_m = \max_i S'_{im}$. *Finally, we define* $D\mathbf{S}_m$ *as the diagonal matrix* $diag(S'_{im})$.

Neurons in population j are connected to neurons in population i. A single action potential from neurons in population j is seen as a post-synaptic potential $PSP_{ij}(t-s)$ by neurons in population i, where s is the time of the spike hitting the synapse and t the time after the spike. We neglect the delays due to the distance travelled down the axon by the spikes.

Assuming that the post-synaptic potentials sum linearly, the average membrane potential of population i is

$$V_i(t) = \sum_{j,k} PSP_{ij}(t - t_k)$$

where the sum is taken over the arrival times of the spikes produced by the neurons in population j. The number of spikes arriving between t and $t + dt$ is $\nu_j(t)dt$.

Therefore we have

$$V_i(t) = \sum_j \int_{t_0}^{t} PSP_{ij}(t-s)\nu_j(s)\,ds = \sum_j \int_{t_0}^{t} PSP_{ij}(t-s)S_j(V_j(s))\,ds,$$

or, equivalently

$$\nu_i(t) = S_i\left(\sum_j \int_{t_0}^{t} PSP_{ij}(t-s)\nu_j(s)\,ds\right) \tag{4.1}$$

The PSP_{ij}s can depend on several variables in order to account for adaptation, learning, etc ...
There are two main simplifying assumptions that appear in the literature [31] and yield two different models.

The voltage-based model

The assumption, made in [51], is that the post-synaptic potential has the same shape no matter which presynaptic population caused it, the sign and amplitude may vary though. This leads to the relation

$$PSP_{ij}(t) = W_{ij}PSP_i(t).$$

PSP_i represents the unweighted shape of the postsynaptic potentials and W_{ij} is the average strength of the postsynaptic potentials elicited by neurons of type j on neurons of type i. In biophysical connectivity models, like the one presented in figure 1.20, the W_{ij}s should be chosen proportional to the number of presynaptic cells, the average amplitude of postsynaptic potentials and the probability of connection between the considered neuron species [47]. In particular, if $W_{ij} > 0$ the population j excites population i whereas it inhibits it when $W_{ij} < 0$.

Finally, if we assume that $PSP_i(t) = e^{-t/\tau_i}Y(t)$ (where Y is the Heaviside distribution), or equivalently that

$$\tau_i \frac{dPSP_i(t)}{dt} + PSP_i(t) = \tau_i\delta(t), \tag{4.2}$$

we end up with the following system of ordinary first order differential equations

$$\frac{dV_i(t)}{dt} + \frac{V_i(t)}{\tau_i} = \sum_j W_{ij}S_j(V_j(t)) + I^i_{\text{ext}}(t), \tag{4.3}$$

that describes the dynamic behaviour of a cortical column. We have added an external current $I_{\text{ext}}(t)$ to model the non-local connections of population i.

The approach developed in this chapter generalizes easily to the case of more sophisticated postsynaptic potentials models resulting in higher order differential equations, as shown in section 4.5.3.

We introduce the $n \times n$ matrix $\mathbf{W} = (W_{ij})_{i,j}$, and the function $\mathbf{S}\colon \mathbb{R}^n \to \mathbb{R}^n$ such that $\mathbf{S}(\mathbf{x})$ is the vector of coordinates $S_i(x_i)$. We rewrite (4.3) in vector form and obtain the following system of n ordinary differential equations

$$\mathbf{V}' = -\mathbf{L}\mathbf{V} + \mathbf{W}\mathbf{S}(\mathbf{V}) + \mathbf{I}_{\text{ext}}, \tag{4.4}$$

where $\mathbf{L}$ is the diagonal matrix $\mathbf{L} = \mathrm{diag}(1/\tau_{\mathrm{i}})$.

The activity-based model

The assumption is that the shape of a PSP depends only on the nature of the presynaptic cell, that is

$$PSP_{ij}(t) = W_{ij} PSP_j(t).$$

As above we suppose that $PSP_i(t)$ satisfies the differential equation (4.2) and define the activity to be

$$A_j(t) = \int_{t_0}^{t} PSP_j(t-s)\nu_j(s)\,ds.$$

A similar derivation yields the following set of n ordinary differential equations

$$\frac{dA_i(t)}{dt} + \frac{A_i(t)}{\tau_i} = S_i\left(\sum_j W_{ij}A_j(t) + I^i_{\mathrm{ext}}(t)\right), \quad i = 1, \cdots, n.$$

We rewrite this in vector form as

$$\mathbf{A}' = -\mathbf{L}\mathbf{A} + \mathbf{S}(\mathbf{W}\mathbf{A} + \mathbf{I}_{\mathrm{ext}}), \tag{4.5}$$

We introduce the following

Definition 4.1.2. *We note $\tau_{\max}$ the maximum of the decay time constants τ_i, $i = 1, \cdots, n$:*

$$\tau_{\max} = \max_i \tau_i.$$

4.1.2 Neural fields models

We now combine these local models to form a continuum of columns, e.g., in the case of a model of a significant part Ω of the cortex. From now on we consider a compact subset Ω of $\mathbb{R}^q$, $q = 1, 2, 3$. This encompasses several cases of interest.

When $q = 1$ we deal with one-dimensional neural fields. Even though this appears to be of limited biological interest, it is one of the most widely studied cases because of its relative mathematical simplicity and because of the insights one can gain of the more realistic situations.

When $q = 2$ we discuss properties of two-dimensional neural fields. This is perhaps more interesting from a biological point of view since Ω can be viewed as a piece of cortex where the third dimension, its thickness, is neglected. This case has received by far less attention than the previous one, probably because of the increased mathematical difficulty.

Finally $q = 3$ allows us to discuss properties of volumes of neural masses, e.g. cortical sheets where their thickness is taken into account [20, 61].

The results that are presented in this chapter are independent of q. Nevertheless, we have a good first approximation of a real cortical area with $q = 2$, and cortical depth given by the index $i = 1, \cdots, n$ of the considered cortical population, following the idea of a field composed of columns, or equivalently, of interconnected cortical layers.

We note $\mathbf{V}(\mathbf{r}, t)$ (respectively $\mathbf{A}(\mathbf{r}, t)$) the n-dimensional state vector at the point $\mathbf{r}$ of the continuum and at time t. We introduce the $n \times n$ matrix function $\mathbf{W}(\mathbf{r}, \mathbf{r}', t)$

which describes how the neural mass at point r′ influences that at point r at time t. More precisely, $W_{ij}(\mathbf{r}, \mathbf{r}', t)$ describes how population j at point r′ influences population i at point r at time t. We call $\mathbf{W}$ the connectivity matrix function. Neglecting, as in the local case above, the delays due to the distance between the neural masses, we extend equation (4.4) to

$$\mathbf{V}_t(\mathbf{r}, t) = -\mathbf{L}\mathbf{V}(\mathbf{r}, t) + \int_\Omega \mathbf{W}(\mathbf{r}, \mathbf{r}', t)\mathbf{S}(\mathbf{V}(\mathbf{r}', t))\, d\mathbf{r}' + \mathbf{I}_{\text{ext}}(\mathbf{r}, t), \tag{4.6}$$

and equation (4.5) to

$$\mathbf{A}_t(\mathbf{r}, t) = -\mathbf{L}\mathbf{A}(\mathbf{r}, t) + \mathbf{S}\left(\int_\Omega \mathbf{W}(\mathbf{r}, \mathbf{r}', t)\mathbf{A}(\mathbf{r}', t))\, d\mathbf{r}' + \mathbf{I}_{\text{ext}}(\mathbf{r}, t)\right). \tag{4.7}$$

$\mathbf{V}_t$ (resp. $\mathbf{A}_t$) stands for the partial derivative of the multivariate vector $\mathbf{V}$ (resp. $\mathbf{A}$) with respect to the time variable t. A particular case which will be considered later is when $\mathbf{W}$ is translation invariant, $\mathbf{W}(\mathbf{r}, \mathbf{r}', t) = \mathbf{W}(\mathbf{r} - \mathbf{r}', t)$. We give below sufficient conditions on $\mathbf{W}$ and $\mathbf{I}_{\text{ext}}$ for equations (4.6) and (4.7) to be well-defined and study their solutions.

4.2 EXISTENCE AND UNIQUENESS OF A SOLUTION

In this section we deal with the problem of the existence and uniqueness of a solution to (4.6) and (4.7) for a given set of initial conditions. Unlike previous authors [21, 33, 79] we consider the case of a neural field with the effect that we have to use the tools of functional analysis to characterize their properties.

We start with the assumption that the state vectors $\mathbf{V}$ and $\mathbf{A}$ are differentiable (respectively continuous) functions of the time (respectively the space) variable. This is certainly reasonable in terms of the temporal variations because we are essentially modeling large populations of neurons and do not expect to be able to represent time transients. It is far less reasonable in terms of the spatial dependency since one should allow neural masses activity to be spatially distributed in a locally non-smooth fashion with areas of homogeneous cortical activity separated by smooth boundaries. A more general assumption is proposed in section 4.5. But it turns out that most of the groundwork can be done in the setting of continuous functions.

Let $\mathcal{F}$ be the set $\mathbf{C}_n(\Omega)$ of the continuous functions from Ω to $\mathbb{R}^n$. This is a Banach space for the norm $\|\mathbf{V}\|_{n,\infty} = \max_{1\leq i\leq n} \sup_{\mathbf{r}\in\Omega} |\mathbf{V}_i(\mathbf{r})|$, see appendix B. We denote by J a closed interval of the real line containing 0.

We will several times need the following

Lemma 4.2.1. *We have the following inequalities for all* $\mathbf{x}, \mathbf{y} \in \mathcal{F}$ *and* $\mathbf{r}' \in \Omega$

$$\|\mathbf{S}(\mathbf{x}(\mathbf{r}'))-\mathbf{S}(\mathbf{y}(\mathbf{r}'))\|_\infty \leq DS_m\|\mathbf{x}(\mathbf{r}')-\mathbf{y}(\mathbf{r}')\|_\infty \quad \textit{and} \quad \|\mathbf{S}(\mathbf{x})-\mathbf{S}(\mathbf{y})\|_{n,\infty} \leq DS_m\|\mathbf{x}-\mathbf{y}\|_{n,\infty}.$$

Proof. S is smooth so we can perform a zeroth-order Taylor expansion with integral remainder, [30], and write

$$\mathbf{S}(\mathbf{x}(\mathbf{r}')) - \mathbf{S}(\mathbf{y}(\mathbf{r}')) = \left(\int_0^1 D\mathbf{S}(\mathbf{y}(\mathbf{r}') + \zeta(\mathbf{x}(\mathbf{r}') - \mathbf{y}(\mathbf{r}')))\, d\zeta\right)(\mathbf{x}(\mathbf{r}') - \mathbf{y}(\mathbf{r}')),$$

and, because of lemma B.2.1 and definition 4.1.1

$$\|\mathbf{S}(\mathbf{x}(\mathbf{r}')) - \mathbf{S}(\mathbf{y}(\mathbf{r}'))\|_\infty \leq \int_0^1 \|D\mathbf{S}(\mathbf{y}(\mathbf{r}') + \zeta(\mathbf{x}(\mathbf{r}') - \mathbf{y}(\mathbf{r}')))\|_\infty\, d\zeta\, \|\mathbf{x}(\mathbf{r}') - \mathbf{y}(\mathbf{r}')\|_\infty \leq DS_m\|\mathbf{x}(\mathbf{r}') - \mathbf{y}(\mathbf{r}')\|_\infty.$$

This proves the first inequality. The second follows immediately. □

4.2.1 General solution

A function $\mathbf{V}(t)$ is thought of as a mapping $\mathbf{V} : \mathrm{J} \to \mathcal{F}$. This means that $\mathbf{V}(t)$ is now a function defined in Ω. Equations (4.6) and (4.7) are formally recast as an initial value problem, see, e.g. [32]:

$$\begin{cases} \mathbf{V}'(t) &= f(t, \mathbf{V}(t)) \\ \mathbf{V}(0) &= \mathbf{V}_0 \end{cases} \tag{4.8}$$

where $\mathbf{V}_0$ is an element of $\mathcal{F}$ and the function f from $\mathrm{J} \times \mathcal{F}$ is equal to f_v defined by the righthand side of (4.6):

$$f_v(t, \mathbf{x})(\mathbf{r}) = -\mathbf{L}\mathbf{x}(\mathbf{r}) + \int_\Omega \mathbf{W}(\mathbf{r}, \mathbf{r}', t)\mathbf{S}(\mathbf{x}(\mathbf{r}'))\, d\mathbf{r}' + \mathbf{I}_{\text{ext}}(\mathbf{r}, t) \quad \forall \mathbf{x} \in \mathcal{F}, \tag{4.9}$$

or to f_a defined by the righthand side of (4.7):

$$f_a(t, \mathbf{x})(\mathbf{r}) = -\mathbf{L}\mathbf{x}(\mathbf{r}) + \mathbf{S}\left(\int_\Omega \mathbf{W}(\mathbf{r}, \mathbf{r}', t)\mathbf{x}(\mathbf{r}')\, d\mathbf{r}' + \mathbf{I}_{\text{ext}}(\mathbf{r}, t)\right) \quad \forall \mathbf{x} \in \mathcal{F}. \tag{4.10}$$

We have the

Proposition 4.2.1. *If the following two hypotheses are satisfied*

1. *The connectivity function* $\mathbf{W}$ *is in* $C(\mathrm{J}; \mathbf{C}_{\mathrm{n}\times\mathrm{n}}(\Omega \times \Omega))$ *(see appendix B),*
2. *The external current* $\mathbf{I}_{\text{ext}}$ *is in* $C(\mathrm{J}; \mathbf{C}_{\mathrm{n}}(\Omega))$,

then the mappings f_v *and* f_a *are from* $\mathrm{J} \times \mathcal{F}$ *to* $\mathcal{F}$, *continuous, and Lipschitz continuous with respect to their second argument, uniformly with respect to the first (*$\mathbf{C}_{n\times n}(\Omega \times \Omega)$ *and* $\mathbf{C}_n(\Omega)$ *are defined in appendix B).*

Proof. Let $t \in \mathrm{J}$ and $\mathbf{x} \in \mathcal{F}$. We introduce the mapping

$$F_v : (t, \mathbf{x}) \to F_v(t, \mathbf{x}) \quad \text{such that} \quad F_v(t, \mathbf{x})(\mathbf{r}) = \int_\Omega \mathbf{W}(\mathbf{r}, \mathbf{r}', t)\mathbf{S}(\mathbf{x}(\mathbf{r}'))\, d\mathbf{r}' \tag{4.11}$$

$F_v(t, \mathbf{x})$ is well defined for all $\mathbf{r} \in \Omega$ because, thanks to the first hypothesis, it is the integral of the continuous function $\mathbf{W}(\mathbf{r}, ., t)\mathbf{S}(\mathbf{x}(.))$ on a compact domain. For all $\mathbf{r}' \in \Omega$, $\mathbf{W}(., \mathbf{r}', t)\mathbf{S}(\mathbf{x}(\mathbf{r}'))$ is continuous (first hypothesis again) and we have (lemma B.2.1)

$$\|\mathbf{W}(\mathbf{r}, \mathbf{r}', t)\mathbf{S}(\mathbf{x}(\mathbf{r}'))\|_\infty \leq \|\mathbf{W}(., ., t)\|_{n\times n, \infty}\|\mathbf{S}(\mathbf{x}(\mathbf{r}'))\|_\infty.$$

Since $\|\mathbf{S}(\mathbf{x}(.))\|_\infty$ is bounded, it is integrable in Ω and we conclude that $F_v(t, \mathbf{x})$ is continuous on Ω. Then it is easy to see that $f_v(t, \mathbf{x})$ is well defined and belongs to $\mathcal{F}$.

Let us prove that f_v is continuous.

$$\begin{aligned} f_v(t, \mathbf{x}) - f_v(s, \mathbf{y}) = -\mathbf{L}(\mathbf{x} - \mathbf{y}) + \int_\Omega \big(\mathbf{W}(\cdot, \mathbf{r}', t)\mathbf{S}(\mathbf{x}(\mathbf{r}')) - \mathbf{W}(\cdot, \mathbf{r}', s)\mathbf{S}(\mathbf{y}(\mathbf{r}'))\big)\, d\mathbf{r}' \\ + \mathbf{I}_{\text{ext}}(\cdot, t) - \mathbf{I}_{\text{ext}}(\cdot, s) \\ = -\mathbf{L}(\mathbf{x} - \mathbf{y}) + \int_\Omega (\mathbf{W}(\cdot, \mathbf{r}', t) - \mathbf{W}(\cdot, \mathbf{r}', s))\mathbf{S}(\mathbf{x}(\mathbf{r}'))\, d\mathbf{r}' \\ + \int_\Omega \mathbf{W}(\cdot, \mathbf{r}', s)(\mathbf{S}(\mathbf{x}(\mathbf{r}')) - \mathbf{S}(\mathbf{y}(\mathbf{r}'))\, d\mathbf{r}' + \mathbf{I}_{\text{ext}}(\cdot, t) - \mathbf{I}_{\text{ext}}(\cdot, s) \end{aligned}$$

It follows from lemma 4.2.1 that

$$\|f_v(t,\mathbf{x}) - f_v(s,\mathbf{y})\|_{n,\infty} \leq \|\mathbf{L}\|_\infty \, \|\mathbf{x}-\mathbf{y}\|_{n,\infty} + |\Omega| \, S_m \|\mathbf{W}(\cdot,\cdot,t) - \mathbf{W}(\cdot,\cdot,s)\|_{n\times n,\infty} + \\ |\Omega| \, \|\mathbf{W}(\cdot,\cdot,s)\|_{n\times n,\infty} DS_m \, \|\mathbf{x}-\mathbf{y}\|_{n,\infty} + \|\mathbf{I}_{\text{ext}}(\cdot,t) - \mathbf{I}_{\text{ext}}(\cdot,s)\|_{n,\infty}.$$

Because of the hypotheses we can choose $|t-s|$ small enough so that $\|\mathbf{W}(\cdot,\cdot,t) - \mathbf{W}(\cdot,\cdot,s)\|_{n\times n,\infty}$ and $\|\mathbf{I}_{\text{ext}}(\cdot,t) - \mathbf{I}_{\text{ext}}(\cdot,s)\|_{n,\infty}$ are arbitrarily small. Similarly, since $\mathbf{W}$ is continuous on the compact interval J, it is bounded there and $\|\mathbf{W}(\cdot,\cdot,s)\|_{n\times n,\infty} \leq w > 0$ for all $s \in$ J. This proves the continuity of f_v.

It follows from the previous inequality that

$$\|f_v(t,\mathbf{x}) - f_v(t,\mathbf{y})\|_{n,\infty} \leq \|\mathbf{L}\|_\infty \, \|\mathbf{x}-\mathbf{y}\|_{n,\infty} + |\Omega| \, \|\mathbf{W}(\cdot,\cdot,t)\|_{n\times n,\infty} DS_m \, \|\mathbf{x}-\mathbf{y}\|_{n,\infty},$$

and because $\|\mathbf{W}(\cdot,\cdot,t)\|_{n\times n,\infty} \leq w > 0$ for all ts in J, this proves the Lipschitz continuity of f_v with respect to its second argument, uniformly with respect to the first. A very similar proof applies to f_a. □

We continue with the proof that there exists a unique solution to the abstract initial value problem (4.8) in the two cases of interest.

Proposition 4.2.2. *Subject to the hypotheses of proposition 4.2.1 for any element* $\mathbf{V}_0$ *(resp.* $\mathbf{A}_0$*) of* $\mathcal{F}$ *there is a unique solution* $\mathbf{V}$ *(resp.* $\mathbf{A}$*), defined on a subinterval of* J *containing 0 and continuously differentiable, of the abstract initial value problem (4.8) for* $f = f_v$ *(resp.* $f = f_a$*).*

Proof. All conditions of the Picard-Lindelöf theorem on differential equations in Banach spaces [6, 30] are satisfied, hence the proposition. □

This solution, defined on the subinterval J of $\mathbb{R}$ can in fact be extended to the whole real line and we have the

Proposition 4.2.3. *If the following two hypotheses are satisfied*

1. *The connectivity function* $\mathbf{W}$ *is in* $C(\mathbb{R}; \mathbf{C}_{\mathrm{n\times n}}(\Omega\times\Omega))$*,*
2. *The external current* $\mathbf{I}_{\text{ext}}$ *is in* $C(\mathbb{R}; \mathbf{C}_{\mathrm{n}}(\Omega))$*,*

then for any function $\mathbf{V}_0$ *(resp.* $\mathbf{A}_0$*) in* $\mathcal{F}$ *there is a unique solution* $\mathbf{V}$ *(resp.* $\mathbf{A}$*), defined on* $\mathbb{R}$ *and continuously differentiable, of the abstract initial value problem (4.8) for* $f = f_v$ *(resp.* $f = f_a$*).*

Proof. In theorem C.1.1 of appendix C, we prove the existence of a constant $\tau > 0$ such that for any initial condition $(t_0, \mathbf{V}_0) \in \mathbb{R}\times\mathcal{F}$, there is a unique solution defined on the closed interval $[t_0-\tau, t_0+\tau]$. We can then cover the real line with such intervals and finally obtain the global existence and uniqueness of the solution of the initial value problem. □

4.2.2 Homogeneous solution

A homogeneous solution to (4.6) or (4.7) is a solution $\mathbf{U}$ that does not depend upon the space variable $\mathbf{r}$, for a given homogeneous input $\mathbf{I}_{\text{ext}}(t)$ and a constant initial condition $\mathbf{U}_0$. If such a solution $\mathbf{U}(t)$ exists, then it satisfies the following equation

$$\mathbf{U}'(t) = -\mathbf{L}\mathbf{U}(t) + \int_\Omega \mathbf{W}(\mathbf{r},\mathbf{r}',t)\mathbf{S}(\mathbf{U}(t))\,d\mathbf{r}' + \mathbf{I}_{\text{ext}}(t),$$

in the case of (4.6) and

$$\mathbf{U}'(t) = -\mathbf{L}\mathbf{U}(t) + \mathbf{S}\left(\int_\Omega \mathbf{W}(\mathbf{r}, \mathbf{r}', t)\mathbf{U}(t)\, d\mathbf{r}' + \mathbf{I}_{\text{ext}}(t)\right),$$

in the case of (4.7). The integral $\int_\Omega \mathbf{W}(\mathbf{r}, \mathbf{r}', t)\mathbf{S}(\mathbf{U}(t))\, d\mathbf{r}'$ is equal to $\left(\int_\Omega \mathbf{W}(\mathbf{r}, \mathbf{r}', t)\, d\mathbf{r}'\right)\ \mathbf{S}(\mathbf{U}(t))$. The integral $\int_\Omega \mathbf{W}(\mathbf{r}, \mathbf{r}', t)\mathbf{U}(t)\, d\mathbf{r}'$ is equal to $\left(\int_\Omega \mathbf{W}(\mathbf{r}, \mathbf{r}', t)\, d\mathbf{r}'\right)\ \mathbf{U}(t)$. They must be independent of the position r. Hence a necessary condition for the existence of a homogeneous solution is that

$$\int_\Omega \mathbf{W}(\mathbf{r}, \mathbf{r}', t)\, d\mathbf{r}' = \overline{\mathbf{W}}(t), \tag{4.12}$$

where the $n \times n$ matrix $\overline{\mathbf{W}}(t)$ does not depend on the spatial coordinate $\mathbf{r}$.

In the particular case where $\mathbf{W}(\mathbf{r}, \mathbf{r}', t)$ is translation invariant, $\mathbf{W}(\mathbf{r}, \mathbf{r}', t) \equiv \mathbf{W}(\mathbf{r}-\mathbf{r}', t)$, the condition is not satisfied in general because of the border of Ω. In all cases, the homogeneous solutions satisfy the differential equation

$$\mathbf{U}'(t) = -\mathbf{L}\mathbf{U}(t) + \overline{\mathbf{W}}(t)\mathbf{S}(\mathbf{U}(t)) + \mathbf{I}_{\text{ext}}(t), \tag{4.13}$$

for (4.6) and

$$\mathbf{U}'(t) = -\mathbf{L}\mathbf{U}(t) + \mathbf{S}\left(\overline{\mathbf{W}}(t)\mathbf{U}(t)) + \mathbf{I}_{\text{ext}}(t)\right), \tag{4.14}$$

for (4.7), with initial condition $\mathbf{U}(0) = \mathbf{U}_0$, a vector of $\mathbb{R}^n$. The following proposition gives a sufficient condition for the existence of a homogeneous solution.

Theorem 4.2.1. *If the external current $\mathbf{I}_{\text{ext}}(t)$ and the connectivity matrix $\overline{\mathbf{W}}(t)$ are continuous on some closed interval J containing 0, then for all vector $\mathbf{U}_0$ of $\mathbb{R}^n$, there exists a unique solution $\mathbf{U}(t)$ of (4.13) or (4.14) defined on a subinterval J_0 of J containing 0 such that $\mathbf{U}(0) = \mathbf{U}_0$.*

Proof. The proof is an application of Cauchy's theorem on differential equations. Consider the mapping $f_{hv} : \mathbb{R}^n \times \mathrm{J} \to \mathbb{R}^n$ defined by

$$f_{hv}(\mathbf{x}, t) = -\mathbf{L}\mathbf{x} + \overline{\mathbf{W}}(t)\mathbf{S}(\mathbf{x}) + \mathbf{I}_{\text{ext}}(t)$$

We have

$$\|f_{hv}(\mathbf{x}, t) - f_{hv}(\mathbf{y}, t)\|_\infty \leq \|\mathbf{L}\|_\infty\|\mathbf{x} - \mathbf{y}\|_\infty + \|\overline{\mathbf{W}}(t)\|_\infty\|\mathbf{S}(\mathbf{x}) - \mathbf{S}(\mathbf{y})\|_\infty$$

It follows from lemma 4.2.1 that $\|\mathbf{S}(\mathbf{x}) - \mathbf{S}(\mathbf{y})\|_\infty \leq DS_m\|\mathbf{x} - \mathbf{y}\|_\infty$ and, since $\overline{\mathbf{W}}$ is continuous on the compact interval J, it is bounded there by $w > 0$ and

$$\|f_{hv}(\mathbf{x}, t) - f_{hv}(\mathbf{y}, t)\|_\infty \leq (\|\mathbf{L}\|_\infty + wDS_m)\|\mathbf{x} - \mathbf{y}\|_\infty$$

for all x, y of $\mathbb{R}^n$ and all $t \in \mathrm{J}$. A similar proof applies to (4.14) and the conclusion of the proposition follows. □

As in proposition 4.2.3, this existence and uniqueness result extends to the whole time real line if **I** and $\overline{\mathbf{W}}$ are continuous on $\mathbb{R}$.

This homogeneous solution can be seen as describing a state where the columns of the continuum are synchronized: they receive the same input $\mathbf{I}_{\text{ext}}(t)$ and produce the same output $\mathbf{U}(t)$.

4.2.3 Some remarks about the case $\Omega = \mathbb{R}^q$

A significant amount of work has been done on equations of the type (4.6) or (4.7) in the case of a one-dimensional infinite continuum, $\Omega = \mathbb{R}$, or a two-dimensional infinite continuum, $\Omega = \mathbb{R}^2$. The reader is referred to the review papers by Ermentrout [31] and by Coombes [24] as well as to [38, 92, 93].

Beside the fact that an infinite cortex is unrealistic, the case $\Omega = \mathbb{R}^q$ raises some mathematical questions. Indeed, the choice of the functional space $\mathcal{F}$ is problematic. A natural idea would be to choose $\mathcal{F} = \mathbf{L}^2_n(\mathbb{R}^q)$, the space of square-integrable functions with values in $\mathbb{R}^n$, see appendix B. If we make this choice we immediately encounter the problem that the homogeneous solutions (constant with respect to the space variable) do not belong to that space. A further difficulty is that $\mathbf{S}(\mathbf{x})$ does not in general belong to $\mathcal{F}$ if x does. As shown in this chapter, these difficulties vanish if Ω is compact.

4.3 ABSOLUTE STABILITY OF THE GENERAL SOLUTION

We investigate the absolute stability of a solution to (4.6) and (4.7) for a given input $\mathbf{I}_{\text{ext}}$. Proposition 4.2.3 guarantees that for a given initial condition there exists a unique solution to (4.6) or (4.7) defined for all times.

In order to investigate its absolute stability we choose a different initial condition, which is a way to perturb the solution, in effect the only way because of the existence uniqueness proposition 4.2.3, and look for sufficient conditions for the new solution to converge toward the original one. Absolute stability implies linear stability which is studied by perturbing the solution by adding to it a small function, and performing a first-order Taylor expansion of the equations thereby obtaining a perturbed equation. One then usually has to make some assumptions about the spatio-temporal form of the perturbation, e.g. that it is separable in time and space, ending up with a non-trivial eigenvalue problem which has to be solved in order to find sufficient conditions for the perturbation to converge to 0, up to first-order [24, 31, 33, 38, 69, 79, 92, 93, 94]. This is also the case of [5] and [23] who study the convolution case for $n = q = 1$ but incorporate propagation delays. Linear stability is local because it is derived for a particular solution. The functional analysis approach that we use in this chapter allows us to find simple sufficient conditions for the absolute stability of the system, hence for all its solutions, regardless of the initial condition or input. In this sense it is a global approach. This is achieved by constructing a Lyapunov function measuring some distance between two state vectors at each time instant. This function has a single minimum corresponding to the equality of the states. One then finds sufficient conditions for the time derivative of this function to be strictly negative thereby guaranteeing the asymptotic equality of the states. This approach has been followed by much fewer people. In [67] the authors study the case where $\mathbf{W}(\mathbf{r}, \mathbf{r}')$ is symmetric in with respect to the space variables r and r′ for $n = q = 1$ for a finite interval and add the translation invariance assumption when the interval is infinite. They do not study the case of general time-varying input currents.

Absolute stability is a relevant concept for systems of neurons. Indeed, absolutely stable systems forget their initial state exponentially fast, but do not forget their input. Hence such systems can differentiate distinct stimuli by converging to the corresponding states without being influenced by their initial state. This property is desirable for example in modelling visual perception: different forms elicit different percepts but the percepts should not depend on the initial state of the visual system. We first look at the general case then at the convolution case.

4.3.1 The general case

We define a number of matrices and linear operators that are useful in the sequel

Definition 4.3.1. *Let*

$$\mathbf{W}_{cm} = \mathbf{W}D\mathbf{S}_m \quad \mathbf{W}_{mc} = D\mathbf{S}_m\mathbf{W}$$

Consider also the linear operators, noted g, g_m, *and* h_m *defined on* $\mathcal{F}$:

$$g(\mathbf{x})(\mathbf{r}, t) = \int_\Omega \mathbf{W}(\mathbf{r}, \mathbf{r}', t)\mathbf{x}(\mathbf{r}')\, d\mathbf{r}' \quad \forall \mathbf{x} \in \mathcal{F},$$

$$g_m(\mathbf{x})(\mathbf{r}, t) = \int_\Omega \mathbf{W}_{cm}(\mathbf{r}, \mathbf{r}', t)\mathbf{x}(\mathbf{r}')\, d\mathbf{r}' \quad \forall \mathbf{x} \in \mathcal{F},$$

and

$$h_m(\mathbf{x})(\mathbf{r}, t) = \int_\Omega \mathbf{W}_{mc}(\mathbf{r}, \mathbf{r}', t)\mathbf{x}(\mathbf{r}')\, d\mathbf{r}' \quad \forall \mathbf{x} \in \mathcal{F}.$$

We start with a lemma.

Lemma 4.3.1. *With the hypotheses of proposition 4.2.1, the operators* g, g_m, *and* h_m *are compact operators from* $\mathcal{F}$ *to* $\mathcal{F}$ *for each time* $t \in \mathrm{J}$.

Proof. This is a direct application of the theory of Fredholm's integral equations [30]. We prove it for g.

Because of the hypothesis 1 in proposition 4.2.1, at each time instant t in J, $\mathbf{W}$ is continuous on the compact set $\Omega \times \Omega$, therefore it is uniformly continuous. Hence, for each $\varepsilon > 0$ there exists $\eta(t) > 0$ such that $\|\mathbf{r}_1 - \mathbf{r}_2\| \leq \eta(t)$ implies that $\|\mathbf{W}(\mathbf{r}_1, \mathbf{r}', t) - \mathbf{W}(\mathbf{r}_2, \mathbf{r}', t)\|_\infty \leq \varepsilon$ for all $\mathbf{r}' \in \Omega$, and, for all $\mathbf{x} \in \mathcal{F}$

$$\|g(\mathbf{x})(\mathbf{r}_1, t) - g(\mathbf{x})(\mathbf{r}_2, t)\|_\infty \leq \varepsilon|\Omega|\|\mathbf{x}\|_{n,\infty}$$

This shows that the image $g(B)$ of any bounded subset B of $\mathcal{F}$ is equicontinuous.

Similarly, if we set $w(t) = \|\mathbf{W}(.,.,t)\|_{n\times n,\infty}$, we have $\|g(\mathbf{x})(\mathbf{r}, t)\|_\infty \leq w(t)|\Omega|\|\mathbf{x}\|_{n,\infty}$. This shows that for every $\mathbf{r} \in \Omega$, the set $\{\mathbf{y}(\mathbf{r}), \mathbf{y} \in g(B)\}$, is bounded in $\mathbb{R}^n$, hence relatively compact. From the Arzelà-Ascoli theorem, we conclude that the subset $g(B)$ of $\mathcal{F}$ is relatively compact for all $t \in \mathrm{J}$. And so the operator is compact.

The same proof applies to g_m and h_m. □

To study the absolute stability of the solutions of (4.6) and (4.7) it is convenient to use an inner product on $\mathcal{F}$. It turns out that the natural inner-product will pave the ground for the generalization in section 4.5. We therefore consider the pre-Hilbert space $\mathcal{G}$ defined on $\mathcal{F}$ by the usual inner product

$$\langle \mathbf{x},\, \mathbf{y} \rangle = \int_\Omega \mathbf{x}(\mathbf{r})^T \mathbf{y}(\mathbf{r})\, d\mathbf{r}$$

We note $\|\mathbf{x}\|_{n,2}$ the corresponding norm to distinguish it from $\|\mathbf{x}\|_{n,\infty}$, see appendix B. It is easy to show that all previously defined operators are also compact operators from $\mathcal{G}$ to $\mathcal{G}$. We have the

Lemma 4.3.2. *g, g_m and h_m are compact operators from $\mathcal{G}$ to $\mathcal{G}$ for each time $t \in$ J.*

Proof. We give the proof for g.

The identity mapping $\mathbf{x} \to \mathbf{x}$ from $\mathcal{F}$ to $\mathcal{G}$ is continuous since $\|\mathbf{x}\|_{n,2} \leq \sqrt{n|\Omega|}\,\|\mathbf{x}\|_{n,\infty}$. Consider now g as a mapping from $\mathcal{G}$ to $\mathcal{F}$. As in the proof of lemma 4.3.1, for each $\varepsilon > 0$ there exists $\eta(t) > 0$ such that $\|\mathbf{r}_1 - \mathbf{r}_2\| \leq \eta(t)$ implies $\|\mathbf{W}(\mathbf{r}_1, \mathbf{r}', t) - \mathbf{W}(\mathbf{r}_2, \mathbf{r}', t)\|_\infty \leq \varepsilon$ for all $\mathbf{r}' \in \Omega$. Therefore the ith coordinate $g^i(\mathbf{x})(\mathbf{r}_1, t) - g^i(\mathbf{x})(\mathbf{r}_2, t)$ satisfies (Cauchy-Schwarz' inequalities):

$$|g^i(\mathbf{x})(\mathbf{r}_1, t) - g^i(\mathbf{x})(\mathbf{r}_2, t)| \leq \sum_j \int_\Omega |W_{ij}(\mathbf{r}_1, \mathbf{r}', t) - W_{ij}(\mathbf{r}_2, \mathbf{r}', t)|\, |x_j(\mathbf{r}')|\, d\mathbf{r}' \leq$$

$$\varepsilon \sum_j \int_\Omega |x_j(\mathbf{r}')|\, d\mathbf{r}' \leq \varepsilon\sqrt{|\Omega|} \sum_j \left(\int_\Omega |x_j(\mathbf{r}')|^2\, d\mathbf{r}' \right)^{1/2} \leq \varepsilon\sqrt{n\,|\Omega|}\|\mathbf{x}\|_{n,2},$$

and the image $g(B)$ of any bounded set B of $\mathcal{G}$ is equicontinuous. Similarly, if we set $w(t) = \|\mathbf{W}(.,.,t)\|_{n\times n,\infty}$ in $\Omega \times \Omega$, we have $|g^i(\mathbf{x})(\mathbf{r}, t)| \leq w(t)\sqrt{n\,|\Omega|}\,\|\mathbf{x}\|_{n,2}$. The same reasoning as in lemma 4.3.1 shows that the operator $\mathbf{x} \to g(\mathbf{x})$ from $\mathcal{G}$ to $\mathcal{F}$ is compact and since the identity from $\mathcal{F}$ to $\mathcal{G}$ is continuous, $\mathbf{x} \to g(\mathbf{x})$ is compact from $\mathcal{G}$ to $\mathcal{G}$.

The same proof applies to g_m and h_m. □

We then proceed with the following

Lemma 4.3.3. *The adjoint g^* of the operator g of $\mathcal{G}$ is the operator defined by*

$$g^*(\mathbf{x})(\mathbf{r}, t) = \int_\Omega \mathbf{W}^T(\mathbf{r}', \mathbf{r}, t)\mathbf{x}(\mathbf{r}')\, d\mathbf{r}'$$

It is a compact operator. Similar results apply to g_m^* and h_m^*.

Proof. The adjoint, if it exists, is defined by the condition $\langle g(\mathbf{x}),\, \mathbf{y}\rangle = \langle \mathbf{x},\, g^*(\mathbf{y})\rangle$ for all $\mathbf{x}$, $\mathbf{y}$ in $\mathcal{G}$. We have

$$\langle g(\mathbf{x}),\, \mathbf{y}\rangle = \int_\Omega \mathbf{y}(\mathbf{r})^T \left(\int_\Omega \mathbf{W}(\mathbf{r}, \mathbf{r}', t)\mathbf{x}(\mathbf{r}')\, d\mathbf{r}' \right) d\mathbf{r} =$$

$$\int_\Omega \mathbf{x}(\mathbf{r}')^T \left(\int_\Omega \mathbf{W}^T(\mathbf{r}, \mathbf{r}', t)\mathbf{y}(\mathbf{r})\, d\mathbf{r} \right) d\mathbf{r}',$$

from which the conclusion follows. Since $\mathcal{G}$ is not a Hilbert space the adjoint of a compact operator is not necessarily compact. But the proof of compactness of g in lemma 4.3.2 extends easily to g^*. □

We finally prove two useful lemmas that will complete our toolbox for the proof of the main results of this section.

Lemma 4.3.4. *Given a diagonal matrix $\mathbf{D} = diag(d_1, ..., d_n)$, with $d_1, ..., d_n \in \mathbf{L}^\infty(\Omega)$ and a function $\mathbf{x} \in \mathcal{G}$, we have*

$$\|\mathbf{D}\mathbf{x}\|_{n,2} \leq \max_i(\|d_i\|_\infty)\|\mathbf{x}\|_{n,2}.$$

Proof.

$$\|\mathbf{D}\mathbf{x}\|_{n,2}^2 = \int_\Omega \mathbf{x}(\mathbf{r})^T\mathbf{D}^2(\mathbf{r})\mathbf{x}(\mathbf{r})\, d\mathbf{r} = \sum_i \int_\Omega d_i^2(\mathbf{r})\mathbf{x}_i^2(\mathbf{r})\, d\mathbf{r} \leq \sum_i \|d_i\|_\infty^2 \int_\Omega \mathbf{x}_i^2(\mathbf{r})\, d\mathbf{r},$$

from which the result follows. □

Lemma 4.3.5. *$\|g\|_{\mathcal{G}}$, $\|g_m\|_{\mathcal{G}}$, and $\|h_m\|_{\mathcal{G}}$ satisfy the following inequalities*

$$\|g_m\|_{\mathcal{G}} \le DS_m \|g\|_{\mathcal{G}} \quad \text{and} \quad \|h_m\|_{\mathcal{G}} \le DS_m \|g\|_{\mathcal{G}},$$

where DS_m is defined in definition 4.1.1.

Proof. By definition

$$\|g_m\|_{\mathcal{G}} = \sup_{\|\mathbf{x}\|_{n,2}\le 1} \frac{\|g_m(\mathbf{x})\|_{n,2}}{\|\mathbf{x}\|_{n,2}} = \sup_{\|\mathbf{x}\|_{n,2}\le 1} \frac{\|g(D\mathbf{S}_m\mathbf{x})\|_{n,2}}{\|\mathbf{x}\|_{n,2}}.$$

Let $\mathbf{y} = D\mathbf{S}_m\mathbf{x}$. Since $\{\mathbf{x} \in \mathcal{G}, \|\mathbf{x}\|_{n,2} \le 1\} \subset \{\mathbf{x} \in \mathcal{G}, \|D\mathbf{S}_m\mathbf{x}\|_{n,2} \le DS_m\}$ (lemma 4.3.4),

$$\|g_m\|_{\mathcal{G}} \le \sup_{\|\mathbf{y}\|_{n,2}\le DS_m} \frac{\|g(\mathbf{y})\|_{n,2}}{\|D\mathbf{S}_m^{-1}\mathbf{y}\|_{n,2}} = \sup_{\|\mathbf{y}\|_{n,2}\le 1} \frac{\|g(\mathbf{y})\|_{n,2}}{\|D\mathbf{S}_m^{-1}\mathbf{y}\|_{n,2}} \le \\ \sup_{\|\mathbf{y}\|_{n,2}\le 1} \frac{\|g(\mathbf{y})\|_{n,2}}{\|\mathbf{y}\|_{n,2}} \cdot \sup_{\|\mathbf{y}\|_{n,2}\le 1} \frac{\|\mathbf{y}\|_{n,2}}{\|D\mathbf{S}_m^{-1}\mathbf{y}\|_{n,2}} \le \|g\|_{\mathcal{G}}\, DS_m$$

The last inequality is also obtained from lemma 4.3.4, which is used again to prove the inequality for h_m: $h_m = D\mathbf{S}_m g$ and $\|D\mathbf{S}_m g(\mathbf{x})\|_{n,2} \le DS_m \|g(\mathbf{x})\|_{n,2}$, for all $\mathbf{x} \in \mathcal{G}$, from which the result follows. □

We show in appendix B a table summarizing the main notations introduced so far for future reference.

We now state an important result of this section.

Theorem 4.3.1. *A sufficient condition for the absolute stability of a solution to (4.6) is*

$$DS_m \tau_{\max} \|g\|_{\mathcal{G}} < 1 \tag{4.15}$$

where $\|.\|_{\mathcal{G}}$ is the operator norm.

Proof. Let us note $\underline{\mathbf{S}}$ the function $D\mathbf{S}_m^{-1}\mathbf{S}$ and rewrite equation (4.6) as follows

$$\mathbf{V}_t(\mathbf{r}, t) = -\mathbf{L}\mathbf{V}(\mathbf{r}, t) + \int_\Omega \mathbf{W}_{cm}(\mathbf{r}, \mathbf{r}', t)\, \underline{\mathbf{S}}(\mathbf{V}(\mathbf{r}', t))\, d\mathbf{r}' + \mathbf{I}_{\text{ext}}(\mathbf{r}, t).$$

Let $\mathbf{U}$ be its unique solution with initial conditions $\mathbf{U}(0) = \mathbf{U}_0$, an element of $\mathcal{G}$. Let also $\mathbf{V}$ be the unique solution of the same equation with different initial conditions $\mathbf{V}(0) = \mathbf{V}_0$, another element of $\mathcal{G}$. We introduce the new function $\mathbf{X} = \mathbf{V} - \mathbf{U}$ which satisfies

$$\mathbf{X}_t(\mathbf{r}, t) = -\mathbf{L}\mathbf{X}(\mathbf{r}, t) + \int_\Omega \mathbf{W}_{cm}(\mathbf{r}, \mathbf{r}', t)\, \mathbf{H}(\mathbf{X}, \mathbf{U})(\mathbf{r}', t)\, d\mathbf{r}' = \\ -\mathbf{L}\mathbf{X}(\mathbf{r}, t) + g_m(\mathbf{H}(\mathbf{X}, \mathbf{U}))(\mathbf{r}, t) \tag{4.16}$$

where the vector $\mathbf{H}(\mathbf{X}, \mathbf{U})$ is given by $\mathbf{H}(\mathbf{X}, \mathbf{U})(\mathbf{r}, t)) = \underline{\mathbf{S}}(\mathbf{V}(\mathbf{r}, t)) - \underline{\mathbf{S}}(\mathbf{U}(\mathbf{r}, t)) = \underline{\mathbf{S}}(\mathbf{X}(\mathbf{r}, t) + \mathbf{U}(\mathbf{r}, t)) - \underline{\mathbf{S}}(\mathbf{U}(\mathbf{r}, t))$. Consider now the functional (Lyapunov function)

$$V(\mathbf{X}) = \frac{1}{2} \langle\, \mathbf{X}, \mathbf{L}^{-1}\mathbf{X} \,\rangle,$$

where the symmetric positive definite matrix $\mathbf{L}$ can be seen as defining a metric on the state space. Its time derivative is $\langle\, \mathbf{X}, \mathbf{L}^{-1}\mathbf{X}_t \,\rangle$. We replace $\mathbf{X}_t$ by its value from (4.16) in this expression to obtain

$$\frac{dV(\mathbf{X})}{dt} = -\langle\, \mathbf{X}, \mathbf{X} \,\rangle + \langle\, \mathbf{X}, \mathbf{L}^{-1} g_m(\mathbf{H}(\mathbf{X}, \mathbf{U})) \,\rangle$$

We consider the second term in the righthand side of this equation:

$$
\begin{aligned}
| \left\langle \mathbf{X},\, \mathbf{L}^{-1} g_m(\mathbf{H}(\mathbf{X},\mathbf{U})) \right\rangle | \leq \|\mathbf{X}\|_{n,2}\, \|\mathbf{L}^{-1} g_m(\mathbf{H}(\mathbf{X},\mathbf{U}))\|_{n,2} \leq \\
\tau_{\max} \|\mathbf{X}\|_{n,2}\, \|g_m(\mathbf{H}(\mathbf{X},\mathbf{U}))\|_{n,2} \leq \tau_{\max} \|\mathbf{X}\|_{n,2}\, \|g_m\|_{\mathcal{G}} \|\mathbf{H}(\mathbf{X},\mathbf{U})\|_{n,2} \quad (4.17)
\end{aligned}
$$

Using a zeroth-order Taylor expansion with integral remainder, as in the proof of lemma 4.2.1, we write $\mathbf{H}(\mathbf{X},\mathbf{U}) = \mathcal{D}_m \mathbf{X}$, where $\mathcal{D}_m$ is a diagonal matrix whose diagonal elements are continuous functions with values between 0 and 1:

$$
\mathcal{D}_m(\mathbf{r},t) = \int_0^1 D\underline{\mathbf{S}}(\mathbf{U}(\mathbf{r},t) + \zeta(\mathbf{V}(\mathbf{r},t) - \mathbf{U}(\mathbf{r},t)))\, d\zeta.
$$

Hence, according to lemma 4.3.4,

$$
\|\mathbf{H}(\mathbf{X},\mathbf{U})\|_{n,2} = \|\mathcal{D}_m \mathbf{X}\|_{n,2} \leq \|\mathbf{X}\|_{n,2}
$$

We use this result and lemma 4.3.5 in equation (4.17) to obtain

$$
| \left\langle \mathbf{X},\, \mathbf{L}^{-1} g_m(\mathbf{H}(\mathbf{X},\mathbf{U})) \right\rangle | \leq \tau_{\max} DS_m \, \|g\|_{\mathcal{G}} \, \|\mathbf{X}\|_{n,2}^2,
$$

and the conclusion follows. □
An identical sufficient condition holds for the stability of a solution to (4.7).

Theorem 4.3.2. *A sufficient condition for the absolute stability of a solution to (4.7) is*

$$
DS_m \tau_{\max} \, \|g\|_{\mathcal{G}} < 1
$$

Proof. Let $\mathbf{U}$ be the unique solution of (4.7) with an external current $\mathbf{I}_{\text{ext}}(\mathbf{r},t)$ and initial conditions $\mathbf{U}(0) = \mathbf{U}_0$. As in the proof of theorem 4.3.1 we introduce the new function $\mathbf{X} = \mathbf{V} - \mathbf{U}$, where $\mathbf{V}$ is the unique solution of the same equation with different initial conditions. We have

$$
\begin{aligned}
\mathbf{X}_t(\mathbf{r},t) = -\mathbf{L}\mathbf{X}(\mathbf{r},t) + \mathbf{S}\left(\int_\Omega \mathbf{W}(\mathbf{r},\mathbf{r}',t)\mathbf{V}(\mathbf{r}',t)\, d\mathbf{r}' + \mathbf{I}_{\text{ext}}(\mathbf{r},t) \right) - \\
\mathbf{S}\left(\int_\Omega \mathbf{W}(\mathbf{r},\mathbf{r}',t)\mathbf{U}(\mathbf{r}',t)\, d\mathbf{r}' + \mathbf{I}_{\text{ext}}(\mathbf{r},t) \right) \quad (4.18)
\end{aligned}
$$

Using a zeroth-order Taylor expansion, as in the proof of lemma 4.2.1, this equation can be rewritten as

$$
\begin{aligned}
\mathbf{X}_t(\mathbf{r},t) = -\mathbf{L}\mathbf{X}(\mathbf{r},t) + \Bigg(\int_0^1 D\mathbf{S}\Big(\int_\Omega \mathbf{W}(\mathbf{r},\mathbf{r}',t)\mathbf{U}(\mathbf{r}'t)\, d\mathbf{r}' + \mathbf{I}_{\text{ext}}(\mathbf{r},t) + \\
\zeta \int_\Omega \mathbf{W}(\mathbf{r},\mathbf{r}',t)\mathbf{X}(\mathbf{r}',t)\, d\mathbf{r}' \Big)\, d\zeta \Bigg) \left(\int_\Omega \mathbf{W}(\mathbf{r},\mathbf{r}',t)\mathbf{X}(\mathbf{r}',t)\, d\mathbf{r}' \right)
\end{aligned}
$$

We use the same functional as in the proof of theorem 4.3.1

$$
V(\mathbf{X}) = \frac{1}{2} \left\langle \mathbf{X},\, \mathbf{L}^{-1}\mathbf{X} \right\rangle.
$$

Its time derivative is readily obtained with the help of equation (4.18)

$$
\frac{dV(\mathbf{X})}{dt} = -\left\langle \mathbf{X},\, \mathbf{X} \right\rangle + \left\langle \mathbf{X},\, \mathbf{L}^{-1}\mathcal{D}_m h_m(\mathbf{X}) \right\rangle, \quad (4.19)
$$

where $\mathcal{D}_m$ is defined by

$$\mathcal{D}_m(\mathbf{U},\mathbf{X},\mathbf{r},t) = \int_0^1 D\mathbf{S}\Big(\int_\Omega \mathbf{W}(\mathbf{r},\mathbf{r}',t)\mathbf{U}(t)\,d\mathbf{r}' + \mathbf{I}_{\rm ext}(\mathbf{r},t) + \zeta\int_\Omega \mathbf{W}(\mathbf{r},\mathbf{r}',t)\mathbf{X}(\mathbf{r}',t)\,d\mathbf{r}'\Big)\,D\mathbf{S}_m^{-1}\,d\zeta,$$

a diagonal matrix whose diagonal elements are continuous functions with values between 0 and 1. We consider the second term in the righthand side of equation (4.19) and use the property of matrix $\mathcal{D}_m$ and lemma 4.3.5 to obtain

$$\begin{aligned}|\,\langle\,\mathbf{X},\,\mathbf{L}^{-1}\mathcal{D}_m h_m(\mathbf{X})\,\rangle\,| &\leq \|\mathbf{X}\|_{n,2}\|\mathbf{L}^{-1}\mathcal{D}_m h_m(\mathbf{X})\|_{n,2}\\ &\leq \tau_{\max}\|\mathbf{X}\|_{n,2}\,\|h_m(\mathbf{X})\|_{n,2} \leq \tau_{\max}\,DS_m\,\|g\|_{\mathcal{G}}\,\|\mathbf{X}\|_{n,2}^2,\end{aligned}$$

from which the result follows. □
Note that $\|g\|_{\mathcal{G}} = \|g\|_{\mathbf{L}^2}$ by density of $\mathcal{G}$ in $\mathbf{L}^2$ (see section 4.5). In appendix C, we show how to compute such operator norms.

4.3.2 The convolution case

In the case where $\mathbf{W}$ is translation invariant we can obtain a slightly easier to exploit sufficient condition for the stability of the solutions than in the theorems 4.3.1 and 4.3.2. We first consider the case of a general compact Ω and then the case where Ω is an interval. Translation invariance means that $\mathbf{W}(\mathbf{r}+\mathbf{a},\mathbf{r}'+\mathbf{a},t) = \mathbf{W}(\mathbf{r},\mathbf{r}',t)$ for all $\mathbf{a}$ such that $\mathbf{a}+\mathbf{r}\in\Omega$ and $\mathbf{a}+\mathbf{r}'\in\Omega$, so we can write $\mathbf{W}(\mathbf{r},\mathbf{r}',t) = \mathbf{W}(\mathbf{r}-\mathbf{r}',t)$. Hence $\mathbf{W}(\mathbf{r},t)$ must be defined for all $\mathbf{r}\in\widehat{\Omega} = \{\mathbf{r}-\mathbf{r}',\text{ with }\mathbf{r},\,\mathbf{r}'\in\Omega\}$ and we suppose it continuous on $\widehat{\Omega}$ for each t. $\widehat{\Omega}$ is a symmetric with respect to the origin, compact subset of $\mathbb{R}^q$.

General Ω

We note $\mathbf{1}_A$ the characteristic function of the subset A of $\mathbb{R}^q$ and $\mathbf{M}^* = \overline{\mathbf{M}}^T$ the conjugate transpose of the complex matrix $\mathbf{M}$.

We prove the following

Theorem 4.3.3. *If the eigenvalues of the Hermitian matrix*

$$\widetilde{\mathbf{W}}^*(\mathbf{f},t)\,\widetilde{\mathbf{W}}(\mathbf{f},t) \tag{4.20}$$

are strictly less than $(\tau_{\max}DS_m)^{-2}$ *for almost all* $\mathbf{f}\in\mathbb{R}^q$ *and* $t\in$ J, *then the system (4.6) is absolutely stable*[1]. $\widetilde{\mathbf{W}}(\mathbf{f},t)$ *is the Fourier transform with respect to the space variable* $\mathbf{r}$ *of* $\mathbf{1}_{\widehat{\Omega}}(\mathbf{r})\,\mathbf{W}(\mathbf{r},t)$,

$$\widetilde{\mathbf{W}}(\mathbf{f},t) = \int_{\widehat{\Omega}} \mathbf{W}(\mathbf{r},t)e^{-2i\pi\mathbf{r}\cdot\mathbf{f}}\,d\mathbf{r}$$

Proof. We recall that

$$\|g\|_{\mathcal{G}}^2 = \sup_{\|\mathbf{x}\|_{n,2}\leq 1}\frac{\|g(\mathbf{x})\|_{n,2}^2}{\|\mathbf{x}\|_{n,2}^2}.$$

---

[1] Remark that since $\widetilde{\mathbf{W}}$ is continuous with respect to $\mathbf{f}$, some eigenvalues of the Hermitian matrix may be equal to $(\tau_{\max}DS_m)^{-2}$ on a zero measure domain.

We then note that, by definition

$$\|g(\mathbf{x})\|_{n,2} = \|(\mathbf{1}_{\widehat{\Omega}}\mathbf{W}) \otimes (\mathbf{1}_{\Omega}\mathbf{x})\|_{\mathbb{R}^q,\,n,\,2},$$

where $\otimes$ indicates the convolution over $\mathbb{R}^q$. Parseval's theorem gives

$$\|(\mathbf{1}_{\widehat{\Omega}}\mathbf{W}) \otimes (\mathbf{1}_{\Omega}\mathbf{x})\|^2_{\mathbb{R}^q,\,n,\,2} = \int_{\mathbb{R}^q} \widetilde{\mathbf{x}}^*(\mathbf{f},t)\widetilde{\mathbf{W}}^*(\mathbf{f},t)\widetilde{\mathbf{W}}(\mathbf{f},t)\widetilde{\mathbf{x}}(\mathbf{f},t)\, d\mathbf{f},$$

where $\widetilde{\mathbf{x}}$ is the Fourier transform of $\mathbf{1}_{\Omega}\mathbf{x}$.
As an Hermitian matrix, $\widetilde{\mathbf{W}}^*(\mathbf{f},t)\widetilde{\mathbf{W}}(\mathbf{f},t)$ can be rewritten as $\mathbf{U}^*(\mathbf{f},t)\mathbf{D}(\mathbf{f},t)\mathbf{U}(\mathbf{f},t)$, with $\mathbf{U}^*\mathbf{U} = \mathrm{Id_n}$ and $\mathbf{D}$ real and diagonal. In particular, $\mathbf{U}$ preserves length ($\|\mathbf{U}\mathbf{v}\|_2 = \|\mathbf{v}\|_2$). Besides, $\widetilde{\mathbf{W}}^*\widetilde{\mathbf{W}}$ is positive because for any complex vector $\mathbf{v}$,

$$\mathbf{v}^*\widetilde{\mathbf{W}}^*\widetilde{\mathbf{W}}\mathbf{v} = \|\widetilde{\mathbf{W}}\mathbf{v}\|_2^2 \geq 0.$$

So, all values of $\mathbf{D}$ are positive and if the hypothesis of the theorem is satisfied, lemma 4.3.4 yields

$$\int_{\mathbb{R}^q} \widetilde{\mathbf{x}}^*(\mathbf{f},t)\widetilde{\mathbf{W}}^*(\mathbf{f},t)\widetilde{\mathbf{W}}(\mathbf{f},t)\widetilde{\mathbf{x}}(\mathbf{f},t)\, d\mathbf{f} = \|\sqrt{\mathbf{D}}\mathbf{U}\widetilde{\mathbf{x}}\|^2_{\mathbb{R}^q,\,n,\,2} \leq$$
$$(\tau_{\max}DS_m)^{-2}\|\mathbf{U}\widetilde{\mathbf{x}}\|^2_{\mathbb{R}^q,\,n,\,2} = (\tau_{\max}DS_m)^{-2}\|\widetilde{\mathbf{x}}\|^2_{\mathbb{R}^q,\,n,\,2} = (\tau_{\max}DS_m)^{-2}\|\mathbf{x}\|^2_{n,2},$$

hence $\|g\|_{\mathcal{G}} < (\tau_{\max}DS_m)^{-1}$ and theorem 4.3.1 applies. □
Since the sufficient condition for the absolute stability of the solution of the activation-based model is identical, we have the

Theorem 4.3.4. *If the eigenvalues of the Hermitian matrix*

$$\widetilde{\mathbf{W}}^*(\mathbf{f},t)\,\widetilde{\mathbf{W}}(\mathbf{f},t)$$

are strictly less than $(\tau_{\max}DS_m)^{-2}$ *for almost all* $\mathbf{f}$ *and* $t \in \mathrm{J}$ *then the system (4.7) is absolutely stable.* $\widetilde{\mathbf{W}}(\mathbf{f},t)$ *is the Fourier transform of* $\mathbf{1}_{\widehat{\Omega}}(\mathbf{r})\mathbf{W}(\mathbf{r},t)$ *with respect to the space variable* $\mathbf{r}$.

These two theorems are somewhat unsatisfactory since they replace a condition that must be satisfied over a countable set, the spectrum of a compact operator, as in theorems 4.3.1 and 4.3.2, by a condition that must be satisfied over a continuum, i.e. $\mathbb{R}^q$. Nonetheless one may consider that the computation of the Fourier transforms of the matrix $\mathbf{W}$, extended by zeros outside $\widehat{\Omega}$, is easier than that of the spectrum of the operator g, for which a method is given in appendix C.

Ω is an interval

In the case where Ω is an interval, i.e. an interval of $\mathbb{R}$ ($q = 1$), a parallelogram ($q = 2$), or a parallelepiped ($q = 3$), we can state different sufficient conditions. We can always assume that Ω is the q-dimensional interval $[0,1]^q$ by applying an affine change of coordinates. The connectivity matrix $\mathbf{W}$ is defined on $\mathrm{J} \times [-1,1]^{\mathrm{q}}$ and extended to a q-periodic function of periods 2 on $\mathrm{J} \times \mathbb{R}^{\mathrm{q}}$, reflecting periodic boundary conditions. Similarly, the state vectors $\mathbf{V}$ and $\mathbf{A}$ as well as the external current $\mathbf{I}_{\mathrm{ext}}$ defined on $\mathrm{J} \times [0,1]^{\mathrm{q}}$ are extended to q-periodic functions of the same periods over $\mathrm{J} \times \mathbb{R}^{\mathrm{q}}$ by padding them with zeros in the complement in the interval $[-1,1]^q$ of the

interval $[0,1]^q$. $\mathcal{G}$ is now the space $\mathbf{L}_n^2(2)$ of the square integrable q-periodic functions of periods 2 with values in $\mathbb{R}^n$.
We define the functions $\psi_{\mathbf{m}}(\mathbf{r}) \equiv e^{-\pi i(r_1 m_1 + \cdots + r_q m_q)}$, for $\mathbf{m} \in \mathbb{Z}^q$ and consider the matrix $\widetilde{\mathbf{W}}(\mathbf{m}, t)$ whose elements are given by

$$\widetilde{W}_{ij}(\mathbf{m}, t) = \int_{[0,2]^q} W_{ij}(\mathbf{r}, t) \psi_{\mathbf{m}}(\mathbf{r})\, d\mathbf{r} \quad 1 \leq i,\, j \leq n.$$

We recall the

Definition 4.3.2. *The matrix* $\widetilde{\mathbf{W}}(\mathbf{m})$ *is the* $\mathbf{m}$*th element of the Fourier series of the periodic matrix function* $\mathbf{W}(\mathbf{r})$.

The theorems 4.3.3 and 4.3.4 can be stated in this framework.

Theorem 4.3.5. *If the eigenvalues of the Hermitian matrix*

$$\widetilde{\mathbf{W}}^*(\mathbf{m}, t)\, \widetilde{\mathbf{W}}(\mathbf{m}, t) \tag{4.21}$$

are strictly less than $(\tau_{\max} DS_m)^{-2}$ *for all* $\mathbf{m} \in \mathbb{Z}^q$ *and all* $t \in \mathrm{J}$, *then the system (4.6) (resp. (4.7)) is absolutely stable.* $\widetilde{\mathbf{W}}(\mathbf{m}, t)$ *is the* $\mathbf{m}$*th element of the Fourier series of the* q*-periodic matrix function* $\mathbf{W}(\mathbf{r}, t)$ *with periods 2 at time* t.

4.4 ABSOLUTE STABILITY OF THE HOMOGENEOUS SOLUTION

We next investigate the absolute stability of a homogeneous solution to (4.6) and (4.7). As in the previous section we distinguish the general and convolution cases.

4.4.1 The general case

The homogeneous solutions are characterized by the fact that they are spatially constant at each time instant. We consider the subspace $\mathcal{G}_c$ of $\mathcal{G}$ of the constant functions. We have the following

Lemma 4.4.1. *$\mathcal{G}_c$ is a complete linear subspace of $\mathcal{G}$. The orthogonal projection operator $\mathcal{P}_{\mathcal{G}_c}$ from $\mathcal{G}$ to $\mathcal{G}_c$ is defined by*

$$\mathcal{P}_{\mathcal{G}_c}(\mathbf{x}) = \overline{\mathbf{x}} = \frac{1}{|\Omega|} \int_\Omega \mathbf{x}(\mathbf{r})\, d\mathbf{r}$$

The orthogonal complement $\mathcal{G}_c^\perp$ of $\mathcal{G}_c$ is the subset of functions of $\mathcal{G}$ that have a zero average. The orthogonal projection[2] *operator $\mathcal{P}_{\mathcal{G}_c^\perp}$ is equal to $\mathrm{Id} - \mathcal{P}_{\mathcal{G}_c}$. We also have*

$$\mathcal{P}_{\mathcal{G}_c^\perp} \mathbf{M} \mathbf{x} = \mathbf{M} \mathcal{P}_{\mathcal{G}_c^\perp} \mathbf{x} \quad \forall \mathbf{x} \in \mathcal{G},\, \mathbf{M} \in \mathcal{M}_{n \times n} \tag{4.22}$$

Proof. The constant functions are clearly in $\mathcal{G}$. Any Cauchy sequence of constants is converging to a constant hence $\mathcal{G}_c$ is closed in the pre-Hilbert space $\mathcal{G}$. Therefore there exists an orthogonal projection operator from $\mathcal{G}$ to $\mathcal{G}_c$ which is linear, continuous, of unit norm, positive and self-adjoint. $\mathcal{P}_{\mathcal{G}_c}(\mathbf{x})$ is the minimum with respect to the constant vector a of the integral $\int_\Omega \|\mathbf{x}(\mathbf{r})-\mathbf{a}\|^2\,d\mathbf{r}$. Taking the derivative with respect to a, we obtain the necessary condition

---

[2] To be accurate, this is the projection on the closure of $\mathcal{G}_c^\perp$ in the closure of $\mathcal{G}$ which is the Hilbert space $\mathbf{L}_n^2(\Omega)$.

$$\int_\Omega (\mathbf{x}(\mathbf{r})-\mathbf{a})\,d\mathbf{r}=0$$

and hence $\mathbf{a}_{min}=\overline{\mathbf{x}}$. Conversely, $\mathbf{x}-\mathbf{a}_{min}$ is orthogonal to $\mathcal{G}_c$ since $\int_\Omega (\mathbf{x}(\mathbf{r})-\mathbf{a}_{min})\mathbf{b}\,d\mathbf{r}=0$ for all $\mathbf{b}\in\mathcal{G}_c$.

Let $\mathbf{y}\in\mathcal{G}$, $\int_\Omega \mathbf{x}\,\mathbf{y}(\mathbf{r})\,d\mathbf{r}=\mathbf{x}\int_\Omega \mathbf{y}(\mathbf{r})\,d\mathbf{r}=0$ for all $\mathbf{x}\in\mathcal{G}_c$ if and only if $\mathbf{y}\in\mathcal{G}_c^\perp$.

Finally

$$\mathcal{P}_{\mathcal{G}_c^\perp}\mathbf{M}\mathbf{x}=\mathbf{M}\mathbf{x}-\overline{\mathbf{M}\mathbf{x}}=\mathbf{M}\mathbf{x}-\mathbf{M}\overline{\mathbf{x}}=\mathbf{M}(\mathbf{x}-\overline{\mathbf{x}})=\mathbf{M}\mathcal{P}_{\mathcal{G}_c^\perp}\mathbf{x}$$

□

We are now ready to prove the theorem on the absolute stability of the homogeneous solutions to (4.6).

Theorem 4.4.1. *If* $\mathbf{W}$ *satisfies (4.12), a sufficient condition for the absolute stability of a homogeneous solution to (4.6) is that the norm* $\|g^*\|_{\mathcal{G}_c^\perp}$ *of the restriction to* $\mathcal{G}_c^\perp$ *of the compact operator* g^* *be less than* $(\tau_{\max}DS_m)^{-1}$ *for all* $t\in$ J.

Proof. This proof is inspired by [90]. Note that $\mathcal{G}_c^\perp$ is invariant by g^* and hence by g_m^*. Indeed, from lemma 4.3.3 and equation (4.12) we have

$$\overline{g^*(\mathbf{x})}=\overline{\mathbf{W}}^T(t)\overline{\mathbf{x}}=0\quad\forall\mathbf{x}\in\mathcal{G}_c^\perp$$

Let $\mathbf{V}_p$ be the unique solution of (4.6) with homogeneous input $\mathbf{I}_{\text{ext}}(t)$ and initial conditions $\mathbf{V}_p(0)=\mathbf{V}_{p0}\in\mathcal{G}$, and consider the initial value problem:

$$\left\{\begin{array}{rcl}\mathbf{X}'(t)&=&\mathcal{P}_{\mathcal{G}_c^\perp}\Big(f_v(t,\mathcal{P}_{\mathcal{G}_c^\perp}\mathbf{X}+\mathcal{P}_{\mathcal{G}_c}\mathbf{V}_p)\Big)\\ \mathbf{X}(0)&=&\mathbf{X}_0\end{array}\right.\tag{4.23}$$

$\mathbf{X}=\mathcal{P}_{\mathcal{G}_c^\perp}\mathbf{V}_p$ is a solution with initial condition $\mathbf{X}_0=\mathcal{P}_{\mathcal{G}_c^\perp}\mathbf{V}_{p0}$, since $\mathcal{P}^2_{\mathcal{G}_c^\perp}=\mathcal{P}_{\mathcal{G}_c^\perp}$, and $\mathcal{P}_{\mathcal{G}_c^\perp}\mathbf{V}_p+\mathcal{P}_{\mathcal{G}_c}\mathbf{V}_p=\mathbf{V}_p$. But $\mathbf{X}=0$ is also a solution with initial condition $\mathbf{X}_0=0$. Indeed $\mathcal{G}_c$ is flow-invariant because of (4.12), that is $f_v(t,\mathcal{G}_c)\subset\mathcal{G}_c$, and hence $\mathcal{P}_{\mathcal{G}_c^\perp}(f_v(t,\mathcal{G}_c))=0$. We therefore look for a sufficient condition for the system (4.23) to be absolutely stable at $\mathbf{X}=0$.

We consider again the functional $V(\mathbf{X})=\frac{1}{2}\left\langle\mathbf{X},\,\mathbf{L}^{-1}\mathbf{X}\right\rangle$ with time derivative $\frac{dV(\mathbf{X})}{dt}=\left\langle\,\mathbf{X},\,\mathbf{L}^{-1}\mathbf{X}_t\,\right\rangle$. We substitute $\mathbf{X}_t$ with its value from (4.23) which can be rewritten as

$$\mathbf{X}_t=\mathcal{P}_{\mathcal{G}_c^\perp}\left(-\mathbf{L}(\mathcal{P}_{\mathcal{G}_c^\perp}\mathbf{X}+\mathcal{P}_{\mathcal{G}_c}\mathbf{V}_p)+\int_\Omega\mathbf{W}(\mathbf{r},\mathbf{r}',t)\,\mathbf{S}(\mathcal{P}_{\mathcal{G}_c^\perp}\mathbf{X}(\mathbf{r}',t)+\mathcal{P}_{\mathcal{G}_c}\mathbf{V}_p(\mathbf{r}',t))\,d\mathbf{r}'\right)$$

Because of lemma 4.4.1 this yields

$$\mathbf{X}_t=-\mathbf{L}\mathcal{P}_{\mathcal{G}_c^\perp}\mathbf{X}+\mathcal{P}_{\mathcal{G}_c^\perp}\left(\int_\Omega\mathbf{W}_{cm}(\mathbf{r},\mathbf{r}',t)\,\underline{\mathbf{S}}(\mathcal{P}_{\mathcal{G}_c^\perp}\mathbf{X}(\mathbf{r}',t)+\mathcal{P}_{\mathcal{G}_c}\mathbf{V}_p(\mathbf{r}',t))\,d\mathbf{r}'\right)$$

Using a zeroth-order Taylor expansion, as in the proof of lemma 4.2.1, we write

$$\underline{\mathbf{S}}(\mathcal{P}_{\mathcal{G}_c^\perp}\mathbf{X}+\mathcal{P}_{\mathcal{G}_c}\mathbf{V}_p)=\underline{\mathbf{S}}(\mathcal{P}_{\mathcal{G}_c}\mathbf{V}_p)+\left(\int_0^1 D\underline{\mathbf{S}}(\mathcal{P}_{\mathcal{G}_c}\mathbf{V}_p+\zeta\mathcal{P}_{\mathcal{G}_c^\perp}\mathbf{X})\,d\zeta\right)\mathcal{P}_{\mathcal{G}_c^\perp}\mathbf{X},$$

and since $\underline{\mathbf{S}}(\mathcal{P}_{\mathcal{G}_c}\mathbf{V}_p) \in \mathcal{G}_c$, and because of (4.12)

$$\mathcal{P}_{\mathcal{G}_c^\perp}\left(\int_\Omega \mathbf{W}_{cm}(\mathbf{r},\mathbf{r}',t)\,\underline{\mathbf{S}}(\mathcal{P}_{\mathcal{G}_c^\perp}\mathbf{X}(\mathbf{r}',t) + \mathcal{P}_{\mathcal{G}_c}\mathbf{V}_p(\mathbf{r}',t))\,d\mathbf{r}'\right) =$$
$$\mathcal{P}_{\mathcal{G}_c^\perp}\left(\int_\Omega \mathbf{W}_{cm}(\mathbf{r},\mathbf{r}',t)\left(\int_0^1 D\underline{\mathbf{S}}(\mathcal{P}_{\mathcal{G}_c}\mathbf{V}_p(\mathbf{r}',t) + \zeta\mathcal{P}_{\mathcal{G}_c^\perp}\mathbf{X}(\mathbf{r}',t))\,d\zeta\right)\mathcal{P}_{\mathcal{G}_c^\perp}\mathbf{X}(\mathbf{r}',t)\,d\mathbf{r}'\right)$$

We use (4.22) and the fact that $\mathcal{P}_{\mathcal{G}_c^\perp}$ is self-adjoint and idempotent to write

$$\frac{dV(\mathbf{X})}{dt} = -\langle \mathcal{P}_{\mathcal{G}_c^\perp}\mathbf{X},\, \mathcal{P}_{\mathcal{G}_c^\perp}\mathbf{X}\rangle +$$
$$\left\langle \mathcal{P}_{\mathcal{G}_c^\perp}\mathbf{X},\, \mathbf{L}^{-1}\int_\Omega \mathbf{W}_{cm}(\mathbf{r},\mathbf{r}',t)\left(\int_0^1 D\underline{\mathbf{S}}(\mathcal{P}_{\mathcal{G}_c}\mathbf{V}_p(\mathbf{r}',t)+\zeta\mathcal{P}_{\mathcal{G}_c^\perp}\mathbf{X}(\mathbf{r}',t))\,d\zeta\right)\mathcal{P}_{\mathcal{G}_c^\perp}\mathbf{X}(\mathbf{r}',t)\,d\mathbf{r}'\right\rangle$$

Let us denote by $\mathcal{D}_v(\mathbf{r}',t)$ the diagonal matrix $\int_0^1 D\underline{\mathbf{S}}(\mathcal{P}_{\mathcal{G}_c}\mathbf{V}_p(\mathbf{r}',t)+\zeta\mathcal{P}_{\mathcal{G}_c^\perp}\mathbf{X}(\mathbf{r}',t))\,d\zeta$. Its diagonal elements are continuous functions with values between 0 and 1. Letting $\mathbf{Y} = \mathcal{P}_{\mathcal{G}_c^\perp}\mathbf{X}$ we rewrite the previous equation in operator form, introducing the operator g_m (definition 4.3.1), as

$$\frac{dV(\mathbf{X})}{dt} = -\langle \mathbf{Y},\, \mathbf{Y}\rangle + \left\langle \mathbf{Y},\, \mathbf{L}^{-1}g_m(\mathcal{D}_v\,\mathbf{Y})\right\rangle$$

By definition of the adjoint

$$\left\langle \mathbf{Y},\, \mathbf{L}^{-1}g_m(\mathcal{D}_v\,\mathbf{Y})\right\rangle = \left\langle g_m^*\left(\mathbf{L}^{-1}\mathbf{Y}\right),\, \mathcal{D}_v\,\mathbf{Y}\right\rangle$$

Using the Cauchy-Schwarz' inequality and lemma 4.3.4

$$\left|\left\langle g_m^*\left(\mathbf{L}^{-1}\mathbf{Y}\right),\, \mathcal{D}_v\,\mathbf{Y}\right\rangle\right| \le \left\|g_m^*\left(\mathbf{L}^{-1}\mathbf{Y}\right)\right\|_{n,2}\|\mathcal{D}_v\,\mathbf{Y}\|_{n,2} \le \left\|g_m^*\left(\mathbf{L}^{-1}\mathbf{Y}\right)\right\|_{n,2}\|\mathbf{Y}\|_{n,2},$$

and since

$$\left\|g_m^*\left(\mathbf{L}^{-1}\mathbf{Y}\right)\right\|_{n,2} \le \|g_m^*\|_{\mathcal{G}_c^\perp}\left\|\mathbf{L}^{-1}\mathbf{Y}\right\|_{n,2} \le \tau_{\max}DS_m\|g^*\|_{\mathcal{G}_c^\perp}\|\mathbf{Y}\|_{n,2},$$

the conclusion follows. □
Note that $\|g^*\|_{\mathcal{G}_c^\perp} = \|g^*\|_{\mathbf{L}_0^2}$ by density of $\mathcal{G}_c^\perp$ in $\mathbf{L}_0^2$, where $\mathbf{L}_0^2$ is the subspace of $\mathbf{L}^2$ of zero mean functions. We show in appendix C how to compute this norm.

We prove a similar theorem in the case of (4.7).

Theorem 4.4.2. *If* W *satisfies (4.12), a sufficient condition for the stability of a homogeneous solution to (4.7) is that the norm* $\|g\|_{\mathcal{G}_c^\perp}$ *of the restriction to* $\mathcal{G}_c^\perp$ *of the compact operator* g *be less than* $(\tau_{\max}DS_m)^{-1}$ *for all* $t \in$ J.

Proof. The proof is similar to that of theorem 4.4.1. We consider $\mathbf{A}_p$ the unique solution to (4.7) with homogeneous input $\mathbf{I}_{\text{ext}}(t)$, initial conditions $\mathbf{A}_p(0) = \mathbf{A}_{p0}$, and consider the initial value problem

$$\begin{cases} \mathbf{A}'(t) &=& \mathcal{P}_{\mathcal{G}_c^\perp}\left(f_a(t, \mathcal{P}_{\mathcal{G}_c^\perp}\mathbf{A} + \mathcal{P}_{\mathcal{G}_c}\mathbf{A}_p)\right) \\ \mathbf{A}(0) &=& \mathbf{A}_0 \end{cases} \tag{4.24}$$

$\mathbf{A} = \mathcal{P}_{\mathcal{G}_c^\perp}\mathbf{A}_p$ is a solution with initial conditions $\mathbf{A}_0 = \mathcal{P}_{\mathcal{G}_c^\perp}\mathbf{A}_{p0}$ since $\mathcal{P}_{\mathcal{G}_c^\perp}\mathbf{A}_p + \mathcal{P}_{\mathcal{G}_c}\mathbf{A}_p = \mathbf{A}_p$. But $\mathbf{A} = 0$ is also a solution with initial conditions $\mathbf{A}_0 = 0$. Indeed $\mathcal{G}_c$ is flow-invariant because of (4.12), that is $f_a(t, \mathcal{G}_c) \subset \mathcal{G}_c$, and hence $\mathcal{P}_{\mathcal{G}_c^\perp}(f_a(t, \mathcal{G}_c)) = 0$. We therefore look for a sufficient condition for the system (4.24) to be absolutely stable at $\mathbf{A} = 0$.

Consider again the functional $V(\mathbf{A}) = \frac{1}{2}\left\langle \mathbf{A},\, \mathbf{L}^{-1}\mathbf{A} \right\rangle$ with time derivative $\frac{dV(\mathbf{A})}{dt} = \left\langle \mathbf{A},\, \mathbf{L}^{-1}\mathbf{A}_t \right\rangle$. We substitute $\mathbf{A}_t$ with its value from (4.24) which, using (4.12), can be rewritten as

$$\mathbf{A}_t =$$
$$\mathcal{P}_{\mathcal{G}_c^\perp}\left(-\mathbf{L}(\mathcal{P}_{\mathcal{G}_c^\perp}\mathbf{A} + \mathcal{P}_{\mathcal{G}_c}\mathbf{A}_p) + \mathbf{S}\left(\int_\Omega \mathbf{W}(\mathbf{r}, \mathbf{r}', t)\, \mathcal{P}_{\mathcal{G}_c^\perp}\mathbf{A}(\mathbf{r}', t)\, d\mathbf{r}' + \overline{\mathbf{W}}(t)\mathcal{P}_{\mathcal{G}_c}\mathbf{A}_p + \mathbf{I}_{\text{ext}}(t) \right) \right)$$

We perform a first-order Taylor expansion with integral remainder of the $\mathbf{S}$ term and introduce the operator h_m (definition 4.3.1):

$$\mathbf{S}\left(\int_\Omega \mathbf{W}(\mathbf{r}, \mathbf{r}', t)\, \mathcal{P}_{\mathcal{G}_c^\perp}\mathbf{A}(\mathbf{r}', t)\, d\mathbf{r}' + \overline{\mathbf{W}}(t)\mathcal{P}_{\mathcal{G}_c}\mathbf{A}_p + \mathbf{I}_{\text{ext}}(t) \right) = \mathbf{S}\left(\overline{\mathbf{W}}(t)\mathcal{P}_{\mathcal{G}_c}\mathbf{A}_p + \mathbf{I}_{\text{ext}}(t) \right) +$$
$$\left(\int_0^1 D\underline{\mathbf{S}}\Big(\overline{\mathbf{W}}(t)\mathcal{P}_{\mathcal{G}_c}\mathbf{A}_p + \mathbf{I}_{\text{ext}}(t) + \zeta \int_\Omega \mathbf{W}(\mathbf{r}, \mathbf{r}', t)\, \mathcal{P}_{\mathcal{G}_c^\perp}\mathbf{A}(\mathbf{r}', t)\, d\mathbf{r}' \Big) d\zeta \right) h_m(\mathcal{P}_{\mathcal{G}_c^\perp}\mathbf{A})(\mathbf{r}, t)$$

Let us define

$$\mathcal{D}_a(\mathbf{r}, t) = \int_0^1 D\underline{\mathbf{S}}\Big(\overline{\mathbf{W}}(t)\mathcal{P}_{\mathcal{G}_c}\mathbf{A}_p + \mathbf{I}_{\text{ext}}(t) + \zeta \int_\Omega \mathbf{W}(\mathbf{r}, \mathbf{r}', t)\, \mathcal{P}_{\mathcal{G}_c^\perp}\mathbf{A}(\mathbf{r}', t)\, d\mathbf{r}' \Big) d\zeta,$$

a diagonal matrix whose diagonal elements are continuous functions with values between 0 and 1. Letting $\mathbf{Y} = \mathcal{P}_{\mathcal{G}_c^\perp}\mathbf{A}$ we write

$$\frac{dV(\mathbf{A})}{dt} = -\langle \mathbf{Y},\, \mathbf{Y} \rangle + \left\langle \mathbf{Y},\, \mathbf{L}^{-1}\mathcal{D}_a\, h_m(\mathbf{Y}) \right\rangle$$

and the conclusion follows from the Cauchy-Schwarz' inequality and lemmas 4.3.4 and 4.3.5

$$\left| \left\langle \mathbf{Y},\, \mathbf{L}^{-1}\mathcal{D}_a\, h_m(\mathbf{Y}) \right\rangle \right| \le \|\mathbf{Y}\|_{n,2}\, \left\| \mathbf{L}^{-1}\mathcal{D}_a\, h_m(\mathbf{Y}) \right\|_{n,2} \le$$
$$\tau_{\max} \|\mathbf{Y}\|_{n,2}\, \|h_m(\mathbf{Y})\|_{n,2} \le \tau_{\max} DS_m \|g\|_{\mathcal{G}_c^\perp}\, \|\mathbf{Y}\|_{n,2}^2$$

□

4.4.2 The convolution case

As $\mathbf{W}$ is translation invariant $\int_\Omega \mathbf{W}(\mathbf{r} - \mathbf{r}', t)\, d\mathbf{r}'$ is in general a function of $\mathbf{r}$, unless Ω has no border. In our framework, this case only occurs as Ω is an interval with periodic conditions and we have the following

Theorem 4.4.3. *A sufficient condition for the stability of a homogeneous solution to (4.6) (resp. (4.7)) is that the eigenvalues of the Hermitian matrices*

$$\widetilde{\mathbf{W}}^*(\mathbf{m}, t)\widetilde{\mathbf{W}}(\mathbf{m}, t)$$

are strictly less than $(\tau_{\max}\, DS_m)^{-2}$ *for all* $\mathbf{m} \neq \mathbf{0} \in \mathbb{Z}^q$ *and all* $t \in \mathrm{J}$. $\widetilde{\mathbf{W}}(\mathbf{m}, t)$ *is the* $\mathbf{m}$*th element of the Fourier series of the* q*-periodic matrix function* $\mathbf{W}(\mathbf{r}, t)$ *with respect to the space variable* $\mathbf{r}$.

The only difference with theorem 4.3.5 is that there are no constraints on the Fourier coefficient $\mathbf{m} = 0$. This is due to the fact that we only “look” at the subspace of $\mathcal{G}$ of functions with zero spatial average.

4.4.3 Complete synchronization

The property of absolute stability of the solution that is characterized in theorems 4.4.1, 4.4.2 and 4.4.3 can be seen as the ability for the neural masses in the continuum to synchronize. By synchronization we mean that the state vectors at all points in the continuum converge to a unique state vector that is a function only of the common input $\mathbf{I}_{\text{ext}}$ and not of the initial states of the neural masses. The state vector is the homogeneous solution of (4.6) and (4.7). This effect is called complete synchronization [91].

4.5 EXTENDING THE THEORY

We have developed our analysis of (4.6) and (4.7) in the Banach space $\mathcal{F}$ of continuous functions of the spatial coordinate r even though we have used a structure of pre-Hilbert space $\mathcal{G}$ on top of it. But there remains the fact that the solutions that we have been discussing are smooth, i.e., continuous with respect to the space variable. It may be interesting to also consider non-smooth solutions, e.g., piecewise continuous solutions that can be discontinuous along curves of Ω. A natural setting, given the fact that we are interested in having a structure of Hilbert space, is $\mathbf{L}^2_n(\Omega)$, the space of square-integrable functions from Ω to $\mathbb{R}^n$, see appendix B. It is a Hilbert space and $\mathcal{G}$ is a dense subspace: $\overline{\mathcal{G}} = \mathbf{L}^2_n(\Omega)$, where $\overline{A}$ indicates the topological closure of the set A.

4.5.1 Existence, uniqueness and stability of a solution

The theory developed in the previous sections can be readily extended to $\mathbf{L}^2_n(\Omega)$: the analysis of the stability of the general and homogeneous solutions has been done using the pre-Hilbert space structure of $\mathcal{G}$ and all the operators that have been shown to be compact in $\mathcal{G}$ are also compact in its closure $\mathbf{L}^2_n(\Omega)$ [30]. The only point that has to be re-worked is the problem of existence and uniqueness of a solution addressed in propositions 4.2.1 and 4.2.2. This allows us to *relax* the rather stringent spatial smoothness hypotheses imposed on the connectivity function $\mathbf{W}$ and the external current $\mathbf{I}_{\text{ext}}$, thereby bringing in more flexibility to the model. We have the following

Proposition 4.5.1. *If the following two hypotheses are satisfied*

1. *The mapping* $\mathbf{W}$ *is in* $C(\mathrm{J}; \mathbf{L}^2_{\mathrm{n\times n}}(\Omega\times\Omega))$,
2. *The external current* $\mathbf{I}_{\text{ext}}$ *is in* $C(\mathrm{J}; \mathbf{L}^2_{\mathrm{n}}(\Omega))$,

then the mappings f_v *and* f_a *are from* $\mathrm{J}\times\mathbf{L}^2_{\mathrm{n}}(\Omega)$ *to* $\mathbf{L}^2_n(\Omega)$, *continuous, and Lipschitz continuous with respect to their second argument, uniformly with respect to the first.*

Proof. Because of the first hypothesis, the fact that $\mathbf{S}(\mathbf{x})$ is in $\mathbf{L}^2_n(\Omega)$ for all $\mathbf{x} \in \mathbf{L}^2_n(\Omega)$, and lemma B.2.2, f_v is well-defined. Let us prove that it is continuous. As in the proof of proposition 4.2.1 we write

$$f_v(t,\mathbf{x}) - f_v(s,\mathbf{y}) = -\mathbf{L}(\mathbf{x}-\mathbf{y}) + \int_\Omega (\mathbf{W}(\cdot,\mathbf{r}',t) - \mathbf{W}(\cdot,\mathbf{r}',s))\mathbf{S}(\mathbf{x}(\mathbf{r}'))\,d\mathbf{r}' + \\ \int_\Omega \mathbf{W}(\cdot,\mathbf{r}',s)(\mathbf{S}(\mathbf{x}(\mathbf{r}')) - \mathbf{S}(\mathbf{y}(\mathbf{r}'))\,d\mathbf{r}' + \mathbf{I}_{\text{ext}}(\cdot,t) - \mathbf{I}_{\text{ext}}(\cdot,s),$$

from which we obtain, using lemma B.2.2

$$\|f_v(t,\mathbf{x}) - f_v(s,\mathbf{y})\|_{n,2} \leq \|\mathbf{L}\|_F \|\mathbf{x}-\mathbf{y}\|_{n,2} + \sqrt{n|\Omega|} S_m \|\mathbf{W}(\cdot,\cdot,t) - \mathbf{W}(\cdot,\cdot,s)\|_F + \\ DS_m \|\mathbf{W}(\cdot,\cdot,s)\|_F \|\mathbf{x}-\mathbf{y}\|_{n,2} + \|\mathbf{I}_{\text{ext}}(\cdot,t) - \mathbf{I}_{\text{ext}}(\cdot,s)\|_{n,2},$$

and the continuity follows from the hypotheses. $\| \ \|_F$ is the Frobenius norm, see appendix B. Note that since $\mathbf{W}$ is continuous on the compact interval J, it is bounded and $\|\mathbf{W}(\cdot,\cdot,t)\|_F \leq w$ for all $t \in$ J for some positive constant w. The Lipschitz continuity with respect to the second argument uniformly with respect to the first one follows from the previous inequality by choosing $s = t$.

The proof for f_a is similar. □

From this proposition we deduce the existence and uniqueness of a solution over a subinterval of $\mathbb{R}$:

Proposition 4.5.2. *Subject to the hypotheses of proposition 4.5.1 for any element* $\mathbf{V}_0$ *of* $\mathbf{L}^2_n(\Omega)$ *there is a unique solution* $\mathbf{V}$*, defined on a subinterval of* J *containing 0 and continuously differentiable, of the abstract initial value problem (4.8) for* $f = f_v$ *and* $f = f_a$ *such that* $\mathbf{V}(0) = \mathbf{V}_0$.

Proof. All conditions of the Picard-Lindelöf theorem on differential equations in Banach spaces (here a Hilbert space) [6, 30] are satisfied, hence the proposition. □

We can also prove that this solution exists for all times, as in proposition 4.2.3:

Proposition 4.5.3. *If the following two hypotheses are satisfied*

1. *The connectivity function* $\mathbf{W}$ *is in* $C(\mathbb{R}; \mathbf{L}^2_{\mathrm{n}\times\mathrm{n}}(\Omega\times\Omega))$,
2. *The external current* $\mathbf{I}_{\text{ext}}$ *is in* $C(\mathbb{R}; \mathbf{L}^2_{\mathrm{n}}(\Omega))$,

then for any function $\mathbf{V}_0$ *in* $\mathbf{L}^2_n(\Omega)$ *there is a unique solution* $\mathbf{V}$*, defined on* $\mathbb{R}$ *and continuously differentiable, of the abstract initial value problem (4.8) for* $f = f_v$ *and* $f = f_a$.

Proof. The proof is similar to the one of proposition 4.2.3. □

The absolute stability of the solution can be studied exactly as in theorems 4.3.1 and 4.3.2. Since $\mathcal{G}$ is dense in $\mathbf{L}^2_n(\Omega)$ we have $\|g\|_{\mathcal{G}} = \|g\|_{\mathbf{L}^2_n(\Omega)}$ and similar relations for all the other operators. We have the following

Theorem 4.5.1. *If the compact operator* g *satisfies the condition of theorem 4.3.1 the solution of the abstract initial value problem (4.8) for* $f = f_v$ *and* $f = f_a$ *is absolutely stable.*

4.5.2 Locally homogeneous solutions

An application of the previous extension is the following. Consider a partition of Ω into P subregions Ω_i, $i = 1, \cdots, P$. We assume that the Ω_is are closed, hence compact, subsets of Ω intersecting along finitely many piecewise regular curves. These curves form a set of 0 Lebesgue measure of Ω. We consider locally homogeneous input current functions

$$\mathbf{I}_{\text{ext}}(\mathbf{r},t) = \sum_{k=1}^{P} \mathbf{1}_{\Omega_k}(\mathbf{r}) \mathbf{I}^k_{\text{ext}}(t), \tag{4.25}$$

where the P functions $\mathbf{I}^k_{\text{ext}}(t)$ are continuous on some closed interval J containing 0. On the border between two adjacent regions the value of $\mathbf{I}_{\text{ext}}(\mathbf{r},t)$ is undefined. Since this set of borders is of 0 measure, the functions defined by (4.25) are in $\mathbf{L}^2_n(\Omega)$ at each time instant.

Existence and uniqueness

We are interested in the existence of solutions to the abstract initial value problem (4.8) that are homogeneous in each subregion Ω_i, $i = 1, \cdots, P$. We call them locally homogeneous solutions.

We assume that the connectivity matrix $\mathbf{W}$ satisfies the following conditions

$$\int_{\Omega_k} \mathbf{W}(\mathbf{r}, \mathbf{r}', t)\, d\mathbf{r}' = \sum_{i=1}^{P} \mathbf{1}_{\Omega_i}(\mathbf{r}) \mathbf{W}_{ik}(t) \quad k = 1, \cdots, P. \tag{4.26}$$

These conditions are analogous to (4.12). A locally homogeneous solution of (4.6) or (4.7) can be written

$$\mathbf{V}(\mathbf{r}, t) = \sum_{i=1}^{P} \mathbf{1}_{\Omega_i}(\mathbf{r}) \mathbf{V}_i(t),$$

where the functions $\mathbf{V}_i$ satisfy the following system of ordinary differential equations

$$\mathbf{V}_i'(t) = -\mathbf{L}\mathbf{V}_i(t) + \sum_{k=1}^{P} \mathbf{W}_{ik}(t) \mathbf{S}(\mathbf{V}_k(t)) + \mathbf{I}_{\text{ext}}^i(t), \tag{4.27}$$

for the voltage-based model and

$$\mathbf{V}_i'(t) = -\mathbf{L}\mathbf{V}_i(t) + \mathbf{S}\left(\sum_{k=1}^{P} \mathbf{W}_{ik}(t) \mathbf{V}_k(t) + \mathbf{I}_{\text{ext}}^i(t) \right), \tag{4.28}$$

for the activity-based model. The conditions for the existence and uniqueness of a locally homogeneous solution are given in the following theorem, analog to theorem 4.2.1:

Theorem 4.5.2. *If the external currents $\mathbf{I}_{\text{ext}}^k(t)$, $k = 1, \cdots, P$ and the connectivity matrices $\mathbf{W}_{ik}(t)$, $i, k = 1, \cdots, P$ are continuous on some closed interval J containing 0, then for all sets of P vectors $\mathbf{U}_0^k, k = 1, \cdots, P$ of $\mathbb{R}^n$, there exists a unique solution $(\mathbf{U}_1(t), \cdots, \mathbf{U}_P(t))$ of (4.27) or (4.28) defined on a subinterval J_0 of J containing 0 such that $\mathbf{U}_k(0) = \mathbf{U}_0^k, k = 1, \cdots, P$.*

Proof. The system (4.27) can be written in the form

$$\mathcal{V}'(t) = -\mathcal{L}\mathcal{V}(t) + \mathcal{W}(t)\mathcal{S}(\mathcal{V}(t)) + \mathcal{I}_{\text{ext}}(t), \tag{4.29}$$

where $\mathcal{V}$ is the nP dimensional vector $\begin{pmatrix} \mathbf{V}_1 \\ \vdots \\ \mathbf{V}_P \end{pmatrix}$, $\mathcal{I}_{\text{ext}} = \begin{pmatrix} \mathbf{I}_{\text{ext}}^1 \\ \vdots \\ \mathbf{I}_{\text{ext}}^P \end{pmatrix}$, $\mathcal{S}(\mathcal{X}) = \begin{pmatrix} \mathbf{S}(\mathbf{X}_1) \\ \vdots \\ \mathbf{S}(\mathbf{X}_P) \end{pmatrix}$, $\mathcal{W}$ is the block matrix $(\mathbf{W}_{ik})_{i,k}$ and $\mathcal{L}$ is the block diagonal matrix whose diagonal elements are all equal to $\mathbf{L}$. Then we are dealing with a classical initial value problem of dimension nP and the proof of existence and uniqueness is similar to the one of theorem 4.2.1. A similar proof can be written in the case of system (4.28). □

Again, if $\mathcal{I}_{\text{ext}}$ and $\mathcal{W}$ are continuous on $\mathbb{R}$, the existence and uniqueness result extends to the whole time line $\mathbb{R}$.

Absolute stability

Having proved the existence and uniqueness of a locally homogeneous solution we consider the problem of characterizing its absolute stability. The method is the same as in section 4.4. We consider the subset, noted $\mathcal{G}_c^P$, of the functions that are constant in the interior $\overset{\circ}{\Omega}_i$ of each region $\Omega_i, i = 1, \cdots, P$ (the interior $\overset{\circ}{A}$ of a subset A is defined as the biggest open subset included in A). We have the following lemma that echoes lemma 4.4.1

Lemma 4.5.1. *$\mathcal{G}_c^P$ is a complete linear subspace of $\mathbf{L}_n^2(\Omega)$. The orthogonal projection operator $\mathcal{P}_{\mathcal{G}_c^P}$ from $\mathbf{L}_n^2(\Omega)$ to $\mathcal{G}_c^P$ is defined by*

$$\mathcal{P}_{\mathcal{G}_c^P}(\mathbf{x})(\mathbf{r}) = \overline{\mathbf{x}}^P = \sum_{k=1}^{P} \mathbf{1}_{\Omega_k}(\mathbf{r}) \frac{1}{|\Omega_k|} \int_{\Omega_k} \mathbf{x}(\mathbf{r}')\, d\mathbf{r}'$$

The orthogonal complement $\mathcal{G}_c^{P\perp}$ of $\mathcal{G}_c^P$ is the subset of functions of $\mathbf{L}_n^2(\Omega)$ that have a zero average in each $\Omega_i, i = 1, \cdots, P$. The orthogonal projection operator $\mathcal{P}_{\mathcal{G}_c^{P\perp}}$ is equal to $\mathrm{Id} - \mathcal{P}_{\mathcal{G}_c^{\mathrm{P}}}$. We also have

$$\mathcal{P}_{\mathcal{G}_c^{P\perp}} \mathbf{M}\mathbf{x} = \mathbf{M}\mathcal{P}_{\mathcal{G}_c^{P\perp}} \mathbf{x} \quad \forall\, \mathbf{x} \in \mathbf{L}_n^2(\Omega),\ \mathbf{M} \in \mathcal{M}_{n\times n} \tag{4.30}$$

Proof. The proof of this lemma is similar to the one of lemma 4.4.1. □

We have the following theorem, corresponding to theorems 4.4.1 and 4.4.2.

Theorem 4.5.3. *If* W *satisfies (4.26), a sufficient condition for the absolute stability of a locally homogeneous solution to (4.6) (respectively (4.7)) is that the norm $\|g^*\|_{\mathcal{G}_c^{P\perp}}$ (respectively $\|g\|_{\mathcal{G}_c^{P\perp}}$) of the restriction to $\mathcal{G}_c^{P\perp}$ of the compact operator g^* (respectively g) be less than $(\tau_{\max} DS_m)^{-1}$ for all $t \in$ J.*

Proof. The proof strictly follows the lines of the ones of theorems 4.4.1 and 4.4.2. □

Note that the condition on the operator norm in theorems 4.3.1 and 4.3.2 is stronger than the one of theorems 4.4.1 and 4.4.2 which is in turn stronger than the one of theorem 4.5.3 therefore we have the following

Proposition 4.5.4. *If the operator g satisfies the condition of theorem 4.3.1 or if $g*$ (respectively g) satisfies the condition of theorem 4.4.1 (respectively of theorem 4.4.2), then for every partition of Ω, corresponding locally homogeneous current, and* **W** *satisfying (4.26), the locally homogeneous solution of (4.6) (respectively (4.7)) is absolutely stable.*

Proof. Since all spaces are contained in $\mathbf{L}_n^2(\Omega)$ the first part of the proposition is proved. Next it is clear that $\mathcal{G}_c \subset \mathcal{G}_c^P$, therefore $\mathcal{G}_c^{P\perp} \subset \mathcal{G}_c^{\perp}$ and $\|g^*\|_{\mathcal{G}_c^{P\perp}} \leq \|g^*\|_{\mathcal{G}_c^{\perp}}$ (respectively $\|g\|_{\mathcal{G}_c^{P\perp}} \leq \|g\|_{\mathcal{G}_c^{\perp}}$). □

Condition (4.26) depends on the partition of Ω. It is therefore unrealistic since one expects this partition to change over time with the external currents. In this context it is interesting to define the notion of *pseudo locally homogeneous* solution.

Definition 4.5.1. *A pseudo locally homogeneous solution of equation (4.6) (respectively (4.7)) corresponds to a locally homogeneous input current (verifying (4.25)) when the connectivity function satisfies the condition of proposition 4.5.3 (existence and uniqueness of a solution) but not necessarily conditions (4.26).*

How much a pseudo locally homogeneous solution differs from a locally homogeneous solution obviously depends upon how poorly the connectivity function satisfies the conditions (4.26). But since pseudo locally homogeneous solutions are solutions, they enjoy the following property.

Proposition 4.5.5. *If the operator g satisfies the condition of theorem 4.3.1, the unique pseudo locally homogeneous solution of equations (4.6) (respectively of equations (4.7)) corresponding to a locally homogeneous input current, is absolutely stable.*

A numerical example of pseudo locally homogeneous solution is given in section 4.6 (figures 4.16 and 4.17).

Complete local synchronization

The property of absolute stability of the solution that is characterized in theorem 4.5.3 can be seen as the ability for the neural masses in the continuum to synchronize locally within each region Ω_i, $i = 1, \ldots, P$. By local synchronization we mean that the state vectors at all points of each region Ω_i converge to a unique state vector that is a function only of the common input $\mathbf{I}^i_{\text{ext}}$ within Ω_i and not of the initial states of the neural masses. The state vector is the locally homogeneous solution of (4.6) and (4.7). This effect is called complete local synchronization.

4.5.3 Higher order PSPs

We now show how the theory developed so far can be extended to accomodate more complicated time variations of the postsynaptic potentials (PSPs) than the decaying exponential that we adopted so far with the advantage that we only had to deal with a first order differential equation. We only show how to proceed in the case of a second order differential equation, going to a higher order does not bring in new difficulties. We also treat only the case of the voltage-based model, the case of the activity-based model being similar.

We therefore assume that, with the notations of section 4.1.1, we have $PSP_i(t) = te^{-t/\tau_i}Y(t)$ or equivalently that

$$\frac{d^2 PSP_i(t)}{dt^2} + \frac{2}{\tau_i}\frac{dPSP_i(t)}{dt} + \frac{1}{\tau_i^2} = \delta(t)$$

The analog of equation (4.4) being

$$\mathbf{V}'' = -2\mathbf{L}\mathbf{V}' - \mathbf{L}^2\mathbf{V} + \mathbf{W}\,\mathbf{S}(\mathbf{V}) + \mathbf{I}_{\text{ext}}. \tag{4.31}$$

We rewrite this as a first order system of differential equation by introducing the vector $\boldsymbol{\mathcal{V}} = \begin{bmatrix} \mathbf{V} \\ \mathbf{V}' \end{bmatrix}$:

$$\boldsymbol{\mathcal{V}}' = -\boldsymbol{\mathcal{L}}\boldsymbol{\mathcal{V}} + \begin{bmatrix} \mathbf{0} \\ \mathbf{W}\,\mathbf{S}(\mathbf{V}) \end{bmatrix} + \begin{bmatrix} \mathbf{0} \\ \mathbf{I}_{\text{ext}} \end{bmatrix}, \quad \boldsymbol{\mathcal{L}} = \begin{bmatrix} \mathbf{0} & -\mathrm{Id} \\ \mathbf{L}^2 & 2\mathbf{L} \end{bmatrix}$$

The dynamic system $\boldsymbol{\mathcal{V}}' = -\boldsymbol{\mathcal{L}}\boldsymbol{\mathcal{V}}$ is globally asymptotically stable since all the eigenvalues of the $2n \times 2n$ matrix $\boldsymbol{\mathcal{L}}$ have a strictly positive real part, as can be easily verified[3]. This has the following consequence [75, 102] that is used below and that we cite without proof.

---

[3] In fact the eigenvalues of $\boldsymbol{\mathcal{L}}$ are the ones of $\mathbf{L}$, $1/\tau_i$s, with multiplicity 2.

Theorem 4.5.4 (Lyapunov). *The symmetric positive definite matrix*

$$\boldsymbol{\mathcal{M}} = \int_0^\infty e^{-\boldsymbol{\mathcal{L}}^T t} e^{-\boldsymbol{\mathcal{L}} t}\, dt$$

satisfies

$$\boldsymbol{\mathcal{M}}\boldsymbol{\mathcal{L}} + \boldsymbol{\mathcal{L}}^T \boldsymbol{\mathcal{M}} = \mathrm{Id}_{2n}, \tag{4.32}$$

where Id_{2n} *is the* $2n \times 2n$ *identity matrix.*

The analog of equation (4.6) is readily found to be

$$\boldsymbol{\mathcal{V}}_t(\mathbf{r}, t) = -\boldsymbol{\mathcal{L}}\boldsymbol{\mathcal{V}}(\mathbf{r}, t) + \left[\begin{array}{c} \mathbf{0} \\ \int_\Omega \mathbf{W}(\mathbf{r}, \mathbf{r}', t)\mathbf{S}(\mathbf{V}(\mathbf{r}', t))\, d\mathbf{r}' \end{array} \right] + \left[\begin{array}{c} \mathbf{0} \\ \mathbf{I}_{\mathrm{ext}} \end{array} \right] \tag{4.33}$$

The state is now $2n$-dimensional, the corresponding functional space is $\mathbf{L}^2_{2n}(\Omega)$ and the operator g is defined on the subspace $\mathbf{L}^2_n(\Omega)$ of $\mathbf{L}^2_{2n}(\Omega)$. It keeps all its previous properties. All proofs of the existence and uniqueness of a solution to (4.6) extend *mutatis mutandis* to this new setting.

Let us now examine the problem of the absolute stability of the solution, the analog of theorem 4.3.1.

Theorem 4.5.5. *A sufficient condition for the solution of (4.6) to be absolutely stable is*

$$2\, \lambda_{\max}\, DS_m\, \|g\|_{\mathbf{L}^2_n(\Omega)} < 1,$$

where $\lambda_{\max}$ *is the largest eigenvalue of the* $2n \times 2n$ *matrix* $\boldsymbol{\mathcal{M}}$ *defined in theorem 4.5.4.*

Proof. We consider the equation

$$\boldsymbol{\mathcal{V}}_t(\mathbf{r}, t) = -\boldsymbol{\mathcal{L}}\boldsymbol{\mathcal{V}}(\mathbf{r}, t) + \left[\begin{array}{c} \mathbf{0} \\ \int_\Omega \mathbf{W}_{cm}(\mathbf{r}, \mathbf{r}', t)\underline{\mathbf{S}}(\mathbf{V}(\mathbf{r}', t))\, d\mathbf{r}' \end{array} \right] + \left[\begin{array}{c} \mathbf{0} \\ \mathbf{I}_{\mathrm{ext}} \end{array} \right],$$

where $\mathbf{V}$ is the vector composed of the first n components of vector $\boldsymbol{\mathcal{V}}$ (the same convention will be used in the following for subvectors of $\boldsymbol{\mathcal{U}}$ and $\boldsymbol{\mathcal{X}}$). Let $\boldsymbol{\mathcal{U}}$ be its unique solution with initial condition $\boldsymbol{\mathcal{U}}(0) = \boldsymbol{\mathcal{U}}_0$, an element of $\mathbf{L}^2_{2n}(\Omega)$. Let also $\boldsymbol{\mathcal{V}}$ be the unique solution of the same equation with different initial conditions $\boldsymbol{\mathcal{V}}(0) = \boldsymbol{\mathcal{V}}_0$, another element of $\mathbf{L}^2_{2n}(\Omega)$. We introduce the new function $\boldsymbol{\mathcal{X}} = \boldsymbol{\mathcal{V}} - \boldsymbol{\mathcal{U}}$ which satisfies

$$\begin{aligned} \boldsymbol{\mathcal{X}}_t(\mathbf{r}, t) = -\boldsymbol{\mathcal{L}}\boldsymbol{\mathcal{X}}(\mathbf{r}, t) + \left[\begin{array}{c} \mathbf{0} \\ \int_\Omega \mathbf{W}_{cm}(\mathbf{r}, \mathbf{r}', t)\, \mathbf{H}(\mathbf{X}, \mathbf{U})(\mathbf{r}', t)\, d\mathbf{r}' \end{array} \right] = \\ -\boldsymbol{\mathcal{L}}\boldsymbol{\mathcal{X}}(\mathbf{r}, t) + \left[\begin{array}{c} \mathbf{0} \\ g_m(\mathbf{H}(\mathbf{X}, \mathbf{U}))(\mathbf{r}, t) \end{array} \right] \end{aligned} \tag{4.34}$$

where the vector $\mathbf{H}(\mathbf{X}, \mathbf{U})$ is given by $\mathbf{H}(\mathbf{X}, \mathbf{U})(\mathbf{r}, t) = \underline{\mathbf{S}}(\mathbf{V}(\mathbf{r}, t)) - \underline{\mathbf{S}}(\mathbf{U}(\mathbf{r}, t)) = \underline{\mathbf{S}}(\mathbf{X}(\mathbf{r}, t) + \mathbf{U}(\mathbf{r}, t)) - \underline{\mathbf{S}}(\mathbf{U}(\mathbf{r}, t))$. Consider now the functional

$$V(\boldsymbol{\mathcal{X}}) = \frac{1}{2} \langle\, \boldsymbol{\mathcal{X}},\, \boldsymbol{\mathcal{M}}\boldsymbol{\mathcal{X}}\, \rangle,$$

where the symmetric positive definite matrix $\boldsymbol{\mathcal{M}}$ can be seen as defining a metric on the state space. Its time derivative is $\langle\, \boldsymbol{\mathcal{X}},\, \boldsymbol{\mathcal{M}}\boldsymbol{\mathcal{X}}_t\, \rangle$. We replace $\boldsymbol{\mathcal{X}}_t$ by its value from (4.34) in this expression to obtain

$$\frac{dV(\boldsymbol{\mathcal{X}})}{dt} = -\frac{1}{2} \langle\, \boldsymbol{\mathcal{X}},\, (\boldsymbol{\mathcal{L}}^T\boldsymbol{\mathcal{M}} + \boldsymbol{\mathcal{M}}\boldsymbol{\mathcal{L}})\boldsymbol{\mathcal{X}}\, \rangle + \left\langle \boldsymbol{\mathcal{X}},\, \boldsymbol{\mathcal{M}} \left[\begin{array}{c} \mathbf{0} \\ g_m(\mathbf{H}(\mathbf{X}, \mathbf{U})) \end{array} \right] \right\rangle$$

Using the property (4.32) of $\boldsymbol{\mathcal{M}}$ we obtain

$$\frac{dV(\boldsymbol{\mathcal{X}})}{dt} = -\frac{1}{2}\left\langle \boldsymbol{\mathcal{X}},\, \boldsymbol{\mathcal{X}} \right\rangle + \left\langle \boldsymbol{\mathcal{X}},\, \boldsymbol{\mathcal{M}} \begin{bmatrix} \mathbf{0} \\ g_m(\mathbf{H}(\mathbf{X},\mathbf{U})) \end{bmatrix} \right\rangle$$

We consider the second term in the righthand side of this equation. Since $\boldsymbol{\mathcal{M}}$ is symmetric

$$\begin{aligned} \left|\left\langle \boldsymbol{\mathcal{X}},\, \boldsymbol{\mathcal{M}} \begin{bmatrix} \mathbf{0} \\ g_m(\mathbf{H}(\mathbf{X},\mathbf{U})) \end{bmatrix} \right\rangle\right| &= \left|\left\langle \boldsymbol{\mathcal{M}}\boldsymbol{\mathcal{X}},\, \begin{bmatrix} \mathbf{0} \\ g_m(\mathbf{H}(\mathbf{X},\mathbf{U})) \end{bmatrix} \right\rangle\right| \\ &\le \|\boldsymbol{\mathcal{M}}\boldsymbol{\mathcal{X}}\|_{2n,2}\, \|g_m(\mathbf{H}(\mathbf{X},\mathbf{U}))\|_{n,2} \le \lambda_{\max}\|\boldsymbol{\mathcal{X}}\|_{2n,2}\, \|g_m(\mathbf{H}(\mathbf{X},\mathbf{U}))\|_{n,2} \\ &\le \lambda_{\max}\, \|\boldsymbol{\mathcal{X}}\|_{2n,2}\, \|g_m\|_{\mathbf{L}^2_n} \|\mathbf{H}(\mathbf{X},\mathbf{U})\|_{n,2} \end{aligned} \tag{4.35}$$

The inequality $\|\boldsymbol{\mathcal{M}}\boldsymbol{\mathcal{X}}\|_{2n,2} \le \lambda_{\max}\|\boldsymbol{\mathcal{X}}\|_{2n,2}$ is obtained using the spectral properties of the symmetric positive definite matrix $\boldsymbol{\mathcal{M}}$ and lemma 4.3.4.
Using the idea in the proof of lemma 4.2.1, we write $\mathbf{H}(\mathbf{X},\mathbf{U}) = \mathcal{D}_m\mathbf{X}$, where $\mathcal{D}_m$ is a diagonal matrix whose diagonal elements are continuous functions with values between 0 and 1. Hence, because of lemma 4.3.4

$$\|\mathbf{H}(\mathbf{X},\mathbf{U})\|_{n,2} = \|\mathcal{D}_m\mathbf{X}\|_{n,2} \le \|\mathbf{X}\|_{n,2} \le \|\boldsymbol{\mathcal{X}}\|_{2n,2}$$

We use this result and lemma 4.3.5 in (4.35) to obtain

$$\left|\left\langle \boldsymbol{\mathcal{X}},\, \boldsymbol{\mathcal{M}} \begin{bmatrix} \mathbf{0} \\ g_m(\mathbf{H}(\mathbf{X},\mathbf{U})) \end{bmatrix} \right\rangle\right| \le \lambda_{\max}\, DS_m\, \|g\|_{\mathbf{L}^2_n}\, \|\boldsymbol{\mathcal{X}}\|^2_{2n,2},$$

and the conclusion follows. □
All other theorems in sections 4.3, 4.4, 4.5 and in this section can be similarly extended to this more general setting. Complements on $\boldsymbol{\mathcal{M}}$ and $\lambda_{\max}$ can be found in appendix C.

4.6 NUMERICAL EXAMPLES

We consider two ($n = 2$) one-dimensional ($q = 1$) populations of neurons, population 1 being excitatory and population 2 inhibitory. The set Ω is the closed interval $[0, 1]$. We note x the spatial variable and f the spatial frequency variable. We consider Gaussian functions, noted $G_{ij}(x), i, j = 1, 2$, from which we define the connectivity functions. Hence we have $G_{ij} = \mathcal{G}(0, \sigma_{ij})$. We consider three cases. In the first case, section 4.6.1, we assume that the connectivity matrix is translation invariant (see sections 4.3.2 and 4.4.2). In the second case, section 4.6.2, we relax this assumption and study the stability of the homogeneous solutions. The third case, finally, section 4.6.3, covers the case of the locally homogeneous solutions and their stability. In this section we have $S_1(x) = S_2(x) = 1/(1 + e^{-x})$. Therefore

$$D\mathbf{S}_m = \begin{bmatrix} 0 & \frac{1}{4} \\ \frac{1}{4} & 0 \end{bmatrix},$$

hence $DS_m = 1/4$. We also choose $\tau_1 = \tau_2 = 4$, therefore $\tau_{\max} = 4$, and the product $DS_m\, \tau_{\max}$ is equal to 1.

4.6.1 The convolution case

We define $W_{ij}(x, x') = \pm\alpha_{ij}\, G_{ij}(x - x')$, where the α_{ij}s are positive weights and the sign determines whether population j excites (+) or inhibits (−) population i. As explained in section 4.3.2, $\mathbf{W}(\mathbf{r})$ is defined on the closed interval $\widehat{\Omega} = [-1, 1]$. For simplicity we use the approach described in section 4.3.2 and approximate the Fourier transform of $\mathbf{1}_{\widehat{\Omega}}(x)\mathbf{W}(x)$ by that of $\mathbf{W}(x)$ for which we have an analytical formula. This approximation is good as long as the σ_{ij}s are small with respect to 1.

The connectivity functions and their Fourier transforms are then given by

$$W_{ij}(x) = \pm\frac{\alpha_{ij}}{\sqrt{2\pi\sigma_{ij}^2}} e^{-\dfrac{x^2}{2\sigma_{ij}^2}} \quad \widetilde{W}_{ij}(f) = \pm\alpha_{ij} e^{-2\pi^2 f^2 \sigma_{ij}^2}$$

The matrices $\mathbf{W}(x)$ and $\widetilde{\mathbf{W}}(f)$ can be written

$$\mathbf{W}(x) = \begin{bmatrix} \dfrac{\alpha_{11}}{\sqrt{2\pi\sigma_{11}^2}} e^{-\dfrac{x^2}{2\sigma_{11}^2}} & -\dfrac{\alpha_{12}}{\sqrt{2\pi\sigma_{12}^2}} e^{-\dfrac{x^2}{2\sigma_{12}^2}} \\ \dfrac{\alpha_{21}}{\sqrt{2\pi\sigma_{21}^2}} e^{-\dfrac{x^2}{2\sigma_{21}^2}} & -\dfrac{\alpha_{22}}{\sqrt{2\pi\sigma_{22}^2}} e^{-\dfrac{x^2}{2\sigma_{22}^2}} \end{bmatrix}$$

$$\widetilde{\mathbf{W}}(f) = \begin{bmatrix} \alpha_{11} e^{-2\pi^2 f^2 \sigma_{11}^2} & -\alpha_{12} e^{-2\pi^2 f^2 \sigma_{12}^2} \\ \alpha_{21} e^{-2\pi^2 f^2 \sigma_{21}^2} & -\alpha_{22} e^{-2\pi^2 f^2 \sigma_{22}^2} \end{bmatrix}$$

Therefore we have, with the notations of theorem 4.3.3

$$\widetilde{\mathbf{W}}^*(f)\widetilde{\mathbf{W}}(f) \overset{def}{=} \mathbf{X}(f) = \begin{bmatrix} A & C \\ C & B \end{bmatrix}.$$

It can be easily verified that

$$A = \tau_1 \left(\alpha_{11}^2 \tau_1 e^{-4\pi^2 \sigma_{11}^2 f^2} + \alpha_{21}^2 \tau_2 e^{-4\pi^2 \sigma_{21}^2 f^2} \right)$$

$$B = \tau_2 \left(\alpha_{22}^2 \tau_2 e^{-4\pi^2 \sigma_{22}^2 f^2} + \alpha_{12}^2 \tau_1 e^{-4\pi^2 \sigma_{12}^2 f^2} \right),$$

and

$$C = -\sqrt{\tau_1\tau_2} \left(\alpha_{21}\alpha_{22}\tau_2 e^{-2\pi^2(\sigma_{21}^2 + \sigma_{22}^2) f^2} + \alpha_{12}\alpha_{11}\tau_1 e^{-2\pi^2(\sigma_{12}^2 + \sigma_{11}^2) f^2} \right)$$

By construction the eigenvalues of the matrix $\mathbf{X}$ are positive (it is Hermitian), the largest one, $\lambda_{\max}$, being given by

$$\lambda_{\max} = \frac{1}{2}\left(A + B + \sqrt{(A - B)^2 + 4C^2} \right)$$

Introducing the parameters $A_1 = (\tau_1\alpha_{11})^2$, $A_2 = (\tau_2\alpha_{22})^2$, $r = \tau_1/\tau_2$, $x_1 = \alpha_{21}/\alpha_{11}$, $x_2 = \alpha_{12}/\alpha_{22}$ we can rewrite A, B and C as follows

$$A = A_1 \left(e^{-4\pi^2 \sigma_{11}^2 f^2} + \frac{x_1^2}{r} e^{-4\pi^2 \sigma_{21}^2 f^2} \right) \quad B = A_2 \left(e^{-4\pi^2 \sigma_{22}^2 f^2} + r x_2^2 e^{-4\pi^2 \sigma_{12}^2 f^2} \right),$$

and

$$C = -\sqrt{A_1 A_2}\left(\frac{x_1}{\sqrt{r}} e^{-2\pi^2(\sigma_{21}^2 + \sigma_{22}^2)f^2} + x_2\sqrt{r} e^{-2\pi^2(\sigma_{12}^2 + \sigma_{11}^2)f^2}\right)$$

The necessary and sufficient condition that the two eigenvalues are less than 1 for all f is therefore $\lambda_{\max} < 1$ or

$$c(f) \overset{def}{=} 2 - A - B - \sqrt{(A-B)^2 + 4C^2} > 0 \quad \forall f \tag{4.36}$$

The function $c(f)$ depends on the spatial frequency f and the nine parameters A_1, A_2, x_1, x_2, r, and $\boldsymbol{\sigma}$, the 2×2 matrix σ_{ij}, $i, j = 1, 2$.

We have solved equation (4.6) on $\Omega = [0, 1]$. We have sampled the interval with 100 points corresponding to 100 neural masses. The input $\mathbf{I}_{\text{ext}}$ is equal to $[W_1(t), W_2(t)]^T$, where where the $W_i(t)$s, $i = 1, 2$ are realizations of independent standard Brownian/Wiener processes shown in figure 4.1. We know that the solution is not homogeneous because $\mathbf{W}$ is translation invariant. This is illustrated in figure 4.2. The initial conditions are homogeneous and equal to $(0, 0)$ for all neural masses state vectors $\mathbf{V}$.

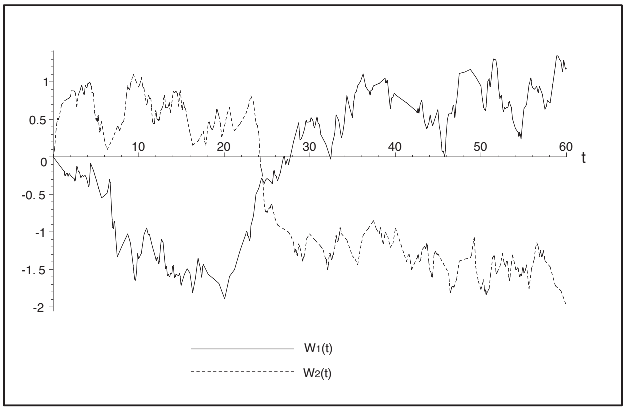

Figure 4.1: *The two coordinates of the input* $\mathbf{I}_{\text{ext}}(t)$ *are realizations of independent standard Brownian / Wiener processes. Time runs along the horizontal axis.*

Absolute stability of the solution

Let us now study the absolute stability of the solutions. According to theorem 4.3.3 and the previous analysis, a sufficient condition for absolute stability is that $c(f) > 0$ for all frequencies f. As shown in figure 4.3, the following choice of the parameters $\boldsymbol{\alpha}$ and $\boldsymbol{\sigma}$ produces a curve $c(f)$ that is positive for all frequencies.

$$\boldsymbol{\alpha} = \begin{bmatrix} 2 & 1.414 \\ 1.414 & 2 \end{bmatrix} \quad \boldsymbol{\sigma} = \begin{bmatrix} 1 & 0.1 \\ 0.1 & 1 \end{bmatrix}$$

We can check that this is indeed the case in figure 4.4 which shows the absolute stability of the solution at the point of coordinate 0.5 of the interval $[0, 1]$.

Loss of absolute stability

The following choice of the parameters $\boldsymbol{\alpha}$ and $\boldsymbol{\sigma}$ produces a curve $c(f)$ that is not positive for all frequencies, see figure 4.5.

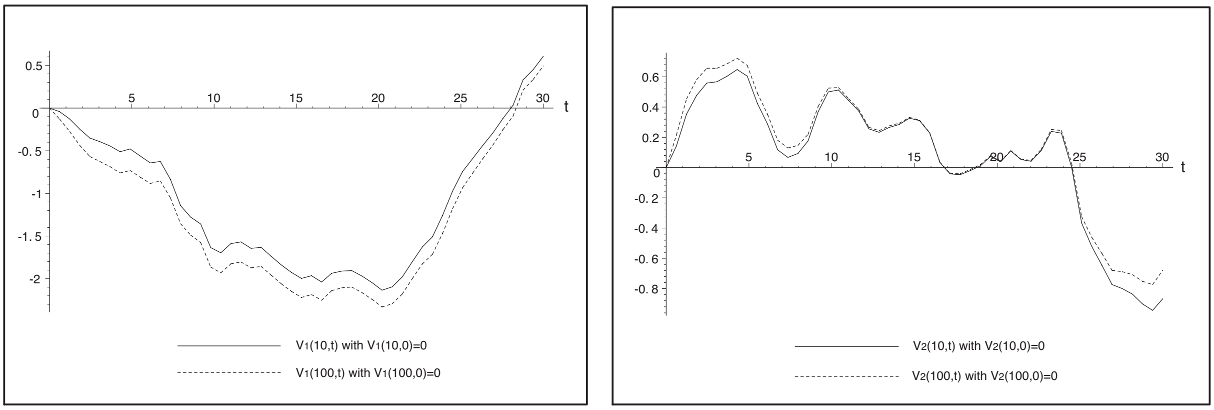

Figure 4.2: *An illustration of the fact that when the connectivity matrix is translation invariant there does not exist in general a homogeneous solution: the state vectors of different neural masses follow different trajectories even when the input and the initial condition are homogeneous (independent of the location x). Left side graph: the time variation of the first coordinate of the solution at points of coordinates* 0.1 *(continuous line) and 1 (dotted line) of the interval* $[0, 1]$. *Right side graph: same for the second coordinate. The initial condition is 0 in both cases.*

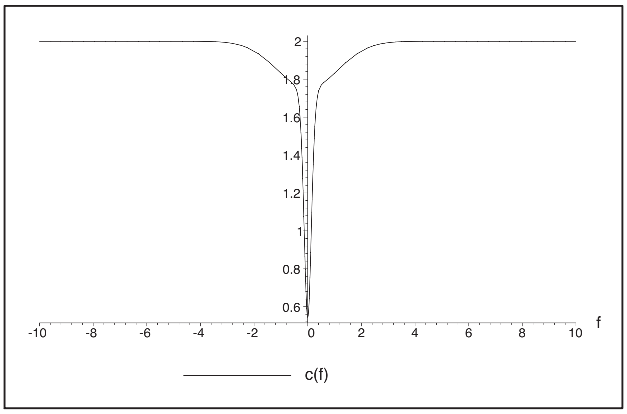

Figure 4.3: *The function* $c(f)$ *defined in (4.36) is positive for all spatial frequencies* f*: the system is absolutely stable.*

$$\boldsymbol{\alpha} = \begin{bmatrix} 565.7 & 565.7 \\ 565.7 & 565.7 \end{bmatrix} \quad \boldsymbol{\sigma} = \begin{bmatrix} 0.01 & 0.01 \\ 0.1 & 0.1 \end{bmatrix}$$

Therefore absolute stability is not guaranteed. We show in figure 4.6 that this is indeed the case.

4.6.2 Homogeneous solutions

In the previous case the translation invariance of the connectivity matrix forbids the existence of homogeneous solutions. We can obtain a connectivity matrix satisfying condition (4.12) by defining

$$W_{ij}(x, x') = \pm\alpha\alpha_{ij} \frac{G_{ij}(x - x')}{\int_0^1 G_{ij}(x - y)\, dy} \quad i, j = 1, 2,$$

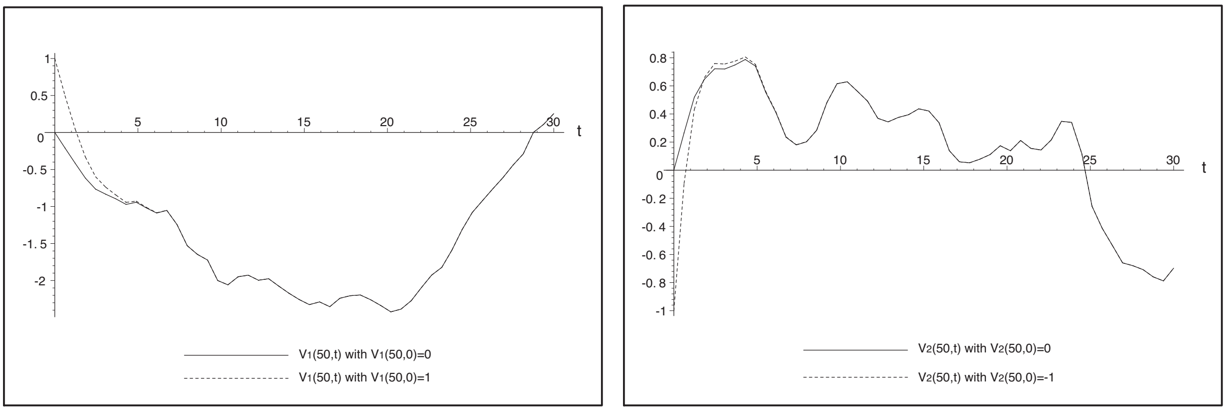

Figure 4.4: *An illustration of the absolute stability of the solution: independently of the choice of the initial condition, the trajectories of the state vector converge to a single trajectory. Results are shown for the neural mass of spatial coordinate* 0.5. *Left: the first coordinate of the state vector. Right: the second coordinate. Initial condition* $(0,0)$, *continuous curves. Initial condition* $(1,-1)$, *dotted line.*

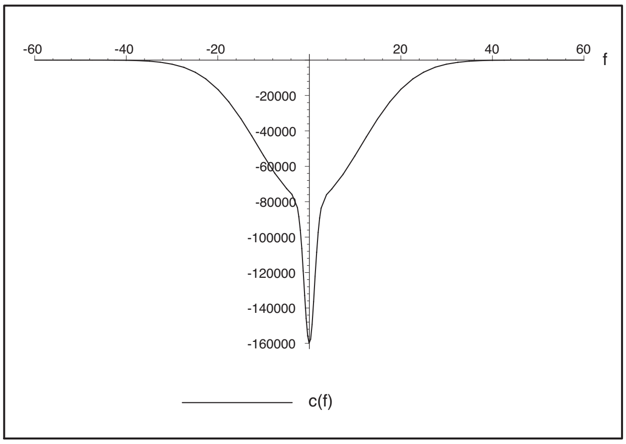

Figure 4.5: *The function* $c(f)$ *defined in (4.36) is not positive for all spatial frequencies* f*: the system may lose its absolute stability.*

where α and the α_{ij}s are connectivity weights. These functions are well defined since the denominator is never equal to 0 and the resulting connectivity matrix is in $\mathbf{L}^2_{2\times 2}([0,1]\times[0,1])$. It is shown in figure 4.7. The values of the parameters are given in (4.37). Proposition 4.5.3 guarantees the existence and uniqueness of a homogeneous solution for an initial condition in $\mathbf{L}^2_2(\Omega)$. According to theorem 4.4.1 and our choice for the values of $\tau_{\max}$ and DS_m, a sufficient condition for this solution to be absolutely stable is that $\|g*\|_{\mathcal{G}_c^\perp} < 1$.

Absolute stability

The following values of the parameters

$$\boldsymbol{\alpha} = \begin{bmatrix} 5.20 & 5.20 \\ 2.09 & 2.09 \end{bmatrix} \quad \boldsymbol{\sigma} = \begin{bmatrix} 0.1 & 0.1 \\ 1 & 1 \end{bmatrix} \quad \tau_1 = \tau_2 = 1 \quad \alpha = 1/20 \tag{4.37}$$

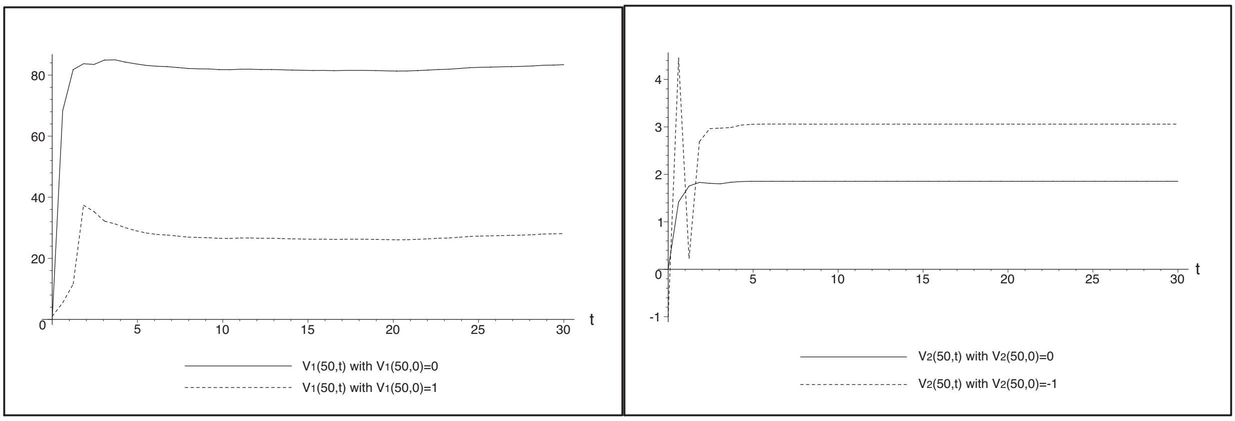

Figure 4.6: *An illustration of the lack of absolute stability of the solution: different initial conditions result in different trajectories of the state vectors. Results are shown for the neural mass of spatial coordinate* 0.5. *Left: the first coordinate of the state vector. Right: the second coordinate. Initial condition* $(0, 0)$*, continuous curves. Initial condition* $(1, -1)$*, dotted curves.*

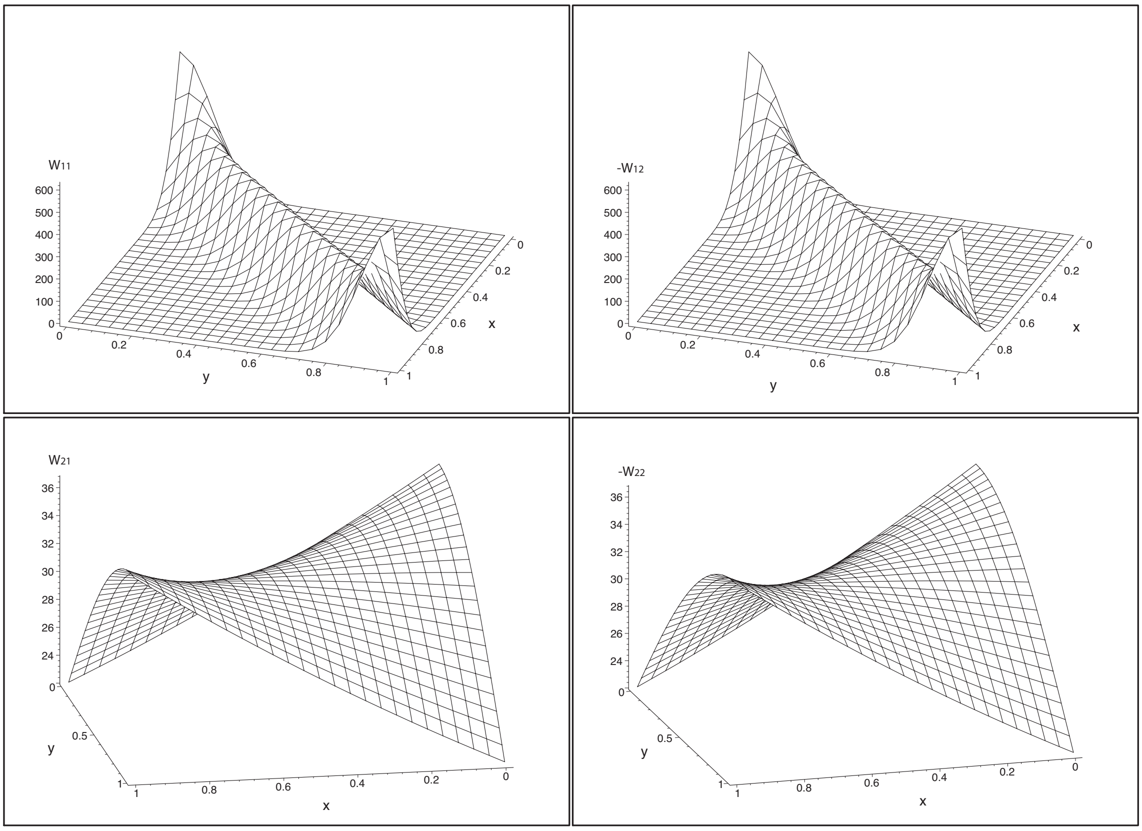

Figure 4.7: *The four elements of the matrix* $\mathbf{W}(x, y)$ *in the homogeneous case. Upper left:* $W_{11}(x, y)$*. Upper right:* $-W_{12}(x, y)$*. Lower left:* $W_{21}(x, y)$*. Lower right:* $-W_{22}(x, y)$*.*

yield $\|g^*\|_{\mathcal{G}_c^\perp} \simeq 0.01$, hence the homogeneous solutions are absolutely stable. All operator norms have been computed using the method described in appendix C.

The initial conditions are drawn randomly and independently from the uniform distribution on $[-2, 2]$. The input $\mathbf{I}_{\text{ext}}(t)$ is equal to $[W_1(t), W_2(t)]^T$, where the $W_i(t)$s,

$i = 1, 2$ are realizations of independent standard Brownian/Wiener processes shown in figure 4.1.

We show in figure 4.8 the complete synchronization of four (numbers 10, 36, 63 and 90) of the hundred neural masses that results from the absolute stability of the homogeneous solution.

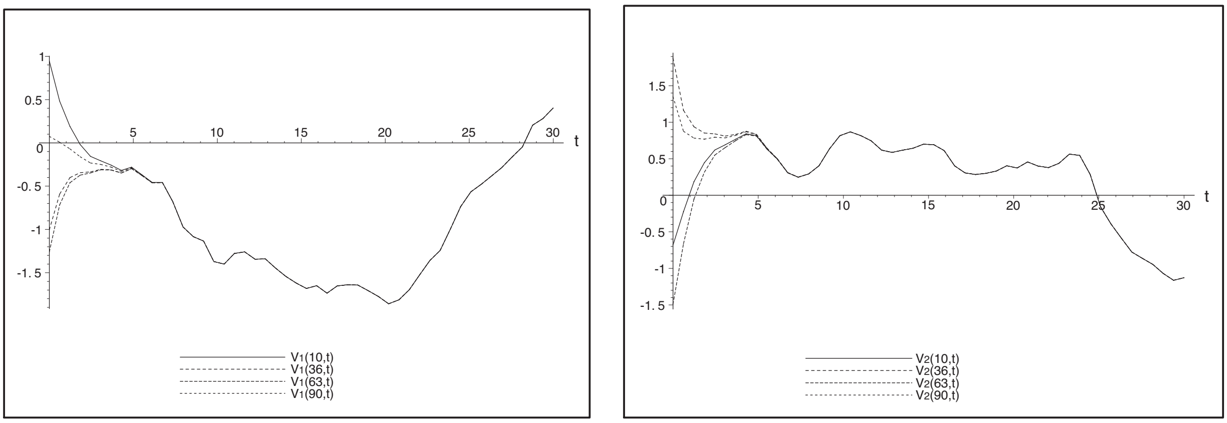

Figure 4.8: *The absolute stability of the homogeneous solution results in the complete synchronization of the neural masses. This is shown for four out of the hundred (coordinates 0.1, 0.36, 0.63 and 0.9). The input is shown in figure 4.1. The initial conditions are drawn independently from the uniform distribution on* $[-2, 2]$. *Left: The first components of the four state vectors. Right: the second components.*

Loss of absolute stability

If we increase the value of α it has the effect of increasing $\|g^*\|_{\mathcal{G}_c^\perp}$. The sufficient condition will eventually not be satisfied and we may lose the absolute stability of the homogeneous solution and hence the complete synchronization of the solution. Such a case is shown in figure 4.9 for $\alpha = 15$ corresponding to an operator norm $\|g^*\|_{\mathcal{G}_c^\perp} \simeq 2.62$.

4.6.3 Locally homogeneous solutions

We partition $\Omega = [0, 1]$ into $\Omega_1 = [0, 1/2[$ and $\Omega_2 = [1/2, 1]$, hence with the notations of section 4.5.2, $P = 2$. We can obtain a connectivity matrix satisfying condition (4.26) by defining

$$W_{ij}(x, x') = \begin{cases} \pm\alpha\alpha_{ij}(x, x') \dfrac{G_{ij}(x - x')}{\displaystyle\int_0^{1/2} G_{ij}(x - y)\, dy}, \; x' \in \Omega_1 \\ \pm\alpha\alpha_{ij}(x, x') \dfrac{G_{ij}(x - x')}{\displaystyle\int_{1/2}^{1} G_{ij}(x - y)\, dy}, \; x' \in \Omega_2 \end{cases},$$

with $\alpha_{ij}(x, x') = \alpha_{ij}^{kl}, \; x \in \Omega_k, \; x' \in \Omega_l, \; k, l = 1, 2.$

The resulting connectivity matrix is in $\mathbf{L}^2_{2\times 2}([0, 1] \times [0, 1])$. It is shown in figure 4.10. The input $\mathbf{I}_{\text{ext}}(t)$ is equal to $[W_1(t), W_2(t)]^T$ in Ω_1 and to $[W_3(t), W_4(t)]^T$ in Ω_2, where the $W_i(t)$s, $i = 1, \cdots, 4$ are realizations of independent standard Brownian/Wiener

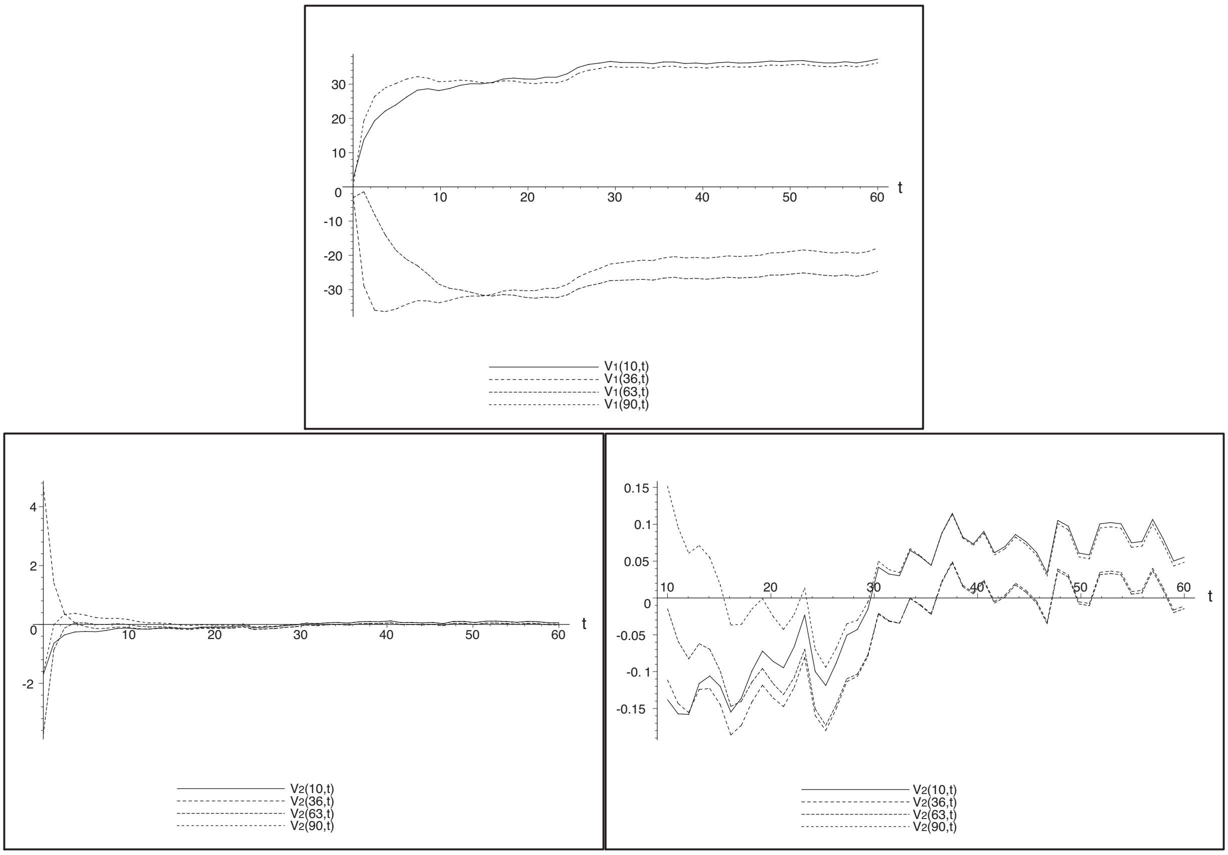

Figure 4.9: *The loss of the absolute stability of the homogeneous solution results in the loss of the complete synchronization of neural masses when the sufficient condition of theorem 4.4.1 is not satisfied. This is shown for four out of the hundred (coordinates 0.1, 0.36, 0.63 and 0.9). The input is the same as in the previous example. Top: The first components of the four state vectors. Bottom left: The second components of the four state vectors for* $0 \leq t \leq 60s$. *Bottom right: Zoom on the second components of the four state vectors for* $10 \leq t \leq 60s$.

processes shown in figure 4.11. Hence it is homogeneous in Ω_1 (respectively in Ω_2) but not in $\Omega = \Omega_2 \cup \Omega_2$. According to proposition 4.5.3 there exists a unique solution to (4.6) for a given initial condition in $\mathbf{L}_2^2(\Omega)$. This solution is locally homogeneous if the initial condition is locally homogeneous (theorem 4.5.2) given the fact that the input is locally homogeneous.

Absolute stability

The parameters

$$\begin{array}{ll} \boldsymbol{\alpha}^{11} = \begin{bmatrix} 5.21 & 0.23 \\ 0.23 & 5.21 \end{bmatrix} & \boldsymbol{\alpha}^{12} = \begin{bmatrix} 4.98 & 0.34 \\ 0.34 & 4.98 \end{bmatrix} \\ \boldsymbol{\alpha}^{21} = \begin{bmatrix} 4.75 & 0.45 \\ 0.45 & 4.75 \end{bmatrix} & \boldsymbol{\alpha}^{22} = \begin{bmatrix} 5.39 & 0.13 \\ 0.13 & 5.39 \end{bmatrix} \end{array} \quad \boldsymbol{\sigma} = \begin{bmatrix} 0.05 & 0.075 \\ 0.1 & 0.03 \end{bmatrix}$$

result in an operator norm $\|g^*\|_{\mathcal{G}_c^{2\perp}} \simeq 0.23$. Therefore, according to theorem 4.5.3, the locally homogeneous solutions are absolutely stable, resulting in the complete local synchronization of the neural masses (within Ω_1 and Ω_2).

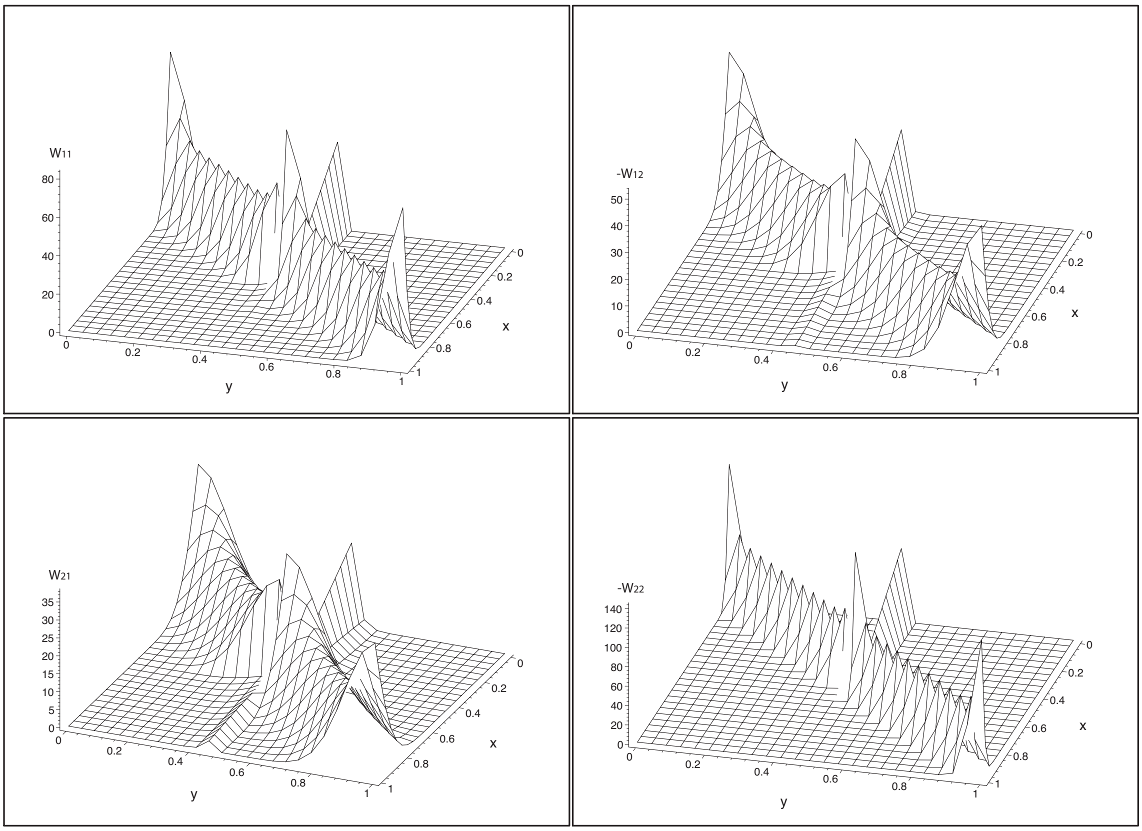

Figure 4.10: *The four elements of the matrix* $\mathbf{W}(x, y)$ *in the locally homogeneous case. Upper left:* $W_{11}(x, y)$*. Upper right:* $-W_{12}(x, y)$*. Lower left:* $W_{21}(x, y)$*. Lower right:* $-W_{22}(x, y)$*.*

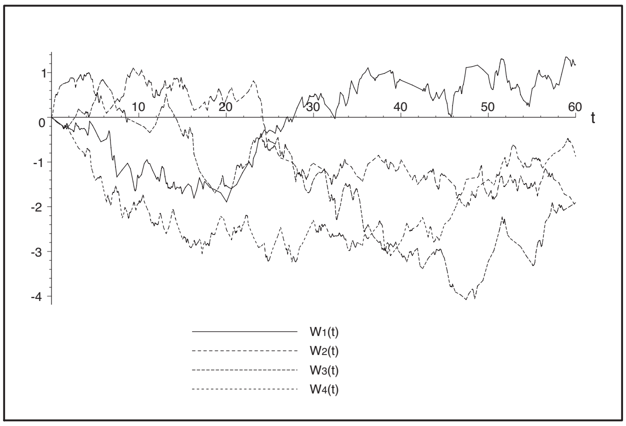

Figure 4.11: *The two coordinates of the input* $\mathbf{I}_{\text{ext}}(t)$ *in* Ω_1 *and* Ω_2 *are realizations of four independent Wiener processes (*W_1 *and* W_2 *are identical to those shown in figure 4.1).*

We show in figure 4.12 (respectively figure 4.13) the complete synchronization of two neural masses (numbers 10 and 36) in Ω_1 (respectively two neural masses (numbers 63 and 90) in Ω_2). The initial conditions are drawn randomly and independently from the uniform distribution on $[-10, 10]$ and $[-2, 2]$ for Ω_1 and on $[-20, 20]$ and $[-2, 2]$ for Ω_2.

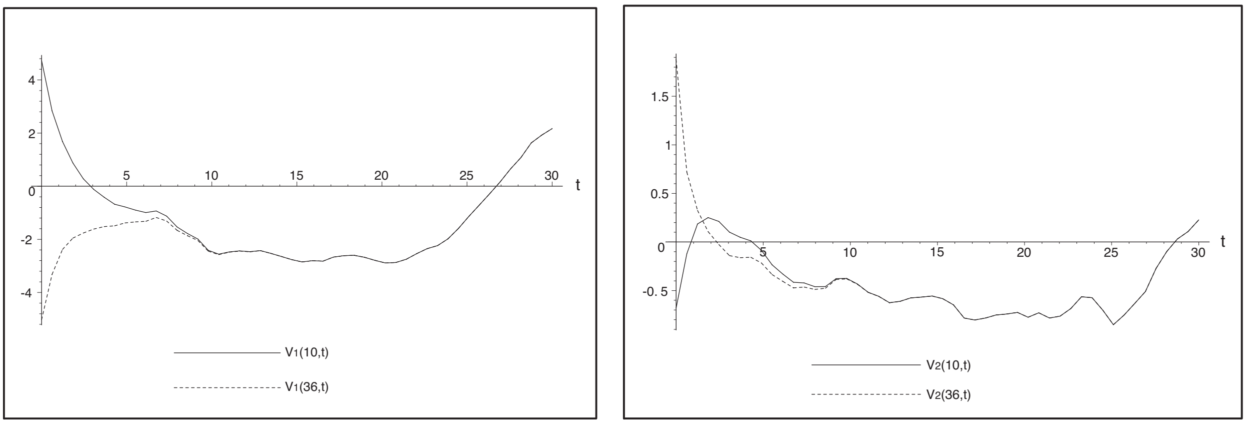

Figure 4.12: *The complete synchronization of two neural masses in Ω_1 of coordinates 0.1 and 0.36. The input is shown in figure 4.11. Left: the first components of the two state vectors. Right: the second components of the two state vectors.*

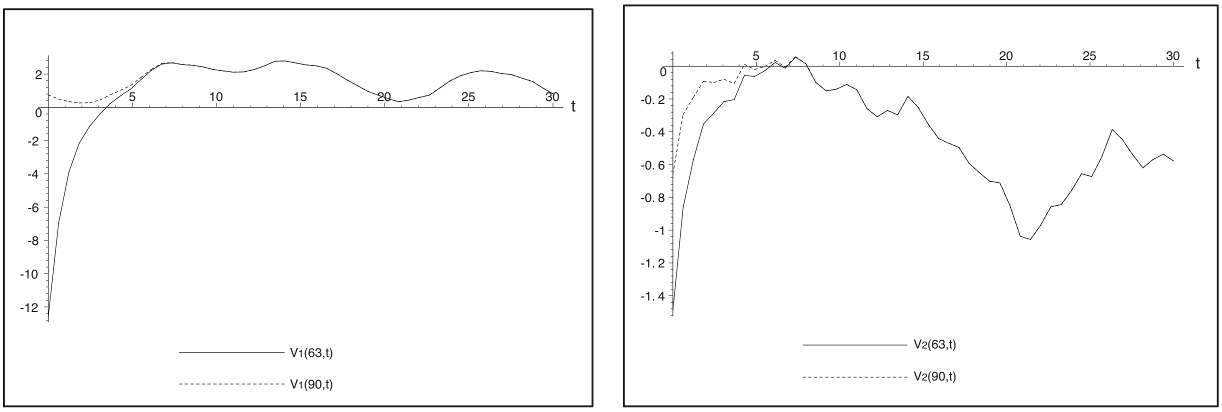

Figure 4.13: *The complete synchronization of two neural masses in Ω_2 of coordinates 0.63 and 0.9. The input is shown in figure 4.11. Left: the first components of the two state vectors. Right: the second components of the two state vectors.*

Loss of absolute stability

If we increase the value of α, it has the effect of increasing $\|g^*\|_{\mathcal{G}_c^{2,\perp}}$. The sufficient condition for absolute stability will eventually not be satisfied and we may lose the absolute stability of the locally homogeneous solution and hence the complete local synchronization of the solution. This is shown in figures 4.14 and 4.15 for $\alpha = 10$ corresponding to an operator norm $\|g_m^{L*}\|_{\mathcal{G}_c^{2}\perp} \simeq 2.3$.

4.6.4 Absolute stability of pseudo locally homogeneous solutions

As mentioned at the end of section 4.5.2, even if the connectivity function does not satisfy condition (4.26) and the operator g^* satifies only the condition of theorem 4.3.1 but not that of theorem 4.5.3 the existence of locally homogeneous solutions is not guaranteed but the absolute stability of the solution is, because of proposition 4.5.4. As shown in figures 4.16 and 4.17 these solutions can be very close to being locally homogeneous and thus enjoy the property of complete local synchronization. This is potentially very interesting from the application viewpoint since one may say

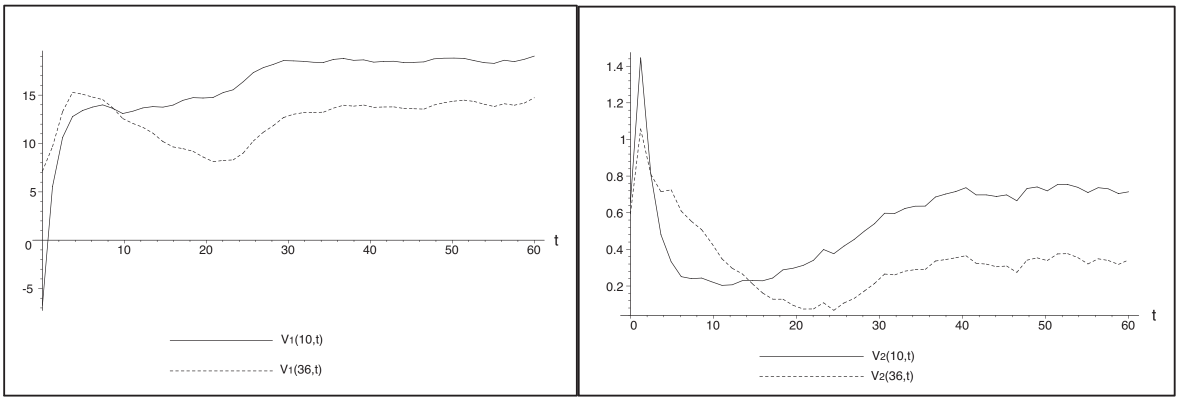

Figure 4.14: *The loss of the absolute stability of the locally homogeneous solution results in the loss of the complete local synchronization of neural masses when the sufficient condition of theorem 4.5.3 is not satisfied. This is shown for two out of the fifty (coordinates 0.1, 0.36) neural masses in* Ω_1. *The input is the same as in the previous example. Left: The first components of the two state vectors. Right: The second components of the two state vectors.*

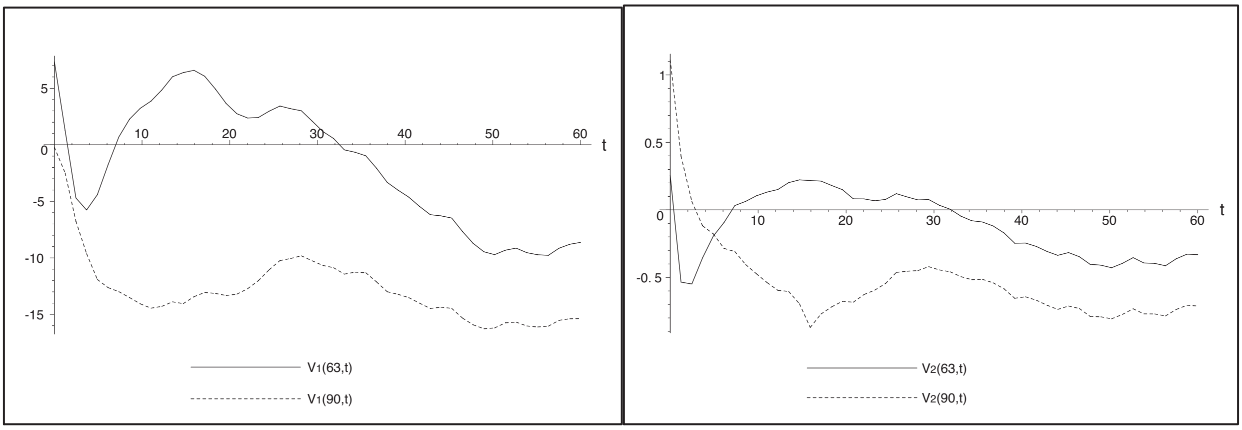

Figure 4.15: *The loss of the absolute stability of the locally homogeneous solution results in the loss of the complete local synchronization of neural masses when the sufficient condition of theorem 4.5.3 is not satisfied. This is shown for two out of the fifty (coordinates 0.63, 0.9) neural masses in* Ω_2. *The input is the same as in the previous example. Left: The first components of the two state vectors. Right: The second components of the two state vectors.*

that if the system admits homogeneous solutions and if they are absolutely stable it can have locally homogeneous solutions without “knowing” the partition, and they are absolutely stable. These results are illustrated by two animations (files pseudo-local-homogeneous-synchro-1.gif and pseudo-local-homogeneous-synchro-2.gif of the supplemental material). The axes are the same as previously.

4.7 CONCLUSION

We have studied the existence, uniqueness, and absolute stability of a solution of two examples of nonlinear integro-differential equations that describe the spatio-temporal activity of sets of neural masses. These equations involve space and

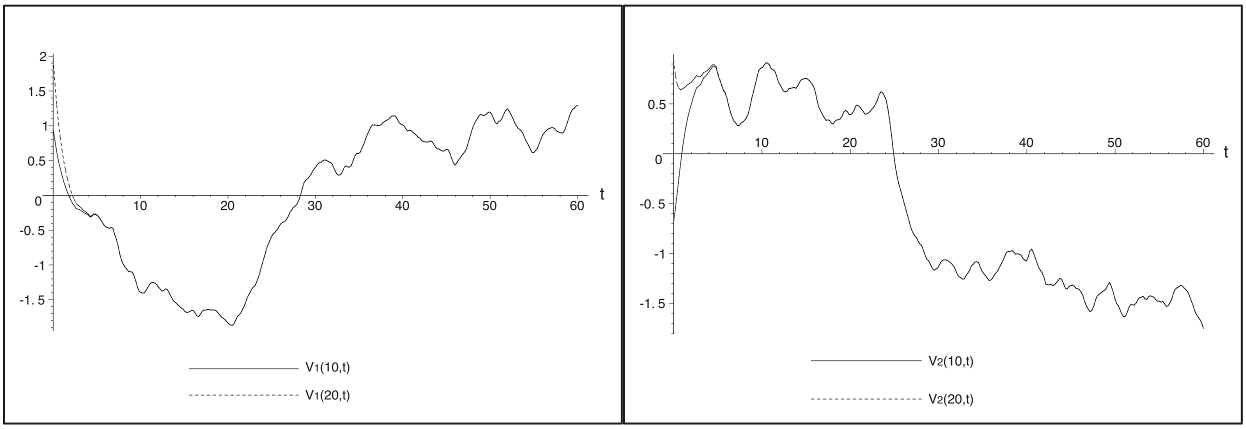

Figure 4.16: *The connectivity function satisfies condition (4.12) but not condition (4.26) and the operator g^* satifies the condition of theorem 4.4.1, not that of theorem 4.5.3. The input is locally homogeneous, as in figures 4.12 and 4.13. The solution is absolutely stable, because of theorem 4.4.1 and almost locally homogeneous. Something very close to complete local synchronization is observed. This is shown for two out of the fifty (coordinates 0.1, 0.2) neural masses in Ω_1. Left: The first components of the two state vectors. Right: The second components of the two state vectors.*

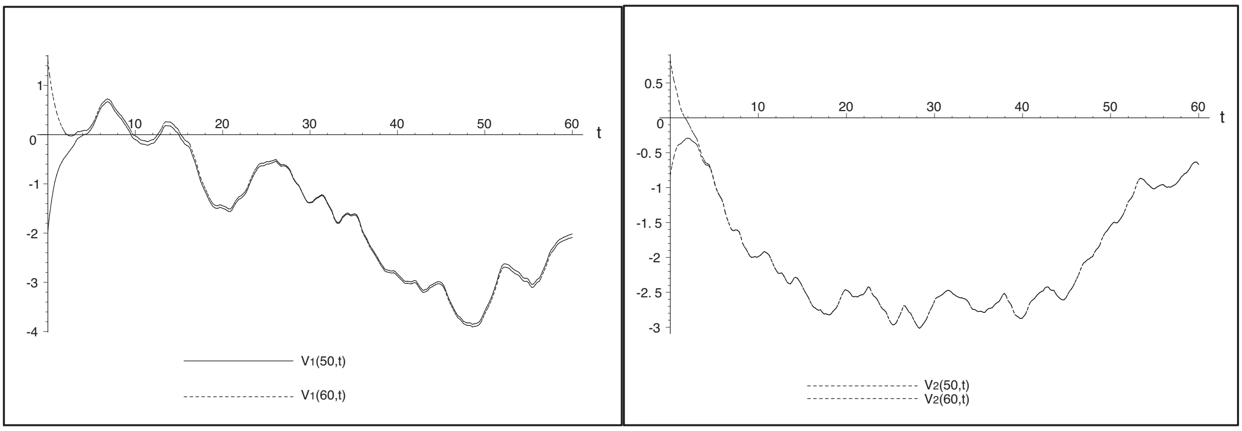

Figure 4.17: *Same as in figure 4.16. The complete local synchronization is shown for two out of the fifty (coordinates 0.5, 0.6) neural masses in Ω_2.*

time varying, possibly non-symmetric, intra-cortical connectivity kernels. The time dependency of the connectivity kernels opens the door to the study, in this framework, of plasticity and learning. Contributions from white matter afferents are represented by external inputs. Sigmoidal nonlinearities arise from the relation between average membrane potentials and instantaneous firing rates. The intra-cortical connectivity functions have been shown to naturally define compact operators of the functional space of interest. Using methods of functional analysis, we have given sufficient conditions for the existence and uniqueness of a solution of these equations for general, homogeneous (i.e. independent of the spatial variable), and locally homogeneous inputs. In all cases we have provided sufficient conditions for the solutions to be absolutely stable, that is to say independent of the initial state of the neural field. These conditions involve the connectivity functions, the maximum slopes of the sigmoids, as well as the time constants used to described the time variation of the postsynaptic potentials. They are very relevant to neuroscience where dynamical neuronal systems that “recognize” a given input regardless of their initial state are quite common. To our knowledge this is the first time that such a complete analysis of the problem of the existence and uniqueness of a solution of these equations has been obtained. An important contribution also is the analysis of the absolute stability of these solutions which had been considered as much more difficult to perform than the linear stability analysis which it implies. This application may not be limited to the specific topic of this chapter.

The reason why we have been able to complete this work programme is our use of the functional analysis framework and the theory of compact operators in a Hilbert space with the effect of providing simple mathematical answers to some of the questions raised by modellers in neuroscience. For example, the issue of bump solutions in such bounded neural fields has been tackled in the technical report [35], which has been accepted for publication in *Neural Computation*.

In the last part of this thesis, we use neural fields to model optical imaging experiments.

Part III

Biophysical neural fields for VSD optical imaging modeling

CHAPTER 5

A NEURAL FIELD MODEL FOR VSD OPTICAL IMAGING SIGNALS

OVERVIEW

In this chapter we propose a solution to the direct problem of VSD optical imaging based on a neural field model of a cortical area. We first present a biophysical approach to neural fields and show that these easily integrate the biological knowledge on cortical structure, especially horizontal and vertical connectivity patterns. Then we introduce the reader to VSD optical imaging. Finally, we propose a biophysical formula expressing the optical imaging signal in terms of the activity of the field. This chapter and the following are part of the research report [47] (2007) and the corresponding paper is in preparation.

Contents

5.1 Neural field model of a cortical area 126
5.2 Principle of VSD optical imaging 130
5.3 Model of the OI signal 132

5.1 NEURAL FIELD MODEL OF A CORTICAL AREA

In mammals brain, gray matter (intracortical) projections almost exclusively connect neurons within the same area and white matter projections mostly connect neurons from different areas [97]. In the following, we will see a cortical area as an autonomous intracortical network, described by a neural field equation, including several layers and receiving distributed sensory input from white matter afferents (see figure 5.1).

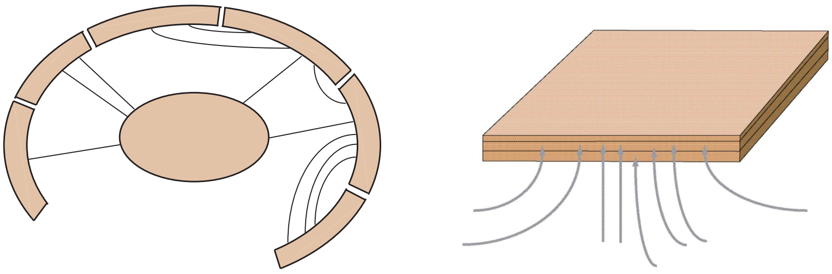

Figure 5.1: *Left. Simplified representation of the brain that we assume in our modeling of a cortical area: areas are defined as autonomous structures receiving input from other parts of the brain. The central ovoid form represents the thalamus, the other brown regions being cortical areas. Black curves account for white matter connections. Right. Focus on a single area. We see it as a layered intracortical network receiving sensory input via white matter projections.*

In this section, we want to show that neural field models parameters and variables can naturally be related to well-known biological facts.

We start from classical neural field models and analyze them from a biophysical viewpoint.

$$\dot{\mathbf{V}}(\mathbf{r},t) = -\mathbf{L}\mathbf{V}(\mathbf{r},t) + \int_\Omega \mathbf{W}(\mathbf{r},\mathbf{r}')\mathbf{S}(\mathbf{V}(\mathbf{r}',t))\,d\mathbf{r}' + \mathbf{I}_{\text{ext}}(\mathbf{r},t), \tag{5.1}$$

and

$$\dot{\mathbf{A}}(\mathbf{r},t) = -\mathbf{L}\mathbf{A}(\mathbf{r},t) + \mathbf{S}\left(\int_\Omega \mathbf{W}(\mathbf{r},\mathbf{r}')\mathbf{A}(\mathbf{r}',t))\,d\mathbf{r}' + \mathbf{I}_{\text{ext}}(\mathbf{r},t)\right)^1. \tag{5.2}$$

Ω is the spatial domain defining the area, a compact subdomain of $\mathbb{R}^2$ (e.g. a square or a disk). For each spatial position $\mathbf{r} \in \Omega$, the underlying cortical column is described, at time t, by an N-dimensional vector $\mathbf{V}(\mathbf{r},t)$ or $\mathbf{A}(\mathbf{r},t)$. $\mathbf{V}(\mathbf{r},t)$ contains the average soma membrane potentials of the different neural masses present in the column. So, N is the number of neuronal types considered in every column. Each neuronal type can be thought of as belonging to a particular cortical layer, the layer the corresponding somata belong to. $\mathbf{A}(\mathbf{r},t)$ contains the average activities of the masses.

$$A_i = PSP_i * \nu_i,$$

where $*$ represents the temporal convolution, ν_i the average firing rate of mass i and PSP_i the normalized[2] postsynaptic potential induced by mass i on its postsynaptic

---

[1] These equations are particular cases of equations (4.6) and (4.7).

[2] *Normalized* in the sense that it does not include the strength and sign of connections from mass i to its postsynaptic partner.

targets. So A_i is the potential quantity of post-synaptic potential induced by mass i on the dendrites of all its postsynaptic partners. The actual quantity depends on the strength and sign (excitatory or inhibitory) of the projections.

Here it is assumed that postsynaptic potentials have a decreasing exponential form, completely characterized by their time constant (up to the sign and intensity of connections, see figure 5.2):

$$PSP_i(t) = \begin{cases} e^{-t/\tau_i}, & t > 0 \\ 0, & t \leq 0 \end{cases} .$$

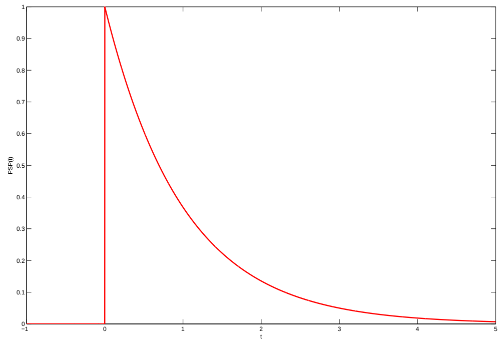

Figure 5.2: *Form of a normalized postsynaptic potential that we assume in our models. As τ gets bigger, PSP gets broader.*

$\mathbf{L}$ is an $N \times N$ diagonal matrix containing the synaptic decay time constants τ_i of the postsynaptic potentials $PSP_i(t)$ for the different neuronal types. As we have seen before, in the voltage case, the time constants only depend on the postsynaptic population, while in the activity case they only depend on the presynaptic one. In real neurons these constants actually depend on both populations and on their current electrophysiological state (in terms of ionic channels openings), what allows to explain such phenomena as shunting inhibition. However among the two presented models, the activity-based model is the most realistic. Indeed, the characteristic time constant of a postsynaptic potential more likely depends on the neurotransmitter that triggered it, and so, on the presynaptic neuron.

$\mathbf{I}_{\text{ext}}(\mathbf{r}, t)$ is an input term to the system, corresponding to projections that arise from white matter. For example in V1, it would correspond to the input from the lateral geniculate nucleus (LGN, the thalamic relay from the retina to the cortex) and feedbacks from the secondary visual cortex, V2 (see figure 5.3).

The input can be seen as a current (voltage case) or an electric potential (activity case) on the dendrites of thalamo-recipient cells. The main problem concerning the input term is that few is currently known about the coding of sensory information by sensory organs and their thalamic relays to the cortex.

In equations (5.1) and (5.2), the integral terms summate the contributions from columns at different locations on the field to the dynamics of the column located at point $\mathbf{r}$. They feature an intracortical connectivity kernel $\mathbf{W}$ representing the weights of connections between columns located at different positions on the field and a nonlinear function $\mathbf{S} : \mathbb{R}^N \rightarrow \mathbb{R}^N$. $\mathbf{S}$ has N components. Each of them is a

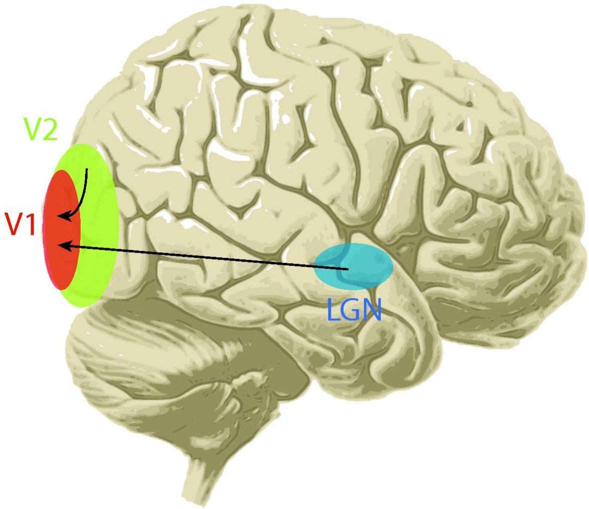

Figure 5.3: *External inputs to V1, arising from white matter fibers: feedforward projections from the LGN and feedback projections from V2.*

static sigmoidal (nonlinear) transformation converting, for a given neuronal type, the average soma potential of a neural mass into its average firing rate. This sigmoidal shape (see figure 2.3) is in agreement with studies made by Walter Freeman in the olfactory bulb. He showed that the mapping between the average membrane potential of a neural mass and its average firing rate was a sigmoidal "wave-to-pulse" transform, by comparing the amplitude of EEG signals produced by neural masses with their firing probabilities [39]. The abscissa of the sigmoid's inflection point can be thought of as the average excitability or firing threshold of the corresponding neuronal population, and the limit of the sigmoid at infinity, as its maximal firing rate.

$\mathbf{W}$ is an $N \times N$ matrix. The terms W_{ij} represent the strength of projections from neurons of type j to neurons of type i. But what does "strength" mean? Each connectivity term can be seen as the product of three quantities:

$$W_{ij} = N_j \, k_{ij} \, w_{ij},$$

where N_j is the number of neurons of type j in one column, k_{ij} the gain of an average postsynaptic potential caused by a neuron of type j on a neuron of type i, and w_{ij}, the average number of synaptic contacts that a neuron of type j makes on a neuron of type i. It can also be seen as the probability of synaptic contact between the axon of a neuron of type j and the postsynaptic compartments of a neuron of type i.
So in first approximation we can think of $\mathbf{W}$ as a wiring diagram such as the one shown in figure 5.4, where the matrix components W_{ij} are represented by arrows linking neuronal types. Figure 5.4 is of course very similar to figure 1.20, which contains the information on the k_{ij}s and the w_{ij}s.
However, a diagram such as figure 5.4 only provides information on the "vertical" intracolumnar connectivity between neural masses. Horizontal intercolumnar connections are also included in $\mathbf{W}$. Each W_{ij} is actually a function depending on two positions on the field and $W_{ij}(\mathrm{r}, \mathrm{r}')$ indicates the strength of projections from the mass

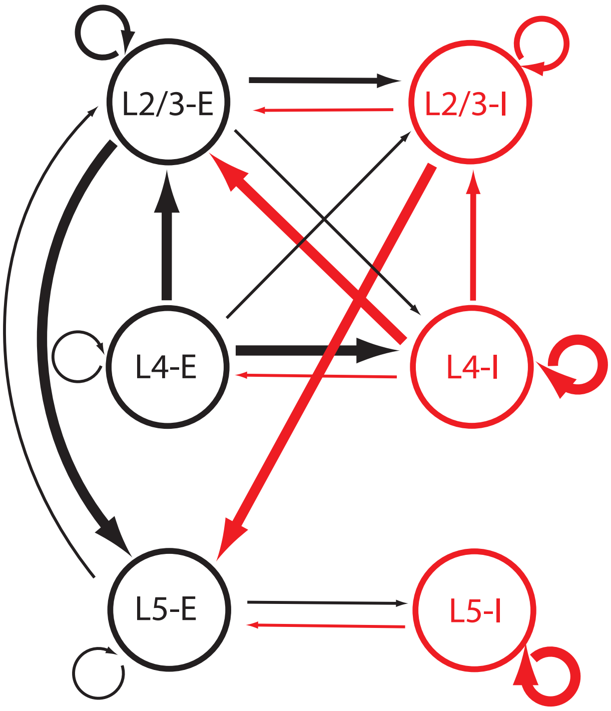

Figure 5.4: *A example of simplified model of cortical interactions based on six neuronal populations. It features three layers corresponding to cortical layers II/III, IV and V, and two types of neurons (excitatory ones in black and inhibitory ones in red). The size of the arrows gives an idea of the strength of the connectivity between populations (adapted from [49]).*

of type j, in column $\mathbf{r}'$ to the mass of type i, in column $\mathbf{r}$. The vertical connectivity information for column $\mathbf{r}$ can be found in $\mathbf{W}(\mathbf{r},\mathbf{r})$. $W_{ij}(\cdot,\mathbf{r}')$ is the spatial horizontal distribution of projections from the mass $(j,\mathbf{r}')$ to masses of type i, which depends on the horizontal spread of both the axonal arborization of mass $(j,\mathbf{r}')$ and the dendrites of masses of type i (see figure 5.5).

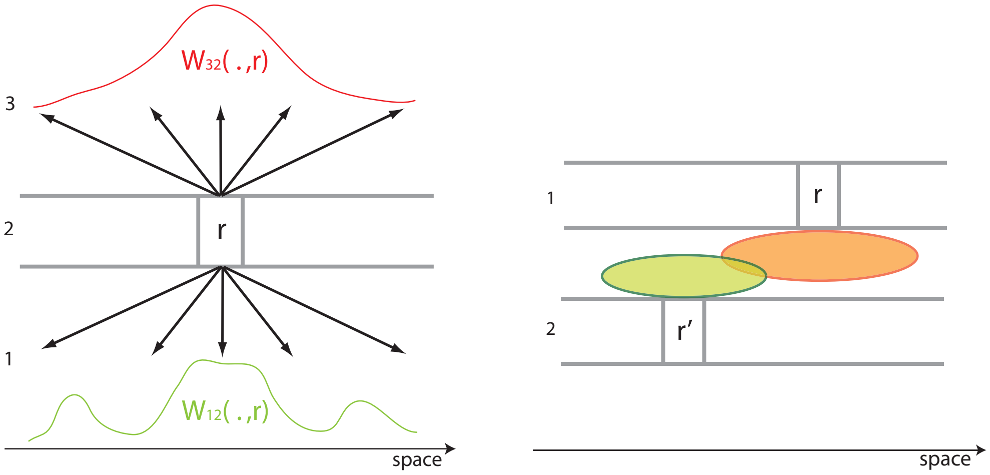

Figure 5.5: *Left. Example featuring three neuronal types (1, 2 and 3). The mass* $(2,\mathbf{r})$ *shows different spatial patterns of horizontal projections, depending on the type of the postsynaptic targets. Right. The axonal arbour of mass* $(1,\mathbf{r})$ *(in red) does not reach* $\mathbf{r}'$ *but since the dendritic tree of* $(2,\mathbf{r}')$ *(in green) is wide enough,* $W_{21}(\mathbf{r}',\mathbf{r}) \neq 0$.

Horizontal connectivity patterns play a major functional role and widely vary from an area to another. We will see examples of these patterns in the next chapter for two different cortices: the primary visual cortex of a wide range of mammals and the rat barrel cortex.

So, we have seen that neural fields can be suitable mesoscopic models of cortical areas. Their parameters can be tuned in agreement with well-known biophysical quantities and account for the complex structure of an area in terms of layers, horizontal and vertical connectivity.
In the following we will focus on the activity-based model, because it is more realistic than the voltage-based model as concerns synaptic integration and facilitate the description of the optical imaging signals that we will propose later.

5.2 PRINCIPLE OF VSD OPTICAL IMAGING

VSD optical imaging[3] (VSDOI) is a recent and popular functional imaging technique that uses fluorescent voltage-sensitive dyes (VSDs) to reveal population activity of cortical neurons in behaving animals [48], with high spatial resolution ($\sim$0.5μm for single cell recordings and $\sim$50μm for population recordings) and a temporal precision inferior to the millisecond. This invasive technique requires an opening in the skull to have direct access to the cortex (see figure 5.6, lower panel). Hence, it has mostly been used in non-human mammals, like monkeys, cats and rodents.
As the cortex is stained with VSD, the dye molecules bind to the plasmic membrane of

---

[3] Also known as *extrinsic optical imaging*.

all types of cells present in the cortex. These include glial cells and all compartments of neurons. VSD molecules are polarized, because of the electric potential at the level of neurons membranes, and emit light with an intensity proportional to this polarization (see figure 5.6, upper right panel). Glial cells are known to have a minimal contribution to VSD signals because of their lower electrical activity compared to neurons. So light patterns emitted from the cortex and recorded by the camera of the optical imaging device (figure 5.6, upper left panel) are mostly due to the electrical activity of neurons. VSDOI signals show a remarkable match with intracellular recordings. Actually, at the level of a single cell, the amplitude of VSD signals is linearly correlated with both the membrane potential and the area of stained neuronal membranes. In neuronal population imaging, a pixel contains the blurred images of various neuronal compartments. How strongly do the different compartments contribute to the VSD signal? The surface of somata is several orders of magnitude smaller than the surface of axons and dendrites. So somata make a minor contribution to the VSD signal. Dendrites are more confined, horizontally, than axonal arbours, and spikes traveling down the axons are too brief events to be well integrated in the population VSD signal. So, the optical signal is mainly due to the subthreshold, dendritic activity of the underlying population of neurons (see the comparison of the optical signal with an intracellular recording on figure 5.6).

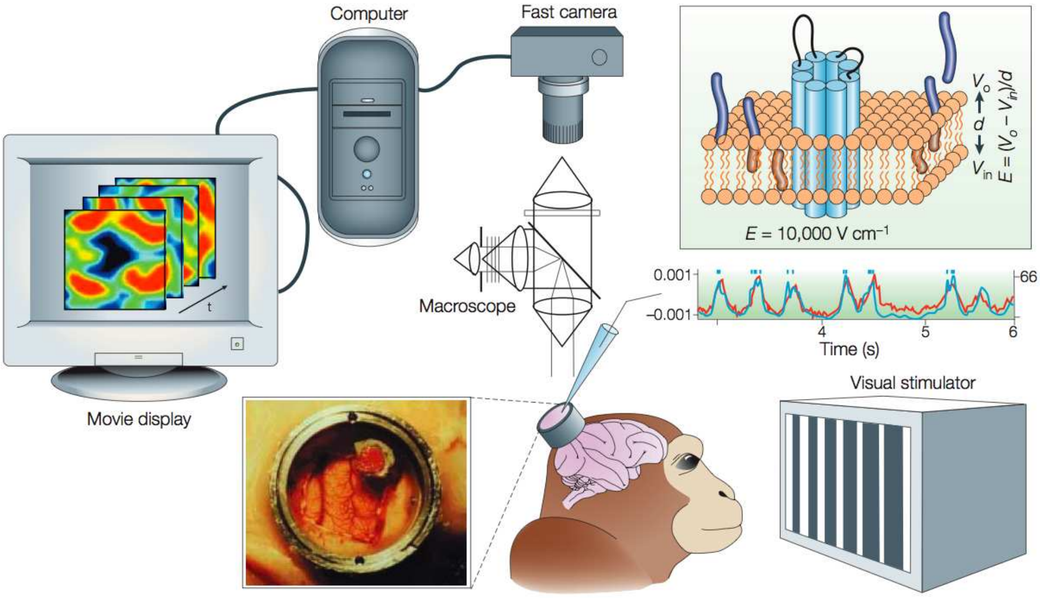

Figure 5.6: *Principle of VSDOI. An opening in the skull of a behaving monkey gives access to its cortex stained with VSD. A camera records the fluorescence caused by polarized VSD molecules bound to the plasmic membrane of cortical neurons, and after appropriate processing, a movie of the distributed population activity is obtained, with high spatial and temporal resolutions. The optical signal (in red on the right central panel) remarkably matches the subthreshold dynamics of neurons obtained by intracellular recordings (in blue; truncated spikes are represented by small blue dots overlying the subthreshold signal) (From [48]).*

The integration of the optical signal across the depth of the cortex is subject to a double gradient. First, VSD molecules mostly diffuse in the superficial layers and

few of them deeply penetrate the cortex. In [70], the authors show that most of the dye molecules[4] lie in layers I-III (70%) (see figure 5.7).
Second, the light emitted by deep VSD molecules undergoes stronger diffusive effects, traveling back to the surface across cortical cells. Hence activity in layers IV-VI poorly contributes to the signal.

We now propose a model for VSDOI signals produced by a cortical area, grounded in the above facts, and based on a neural field description of the spatially distributed activity of neural masses in the area.

5.3 MODEL OF THE OI SIGNAL

In this section we write a formula involving the variables and parameters of a neural field model to solve the direct problem of VSDOI.
To that purpose we start from the whole signal and decompose it, step by step, into elementary contributors until we reach the cellular membrane level, where the optical signal is simply proportional to the membrane potential. Firstly, the signal is a weighted sum of the signals arising from the different layers. We note the whole signal OI, and the unattenuated signal from layer l, OI^l. Here, "unattenuated" means that we suppose that no superimposed layer would hamper the propagation of light towards the camera. We then have the following

$$OI(\mathbf{r},t) = \sum_{l \in \{\text{layers}\}} a_l \, OI^l(\mathbf{r},t),$$

where a_l is a positive attenuation coefficient due absorption and diffusion of the light emitted by layer l through its superimposed layers. Naturally, a_l decreases as the depth of the layer increases. Then it is natural to sum these attenuated light contributions in virtue of the linearity of Maxwell equations.
The propagation of light through the cortical tissue is not well-known, but diffusion and absorption of light by gray matter probably would be more suitably modeled by a spatial blurring of the signals produced by a layer. Hence the previous formula would become

$$OI(\mathbf{r},t) = \sum_{l \in \{\text{layers}\}} a_l \, G_l \otimes OI^l(\mathbf{r},t),$$

where G_l is a two-dimensional Gaussian distribution whose standard deviation increases with the depth of layer l, and $\otimes$ denotes the spatial convolution (see figure 5.8).
Now, what is the local instantaneous quantity of light $OI^l(\mathbf{r},t)$ produced by layer l?

$$OI^l = \sum_{i=1}^{N} OI_i^l,$$

where N is the number of neuronal types considered in the neural field and OI_i^l the contribution of dendrites belonging to neurons of type i and lying in layer l[5] to the unattenuated layer signal (see figure 5.9).

---

[4] They used the blue dye RH1691, developed by Amiram Grinvald's group, in the cortex of the rat.

[5] From now on, we will designate dendritic trees by a doublet (l,i) indicating the layer and the neuronal type it belongs to.

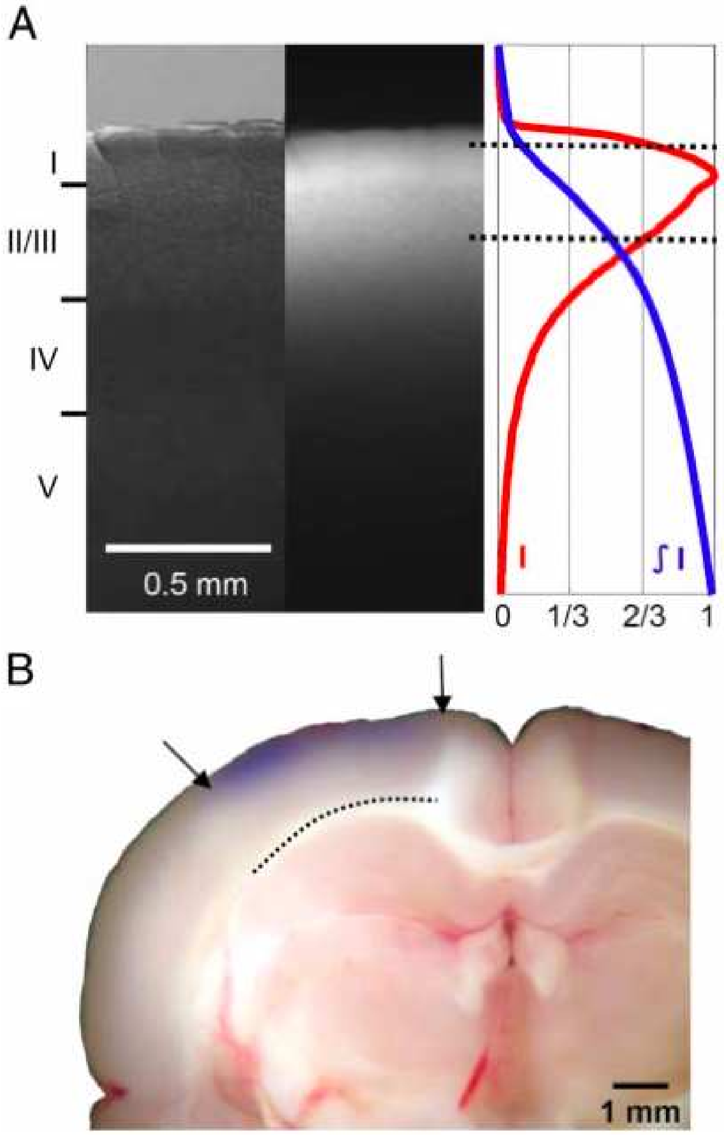

Figure 5.7: *A. Left. Visible light image of a stained cortical slice. Middle. Corresponding fluorescence image showing the density distribution of VSD molecules across the layers. Right. Corresponding fluorescence intensity (red) and integrated intensity (blue). We observe that about 30% of the staining dye molecules are located in layer I and about 70% in layers I-III. B. Stained brain section. Arrows indicate the borders of the previously opened cranial window. Broken line indicates the border between gray and white matter. The staining can be seen by eye in blue (From [70]).*

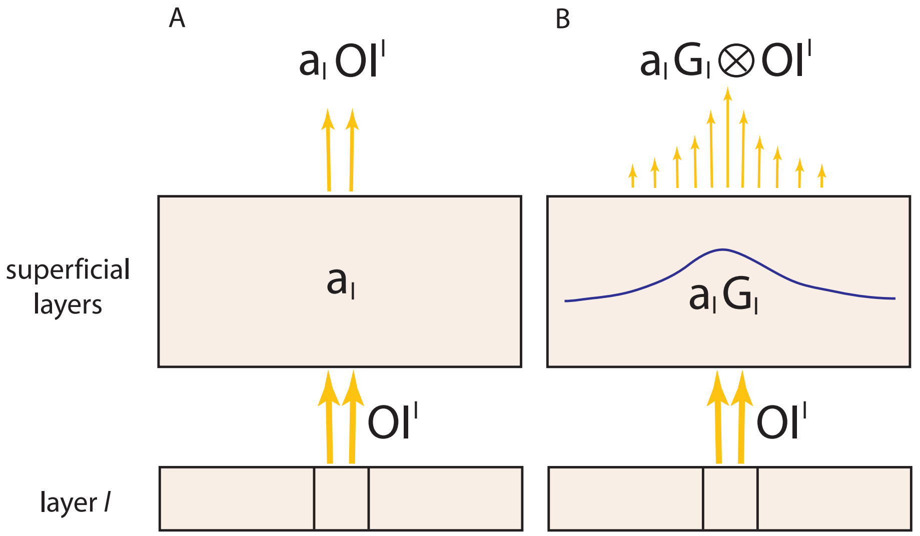
A
B
$a_l OI^l$
$a_l G_l \otimes OI^l$
superficial layers
a_l
$a_l G_l$
OI^l
OI^l
layer *l*

Figure 5.8: *Two models of light absorption / diffusion in superficial layers. A. The fluorescence produced in layer l at the level of one neural mass is simply attenuated by absorption in superficial layers, keeping its initial spatial focus. B. In this model, the same focused emission of light in layer l is attenuated by absorption and horizontally diffused by multiple scattering in the cortical cellular network. This phenomenon can be accounted for by a convolution of the signal with a Gaussian distribution. It results, at the exit of the cortex, in a blurred emission of light.*

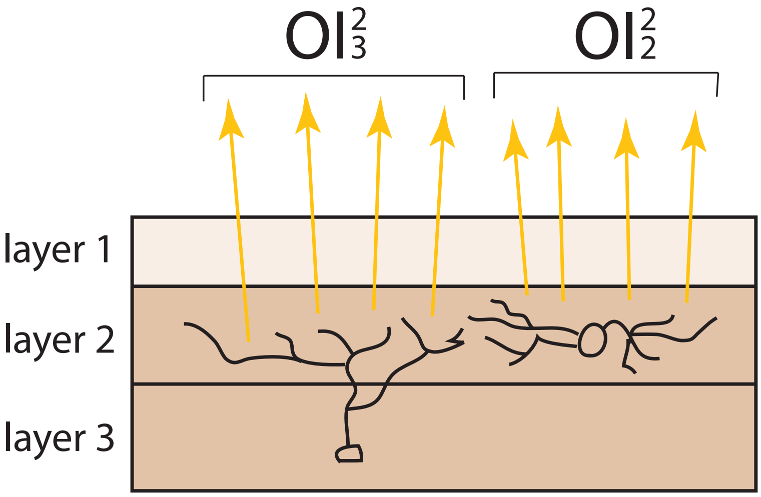
OI_3^2
OI_2^2
layer 1
layer 2
layer 3

Figure 5.9: *The emission of light at the level of a layer (here layer 2), forgetting the attenuation due to superimposed layers (like layer 1, in light color), is the sum of the contributions from neurons which project part of their dendritic trees in the emitting layer, no matter where their somata are located.*

Note that the somata of neurons of type i do not need lie in layer l so that part of their dendritic trees do, and hence contribute to the layer signal. For example deep layers pyramidal cells have several dendritic arbors and some of them reach the most superficial cortical layers (see figure 1.14).

Now we focus on $OI_i^l(\mathbf{r}, t)$, the local unattenuated contribution of the dendritic tree (l, i).

$$OI_i^l(\mathbf{r}, t) = c\, N_i\, s_i^l\, n_l\, P_i^l(\mathbf{r}, t),$$

where P_i^l is the membrane potential of (l, i), n_l the number of VSD molecules per membrane surface unit in layer l, s_i^l the average dendritic surface due to one neuron of type i in layer l and N_i the number of neurons of type i in a cortical column. So, $N_i\, s_i^l\, n_l$ is the total number of dye molecules, in the extent of one cortical column, on the dendritic tree (l, i). Finally, c is the coefficient of the linear transformation converting the local membrane potential into the optical imaging signal (see figure 5.10).

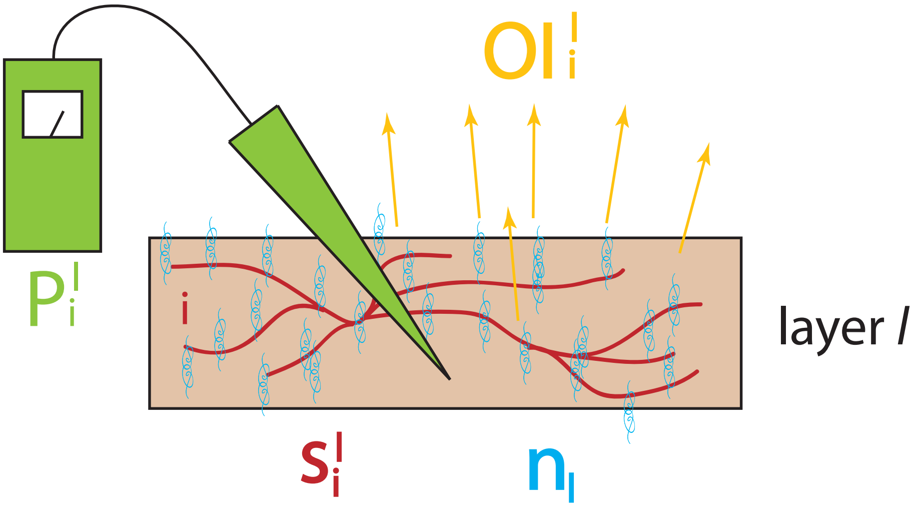

Figure 5.10: *The optical imaging signal (yellow) is locally linearly correlated to the dendritic membrane potential (green), the concentration of VSD molecules (blue) and the dendritic surface (red).*

Now, how can we express the dendritic membrane potentials $P_i^l(\mathbf{r}, t)$ in a model without any specific attention paid to neuronal compartments and where a neural mass is a simple point of the field?
Instead of trying to infer the dendritic potential $P_i^l(\mathbf{r}, t)$ from the knowledge of the activity vector of column $\mathbf{r}$, $\mathbf{A}(\mathbf{r}, t)$, we consider all projections to column $\mathbf{r}$. We note $PSP_{ij}^l(\mathbf{r}, t)$ the total postsynaptic potential caused at time t on the dendritic tree (l, i) of column $\mathbf{r}$ by all masses of type j across the area. Then assuming a linear summation of postsynaptic potentials as we did in neural field models, we have

$$P_i^l(\mathbf{r}, t) = \sum_{j=1}^{N} PSP_{ij}^l(\mathbf{r}, t),$$

with

$$PSP^l_{ij}(\mathbf{r},t) = \alpha^l_{ij} \int_\Omega W_{ij}(\mathbf{r},\mathbf{r}')\, A_j(\mathbf{r}',t)\, d\mathbf{r}'.$$

$\alpha^l_{ij} \in [0,1]$ is the fraction of synapses masses of type j make on dendrites of type i at the level of layer l, i.e. the number of synapses made by neurons of type j on (l,i) divided by the total number of synapses made by neurons of type j on neurons of type i[6]. Hence in general $\sum_l \alpha^l_{ij} \leq 1$. If neurons of type j exclusively target dendrites, then $\sum_l \alpha^l_{ij} = 1$. If in the opposite case they only target somata, $\sum_l \alpha^l_{ij} = 0$.

Now, we are ready to summate all elementary terms to obtain a formula for the direct problem of VSDOI:

$$OI(\mathbf{r},t) = \sum_{i,j=1}^{N} C_{ij} \int_\Omega w_{ij}(\mathbf{r},\mathbf{r}')\, A_j(\mathbf{r}',t)\, d\mathbf{r}', \tag{5.3}$$

with

$$C_{ij} = c\, N_i\, N_j\, k_{ij} \sum_{l\in\{\text{layers}\}} s^l_i\, \alpha^l_{ij}\, a_l\, n_l.$$

If we assume a more realistic, Gaussian diffusion, we have

$$OI(\cdot,t) = \sum_{i,j=1}^{N} C_{ij} \otimes \int_\Omega w_{ij}(\cdot,\mathbf{r}')\, A_j(\mathbf{r}',t)\, d\mathbf{r}', \tag{5.4}$$

with

$$C_{ij} = c\, N_i\, N_j\, k_{ij} \sum_{l\in\{\text{layers}\}} s^l_i\, \alpha^l_{ij}\, n_l\, a_l\, G_l.$$

Formulas (5.3) and (5.4) are equivalent to

$$OI(\mathbf{r},t) = \sum_{j=1}^{N} \int_\Omega \tilde{w}_j(\mathbf{r},\mathbf{r}')\, A_j(\mathbf{r}',t)\, d\mathbf{r}', \tag{5.5}$$

with

$$\tilde{w}_j(\mathbf{r},\mathbf{r}') = \sum_{i=1}^{N} C_{ij}\, w_{ij}(\mathbf{r},\mathbf{r}'),$$

or

$$\tilde{w}_j(\mathbf{r},\mathbf{r}') = \sum_{i=1}^{N} \int_\Omega C_{ij}(\mathbf{r}-\mathbf{r}'')\, w_{ij}(\mathbf{r}'',\mathbf{r}')\, d\mathbf{r}''.$$

We see from (5.3), (5.4) and (5.5) that the horizontal distribution patterns of intracortical connectivity play a primary role in shaping the optical signal.

So, assuming a linear summation of postsynaptic potentials on cellular membranes, we have expressed the direct problem of VSDOI as a time-invariant linear operator providing at each time instant the instantaneous optical signal from the knowledge of the instantaneous activity of the field. If we note this operator $\mathbf{T}$, formulas (5.3), (5.4) and (5.5) reduce to

---

[6] Here we implicitly assumed, for simplicity, that α^l_{ij} does not depend on the relative horizontal position of masses.

$$OI(\cdot,t) = \mathbf{T}\,\mathbf{A}(\cdot,t), \quad \forall t \geq 0.$$

Moreover, $\mathbf{T} : \mathrm{L}^2(\Omega, \mathbb{R}^N) \to \mathrm{L}^2(\Omega, \mathbb{R})$ is obviously compact, as a sum of Hilbert-Schmidt operators.

As concerns the inverse problem, it is most probably ill-posed (due to the higher dimensionality of the activity space compared to the signal space) and is not treated here.

Now that we have a model of cortical activity and a formula for VSDOI signals, we are ready to apply them to the simulation of real optical imaging experiments.

CHAPTER 6

SIMULATIONS OF OPTICAL SIGNALS IN THE VISUAL AND BARREL CORTICES

OVERVIEW

In this chapter, we simulate optical signals that have been observed by experimentalists. We have chosen two experimental sets: the line-motion illusion in the visual cortex of mammals [57] and the spread of activity in the rat barrel cortex [89]. We begin with a structural description of both areas, with a focus on horizontal connectivity. Then we simulate the corresponding neural field equations and extract the optical signal using the direct problem formula developed in the last chapter. We have been able to reproduce the main experimental results. This chapter, as well as the previous one, is part of the research report [47] (2007) and a corresponding paper is in preparation.

Contents

6.1 Horizontal connectivity 140
    6.1.1 Mammals visual cortex 140
    6.1.2 Barrel cortex of the rat 142
6.2 Simulations 144
    6.2.1 Visual cortex 144
    6.2.2 Barrel cortex 152
6.3 Discussion 155

In this chapter, we try to reproduce the results of optical imaging experimental paradigms found in the literature, by simulating adequate neural fields and extracting the optical signals thanks to the formula developed in the previous chapter. We have seen that horizontal connectivity patterns play a major role in shaping VSDOI signals. So, we start with a description of the horizontal connectivity of both cortices we focus on: the primary visual cortex and the barrel cortex. Then, we include the main features of these connectivities in neural field models and perform simulations.

6.1 HORIZONTAL CONNECTIVITY

Horizontal trans-columnar connectivity has an important functional role in the cortex and expresses through different arborization patterns. Two features must be retained as fundamental: a strong intracolumnar connectivity and a global horizontal decrease of connection intensity with the distance separating neural masses.
Neurons axonal trees ramify horizontally and connect to more or less distant postsynaptic targets. Axon collaterals (branches of the axonal tree emerging from the main axon of a neuron) can even make intracortical horizontal projections up to several millimeters. Most interneurones (including spiny stellate cells) essentially make local projections in their column of origin, while pyramidal cells and large basket cells also form extensive trans-columnar projections. The connection strength between two neurons generally decreases with the distance separating the somata. However, strong selective long-range projections, called *patches*, may exist in certain cortices.
Two particular structures have received considerable attention from neuroscientists: the lateral distribution of connections in mammals visual cortex [19, 63, 64, 65, 105, 115, 116] and the barrel organization of rats sensory cortex [2, 16, 37, 44, 73, 98, 99].

6.1.1 Mammals visual cortex

The primary visual cortex of certain mammals (including monkeys and cats, but not rats) can be divided into orientation preference columns [54]. This means that cortical columns in the visual cortex preferentially respond to certain oriented visual stimuli (vertical, horizontal, oblique bars). So, each column can be labeled with a preferred orientation and orientation preference maps of the visual cortex can be reconstructed thanks to different functional imaging techniques (see figure 1.8). The main feature of horizontal connectivity in the primary visual areas of such mammals is the patchy, orientation-preference-biased structure of pyramidal cells long-range projections (see figures 6.1 and 6.2).
In [19], the authors examine the relationship between excitatory lateral connections and orientation maps in the cat primary visual cortex. Thanks to tracer injections they were able to track the axonal projections issued from a small cortical site. They showed that most proximal projections do not discriminate their target in terms of orientation preference while distal patches usually do (figure 6.2). Actually, the regions underlying distal patches tend to have the same orientation preference as the region from which the projections originate. This tendency, which has been observed for projections originating from a localized cluster of cells (i.e. a neural mass), is however not clear when tracking the targets of single cells. Indeed their long-range projections are not necessarily patchy nor orientation selective (see figure 6.3).
So, patchy functional projections made by PC clusters are consistent with our mesoscopic neural mass approach, but they are too coarse to embrace the complexity of the precise functional network.

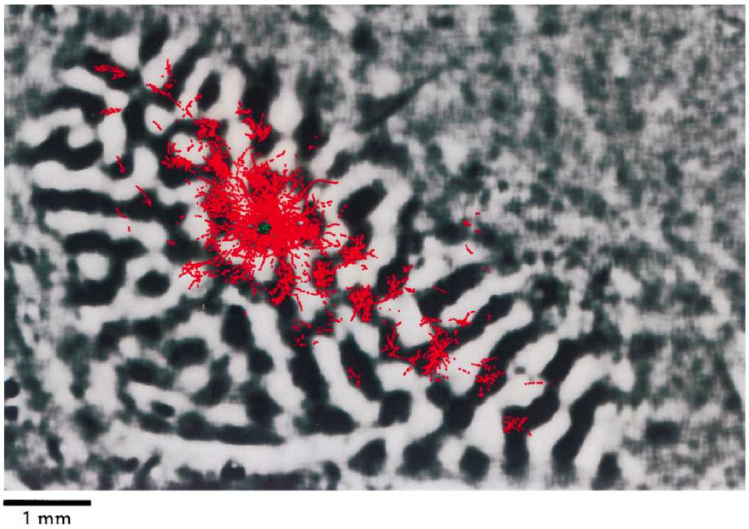

Figure 6.1: *Reconstruction of axonal boutons distibution (red) from a pool of biocytin-injected pyramidal neurons in layer II/III of the tree shrew visual cortex (green central patch). Strongly marked black and white stripes indicate V1 (black stripes are active areas for a* 90° *stimulus). A central patch of radius ∼500μm is observed, surrounded by smaller patches extending over several millimeters (From [14]).*

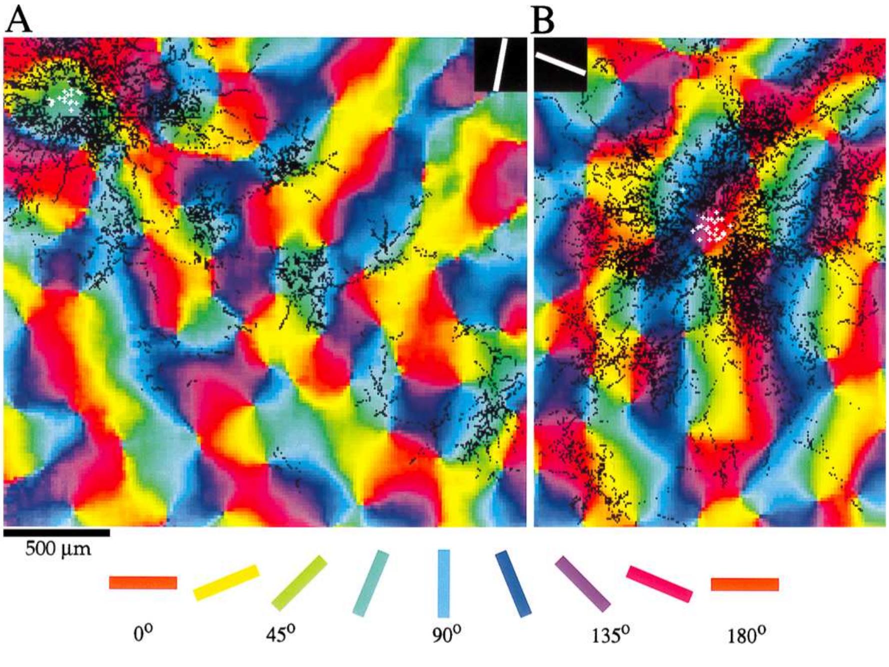

Figure 6.2: *Reconstruction of axonal boutons distibution (black) from a pool of biocytin-injected pyramidal neurons (white crosses) in layer II/III of the tree shrew visual cortex. A central patch of radius ∼500μm is observed, that shows no orientation selectivity. Surrounding smaller patches more acutely match areas with similar orientation preference to the preferred orientation of the injection site. The white bar at the corner of each image indicates the preferred orientation of the injected site (From [14]).*

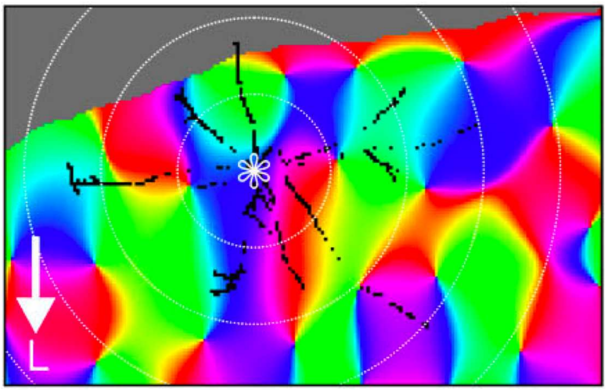

Figure 6.3: *Projections originating from a single layer III PC. They do not show particularly patchy nor selective characteristics (the white arrow shows the lateral direction) (From [19]).*

One last striking feature in PCs long-range projections is the anisotropy observed in the spatial distribution of patches. It appears that the main direction of this distribution is orthogonal to the preferred orientation of the injected site (see figure 6.2).

Large basket cells also make trans-columnar projections, up to one or two millimeters, but these are not patchy and have a lesser, 2-3 times smaller spatial extent than projections from excitatory cells (see figure 6.4) [65].
However, these projections show distance-dependent selectivity according to orientation as well as direction preference. In [64] the authors observe that specificity expresses in two features of the axonal arbour of a large basket cell. The proximal and distal parts of the arbour have distinct orientation and direction selectivities. While local projections show similar preferences to that of the parent soma, distal ones terminate most frequently in regions of non-preferred orientation and opposite preferred direction. Moreover, the axonal arbour of large basket cells can be dissected into two main trees bifurcating near the soma of the cell, which show different orientation selectivity in their distal parts.
So, inhibitory horizontal projections would mainly have two functional roles: distally supressing non-preferred responses, and proximally helping to sharpen orientation and direction tunings because of their looser selectivity compared to excitatory projections.

6.1.2 Barrel cortex of the rat

The barrel cortex of the rat has a striking columnar organization in layer IV (see figure 1.7). This layer can be divided into two main regions: the barrels, that somatotopically correspond to whiskers, and the septa, made of the neurons lying between the barrels. Evidence has been shown that barrel- and septum-related pathways are partially segregated. Barrels and septa receive sensory input from different subcortical pathways, and in layer IV, septum cells preferentially innervate other septum cells while barrel cells mostly innervate neurons in the same barrel. This segregation extends to layer II/III because of the focused vertical projections from layer IV spiny cells [16, 62]. We now focus on the connectivity among barrel-related columns defined

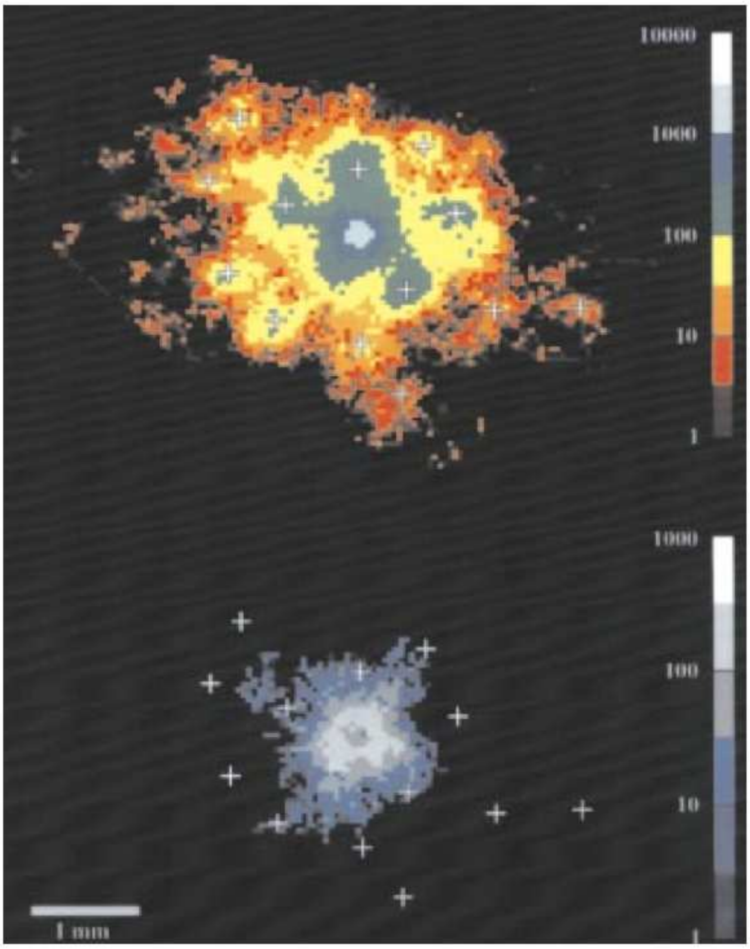
10000
1000
100
10
1
1000
100
10
1
1 mm

Figure 6.4: *Comparative distributions of bouton density for pyramidal (up) and basket cells (down). PCs axonal projections form long-range clusters (white crosses) while basket cells ones do not and are less widely spread (From [65]).*

by the width of barrels in layer IV and spanning the whole depth of the cortex.
Layer IV neurons are basically limited to processing information that originates from the associated whisker and form the predominant source of excitatory inputs to layer II/III, that occur on the basal dendrites of PCs in the same column. On the contrary, layer II/III exhibits both intra- and trans-columnar interactions. So, it appears that this circuitry ensures the segregation of specific tactile stimuli (in layer IV) as well as the transfer of information to neighbouring columns (in layer II/III).
Projections from layer II/III are spatially biased. In this layer, the activity of a single barrel can spread laterally in an oval pattern, preferentially along the rows of the barrel field (corresponding to horizontal rows of whiskers on the rat's muzzle), as anatomically suggested by the bias of elongation in the direction of barrel rows observed in apical dendrites and axonal arborizations of layer II/III PCs (see figure 6.5 and 1.12). This elongation is also observed in the dendritic trees of deep layers PCs.

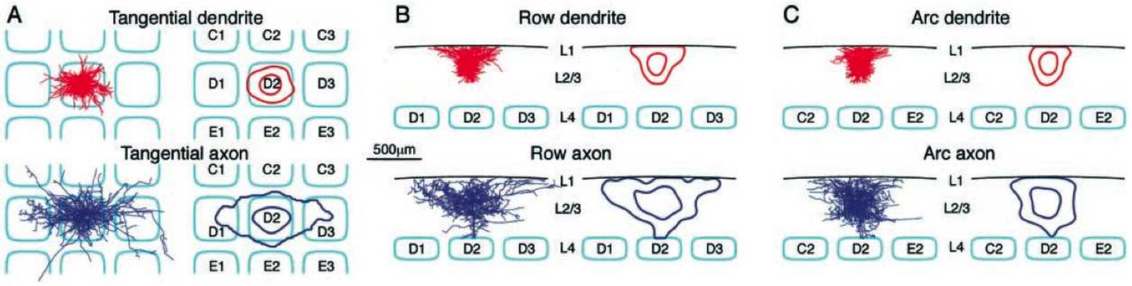

Figure 6.5: *A. Coronal view of rat barrel cortex (barrels in layer IV are delineated by light blue lines, showing three rows, C, D and E, and three arcs, 1, 2 and 3) showing the preferred elongation of axonal and dendritic trees of layer II/III PCs in the direction of rows. B-C. Corresponding side views (From [89]).*

6.2 SIMULATIONS

6.2.1 Visual cortex

The line-motion illusion

The line-motion illusion illustrates a well-known Gestalt principle: non-moving stimuli can induce illusory motion perception. A movie displays a static square for a short period of time, followed by a very short period with no stimulus, and then displays a static bar (rectangle). So the movie is a simple square-blank-bar sequence of static stimuli (see figure 6.6-a). The visual impression is different: it feels like the square is growing into the bar (see figure 6.6-b). Recent experimental findings report that a correlate of the line-motion illusion has been observed, by VSDOI techniques, in the visual cortex of anaesthetized cats [57].
The experimental paradigm is the following. Cats have been shown several stimuli while their cortical activity was simultaneously monitored by VSDOI and extracellular recordings: a static square stimulus, corresponding to the line-motion paradigm where the part displaying the bar has been truncated (see figure 6.6-c), a static bar

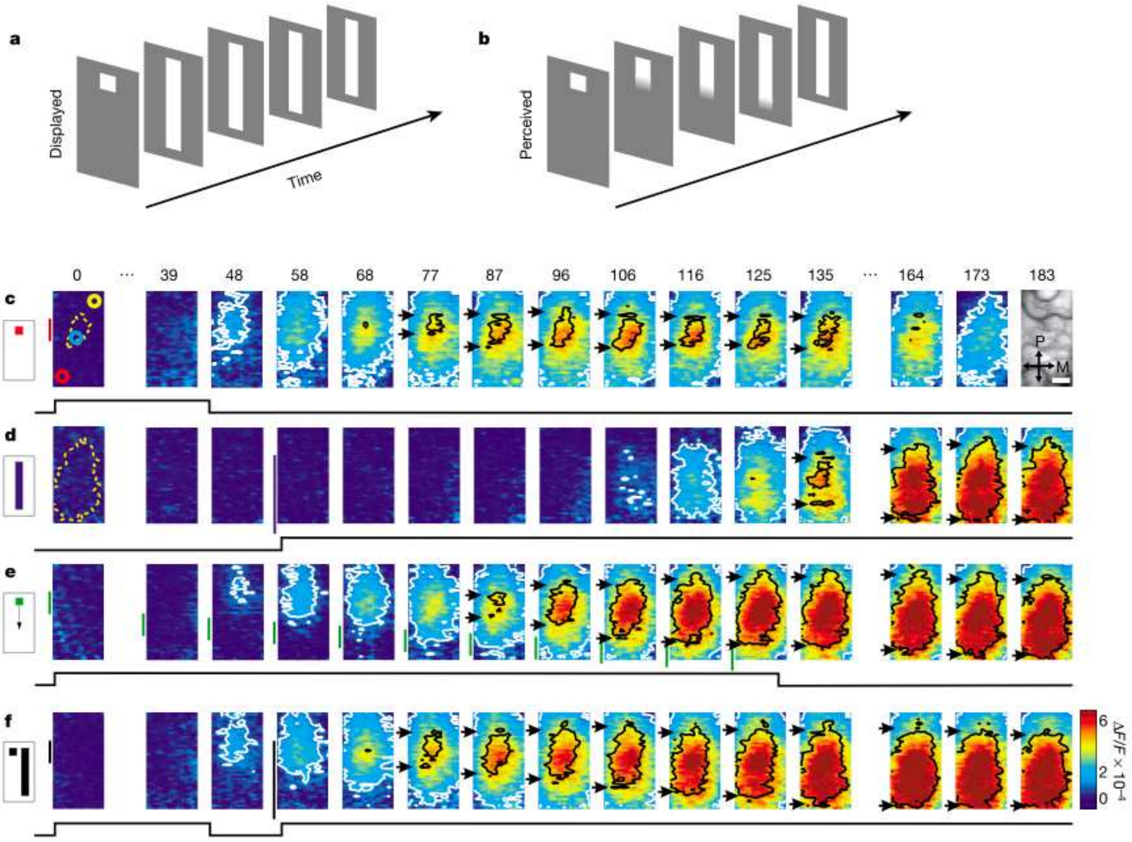

Figure 6.6: *Line-motion illusion and its cortical correlates. (a) Stimulus of the line-motion paradigm. (b) Corresponding illusory motion percept. (c-f) Optical signals recorded for different stimuli (c: flashed small square, d: flashed bar, e: moving small square, f: line-motion paradigm). Stimuli are indicated on the left, their duration at the bottom of optical sequences and time after stimulus onset (in milliseconds), at the top of the panels. Yellow dotted contours approximate retinotopic representation of the stimuli; colored circles indicate extracellular recording sites; white contours delimit low-amplitude activity and black contours, high-amplitude activity. Color scale indicates averaged fractional changes (i.e. normalized with ongoing activity without stimulation) in fluorescence intensity. The cortical area imaged is shown in the upper right panel. Scale bar: 1 mm, P: posterior, M: medial. (From [57]).*

stimulus, corresponding to the line-motion paradigm where the part displaying the square has been truncated (see figure 6.6-d), a moving square stimulus (see figure 6.6-e) and the line-motion paradigm (see figure 6.6-f). Results are shown in figure 6.6. In the line-motion paradigm, the optical pattern induced by the square (compare to figure 6.6-c) grows into the optical pattern induced by the bar (compare to figure 6.6-d). The propagation of the neuronal activity has been confirmed by the simultaneous extracellular recordings, showing that the propagation is not due to a property of optical imaging signals. Moreover, the optical signal obtained in the line-motion paradigm is similar to the signal obtained with a moving stimulus (compare e and f). These results suggest that the line-motion illusion has a correlate in terms of neuronal activity in V1.

Parametrization

We try to reproduce the optical signals presented in figure 6.6.
To that purpose we simulate the activity-based neural field (5.2) with the following parameters:

- *Populations*. We use the populations proposed in [49] ($N = 6$): three layers (II/III, IV and V) with excitatory and inhibitory neurons in each.

- *Field* Ω. Square domain $[0,1] \times [0,1]$ with a side length of $1cm$, discretized in 100×100 units. No orientation preference consideration is made.

- *Time*. We integrate the equation over 80 time steps of $2.5ms$, corresponding to a total duration of $200ms$.

- *Synaptic time constants* **L**. Two synaptic time constants: $\tau_e = 100ms$, used for all excitatory neurons, and $\tau_i = 200ms$ for all inhibitory neurons. Inhibitory postsynaptic potentials are indeed slower than excitatory ones. The time constant of real EPSPs is around $10ms$ and the one of GABA-mediated IPSPs around $100ms$ [97]. However we choose slower synaptic characteristic times to ensure the stability of the numeric scheme we have used for simulations.

- *Wave-to-pulse transforms* **S**. Two transforms: S_e (for all types of excitatory cells) and S_i (for all types of inhibitory cells), of the form

  $$S_x(v) = \frac{\overline{\nu}_x}{1 + \exp(r_x\,(v_0^x - v))}, \quad x \in \{e, i\},$$

  with maximal firing rates $\overline{\nu}_e = \overline{\nu}_i = 7.5Hz$, gains $r_e = r_i = 0.5mV^{-1}$, and excitability thresholds $v_0^e = 3mV$ and $v_0^i = 6mV$. Inhibitory neurons are indeed less excitable than excitatory ones. However, their maximal firing rates are usually higher than the ones of excitatory cells, which has not been taken into account here.

- *Connectivity* **W**. We choose translation-invariant connectivity kernels $W_{ij}(\mathbf{r} - \mathbf{r}')$, defined on $\widehat{\Omega} = [-1,1] \times [-1,1]$, and define *global weights* as

  $$\overline{W}_{ij} = \int_{\widehat{\Omega}} W_{ij}(\mathbf{r})\,d\mathbf{r}.$$

Vertical connectivity is defined by the global weights and horizontal connectivity, by normalized connectivity kernels

$$\widehat{W}_{ij}(\mathbf{r}) = W_{ij}(\mathbf{r})/\overline{W}_{ij}, \quad \mathbf{r} \in \widehat{\Omega},$$

so that

$$\int_{\widehat{\Omega}} \widehat{W}_{ij}(\mathbf{r})\, d\mathbf{r} = 1.$$

The global weights are set in agreement with the six population model proposed in [49] (see figure 1.20). They are scaled by k_{ij}, w_{ij} and N_j. k_{ij} and w_{ij}, the average synaptic gains and connection probabilities, are given in figure 1.20. As concerns N_j, we consider columns with 160 excitatory neurons and 40 inhibitory neurons (in agreement with proportions reported for mammals cortex), and distribute them equally among layers (this choice is supported by recent experimental findings [12]). A color-coded version of the vertical connectivity matrix $\overline{\mathbf{W}}$ is given in figure 6.7.

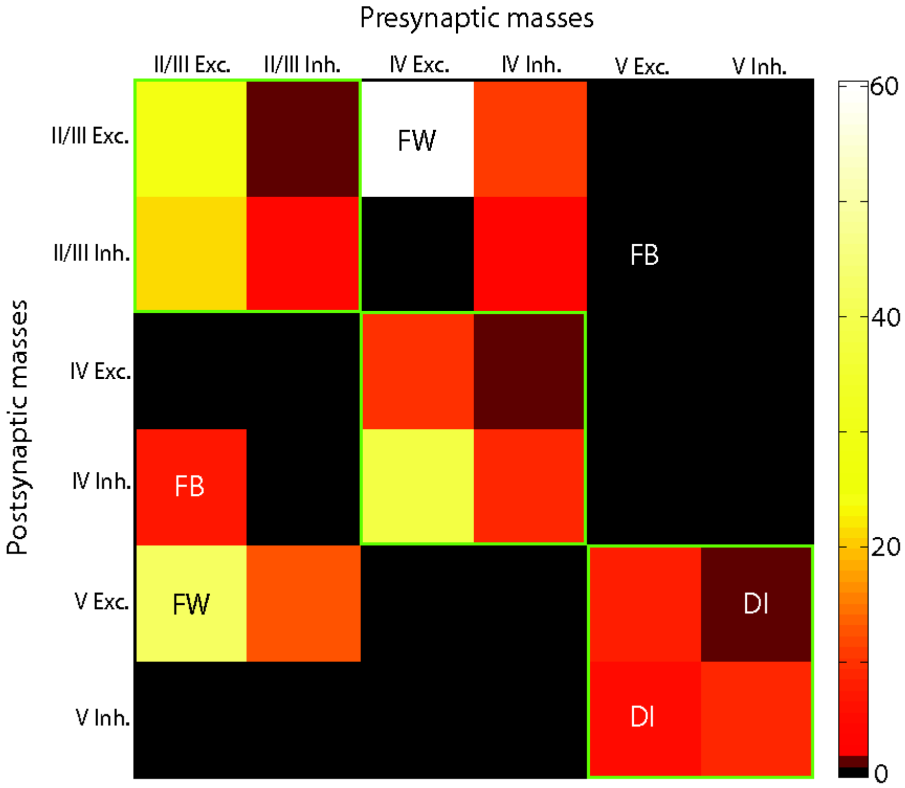

Figure 6.7: *Color-coded vertical connectivity matrix (connection strength* $\overline{W}_{ij}$ *is expressed in* mV*). Green squares indicate intralaminar connections. Well-identified pathways are also mentioned: excitatory forward (FW) and feedback (FB) interlaminar pathways, as well as connections involved in disynaptic inhibition (DI). The feedback arising from layer V PCs and connections corresponding to disynaptic inhibition are probably underestimated in this model, due to a lack of available connectivity data.*

The form of the $\widehat{W}_{ij}$s mostly depends on the horizontal spread of the axonal arbors of neurons of type j[1], and on whether they make patches or not. Local projections from inhibitory neurons are modeled by a circularly symmetric Gaussian distribution with a standard deviation (SD) of $0.7mm$. Projections from layer IV excitatory cells, among which spiny stellate excitatory interneurons are largely represented, are also modeled by a unique local patch, but with a larger extent ($SD = 0.8mm$) to account for longer range projections made by layer IV PCs (see figure 6.8).

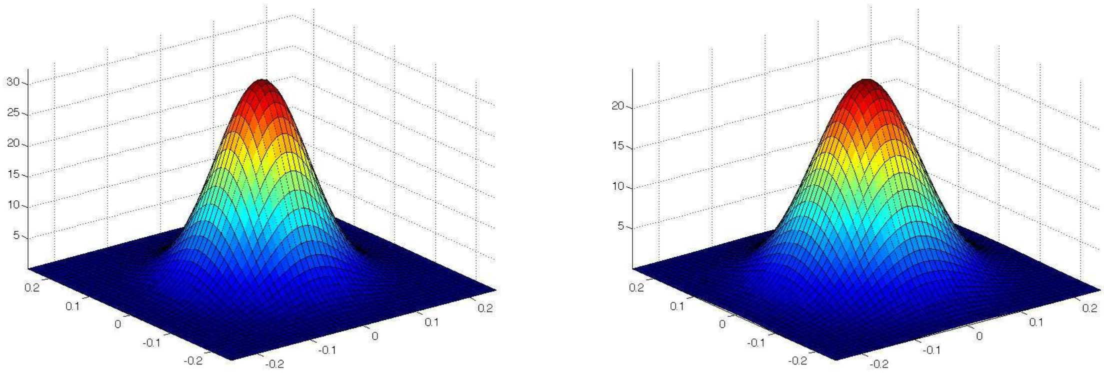

Figure 6.8: . *Form of the non-patchy projections made by inhibitory neurons (left) and layer IV spiny cells (right), represented on a subdomain of* $\widehat{\Omega}$ *(abscissas are expressed in* cm*).*

Finally, projections from PCs in layers II/III and V (see figure 6.9) are modeled by a central local patch $\widehat{W}_{ij}^{\mathrm{c}}$ ($SD = 0.4mm$) surrounded by six satellite patches of the same extent, forming the component $\widehat{W}_{ij}^{\mathrm{sat}}$. Hence

$$\widehat{W}_{ij} = \widehat{W}_{ij}^{\mathrm{c}} + \widehat{W}_{ij}^{\mathrm{sat}}.$$

The distance between the center of the central patch and the centers of the satellite patches is set to $1.25mm$. Actually, most projections corresponding to satellite patches do not stand for local projections in the sense of local connectivity studies, because they outreach the extent of a cortical column. Hence the global weight obtained from local connectivity studies for PCs projections should be mainly attributed to the central patch. So as j corresponds to a PC population, we choose

$$\int_{\widehat{\Omega}} \widehat{W}_{ij}^{\mathrm{c}}(\mathbf{r})\,d\mathbf{r} = 1 \quad \text{and} \quad \int_{\widehat{\Omega}} \widehat{W}_{ij}^{\mathrm{sat}}(\mathbf{r})\,d\mathbf{r} = 1,$$

so that

$$\int_{\widehat{\Omega}} \widehat{W}_{ij}(\mathbf{r})\,d\mathbf{r} = 2.$$

This choice is in good agreement with biological data, since in [19], the authors report a number of axonal boutons in the central patch equivalent to the number of boutons in all satellite patches.

---

[1] Here we neglect the extent of the dendritic trees of neurons of type i.

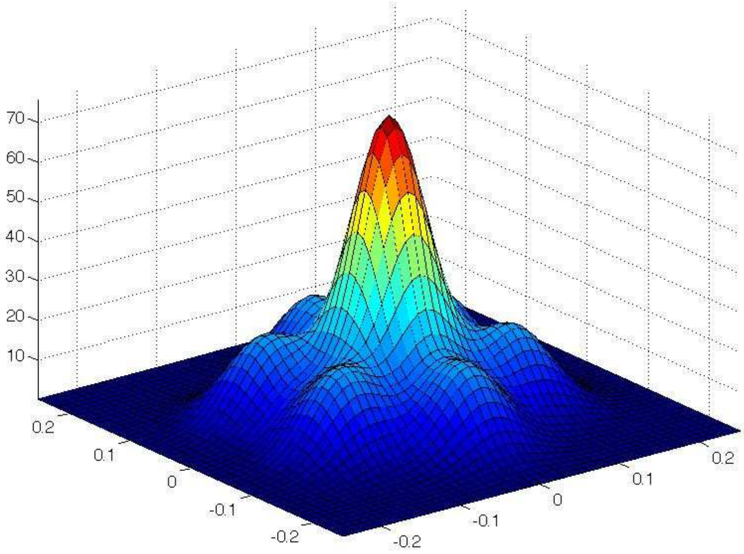

Figure 6.9: *Form of the patchy projections made by PCs from layers II/III and V, represented on a subdomain of* $\widehat{\Omega}$ *(abscissas are expressed in* cm*).*

- *Input* $\mathbf{I}_{\text{ext}}$. The input terms correspond to the various paradigms we want to simulate, modified by a spatiotemporal regularization accounting for the effect of the retino-cortical pathway. So to obtain $\mathbf{I}_{\text{ext}}$ the stimulus is first convoluted with a Gaussian spatial kernel ($SD = 0.35mm$), modeling the horizontal spread of afferent thalamic fibers in layer IV.
  Then a temporal kernel $T(t)$ of the form

  $$T(t) = \begin{cases} e^{-t/\tau}/\tau & t \geq 0 \\ 0 & t < 0 \end{cases}, \quad \tau = 35ms$$

  moderates the signal, accounting for both retino-thalamic persistence and adaptation to the visual input [1]. This kernel acts as follows. Any newly activated pixel in the stimulus sequence will follow the time course of T, regardless of whether the pixels continues to be activated or not. Hence transiently activated pixels will persist at the level of the thalamo-cortical input and persistently activated pixels will undergo adaptation. This retino-thalamic temporal regularization, as suggested in [95], is crucial in the moving square case.
  A delay of $40ms$ for visual input arrival to the cortex is modeled by giving $\mathbf{I}_{\text{ext}}$ an initial $40ms$ of blank, followed by the stimulus. In stimuli, the background is set to zero and light patterns (square or bar) to one. Stimuli project exclusively on layer IV, with an equal repartition between excitatory and inhibitory neurons. The stimuli and the corresponding inputs to the cortex are shown in figure 6.10.

- *Optical signal*. Since dendritic trees lying in layer I-III are the main contributors to the optical signal, we choose to neglect contributions from other layers ($n_{\text{I-III}} = 1$ and other n_ls set to zero). Layer I-III mostly contains dendrites belonging to all types of neurons from layers II/III and PCs from layer V (see

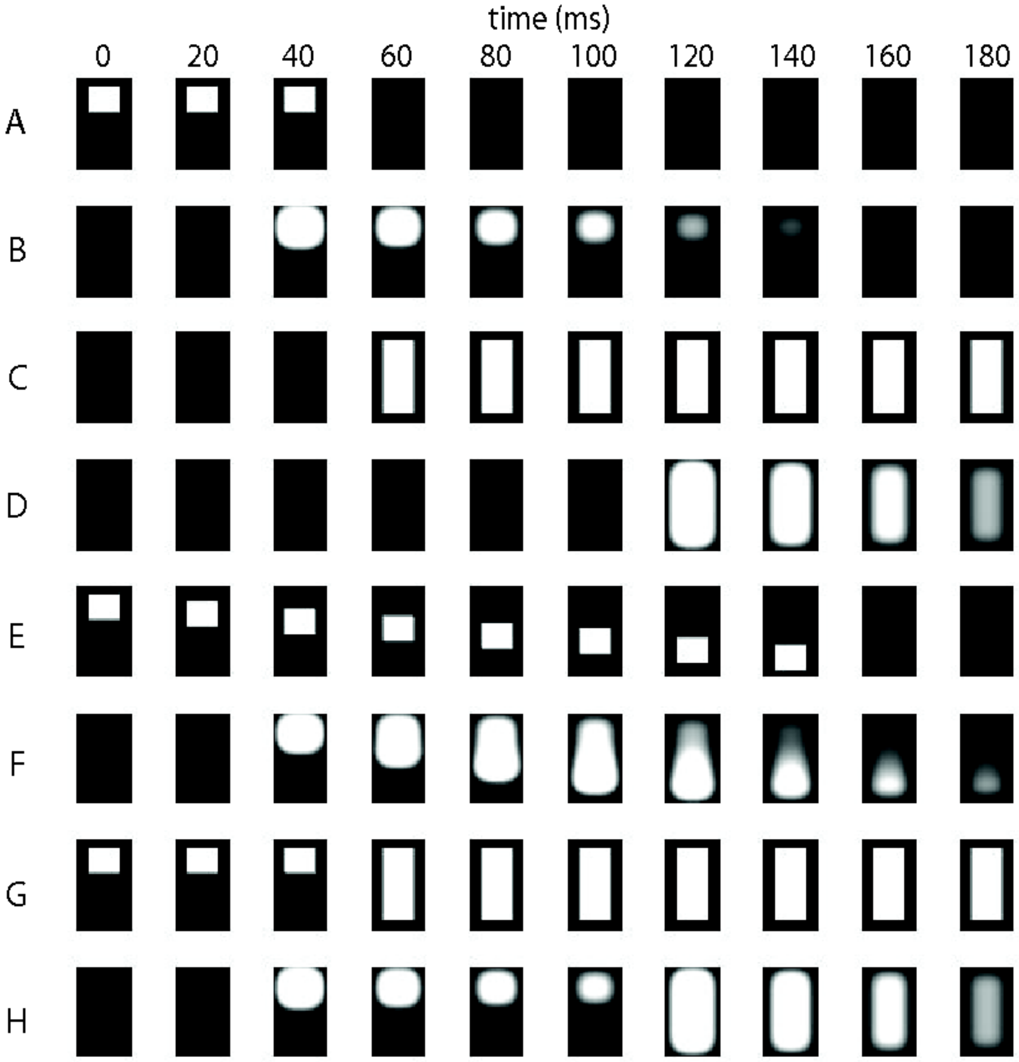
time (ms)
0
20
40
60
80
100
120
140
160
180
A
B
C
D
E
F
G
H

Figure 6.10: *Stimuli and corresponding cortical inputs obtained after spatio-temporal regularization and time translation. They are presented on a subdomain of* Ω *(*$[0.35, 0.65] \times [0.25, 0.75]$*). A-B: square, C-D: bar, E-F: moving square, G-H: line-motion paradigm.*

figure 1.14). Hence, up to a multiplicative constant, the optical signal is

$$\sum_{j=1}^{N} \int_{\Omega} \left(\sum_{i=1}^{3} N_i \, s_i^{\text{I-III}} \, \alpha_{ij}^{\text{I-III}} \, W_{1j}(\mathbf{r}, \mathbf{r}') \right) A_j(\mathbf{r}', t) \, d\mathbf{r}',$$

where $i = 1, 2$ and 3 are, respectively, the indices of layer II/III PCs, layer V PCs and superficial layers interneurons. Now, for clarity, we choose to normalize the coefficients $N_i \, s_i^{\text{I-III}} \, \alpha_{ij}^{\text{I-III}}$ by $N_1 \, s_1^{\text{I-III}} \, \alpha_{1j}^{\text{I-III}}$. We consider that $s_1^{\text{I-III}} \approx s_2^{\text{I-III}}$ and that $N_1 = N_2$ (as assumed in the model). PCs from layer II/III receive all their inputs at the level of layers I-III ($\alpha_{1j}^{\text{I-III}} = 1$) and we assume that PCs from layer V receive half of all their inputs on their superficial dendrites ($\alpha_{2j}^{\text{I-III}} = 1/2$). Hence the normalized coefficient for layer II/III PCs is 1 and the one for layer V PCs, $1/2$. The diameter and total length of interneurons dendrites are inferior to the ones of PCs [12, 13]. Hence the normalized coefficient of inhibitory cells is less than N_2/N_1. We choose it to be $1/10$. So we end up with

$$OI(\mathbf{r}, t) \approx \sum_{j=1}^{N} \int_{\Omega} \left(W_{1j}(\mathbf{r}, \mathbf{r}') + \frac{1}{2} W_{2j}(\mathbf{r}, \mathbf{r}') + \frac{1}{10} W_{3j}(\mathbf{r}, \mathbf{r}') \right) A_j(\mathbf{r}', t) \, d\mathbf{r}'.$$

Results

Figure 6.11 shows the optical imaging sequences obtained from the simulation of the neural field with different stimuli (the observation window is a rectangle of side lengths $3mm$ and $5mm$). The corresponding movies (square.avi, bar.avi, moving.avi and linemotion.avi) can be found in the supplemental material. As in [57], we have normalized the results with blanks (i.e. simulations of a field receiving no input). The intensity of the signal is then expressed as a percentage.
We have been able to reproduce the main features of the optical signals from figure 6.6.

- The optical signals corresponding to the moving square and the line-motion paradigm have similar temporal sequences.
- In both cases, the activity pattern induced by a square stimulus progressively grows into the pattern induced by a bar stimulus[2].
- In the case of the line-motion paradigm, the spatial propagation of activity is obtained with a static input.
- The cortical input corresponding to a *growing square* stimulus (featuring a square growing into a bar) is exactly the same as the one corresponding to the moving square, as an effect of the spatio-temporal regularization. Hence, the optical activity induced by this stimulus is identical to the one obtained for the moving square. This is in good agreement with the results of [57], where the authors observe a very good match between the optical signals recorded for the growing square, the moving square and the line-motion paradigm.
- High activity is maintained for the duration of the simulation, even in the absence of a strong input, for all stimuli but the square.

---

[2] In the moving square case, a bleeding input has been necessary to keep a homogeneous level of signal on the whole extent of the bar pattern.

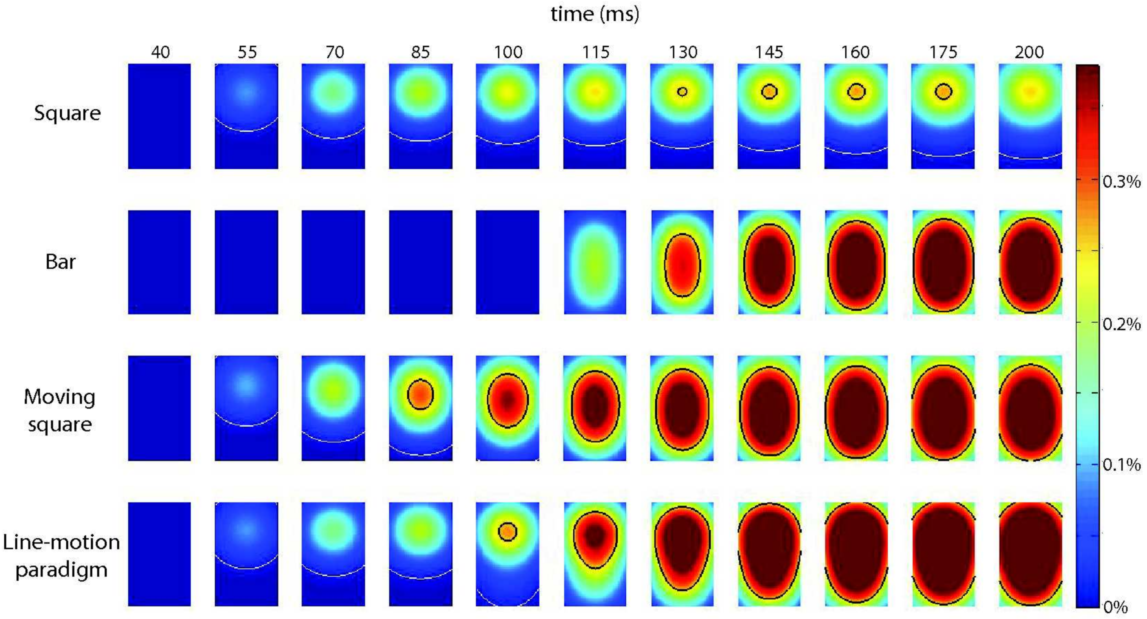

Figure 6.11: *Simulated optical sequences obtained for different stimuli and reproducing the main features of experimental results (see text). White lines delineate low-level activity ($OI < 0.002\%$) and black lines, high-level activity ($OI > 0.25\%$).*

6.2.2 Barrel cortex

Now we try to reproduce the spread of activity in the barrels of the rat's sensory cortex as one whisker is stimulated with different intensities. The results of this experimental paradigm are shown in figure 1.12 [89]. A weak stimulation of a single whisker induces a low, transient activation of the corresponding barrel. As the stimulation strength is increased, cortical activity propagates to the row of the excited barrel. As the stimulation gets strong enough, the activity propagates to the whole barrel field.

Parametrization

For this simulation we use the same neuronal populations, neural field equation, synaptic time constants, wave-to-pulse transforms and optical signal as for the visual cortex case. Changes in parametrization are given below.

- *Field* Ω. Square domain with a side length of $1mm$, discretized in 100×100 units. Barrels and septa regions are segregated (see figure 6.12).

- *Time*. We integrate the equation over 50 time steps of $1ms$, corresponding to a total duration of $50ms$.

- *Connectivity* $\mathbf{W}$. Vertical connectivity is the same as in the visual cortex case. Horizontal connectivity depends on barrels and septa and on the involved types of neurons. We consider two two-dimensional Gaussian distributions G_1 and G_2. G_1 is isotropic and has a small standard deviation $SD = 80\mu m$. G_2 is elongated

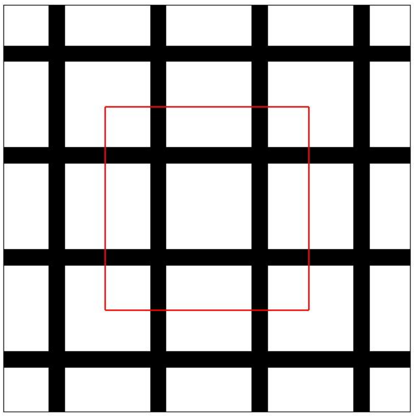

Figure 6.12: *The field Ω is separated into two regions: barrels (in white) and septa (in black). The red contour delineates the observation window on which we will display the results of the simulations.*

in the direction of barrel rows and is defined by two standard deviations corresponding to its principal axes: $SD = 80\mu m$ and $SD' = 400\mu m$ (see figure 6.13).

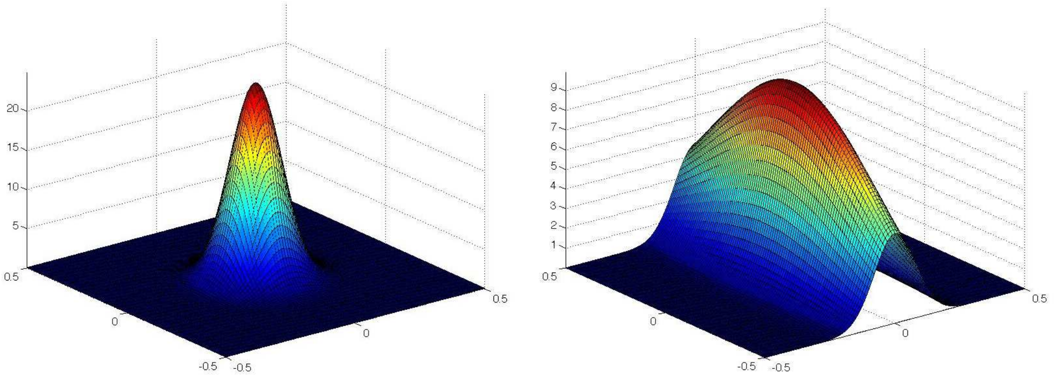

Figure 6.13: *Gaussian connectivity kernels. G_1 (left) is isotropic and has a standard deviation $SD = 80\mu m$. G_2 (right) is elongated in the direction of barrel rows ($SD' = 400\mu m$).*

If the presynaptic neurons belong to a column of the septum, $\widehat{W_{ij}} = G_1$ for all couples (i, j). Hence, septum masses mostly innervate other septum masses in their immediate neighborhood. If the presynaptic neurons belong to a barrel and are not layer II/III PCs, we also have $\widehat{W_{ij}} = G_1$. Hence they mostly target neurons from the same barrel. When presynaptic neurons are layer II/III PCs belonging to a barrel, they can reach more distant postsynaptic targets: neurons in the same layer, via their elongated axonal projections, and layer V PCs, whose basal dendritic trees are also elongated. So $\widehat{W_{ij}} = G_2$ if i is the index of layer II/III PCs, layer II/III inhibitory cells, or layer V PCs. Otherwise, $\widehat{W_{ij}} = G_1$.

- *Input* $\mathbf{I}_{\text{ext}}$. The stimuli are brief and spatially focused stimulations with no bias of elongation in the direction of rows or arcs. The conversion of the stimuli into proper cortical inputs is made by spatiotemporal regularization. We use a temporal kernel T' of the form

$$T'(t) = \begin{cases} t\,e^{-t/\tau}/\tau^2 & t \geq 0 \\ 0 & t < 0 \end{cases}, \qquad \tau = 20ms,$$

and Gaussian spatial kernels that depend on the strength of the stimulus. Indeed stimuli differ by both acceleration and angle, so that we considered that larger deflection angles induced broader stimulations of the central barrel. Hence, although inputs remain confined to the central barrel, we use spatial kernels with different widths to model the different deflection angles used in [89] (see figure 6.14). As in the visual cortex case, we added a delay ($10ms$) for the arrival of the stimuli to layer IV.

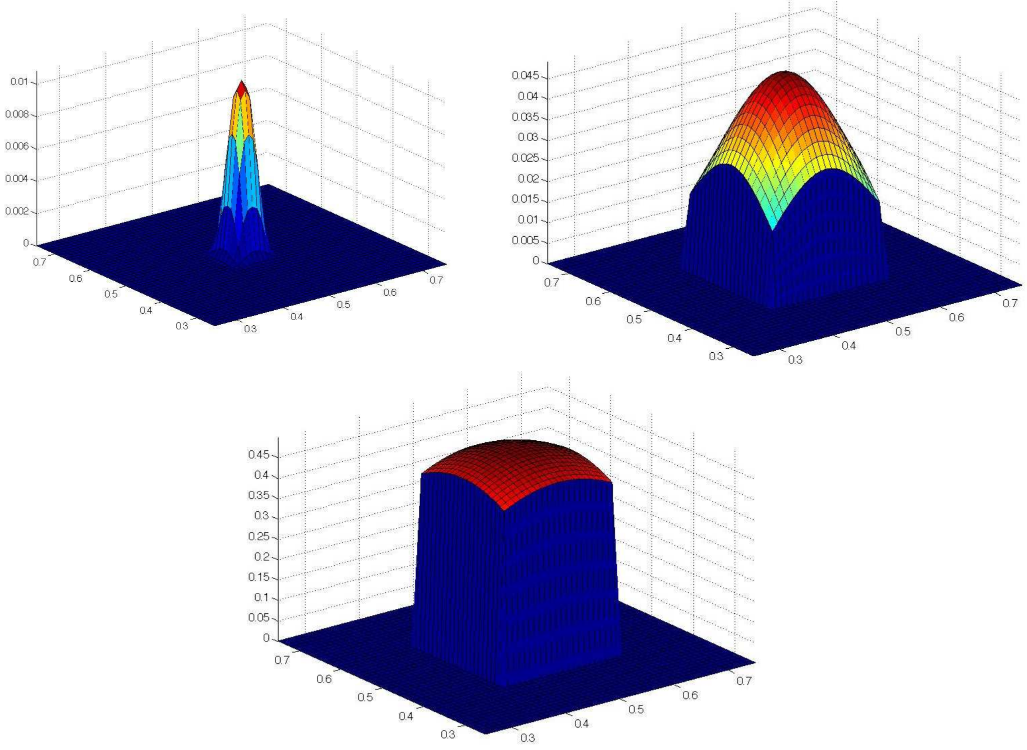

Figure 6.14: *Form of the single whisker stimulations used in the simulations, represented on the observation window domain. All of these stimuli are restricted to the excited barrel and are obtained from isotropic Gaussian kernels. On the upper left panel, a narrow, low intensity input corresponds to a weak stimulation. On the upper right panel, a stronger and wider input accounts for moderate stimulation. The input corresponding to a strong stimulation is represented on the lower panel and shows larger horizontal extent and intensity.*

Results

The results of the simulations are given in figure 6.15. The corresponding movies (rat_weak.avi, rat_moderate.avi and rat_strong.avi) can be found in the supplemental material.

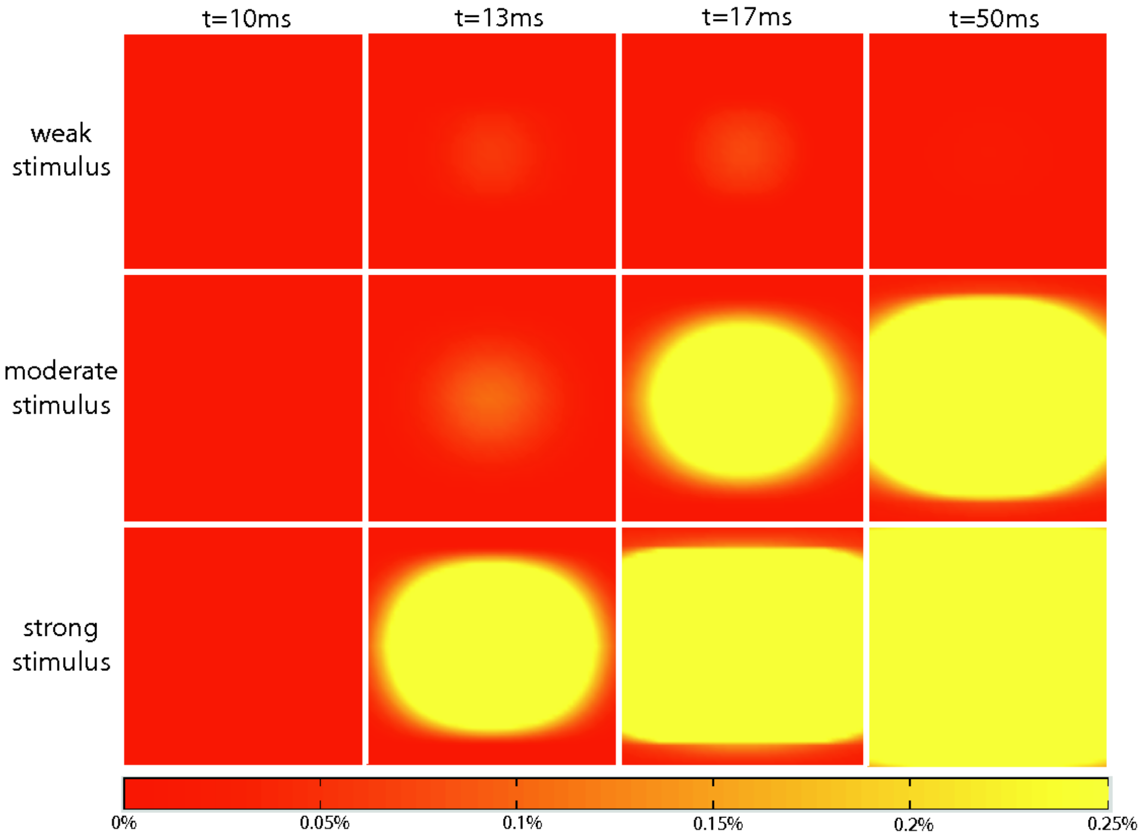

Figure 6.15: *Simulated optical sequences obtained for different intensities of single whisker stimulation. They reproduce the main features of the experimental results presented in [89]. A weak stimulation induces a weak and transient activation of a single barrel (upper panel). As the stimulation intensity increases, the activity propagates to a whole barrel row (middle panel). For strong stimulations, the activation spans the whole barrel field (lower panel).*

The simulations reproduce the main features of the experimental results reported in [89]. For a weak stimulation, we observe a low, transient and isotropic activation of the central barrel. For a moderate stimulation, we first observe an isotropic activity pattern which progressively gets elongated in the direction of the barrel row. The activation fails to propagate efficiently to other rows and remains confined in the row of the stimulated whisker. If the stimulation is strong and wide enough, excitation propagates to other rows, leading to a rapid activation of the whole barrel field.

6.3 DISCUSSION

Starting from biophysical neural field models of sensory cortices and using the direct problem formula developed in the previous chapter, we have been able to reproduce realistic optical imaging sequences from various experimental settings. No sophisticated parameter tuning method (like least square optimization) has been used in this study, showing that the phenomena reproduced here are reliably accounted for by neural field models.

The simulations that we have presented in this chapter mainly involved two phenomena: propagation and persistence of cortical activity.
Propagation of the signal is chiefly a matter of horizontal connectivity: wide horizontal connectivity kernels guarantee a good horizontal propagation. A bias in the direction of propagation can be induced by a bias in the form of the kernels (case of the rat barrel cortex) or by a moving thalamic stimulation (case of the moving square). In the line-motion paradigm, the field is fed by static stimuli and propagation is a nonlinear effect caused by simultaneous contributions from horizontal projections and thalamic inputs: a thalamic stimulation in the neighborhood of an active domain of the field induces a propagation of the activity to the stimulated area. In a linear model, the activation pattern caused by the appearance of the bar in the line-motion stimulus would not induce a propagation of the square pattern to the bar pattern, but a progressive, spatially homogeneous activation of the bar pattern.
The neural field model naturally shows persistence, even in the absence of thalamic stimulation, thanks to the finite speed of dendritic processes. However, a stronger persistence effect is needed in the moving square case. The determining parameter for this phenomenon is the latency of the retino-thalamic pathway τ. τ has been set long enough for the moving square activation to persist on the whole length of the bar activity pattern, and short enough to avoid a strong, sustained thalamic stimulation leading to inhomogeneities in the activation patterns. For example, in the line-motion paradigm, a sustained, strong excitation during the square part of the stimulus will make the subsequent activation due to the rest of the bar relatively small, while we want an homogeneous activation of the pattern induced by the bar, as a natural effect of adaptation.

Biophysical models are probably not necessary to reproduce the most basic features of the optical signals and it would be interesting to develop minimal models for which a rigorous mathematical explanation of the observed phenomena would be tractable. For example, connectivity patches are not needed in the neural field corresponding to the visual cortex for the model to reproduce experimentally observed phenomena. The crown of satellite patches surrounding the central patch of excitatory kernels could be replaced by an isotropic annulus. Although, the models should not be oversimplified. Following the same example, if we replace the patchy connectivity kernels by simple Gaussians, we will observe undesirably narrow or broad spreads of activity. This is avoided in our simulations thanks to the predominance of inhibition between the central excitatory patch and the satellite patches, preventing localized inputs to provoke too broad activations and allowing extended inputs to induce extended activations, via long-range excitation (see figure 6.16).
So, although some aspects of the model could be simplified, the very general framework of neural fields allowed us to integrate biologically plausible parameters and to account for the organizing principles of different cortices within a relatively small set of parameters.

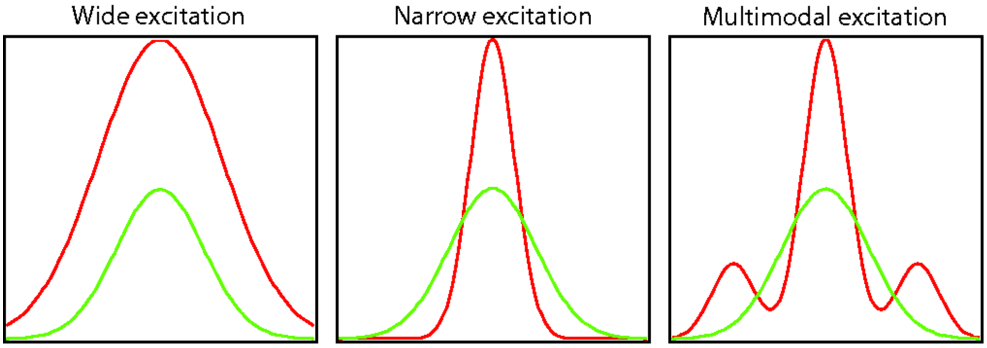

Figure 6.16: *Unimodal vs multimodal excitation. Excitatory (resp. inhibitory) kernels are represented in red (resp. green).Unimodal excitatory connectivity kernels can have two effects on the horizontal propagation of activity. A wide unimodal excitatory kernel that dominates inhibition (left) can induce too broad activations of the field. On the contrary, a narrow unimodal excitatory kernel (center) does not allow broad activations. Finally, a multimodal kernel moderates the spread of localized stimulations thanks to middle-range inhibition, and allows widespread activations thanks to long-range excitation.*

Conclusion and perspectives

In this thesis, we have modeled cortical columns and cortical areas using neural masses as elementary building blocks. We have seen that most of the biophysical data needed to make biologically plausible models is available and can naturally be integrated into mesoscopic models. Then we have been able to reproduce biophysical columnar signals, like alpha rhythms or epileptic bursts, and explain their origin by a theoretical study of the bifurcations of the model. As concerns neural fields, we have mathematically characterized several interesting solutions, like bumps or homogeneous states corresponding to synchrony, and we have simulated VSDOI experiments in different cortices, thanks to a biophysical formulation of the direct problem of optical imaging. So, modeling the activity of cortical structures with mesoscopic models based on differential and integro-differential equations allowed us to reproduce different cortical signals with an arbitrary temporal resolution and a spatial resolution of the order of $100\mu m$, corresponding to a cortical column or a pixel of population optical imaging.

With respect to perspectives, we think that several leads could help to improve the models and their understanding.

First, the development and validation of neural field models through the use of optical imaging experiments should be continued. For example, it would be very interesting to integrate orientation preference in a neural field model of the visual cortex, and instead of only reproducing optical experiments, to be able to predict their results with the models. This would provide a better validation of neural field models and make them serious candidates for the resolution of the inverse problem of optical imaging.

Second it would be interesting to validate the mesoscopic models equations mathematically. Starting from a network of individual neurons and using mean field techniques, we could infer new equations for the dynamics of the average membrane potential or average firing rate of different neuronal populations forming a cortical column or a neural field. Furthermore, this framework would make it possible to study the fluctuations of the signal around its mean through a variance equation, hence opening the door to smaller spatial scales.

Finally, the development of recent experimental techniques will probably allow us to refine these mesoscopic models and integrate them in larger scale models of the sensory pathways. For example, Calcium imaging is already used to understand fine columnar mechanisms by providing single cell precision recordings of cortical activity, and progress in diffusion MRI could in the next few years give precise insights on white matter connections between cortical areas.

Appendices

APPENDIX A

FIRING PATTERNS OF CORTICAL NEURONS

Cortical neurons exhibit numerous firing patterns, i.e. characteristic trains of action potentials in response to stimulation by current injections (usually depolarizing pulses).
We first introduce a few basic notions that will be useful for a further description of firing patterns (see figure A.1).

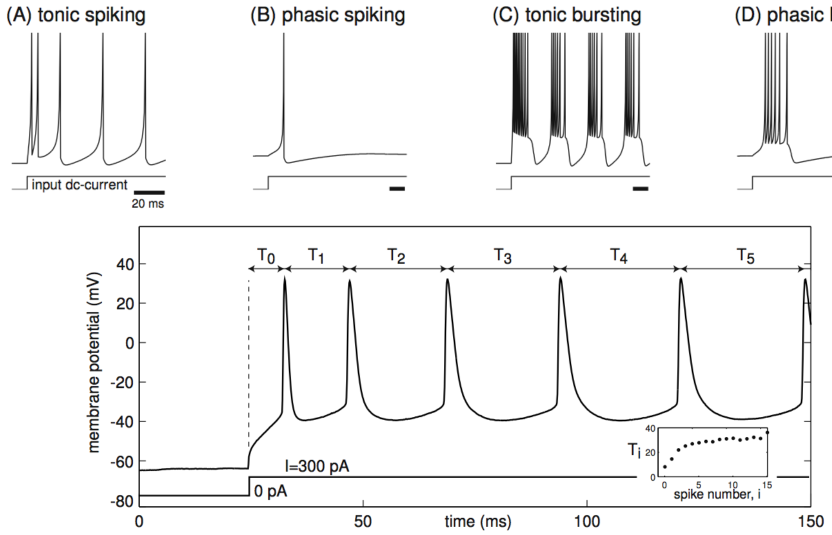

Figure A.1: *Various firing behaviours in response to a sustained depolarizing pulse. Upper panel. Phasic patterns (B,D), tonic patterns (A,C), spiking patterns (A,B) and bursting patterns (C,D). Lower panel. Accommodation of the discharge pattern: interspike intervals increase (From [56]).*

- Tonic and phasic spiking: Tonically spiking cells fire continuous trains of action potentials for the duration of the depolarizing pulse of injected current (see figure A.1-B/D). On the contrary, phasically spiking cells respond to a sustained depolarizing current pulse with a very brief train of action potentials followed by no further firing (see figure A.1-A/C).
- Bursting: Sometimes neurons use rapid clusters of two or more action poten-

tials, called *bursts*, as basic signaling events instead of simple spikes (see figure A.1-C/D).

- Accommodation: Neurons sometimes show spike frequency adaptation, i.e. a decrease of firing frequency in response to a sustained depolarizing pulse. They are said to be *accommodating* (see figure A.1). In contrast, non-accomodating neurons keep a constant discharge frequency to such current injections.

As explained in [56], cortical neurons exhibit six major discharge patterns.

- Regular spiking (RS) is a tonic spiking with adapting frequency in response to a sustained depolarizing pulse. This firing pattern is the most spread among excitatory neurons (see figure A.2).
- Chattering (CH) corresponds to high frequency bursts with a relatively short interburst period. This behaviour has mainly been observed in layer III PCs but also concerns excitatory cells in layers II and IV (see figure A.2).

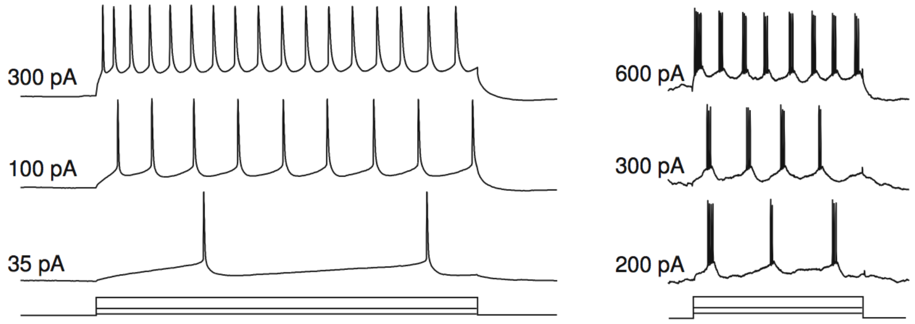

Figure A.2: *Regular spiking (left) and chattering (right) in response to sustained depolarizing pulses of various amplitudes (shown at the bottom of the recordings) (From [56]).*

- Intrinsically bursting (IB) neurons respond with bursts of action potential at the beginning of a strong depolarizing injection, followed by tonic spiking. The main representatives of this firing pattern are found among layer V PCs (see figure A.3).
- Fast spiking (FS) is a high frequency tonic spiking with little adaptation, observed in inhibitory cells (mostly basket and chandelier cells). Fast spiking cells show irregular spiking when injected with weak currents (see figure A.4).
- Low-threshold spiking (LTS) neurons have a tonic firing pattern with strong accommodation. Their name comes from their tendency to exhibit post inhibitory rebounds (spontaneous emission of spikes consecutive to an hyperpolarizing current injection). They can show low frequency firing and phasic responses to weak stimulations (see figure A.4). LTS neurons are inhibitory interneurons (mostly Martinotti, double bouquet and bitufted cells).
- Late spiking (LS) neurons respond to a depolarizing pulse with a slow increase of membrane potential followed, after a delay possibly as long as one second, by low frequency tonic spiking. Late spiking mainly concerns neurogliaform inhibitory interneurons (see figure A.4).

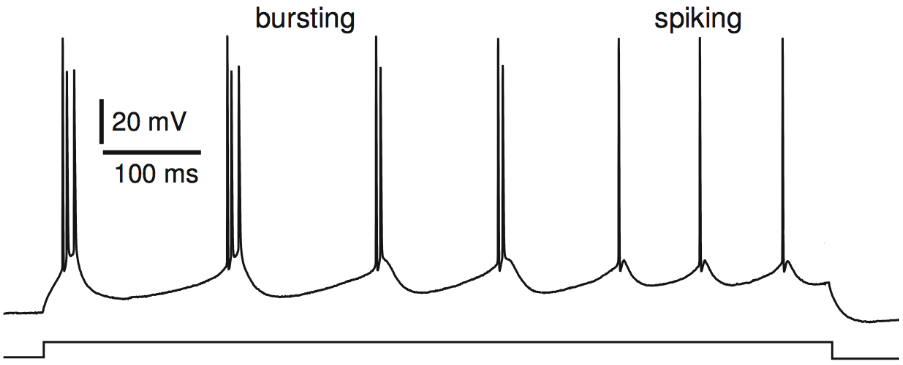

Figure A.3: *Intrinsic bursting in response to a sustained depolarizing pulse. Initial bursting is followed by tonic spiking (From [56]).*

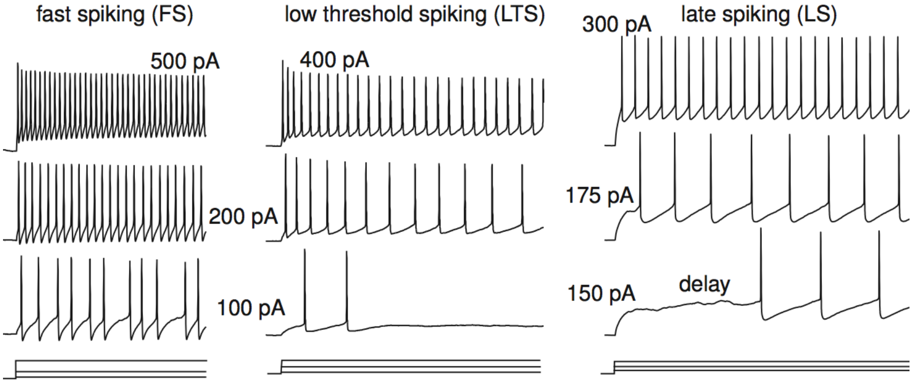

Figure A.4: *Fast spiking (left), low-threshold spiking (center) and late spiking (right) in response to sustained depolarizing pulses of various amplitudes (From [56]).*

It appears from the above description that excitatory and inhibitory cells can both be divided into three electrophysiological classes (RS, CH and IB for excitatory neurons, and FS, LTS and LS for inhibitory interneurons). Actually, the firing patterns displayed by inhibitory cells are way more diversified and an alternative classification has been proposed for them.
In [78], the authors propose the following electrophysiological classes and subclasses to characterize interneurons firing patterns (see figure A.5 and 1.18).

- Non-accomodating (NAC) neurons show tonic firing without spike frequency adaptation in response to a wide range of depolarizing current injections. Many FS and LS neurons exhibit this behaviour. This class of discharge patterns has three subclasses: *c* (classic discharge), *b* (discharge with initial burst) and *d* (discharge with initial delay).

- Accommodating (AC) neurons fire tonically with spike adaptation. Hence they do not reach as high discharge frequencies as NAC cells do. While FS and LS interneurons can exhibit this behaviour, most cells of this type are LTS neurons. This class admits the same subclasses as NAC discharges (c,b and d).

- Stuttering (STUT) can be displayed by some FS and LS cells. It consists in the firing of high frequency clusters of spikes (which are not bursts) separated by unpredictable periods of quiescence. The three subclasses c, b and d are also represented in stuttering patterns.

- Large basket cells are the only interneurons using bursting (BST) as their main signaling event. They fire bursts of spikes after a slow depolarizing wave, followed by strong slow hyperpolarization. This class has three subclasses: *i* (initial burst followed by regular spike emissions) , *r* (repetitive bursting) and *t* (transient, i.e. phasic burst).

- Irregular spiking (IS) cells fire single spikes, in a random fashion, and show strong accomodation. c and b subclasses are represented among irregular firing patterns.

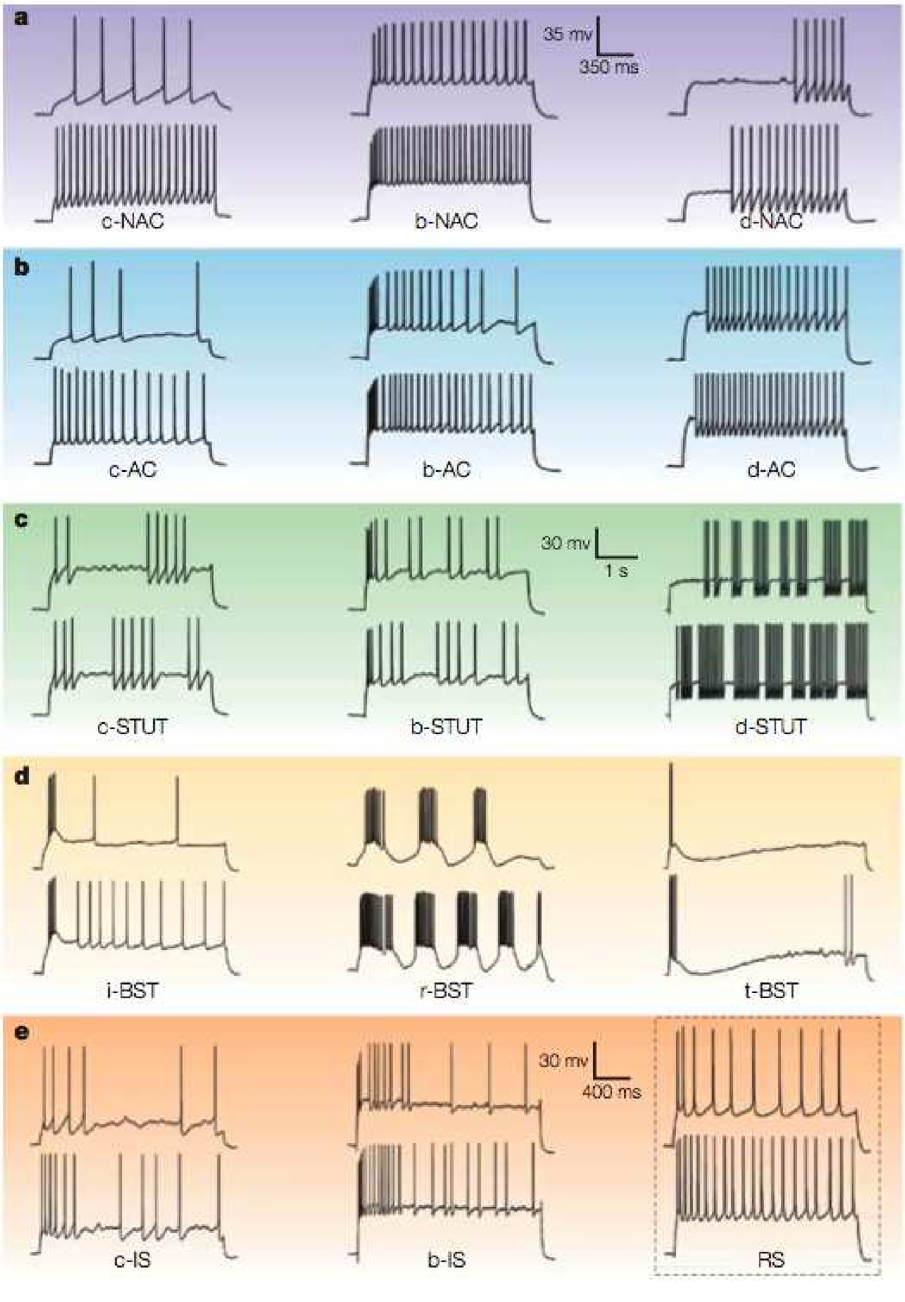

Figure A.5: *The five electrophysiological classes of interneurons (top to bottom) with their subclasses (left to right, see text). In the dashed-lined square at the bottom right corner of the table, examples of regular spiking from excitatory cells are shown for comparison (From [78]).*

APPENDIX **B**

NOTATIONS AND BACKGROUND MATERIAL

B.1 INTRODUCTION

A useful viewpoint that is used here is to consider the state vector of the neural field as a mapping from a closed time interval J containing the origin 0 into one of the spaces discussed in the previous section. We note $C(\mathrm{J};\mathbf{C}_{\mathrm{n}}(\Omega))$ the set of continuous mappings from J to the Banach space $\mathbf{C}_n(\Omega)$ and $C(\mathrm{J};\mathbf{L}^2_{\mathrm{n}}(\Omega))$ the set of continuous mappings from J to the Hilbert (hence Banach) space $\mathbf{L}^2_n(\Omega)$, see, e.g., [32].

B.2 MATRIX NORMS AND SPACES OF FUNCTIONS

We note $\mathcal{M}_{n\times n}$ the set of $n \times n$ real matrices. We consider the matrix norm,

$$\|\mathbf{M}\|_\infty = \max_i \sum_j |M_{ij}|$$

We note $\mathbf{C}_{n\times n}(\Omega)$ the set of continuous functions from Ω to $\mathcal{M}_{n\times n}$ with the infinity norm. This is a Banach space for the norm induced by the infinity norm on $\mathcal{M}_{n\times n}$. Let M be an element of $\mathbf{C}_{n\times n}(\Omega)$, we note and define $\|\mathbf{M}\|_{n\times n,\infty}$ as

$$\|\mathbf{M}\|_{n\times n,\infty} = \sup_{\mathbf{r}\in\Omega} \max_i \sum_j |M_{ij}(\mathbf{r})| = \max_i \sup_{\mathbf{r}\in\Omega} \sum_j |M_{ij}(\mathbf{r})|$$

We also note $\mathbf{C}_n(\Omega)$ the set of continuous functions from Ω to $\mathbb{R}^n$ with the infinity norm. This is also a Banach space for the norm induced by the infinity norm of $\mathbb{R}^n$. Let x be an element of $\mathbf{C}_n(\Omega)$, we note and define $\|\mathbf{x}\|_{n,\infty}$ as

$$\|\mathbf{x}\|_{n,\infty} = \sup_{\mathbf{r}\in\Omega} \max_i |x_i(\mathbf{r})| = \max_i \sup_{\mathbf{r}\in\Omega} |x_i(\mathbf{r})|$$

We can similarly define the norm $\|.\|_{n\times n,\infty}$ (resp. $\|.\|_{n,\infty}$) for the space $\mathbf{C}_{n\times n}(\Omega\times\Omega)$ (resp. $\mathbf{C}_n(\Omega\times\Omega)$).
We have the following

Lemma B.2.1. *Given* $\mathbf{x} \in \mathbf{C}_n(\Omega)$ *and* $\mathbf{M} \in \mathbf{C}_{n\times n}(\Omega)$ *we have*

$$\|\mathbf{M}\,\mathbf{x}\|_{n,\infty} \leq \|\mathbf{M}\|_{n\times n,\infty}\,\|\mathbf{x}\|_{n,\infty}$$

More precisely, we have for all $\mathbf{r} \in \Omega$

$$\|\mathbf{M}(\mathbf{r})\,\mathbf{x}(\mathbf{r})\|_\infty \leq \|\mathbf{M}(\mathbf{r})\|_\infty \|\mathbf{x}(\mathbf{r})\|_\infty$$

The same results hold for $\Omega \times \Omega$ *instead of* Ω.

Proof. Let $\mathbf{y} = \mathbf{M}\,\mathbf{x}$, we have

$$y_i(\mathbf{r}) = \sum_j M_{ij}(\mathbf{r}) x_j(\mathbf{r})$$

and therefore

$$|y_i(\mathbf{r})| \leq \sum_j |M_{ij}(\mathbf{r})|\,|x_j(\mathbf{r})| \leq \sum_j |M_{ij}(\mathbf{r})|\,\|\mathbf{x}(\mathbf{r})\|_\infty,$$

so, taking the $\max_i$

$$\|\mathbf{y}(\mathbf{r})\|_\infty \leq \|\mathbf{M}(\mathbf{r})\|_\infty\,\|\mathbf{x}(\mathbf{r})\|_\infty$$

from which the first statement easily comes. □

We also consider the Frobenius norm on $\mathcal{M}_{n\times n}$

$$\|\mathbf{M}\|_F = \sqrt{\sum_{i,j=1}^{n} M_{ij}^2},$$

and consider the space $\mathbf{L}^2_{n\times n}(\Omega \times \Omega)$ of the functions from $\Omega \times \Omega$ to $\mathcal{M}_{n\times n}$ whose Frobenius norm is in $L^2(\Omega\times\Omega)$. If $\mathbf{W} \in \mathbf{L}^2_{n\times n}(\Omega\times\Omega)$ we note $\|\mathbf{W}\|_F^2 = \int_{\Omega\times\Omega} \|\mathbf{W}(\mathbf{r},\mathbf{r}')\|_F^2\,d\mathbf{r}\,d\mathbf{r}'$. Note that this implies that each element w_{ij}, $i,\ j = 1, \cdots, n$ is in $L^2(\Omega \times \Omega)$. We note $\mathbf{L}^2_n(\Omega)$ the set of square-integrable mappings from Ω to $\mathbb{R}^n$ and $\|\mathbf{x}\|_{n,2} = (\sum_j \|x_j\|_2^2)^{1/2}$ the corresponding norm. We have the following

Lemma B.2.2. *Given* $\mathbf{x} \in \mathbf{L}^2_n(\Omega)$ *and* $\mathbf{W} \in \mathbf{L}^2_{n\times n}(\Omega \times \Omega)$, *we define* $\mathbf{y}(\mathbf{r}) = \int_\Omega \mathbf{W}(\mathbf{r},\mathbf{r}')\mathbf{x}(\mathbf{r}')\,d\mathbf{r}'$. *This integral is well defined for almost all* $\mathbf{r}$, $\mathbf{y}$ *is in* $\mathbf{L}^2_n(\Omega)$ *and we have*

$$\|\mathbf{y}\|_{n,2} \leq \|\mathbf{W}\|_F\,\|\mathbf{x}\|_{n,2}.$$

Proof. Since each w_{ij} is in $L^2(\Omega \times \Omega)$, $w_{ij}(\mathbf{r}, .)$ is in $L^2(\Omega)$ for almost all $\mathbf{r}$, thanks to Fubini's theorem. So $w_{ij}(\mathbf{r}, .)x_j(.)$ is integrable for almost all $\mathbf{r}$ from what we deduce that $\mathbf{y}$ is well-defined for almost all $\mathbf{r}$. Next we have

$$|y_i(\mathbf{r})| \leq \sum_j \left| \int_\Omega w_{ij}(\mathbf{r},\mathbf{r}')\,x_j(\mathbf{r}')\,d\mathbf{r}' \right|$$

and (Cauchy-Schwarz):

$$|y_i(\mathbf{r})| \leq \sum_j \left(\int_\Omega w_{ij}^2(\mathbf{r},\mathbf{r}')\,d\mathbf{r}' \right)^{1/2} \|x_j\|_2,$$

from where it follows that (Cauchy-Schwarz again, discrete version):

$$|y_i(\mathbf{r})| \leq \left(\sum_j \|x_j\|_2^2 \right)^{1/2} \left(\sum_j \int_\Omega w_{ij}^2(\mathbf{r},\mathbf{r}')\,d\mathbf{r}' \right)^{1/2} = \|\mathbf{x}\|_{n,2} \left(\sum_j \int_\Omega w_{ij}^2(\mathbf{r},\mathbf{r}')\,d\mathbf{r}' \right)^{1/2},$$

from what it follows that $\mathbf{y}$ is in $\mathbf{L}^2_n(\Omega)$ (thanks again to Fubini's theorem) and

$$\|\mathbf{y}\|_{n,2}^2 \leq \|\mathbf{x}\|_{n,2}^2 \sum_{i,j} \int_{\Omega\times\Omega} w_{ij}^2(\mathbf{r},\mathbf{r}')\,d\mathbf{r}'\,d\mathbf{r} = \|\mathbf{x}\|_{n,2}^2\,\|\mathbf{W}\|_F^2.$$

□

B.3 SUMMARY OF IMPORTANT NOTATIONS

Table B.1 summarizes some notations which are introduced in chapter 4 and are used in several places.

Matrix functions	Definition (if applicable)	Where defined	Operators (if applicable)
$\mathbf{L}$	diagonal matrix of the inverse synaptic time constants	equation 4.4	
$\tau_{\max}$	largest time constant	definition 4.1.2	
$D\mathbf{S}_m$		definition 4.1.1	
$\mathbf{W}$		equations (4.9), (4.10), (4.11)	f_v, f_a, g_v
$\mathbf{W}_{cm}$	$\mathbf{W}D\mathbf{S}_m$	definition 4.3.1	g_m
$\mathbf{W}_{mc}$	$D\mathbf{S}_m\mathbf{W}$	definition 4.3.1	h_m

Table B.1: Summary of some important definitions.

APPENDIX **C**

COMPLEMENTS TO THE FUNCTIONAL ANALYSIS OF NEURAL FIELD MODELS

C.1 GLOBAL EXISTENCE OF SOLUTIONS

We complete the proof of proposition (4.2.3) by computing the constant $\tau > 0$ such that for any initial condition $(t_0, \mathbf{V}_0) \in \mathbb{R} \times \mathcal{F}$, the existence and uniqueness of the solution $\mathbf{V}$ is guaranteed on the closed interval $[t_0 - \tau, t_0 + \tau]$.
We refer to [6] and exploit the

Theorem C.1.1. *Let $\mathcal{F}$ be a Banach space and $c > 0$. We consider the initial value problem:*

$$\begin{cases} \mathbf{V}'(t) &= f(t, \mathbf{V}(t)) \\ \mathbf{V}(t_0) &= \mathbf{V}_0 \end{cases}$$

for $|t - t_0| < c$ where $\mathbf{V}_0$ is an element of $\mathcal{F}$ and $f : [t_0 - c, t_0 + c] \times \mathcal{F} \to \mathcal{F}$ is continuous. Let $b > 0$. We define the set $Q_{b,c} \equiv \{(t, \mathbf{X}) \in \mathbb{R} \times \mathcal{F},\ |t - t_0| \leq c \quad \text{and} \quad \|\mathbf{X} - \mathbf{V}_0\| \leq b\}$. Assume the function $f : Q_{b,c} \to \mathcal{F}$ is continuous and uniformly Lipschitz continuous with respect to its second argument, ie

$$\|f(t, \mathbf{X}) - f(t, \mathbf{Y})\| \leq K_{b,c} \|\mathbf{X} - \mathbf{Y}\|,$$

*where $K_{b,c}$ is a constant independent of t.
Let $M_{b,c} = \sup_{Q_{b,c}} \|f(t, \mathbf{X})\|$ and $\tau_{b,c} = \min\{b/M_{b,c}, c\}$.
Then the initial value problem has a unique continuously differentiable solution $\mathbf{V}(.)$ defined on the interval $[t_0 - \tau_{b,c}, t_0 + \tau_{b,c}]$.*

In our case, $f = f_v$ and all the hypotheses of the theorem hold, thanks to proposition 4.2.1 and the hypotheses of proposition 4.2.3, with

$$K_{b,c} = \|\mathbf{L}\|_\infty + |\Omega|\, DS_m \sup_{|t - t_0| \leq c} \|\mathbf{W}(\cdot, \cdot, t)\|_{n \times n, \infty},$$

where the $\sup$ is well defined (continuous function on a compact domain).
We have

$$M_{b,c} \leq \|\mathbf{L}\|_\infty \left(\|\mathbf{V}_0\|_{n,\infty} + b \right) + |\Omega|\, S_m W + I,$$

where $W=\sup_{|t-t_0|\leq c}\|\mathbf{W}(\cdot,\cdot,t)\|_{n\times n,\infty}$ and $I=\sup_{|t-t_0|\leq c}\|\mathbf{I}_{\text{ext}}(\cdot,t)\|_{n,\infty}$.
So

$$b/M_{b,c}\geq\frac{1}{\|\mathbf{L}\|_\infty+\frac{\|\mathbf{L}\|_\infty\,\|\mathbf{V}_0\|_{n,\infty}+|\Omega|\,S_m\,W+I}{b}}.$$

Hence, for $c\geq\frac{1}{2\|\mathbf{L}\|_\infty}$ and b big enough, we have $\tau_{b,c}\geq\frac{1}{2\|\mathbf{L}\|_\infty}$ and we can set $\tau=\frac{1}{2\|\mathbf{L}\|_\infty}$. A similar proof applies to the case $f=f_a$ and the one of proposition 4.5.3.

C.2 COMPUTATION OF OPERATOR NORMS

We give a method to compute the norms $\|g\|_{\mathcal{G}}$ and $\|g^*\|_{\mathcal{G}_c^\perp}$ for an operator g of the form

$$g(\mathbf{x})(\mathbf{r})=\int_\Omega\mathbf{W}(\mathbf{r},\mathbf{r}')\,\mathbf{x}(\mathbf{r}')\,d\mathbf{r}'.$$

Since $\mathcal{G}$ (respectively $\mathcal{G}_c^\perp$) is dense in the Hilbert space $\mathbf{L}^2(\Omega)$ (respectively $\mathbf{L}_0^2(\Omega)$, the subspace of $\mathbf{L}^2(\Omega)$ of functions with zero mean), we have $\|g\|_{\mathcal{G}}=\|g\|_{\mathbf{L}^2}$ and $\|g^*\|_{\mathcal{G}_c^\perp}=\|g^*\|_{\mathbf{L}_0^2}$. We consider the compact self-adjoint operators

$$G=g^*g:\mathbf{L}^2\to\mathbf{L}^2$$

and

$$G_c^\perp=g^*\mathcal{P}g:\mathbf{L}_0^2\to\mathbf{L}_0^2,$$

where $\mathcal{P}$ is the orthogonal projection on $\mathbf{L}_0^2$. We compute the norms of the two self-adjoint positive operators G and $G_c^\perp$, and use the relations

$$\|G\|_{\mathbf{L}^2}=\|g\|_{\mathbf{L}^2}^2,$$

and

$$\|G_c^\perp\|_{\mathbf{L}_0^2}=\|g^*\mathcal{P}^*\mathcal{P}g\|_{\mathbf{L}_0^2}=\|g^*\mathcal{P}^*\|_{\mathbf{L}_0^2}^2=\|g^*\|_{\mathbf{L}_0^2}^2.$$

Let T be a compact self-adjoint positive operator on a Hilbert space $\mathcal{H}$. Its largest eigenvalue is $\lambda=\|T\|_{\mathcal{H}}$. Let $x\in\mathcal{H}$. If $x\notin\operatorname{Ker}(\lambda\mathrm{Id}-T)^\perp$, then, according to, e.g., [30],

$$\lim_{n\to\infty}\|T^nx\|_{\mathcal{H}}/\|T^{n-1}x\|_{\mathcal{H}}=\lambda.$$

This method can be applied to g_m^L and h_m^L, and generalized to the computation of the $\|.\|_{\mathcal{G}_c^{P\perp}}$ norm.

C.3 COMPLEMENTS TO THE STUDY OF HIGHER ORDER PSPS

Expressing the exponential as a power series in the definition of $\boldsymbol{\mathcal{M}}$ and computing the powers of the block matrix $\boldsymbol{\mathcal{L}}$, we easily find a block expression of $\boldsymbol{\mathcal{M}}$ depending on $\mathbf{L}$

$$\boldsymbol{\mathcal{M}}=\begin{pmatrix}\mathbf{L}/4+5\mathbf{L}^{-1}/4 & \mathbf{L}^{-2}/2\\ \mathbf{L}^{-2}/2 & \mathbf{L}^{-1}/4+\mathbf{L}^{-3}/4\end{pmatrix}.$$

$\boldsymbol{\mathcal{M}}$ is diagonalizable, as a symmetric positive definite matrix, and has at most $2n$ distinct eigenvalues. More precisely, these eigenvalues are the roots of the second order polynomials

$$\lambda^2-\left(\frac{1}{4\,\tau_i}+\frac{3\,\tau_i}{2}+\frac{\tau_i^3}{4}\right)\lambda+\frac{1}{16}+\frac{3\,\tau_i^2}{8}+\frac{\tau_i^4}{16},\quad 1\leq i\leq n.$$

The largest eigenvalue of each of these polynomials is

$$\lambda(\tau_i) = \frac{1}{8\,\tau_i}\left(1 + 6\,\tau_i^2 + \tau_i^4 + \sqrt{1 + 8\,\tau_i^2 + 14\,\tau_i^4 + 8\,\tau_i^6 + \tau_i^8}\right),$$

so that $\lambda_{\max}$ is simply $\max_i \lambda(\tau_i)$. Note that since the function $\lambda(\tau)$ is not monotonous, $\lambda_{\max}$ is not necessarily equal to $\lambda(\tau_{\max})$.

Glossary

CC cortico-cortical. 40, 41

CT cortico-thalamic. 40, 41

EEG electroencephalography. 50, 53, 55, 60, 65, 128

GABA gamma aminobutyric acid. 41

IB intrinsically bursting. 40

LTS low-threshold spiking. 44–46

PC pyramidal cell. 35, 38–41, 43–45, 140, 142, 144, 147–149, 151, 153

RS regular spiking. 40

SSC spiny stellate cell. 35, 38, 39, 42

V1 primary visual cortex. 31, 35, 127, 128, 141, 146

VSD voltage-sensitive dye. 130–133, 135

Bibliography

[1] LF Abbott and W.G. Regehr. Synaptic computation. *Nature*, 431:796–803, 2004.

[2] A. Ajima and S. Tanaka. Spatial Patterns of Excitation and Inhibition Evoked by Lateral Connectivity in Layer 2/3 of Rat Barrel Cortex. *Cerebral Cortex*, 16(8):1202, 2006.

[3] S.-I. Amari. Dynamics of pattern formation in lateral-inhibition type neural fields. *Biological Cybernetics*, 27(2):77–87, jun 1977.

[4] S.I. Amari. Homogeneous nets of neuron-like elements. *Biological Cybernetics*, 17(4):211–220, 1975.

[5] Fatihcan M. Atay and Axel Hutt. Stability and bifurcations in neural fields with finite propagation speed and general connectivity. *SIAM Journal on Applied Mathematics*, 65(2):644–666, 2005.

[6] Kendall Atkinson and Weimin Han. *Theoretical Numerical Analysis*. Springer-Verlag, 2001.

[7] P Bannister. Inter- and intra-laminar connections of pyramidal cells in the neocortex. *Neuroscience Research*, 53(2):95–103, 2005.

[8] C Beaulieu and M Colonnier. The number of neurons in the different laminae of the binocular and monocular regions of area 17 in the cat. *The Journal of Comparative Neurology*, 217(3):337–344, 1983.

[9] C Beaulieu and M Colonnier. A laminar analysis of the number of round-asymmetrical and flat-symmetrical synapses on spines, dendritic trunks, and cell bodies in area 17 of the cat. *The Journal of Comparative Neurology*, 266(4):478–494, 1987.

[10] N. Berglund. *Geometrical theory of dynamical systems*. Citebase, 2001.

[11] N. Berglund. *Perturbation theory of dynamical systems*. Citebase, 2001.

[12] T. Binzegger, R.J. Douglas, and K.A.C. Martin. Stereotypical Bouton Clustering of Individual Neurons in Cat Primary Visual Cortex. *Journal of Neuroscience*, 27(45):12242, 2007.

[13] Tom Binzegger, R.J. Douglas, and K.A.C. Martin. A quantitative map of the circuit of cat primary visual cortex. *The Journal of Neuroscience*, 24(39):8441–8453, September 2004.

[14] W.H. Bosking, Y. Zhang, B. Schofield, and D. Fitzpatrick. Orientation selectivity and the arrangement of horizontal connections in tree shrew striate cortex. *The Journal of Neuroscience*, 17(6):2112–2127, 1997.

[15] Valentino Braitenberg and Almut Schüz. *Cortex: Statistics and Geometry of Neuronal Connectivity*. Springer, 2nd edition, 1998.

[16] M. Brecht, A. Roth, and B. Sakmann. Dynamic receptive fields of reconstructed pyramidal cells in layers 3 and 2 of rat somatosensory barrel cortex. *The Journal of Physiology*, 553(1):243–265, 2003.

[17] K. Brodmann. *Vergleichende Lokalisationslehre der Grobhirnrinde*. J.A.Barth, Leipzig, 1909.

[18] D.P. Buxhoeveden and M.F. Casanova. The minicolumn hypothesis in neuroscience. *Brain*, 125:935–951, 2002.

[19] P. Buzás, K. Kovacs, A.S. Ferecskó, JM Budd, UT Eysel, and Z.F. Kisvárday. Model-based analysis of excitatory lateral connections in the visual cortex. *J Comp Neurol*, 499(6):861–881, 2006.

[20] L. M. Chalupa and J.S. Werner, editors. *The visual neurosciences*. MIT Press, 2004.

[21] T.P. Chen and S.I. Amari. Exponential convergence of delayed dynamical systems. *Neural Computation*, 13:621–635, 2001.

[22] I. Cobos, M.E. Calcagnotto, A.J. Vilaythong, M.T. Thwin, J.L. Noebels, S.C. Baraban, and J.L.R. Rubenstein. Mice lacking dlx1 show subtype-specific loss of interneurons, reduced inhibition and epilepsy. *Nature Neuroscience*, 8:1059–1068, 2005.

[23] S. Coombes, N.A Venkov, L. Shiau, I. Bojak, D.T.J. Liley, and C.R. Laing. Modeling electrocortical activity through local approximations of integral neural field equations. *Physical Review E*, 76, 2007.

[24] Stephen Coombes. Waves, bumps, and patterns in neural fields theories. *Biological Cybernetics*, 93(2):91–108, 2005.

[25] Olivier David, Diego Cosmelli, and Karl J. Friston. Evaluation of different measures of functional connectivity using a neural mass model. *NeuroImage*, 21:659–673, 2004.

[26] Olivier David and Karl J. Friston. A neural mass model for MEG/EEG: coupling and neuronal dynamics. *NeuroImage*, 20:1743–1755, 2003.

[27] P. Dayan and L. F. Abbott. *Theoretical Neuroscience : Computational and Mathematical Modeling of Neural Systems*. MIT Press, 2001.

[28] J. DeFelipe, P. Marco, I. Busturia, and A. Merchàn-Pérez. Estimation of the number of synapses in the cerebral cortex: Methodological considerations. *Cerebral Cortex*, 9(7):722–732, 1999.

[29] Javier DeFelipe, Lidia Alonso-Nanclares, and Jon I. Arellano. Microstructure of the neocortex: Comparative aspects. *Journal of Neurocytology*, 31:299–316, 2002.

[30] Jean Dieudonné. *Foundations of Modern Analysis*. Academic Press, 1960.

[31] Bard Ermentrout. Neural networks as spatio-temporal pattern-forming systems. *Reports on Progress in Physics*, 61:353–430, 1998.

[32] L.C. Evans. *Partial Differential Equations*, volume 19 of *Graduate Studies in Mathematics*. AMS, 1998.

[33] Y. Fang and T.G. Kincaid. Stability analysis of dynamical neural networks. *IEEE Transactions on Neural Networks*, 7(4):996–1006, jul 1996.

[34] O. Faugeras and F. Grimbert. Bumps in simple two-dimensional neural field models. RR 6375, INRIA, dec 2007.

[35] O. Faugeras, R. Veltz, and F. Grimbert. Persistent neural states: stationary localized activity patterns in nonlinear continuous n-population, q-dimensional neural networks. Research Report 6393, INRIA, 12 2007.

[36] Olivier Faugeras, François Grimbert, and Jean-Jacques Slotine. Stability and synchronization in neural fields. Technical Report RR-6212, INRIA, 2007.

[37] D. Feldmeyer, J. Lübke, and B. Sakmann. Efficacy and connectivity of intracolumnar pairs of layer 2/3 pyramidal cells in the barrel cortex of juvenile rats. *The Journal of Physiology*, 575(2):583, 2006.

[38] Stefanos E. Folias and Paul C. Bressloff. Breathing pulses in an excitatory neural network. *SIAM Journal on Applied Dynamical Systems*, 3(3):378–407, 2004.

[39] W.J. Freeman. Mass action in the nervous system. *Academic Press, New York*, 1975.

[40] W.J. Freeman. Simulation of chaotic EEG patterns with a dynamic model of the olfactory system. *Biological Cybernetics*, 56:139–150, 1987.

[41] W. Gerstner and W. M. Kistler. Mathematical formulations of hebbian learning. *Biological Cybernetics*, 87:404–415, 2002.

[42] PS Goldman-Rakic. Cellular basis of working memory. *Neuron*, 14(3):477–85, 1995.

[43] Geoffrey J. Goodhill and Miguel Á. Carreira-Perpiñán. Cortical columns. *Encyclopedia of Cognitive Science, Macmillan Publishers Ltd.*, 2002.

[44] J.P. Gottlieb and A. Keller. Intrinsic circuitry and physiological properties of pyramidal neurons in rat barrel cortex. *Experimental Brain Research*, 115(1):47–60, 1997.

[45] F. Grimbert. A brief overview of intracortical circuits. RR 6325, INRIA, oct 2007.

[46] F. Grimbert and O. Faugeras. Bifurcation analysis of Jansen's neural mass model. *Neural Computation*, 18(12):3052–3068, December 2006.

[47] F. Grimbert, O. Faugeras, and F. Chavane. Neural field model of VSD optical imaging signals. Research Report 6398, INRIA, 12 2007.

[48] A. Grinvald and R. Hildesheim. VSDI: a new era in functional imaging of cortical dynamics. *Nature Reviews Neuroscience*, 5(11):874–885, 2004.

[49] Stefan Haeusler and Wolfgang Maass. A statistical analysis of information-processing properties of lamina-specific cortical microcircuits models. *Cerebral Cortex*, 17:149–162, jan 2007.

[50] S. Hestrin and M. Galarreta. Electrical synapses define networks of neocortical GABAergic neurons. *TINS*, 28(6):304–309, 2005.

[51] J. J. Hopfield. Neurons with graded response have collective computational properties like those of two-state neurons. *Proceedings of the National Academy of Sciences, USA*, 81(10):3088–3092, 1984.

[52] F.C. Hoppenstaedt and E.M. Izhikevich. *Weakly Connected Neural Networks*. Springer-Verlag, New York, 1997.

[53] D.H. Hubel and T.N. Wiesel. Receptive fields, binocular interaction and functional architecture in the cat visual cortex. *J Physiol*, 160:106–154, 1962.

[54] D.H. Hubel and T.N. Wiesel. Functional architecture of macaque monkey. *Proceedings of the Royal Society, London B*, pages 1–59, 1977.

[55] Gérard Ioos and Moritz Adelmeyer. *Topics in Bifurcation Theory and Applications*. Advanced Series in Nonlinear Dynamics. World Scientific, 2nd edition, 1999.

[56] Eugene M. Izhikevich. *Dynamical Systems in Neuroscience: The Geometry of Excitability and Bursting*. The MIT Press, 2007.

[57] D. Jancke, F. Chavane, S. Naaman, and A. Grinvald. Imaging cortical correlates of illusion in early visual cortex. *Nature*, 428:423–426, 2004.

[58] Ben H. Jansen and Vincent G. Rit. Electroencephalogram and visual evoked potential generation in a mathematical model of coupled cortical columns. *Biological Cybernetics*, 73:357–366, 1995.

[59] Ben H. Jansen, George Zouridakis, and Michael E. Brandt. A neurophysiologically-based mathematical model of flash visual evoked potentials. *Biological Cybernetics*, 68:275–283, 1993.

[60] E.G. Jones and A. Peters, editors. *Cerebral cortex, functional properties of cortical cells*, volume 2. Plenum, New York, 1984.

[61] E.R. Kandel, J.H. Schwartz, and T.M. Jessel. *Principles of Neural Science*. McGraw-Hill, 4th edition, 2000.

[62] U. Kim and F.F. Ebner. Barrels and septa: Separate circuits in rat barrel field cortex. *The Journal of Comparative Neurology*, 408(4):489–505, 1999.

[63] ZF Kisvárday, JM Crook, P. Buzás, and UT Eysel. Combined physiological-anatomical approaches to study lateral inhibition. *J Neurosci Methods*, 103(1):91–106, 2000.

[64] Z.F. Kisvárday, A.S. Ferecskó, K. Kovács, P. Buzás, J.M.L. Budd, and U.T. Eysel. One axon-multiple functions: Specificity of lateral inhibitory connections by large basket cells. *Journal of Neurocytology*, 31(3):255–264, 2002.

[65] ZF Kisvárday, E. Tóth, M. Rausch, and UT Eysel. Orientation-specific relationship between populations of excitatory and inhibitory lateral connections in the visual cortex of the cat. *Cerebral Cortex*, 7:605–618, 1997.

[66] J. Kozloski, F. Hamzei-Sichani, and R. Yuste. Stereotyped position of local synaptic targets in neocortex. *Science*, 293(5531):868–872, 2001.

[67] S. Kubota and K. Aihara. Analyzing global dynamics of a neural field model. *Neural Processing Letters*, 21:133–141, 2005.

[68] Yuri A. Kuznetsov. *Elements of Applied Bifurcation Theory*. Applied Mathematical Sciences. Springer, 2nd edition, 1998.

[69] C.R. Laing, W.C. Troy, B. Gutkin, and G.B. Ermentrout. Multiple Bumps in a Neuronal Model of Working Memory. *SIAM Journal on Applied Mathematics*, 63(1):62–97, 2002.

[70] M.T. Lippert, K. Takagaki, W. Xu, X. Huang, and J.Y. Wu. Methods for Voltage-Sensitive Dye Imaging of Rat Cortical Activity With High Signal-to-Noise Ratio. *Journal of Neurophysiology*, 98(1):502, 2007.

[71] F.H. Lopes da Silva, A. Hoeks, and L.H. Zetterberg. Model of brain rhythmic activity. *Kybernetik*, 15:27–37, 1974.

[72] F.H. Lopes da Silva, A. van Rotterdam, P. Barts, E. van Heusden, and W. Burr. Model of neuronal populations. the basic mechanism of rhythmicity. *M.A. Corner, D.F. Swaab (eds) Progress in brain research, Elsevier, Amsterdam*, 45:281–308, 1976.

[73] J. Lübke, A. Roth, D. Feldmeyer, and B. Sakmann. Morphometric Analysis of the Columnar Innervation Domain of Neurons Connecting Layer 4 and Layer 2/3 of Juvenile Rat Barrel Cortex. *Cerebral Cortex*, 13(10):1051–1063, 2003.

[74] Jennifer S. Lund, Alessandra Angelucci, and Paul C. Bressloff. Anatomical substrates for functional columns in macaque monkey primary visual cortex. *Cerebral Cortex*, 12:15–24, 2003.

[75] A.M. Lyapunov. *Stability of Motion*. Academic Press, 1966.

[76] J.N. MacLean, B.O. Watson, G.B. Aaron, and R. Yuste. Internal dynamics determine the cortical response to thalamic stimulation. *Neuron*, 48:811–823, 2005.

[77] H. Markram. The Blue Brain Project. *Nature Rev. Neurosci*, 7(2):153–160, 2006.

[78] H. Markram, M. Toledo-Rodriguez, Y. Wang, A. Gupta, G. Silberberg, and C. Wu. Interneurons of the neocortical inhibitory system. *Nature Reviews Neuroscience*, 5:793–804, 2004.

[79] Kiyotoshi Matsuoka. Stability conditions for nonlinear continuous neural networks with asymmetric connection weights. *Neural Networks*, 5:495–500, 1992.

[80] C. Monier, F. Chavane, P. Baudot, L. Graham, and Y. Frégnac. Orientation and direction selectivity of excitatory and inhibitory inputs in visual cortical neurons: a diversity of combinations produces spike tuning. *Neuron*, 37:663–680, 2003.

[81] V.B. Mountcastle. Modality and topographic properties of single neurons of cat's somatosensory cortex. *Journal of Neurophysiology*, 20:408–434, 1957.

[82] V.B. Mountcastle. The columnar organization of the neocortex. *Brain*, 120:701–722, 1997.

[83] John Nolte. *The Human Brain*. Mosby, 5th edition, 2001.

[84] K. Ohki, S. Chung, Y.H. Ch'ng, P. Kara, and R.C. Reid. Functional imaging with cellular resolution reveals precise micro-architecture in visual cortex. *Nature*, 433:597–603, 2005.

[85] MR Owen, CR Laing, and S. Coombes. Bumps and rings in a two-dimensional neural field: splitting and rotational instabilities. *New Journal of Physics*, 9(10):378, 2007.

[86] L. Perko. *Differential Equations and Dynamical Systems*. Springer, 2001. Third Edition.

[87] A. Peters and E.G. Jones, editors. *Cerebral cortex, cellular components of the cerebral cortex*, volume 1. Plenum, New York, 1984.

[88] A Peters and E Yilmaz. Neuronal organization in area 17 of cat visual cortex. *Cerebral Cortex*, 3:49–68, 1993.

[89] C.C.H. Petersen, A. Grinvald, and B. Sakmann. Spatiotemporal dynamics of sensory responses in layer 2/3 of rat barrel cortex measured in vivo by voltage-sensitive dye imaging combined with whole-cell voltage recordings and neuron reconstructions. *The Journal of Neuroscience*, 23(3):1298–1309, 2003.

[90] Q.C. Pham and J.J.E. Slotine. Stable concurrent synchronization in dynamic system networks. *Neural Networks*, 20(1), 2007.

[91] Arkady Pikovsky, Jurgen Kurths, and Michael Rosenblum. *Synchronization: A Universal Concept in Nonlinear Sciences*. Cambridge University Press, 2001.

[92] D. Pinto, R. Jackson, and C.E. Wayne. Existence and stability of traveling pulses in a continuous neuronal network. *SIAM J. of Appl. Dyn. Syst.*, 4:954–984, 2005.

[93] D.J. Pinto and G.B. Ermentrout. Spatially structured activity in synaptically coupled neuronal networks: 1. traveling fronts and pulses. *SIAM J. of Appl. Math.*, 62:206–225, 2001.

[94] D.J. Pinto and G.B. Ermentrout. Spatially structured activity in synaptically coupled neuronal networks: 2. standing pulses. *SIAM J. of Appl. Math.*, 62:226–243, 2001.

[95] A.V. Rangan, D. Cai, and D.W. McLaughlin. Inaugural Article: Modeling the spatiotemporal cortical activity associated with the line-motion illusion in primary visual cortex. *Proc Natl Acad Sci US A*, 102(52):18793–18800, 2005.

[96] J. Rinzel and G.B. Ermentrout. *Analysis of neuronal excitability and oscillations, in 'Methods in Neuronal Modeling: From Ions to Networks', Koch, C. and Segev, I. Eds.*, pages 251–291. The MIT Press, 1998.

[97] P.A. Salin and J. Bullier. Corticocortical connections in the visual system: structure and function. *Psychol. Bull.*, 75:107–154, 1995.

[98] D. Schubert, R. Kötter, and J.F. Staiger. Mapping functional connectivity in barrel-related columns reveals layer-and cell type-specific microcircuits. *Brain Structure and Function*, 212(2):107–119, 2007.

[99] D. Schubert, J.F. Staiger, N. Cho, R. Kötter, K. Zilles, and H.J. Luhmann. Layer-Specific Intracolumnar and Transcolumnar Functional Connectivity of Layer V Pyramidal Cells in Rat Barrel Cortex. *Journal of Neuroscience*, 21(10):3580, 2001.

[100] G. Silberberg, A. Gupta, and H. Markram. Stereotypy in neocortical microcircuits. *Trends in Neurosciences*, 25(5):227–230, 2002.

[101] G. Silberberg and H. Markram. Disynaptic inhibition between neocortical pyramidal cells mediated by martinotti cells. *Neuron*, 53:735–746, 2007.

[102] J.J.E. Slotine and W. Li. *Applied nonlinear control*. Prentice Hall Englewood Cliffs, NJ, 1991.

[103] P. Somogyi, G. Tamas, R. Lujan, and E.H. Buhl. Salient features of synaptic organisation in the cerebral cortex. *Brain Res Rev*, 26:113–135, 1998.

[104] S. Song, P.J. Sjöström, M. Reigl, S. Nelson, and D.B. Chklovskii. Highly nonrandom features of synaptic connectivity in local cortical circuits. *PLoS Biology*, 3(3):507–519, 2005.

[105] A. Stepanyants, J.A. Hirsch, L.M. Martinez, Z.F. Kisvárday, A.S. Ferecskó, and D.B. Chklovskii. Local Potential Connectivity in Cat Primary Visual Cortex. *Cerebral Cortex*, 2007.

[106] A. Stepanyants, G. Tamás, and D.B. Chklovskii. Class-specific features of neuronal wiring. *Neuron*, 43:251–259, 2004.

[107] J. Szabadics, A. Lorincz, and G. Tamas. {beta} and {gamma} Frequency Synchronization by Dendritic GABAergic Synapses and Gap Junctions in a Network of Cortical Interneurons. *Journal of Neuroscience*, 21(15):5824, 2001.

[108] G. Tamás, E.H. Buhl, A. Lörincz, and P. Somogyi. Proximally targeted GABAergic synapses and gap junctions synchronize cortical interneurons. *Nature Neuroscience*, 3:366–371, 2000.

[109] G. Tamas, P. Somogyi, and E.H. Buhl. Differentially Interconnected Networks of GABAergic Interneurons in the Visual Cortex of the Cat. *Journal of Neuroscience*, 18(11):4255–4270, 1998.

[110] Alex M. Thomson and A. Peter Bannister. Interlaminar connections in the neocortex. *Cerebral Cortex*, 13:5–14, January 2003.

[111] Alex M. Thomson, A. Peter Bannister, Audrey Mercer, and Oliver T. Morris. Target and temporal pattern selection at neocortical synapses. *The Royal Society*, 357:1781–1791, 2002.

[112] A.M. Thomson and C. Lamy. Functional maps of neocortical local circuitry. *Frontiers in Neuroscience*, 1(1):19–42, nov 2007.

[113] A.M. Thomson and O.T. Morris. Selectivity in the inter-laminar connections made by neocortical neurones. *Journal of Neurocytology*, 31(3-5):239–246, 2004.

[114] R.D. Traub, D. Contreras, M.O. Cunningham, H. Murray, F.E. LeBeau, A. Roopun, A. Bibbig, W.B. Wilent, M.J. Higley, and M.A. Whittington. Single-column thalamocortical network model exhibiting gamma oscillations, sleep spindles, and epileptogenic bursts. *Journal of Neurophysiology*, 93(4):2194–2232, 2005.

[115] T.R. Tucker and L.C. Katz. Recruitment of Local Inhibitory Networks by Horizontal Connections in Layer 2/3 of Ferret Visual Cortex. *Journal of Neurophysiology*, 89(1):501–512, 2003.

[116] T.R. Tucker and L.C. Katz. Spatiotemporal Patterns of Excitation and Inhibition Evoked by the Horizontal Network in Layer 2/3 of Ferret Visual Cortex. *Journal of Neurophysiology*, 89(1):488–500, 2003.

[117] A. van Rotterdam, F.H. Lopes da Silva, J. van den Ende, M.A. Viergever, and A.J. Hermans. A model of the spatial-temporal characteristics of the alpha rhythm. *Bulletin of Mathematical Biology*, 44(2):283–305, 1982.

[118] Jo Watts and Alex M. Thomson. Excitatory and inhibitory connections show selectivity in the neocortex. *Journal of Physiology*, 562.1:89–97, 2005.

[119] F. Wendling, J.J. Bellanger, F. Bartolomei, and P. Chauvel. Relevance of nonlinear lumped-parameter models in the analysis of depth-EEG epileptic signals. *Biological Cybernetics*, 83:367–378, 2000.

[120] H.R. Wilson and J.D. Cowan. Excitatory and inhibitory interactions in localized populations of model neurons. *Biophys. J.*, 12:1–24, 1972.

[121] H.R. Wilson and J.D. Cowan. A mathematical theory of the functional dynamics of cortical and thalamic nervous tissue. *Biological Cybernetics*, 13(2):55–80, sep 1973.

[122] Y. Yoshimura, JL Dantzker, and EM Callaway. Excitatory cortical neurons form fine-scale functional networks. *Nature*, 433(7028):868–73, 2005.